



Technische Universität München

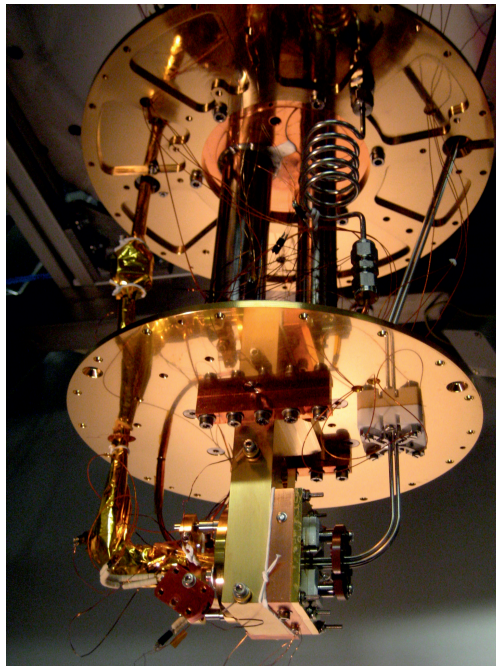


Physik Department



Construction and Operation of a Cryogenic Source for Cold Polar Molecules

Christian Sommer



Dissertation

Max-Planck-Institut für Quantenoptik, Garching
and Physik Department, Technische Universität München

April 2011

Technische Universität München
Max-Planck-Institut für Quantenoptik

Construction and Operation of a Cryogenic Source for Cold Polar Molecules

Christian Sommer

Vollständiger Abdruck der von der Fakultät für Physik der Technischen Universität München zur Erlangung des akademischen Grades eines

Doktors der Naturwissenschaften (Dr. rer. nat.)

genehmigten Dissertation.

Vorsitzender : Univ.-Prof. Dr. H. Friedrich

Prüfer der Dissertation : 1. Hon.-Prof. Dr. G. Rempe
2. Univ.-Prof. Dr. R. Kienberger

Die Dissertation wurde am 11.04.2011 bei der Technischen Universität München eingereicht und durch die Fakultät für Physik am 19.05.2011 angenommen.

Abstract

This thesis reports on the combination of buffer-gas cooling with electric velocity filtering to produce a high-density guided beam of slow and internally cold polar molecules. In the continuous source, warm molecules are first cooled by collisions with a cryogenic helium buffer gas. Cold molecules are then extracted by means of an electric quadrupole guide. For ammonia (ND_3) the source produces fluxes up to $(7 \pm 7) \times 10^{10} \text{ s}^{-1}$ with peak densities up to $(1.0 \pm 0.6) \times 10^9 \text{ cm}^{-3}$. For formaldehyde (H_2CO) the population of individual rotational states in the guide is monitored by depletion spectroscopy, resulting in single-state populations up to $(82 \pm 10) \%$. Furthermore, the technical aspects and the operation of the cryogenic source are described. Several optimization experiments are carried out to obtain the best performance. The versatility of our source is demonstrated by the production of guided beams of different molecular species.

This thesis also reports on a technique to produce pulses of slow, guided molecules with narrow velocity distribution around a tunable velocity. The pulses are generated by sequentially switching the voltages on adjacent segments of an electric quadrupole guide. This is done synchronously with the molecules propagating at the desired velocity. This technique is demonstrated for ND_3 , delivering pulses with a velocity in the range of 20 – 100 m/s and a relative velocity spread of $(16 \pm 2) \%$ full width at half maximum. The observations are in good agreement with numerical simulations and analytical calculations.

Zusammenfassung

Die vorliegende Arbeit berichtet über die erfolgreiche Kombination von Puffergaskühlung mit dem Verfahren der elektrischen Geschwindigkeitsfilterung. Dies dient zur Erzeugung eines geführten Molekülstrahls hoher Dichte, der langsame und intern kalte Moleküle beinhaltet. Warme Moleküle werden in der Quelle zunächst durch Kollisionen mit einem kryogenen Puffergas gekühlt. Die gekühlten Moleküle werden anschließend mittels einer elektrischen Quadrupolführung extrahiert. Für Ammoniak (ND_3) produziert die Quelle Flüsse bis zu $(7 \pm 7) \times 10^{10} \text{ s}^{-1}$ mit Dichten bis zu $(1.0 \pm 1.0) \times 10^9 \text{ cm}^{-3}$ im Strahlzentrum. Für Formaldehyd (H_2CO) wurde die Besetzung der Rotationszustände geführter Moleküle durch Entvölkerungs-Spektroskopie überprüft, wobei sich Besetzungen von bis zu $(82 \pm 10) \%$ für einzelne Zustände ergeben haben. Weiterhin werden die technischen Aspekte und die Bedienung der kryogenen Quelle beschrieben. Zahlreiche Experimente zur Optimierung des Leistungsvermögens wurden durchgeführt. Die breite Anwendbarkeit unserer Quelle wurde durch die Produktion von kalten Molekülstrahlen unterschiedlicher molekularer Spezies demonstriert.

Des Weiteren wird über eine technische Erweiterung des elektrischen Führens berichtet, welche dazu dient Pulse langsamer Moleküle zu generieren. Die Pulse zeichnen sich durch eine schmale Geschwindigkeitsverteilung um eine einstellbare Zentralgeschwindigkeit aus. Die Pulse werden durch folgerichtiges Schalten der Hochspannungen an benachbarten Segmenten der elektrischen Führung erzeugt. Dies wird synchron mit der Bewegung jener Moleküle vollzogen, die die zu selektierende Geschwindigkeit aufweisen. Das Verfahren wurde an ND_3 demonstriert, wo Pulse mit zentralen Geschwindigkeiten von $20 - 100 \text{ m/s}$ und relativen Halbwertsbreiten von $(16 \pm 2) \%$ gemessen wurden. Alle experimentellen Ergebnisse stehen in guter Übereinstimmung mit numerischen Simulationen und analytischen Rechnungen.

Contents

Abstract	v
Zusammenfassung	vi
1 Introduction	1
1.1 Cold molecules	1
1.2 Ultracold molecules	3
1.3 Production of cold molecules	4
1.4 This thesis	7
2 Theory of molecules and their interaction with an external electric field	9
2.1 The molecular Hamiltonian	9
2.2 The rigid rotor	12
2.2.1 Symmetric top molecules	12
2.2.2 Asymmetric top molecules	15
2.3 The response of a neutral molecule to an external electric field	19
2.4 Stark interaction of a rigid rotating molecule	20
2.4.1 Stark effect for symmetric top molecules	21
2.4.2 Stark effect for asymmetric-top molecules	27
3 Electric guiding and production of velocity-selected molecular pulses	29
3.1 Trapping polar molecules	30
3.2 Velocity filtering with an electric guide	32
3.3 Flux of guided molecules	33
3.4 Experimental setup	34
3.5 Continuous guided beam	36
3.6 Velocity-selected molecular pulses	37
3.6.1 Velocity-selection scheme	37
3.6.2 Formation of molecular pulses	39
3.6.3 The widths of the velocity distributions	43
3.6.4 Transverse velocity distribution of velocity-selected molecular pulses	46

3.7	Summary	49
4	Slow molecules extracted from a cryogenic source	51
4.1	Theory of buffer-gas cooling	52
4.1.1	Translational thermalization	52
4.1.2	Rotational relaxation and rotational state population	55
4.1.3	Molecular beams emerging from a buffer-gas source	60
4.2	Experimental setup	63
4.2.1	Cryogenic system	65
4.2.2	Buffer-gas cell and gas supply system	68
4.2.3	Electric guide	72
4.2.4	Ultrahigh-vacuum chamber and differential pumping	73
4.2.5	Data acquisition	74
4.3	Flux and density calibration	74
4.3.1	Gas line calibration	74
4.3.2	Guided flux calibration	75
4.4	Optimization of the source	77
4.4.1	Flux optimization	77
4.4.2	Runtime optimization	80
4.5	Internal cooling	81
4.5.1	Qualitative measurement	81
4.5.2	Quantitative measurement by depletion spectroscopy	85
4.6	Cold beams of different molecular species	92
4.7	Stability of the cold beam	97
4.8	Applications	99
4.8.1	Buffer-gas cooling with Neon	100
4.8.2	Velocity-selected molecular pulses from the cold beam	100
4.8.3	Reactions at low temperatures	101
4.9	Operation of the cryogenic source in the hydrodynamic regime	105
4.10	Summary	108
5	Outlook	109
A	Theoretical aspects of polar molecules in a quadrupole guide	111
A.1	Electric guiding potential	111
A.2	Molecular trajectories in a quadrupole guide	112
A.3	Distributions of guided molecules for quadrupole boundary conditions	115
B	Nuclear spin statistics	119
B.1	Symmetric top with a threefold axis of symmetry	119
B.2	Asymmetric top with a twofold axis of symmetry	122
C	Collision theory	125
C.1	Collision properties of atoms and symmetric-top molecules	125

D Additional plots and pictures	129
Bibliography	133
List of Publications	147
Danksagung	149

Chapter 1

Introduction

The successful implementation of laser cooling of atoms in combination with evaporative cooling culminated in the spectacular realization of Bose-Einstein condensation more than a decade ago [And95, Bra95, Dav95]. Nowadays, ultracold atoms are routinely used in a variety of different experiments, ranging from quantum information science to simulations of problems arising in solid-state physics [Rip05, Blo08].

A natural next step seems to be the realization of similar experiments with cold and ultracold molecules. Their rich internal structure allows for exploring many new properties, which could lead to the observation of novel physics.

In this chapter we briefly discuss some properties of cold and ultracold molecules and outline several experiments that can be performed. A broader and more detailed overview can be found in some recently published articles and special issues on cold and ultracold molecules [Bal01, Kre08, Kre09, Car09].

1.1 Cold molecules

The temperature below which the energy of molecules becomes comparable to the interaction energy of the molecules with an external ‘laboratory’ electric (magnetic) field defines the onset of the cold temperature regime. For polar molecules with dipole moments around ~ 1 Debye (~ 1 Bohr magneton) the cold regime is entered at temperatures below 1 K [Car09]. In this regime molecules can be trapped in suitable electric (magnetic) fields due to the Stark (Zeeman) shift of their energy levels. This allows to isolate the molecules from the environment [Bet00, Rie05, Wei98].

Electric or magnetic fields can also be used to polarize and align the molecules in molecular collisions (stereodynamics). This can result in different collision outcomes compared to the collisions in free space. Thus the effect of external electric (magnetic) fields on the collision behavior of the molecules can be exploited to control inelastic collisions and chemical reactions [Kre05]. Recently, this has been observed in a collision experiment between a guided beam of cold ND₃ molecules and magnet-

ically trapped OH molecules [Saw10]. Here it was found that the total cross section is increased by applying an external electric field over the trap volume.¹

The narrowed Maxwell-Boltzmann velocity distribution and the purified internal-state distribution at low temperatures allow to perform energy- and state-resolved scattering experiments. For example, state-selective scattering cross sections as functions of the collision energy have been obtained for decelerated OH molecules colliding with a beam of Xe atoms [Gil06], He atoms and D₂ molecules [Saw08, Kir10]. Here, threshold phenomena for inelastic scattering cross sections are apparent. In this regime inelastic and reactive collision rates can be favored or suppressed depending on the availability of particular internal states or the availability of sufficient kinetic energy for the colliding molecules to overcome a barrier or open a certain reaction channel.

At low temperatures only a few partial waves contribute to molecular collisions and chemical reactions. Therefore interference effects between scattering states and shape resonances can dominate in the collision dynamics [Kre03]. External fields can be used to couple different partial waves and thereby tune a shape resonance [Kre09].

Collisions in this temperature regime attract great interest in the astrophysics and astrochemistry communities. The lowest temperatures of interstellar space up to date are located around a Kelvin, which will reduce to even lower temperatures with the ongoing expansion of the universe. Here, cold molecular collisions in the laboratory can give insight into reactions of molecules in interstellar clouds for the present and future cosmic eras [Smi00, Smi06].

Cold molecules are suitable candidates for high-precision spectroscopy experiments. These experiments are performed in the regime of low densities where collisions are strongly reduced. Longer interaction times, reduced Doppler-broadening and state-selectivity obtained at low temperatures help to enhance the efficiency of such experiments. In particular, cold molecular samples are beneficial for high-precision tests of fundamental symmetries (CPT).² Here, molecules render themselves as a particularly suitable tool due to their rich internal structure. As a marked example the search for permanent electric dipole moments (EDM) of fundamental particles [Pur50, Lan57, Hun91, Bol08] is discussed in more detail. Permanent electric dipole moments result from the violation of the parity (P) and time reversal (T) symmetry. The violation of these symmetries is predicted by several theoretical models within and beyond the standard model [Com99]. For example for the electron's EDM the standard model predicts a value $< 10^{-38}$ ecm, where e is the elementary charge. On the other hand, extended models including theories beyond the standard model allow for values of dipole moments up to 10^{-26} ecm. Therefore EDM measurements can give information on the validity of different models and thereby give hints for novel physics.

Measurements of the EDM are based on the following principles. For a particle (such as an electron or neutron) carrying spin, the EDM must lie along the axis of the

¹The increased cross section is deduced from an increased trap loss

²The letters in CPT stand for charge conjugation, parity- and time-reversal transformation.

angular momentum. When an electric field is applied perpendicular to the direction of EDM the angular momentum precesses about the electric field axes due to the torque on the particle. This manifests in an energy difference between adjacent magnetic sublevels. In a typical experiment one probes the difference between the frequencies of the Larmor precession for the two cases where the electric field is parallel or antiparallel to a magnetic field, respectively. The longer the interaction with the electric field is, the greater the sensitivity is. Therefore, the use of cold particles can lead to a significant improvement in sensitivity. In 1965 P. G. H. Sanders showed that compared to the free electron case, the EDM of an electron bound in an atom is enhanced due to relativistic effects by a factor of the order of $\alpha^2 Z^3$ (for heavy atoms around $10^2 - 10^3$), with α being the fine structure constant and Z the nuclear charge [San65, Com07]. This has been taken advantage of in experiments using ^{205}Tl [Reg02] or ^{199}Hg [Gri09], which mark the upper bound of the electron's EDM of $d_e < 3 \times 10^{-29}$ ecm.

Further improvement could be obtained from measurements using polar molecules. This can be understood from the following arguments. The EDM interaction of an electron in an atom polarized by an external electric field $E_{\text{ext}}\hat{\mathbf{z}}$ results in an energy $-d_e E_{\text{eff}} P(E_{\text{ext}}) \langle \hat{\sigma} \cdot \hat{\mathbf{z}} \rangle$, where $\hat{\sigma}$ is the unit vector along the electron spin, E_{eff} the electric field at the position of the electron in the atom and $P(E_{\text{ext}})$ the polarization of the atom due to external electric field. The polarization $P(E_{\text{ext}})$ caused by the mixing of the atomic orbitals in typical laboratory fields is relatively weak. In contrast to atoms, diatomic heteronuclear molecules exhibit strong polarization around the internuclear axis due to the chemical bond. Here, the external field is only needed to project the polarization from the molecular frame to the lab frame by mixing the rotational states. In comparison to atomic orbitals these are energetically much closer to each other and thereby are strongly mixed even by weak external electric fields. So far, experiments with warm YbF [Hud02] have been performed as a proof of principle, restricting the electron dipole moment to a value around 10^{-26} ecm. It is widely believed that cold molecular samples can allow measurements of the EDM with accuracies far beyond the current state of the art measurements with heavy atoms.

1.2 Ultracold molecules

By employing further cooling schemes to dense and cold molecular samples the subsequent regime of ultracold temperatures could be reached. The ultracold regime is obtained when a single partial wave dominates the scattering process. For identical bosons (fermions) this is described by s-(p-)wave scattering.³ Temperatures below 1 mK loosely define this regime [Car09]. Molecules at ultracold temperatures offer novel properties in molecular collisions and chemical reactions. In this regime the deBroglie wavelength can become comparable or larger than intermolecular distances

³The cross section for s-wave scattering vanishes for identical fermions due to the Pauli principle.

and even exceed the separation between different molecules. Molecular collisions and reactions can be governed by interference and tunneling effects. The exothermic reaction $F + H_2 \rightarrow FH + H$ is a theoretically well understood example. Despite a reaction barrier of ~ 400 K a high reaction rate of $10^{-12} \text{ cm}^3\text{s}^{-1}$ should emerge at ultracold temperatures, as theoretically shown in [Bal01, Bal02]. Tunneling through the repulsive barrier, enhanced by a virtual state or barely bound state of the van der Waals well in the entrance channel, should guarantee the continuation of the chemical reaction.

Ultracold polar molecules offer exciting prospects in molecular collisions as well. For ultracold fermionic species p-wave scattering is strongly suppressed in case of short range van der Waals interparticle interactions. This is caused by the centrifugal barrier of the orbital angular momentum ($l = 1$) resulting in a basically non interacting gas [Bar01a]. For polar particles the long range dipole-dipole interaction between identical fermionic particles can guarantee sufficient interparticle interaction in a single component Fermi gas. This is required for evaporative cooling procedures, which are employed to reach lower temperatures. P-wave collisions in a polar molecular Fermi gas have been observed in [Osp10], where $^{40}\text{K}^{87}\text{Rb}$ molecules are contained in a pancake shaped dipole trap. The measurements are performed at 300 nK in zero electric field. The inelastic scattering rate is solely determined by the tunneling rate through the centrifugal (p-wave) barrier of approximately $24 \mu\text{K}$. Here, the scattering leads to losses resulting from atom exchange reactions and bimolecular reactions as $\text{KRb} + \text{KRb} \rightarrow \text{K}_2 + \text{Rb}_2$. In a subsequent manuscript [Ni10] the authors show that applying a weak electric field to orient the trapped molecules leads to a large increase in the inelastic scattering rate for bimolecular reactions, resulting from a lowered p-wave scattering barrier for dipolar head-to-tail collisions. For side-to-side collisions the scattering barrier is increased. This anisotropy of the dipole-dipole interaction is confirmed by rethermalization experiments with the trapped molecules. In [Mir10] the anisotropy is used to control the scattering rate. By enlarging the confinement of the dipole trap to a quasi-two-dimensional trap with the electric field along the tight binding direction the reaction rate is strongly suppressed since most of the molecules can approach each other only in side-to-side collisions. Here, the strength of electric field is also used to tune the suppression in the reaction.

1.3 Production of cold molecules

In contrast to atoms, laser cooling of molecules is rather challenging due to the complex internal structure of molecules. The difficulty lies in finding sufficiently closed cycling transitions [Met99]. Since spontaneous emission of an electronically excited molecule is accompanied by a simultaneous vibrational transition that is not bound by strict selection rules, the vibrational state in the excited electronic state is generally coupled to a large number of vibrational states in the electronic

ground state. Therefore, the basic prerequisite to apply laser cooling to molecules is the existence of suitable Franck-Condon factors that favor population in a single or few vibrational states upon many spontaneous decays [DR04, Stu08, Shu10]. Most molecules do not meet this criterion.

To circumvent this limitation, alternative schemes are considered. Methods that use ultracold atoms to generate ultracold molecules are referred to as indirect methods [Dul06, Car09]. These methods employ magnetic Feshbach resonances [Joc03, Reg03, Zwi03] or photoassociation [Tho87, Wan98] to create molecules during atomic collisions. Both are coherent processes which result in molecular samples of roughly the same temperature as the atoms. Nevertheless, the produced molecules in general populate highly excited rovibrational states, resulting from the better coupling of these states to free atom pair states. For photoassociated LiCs molecules favorable Franck-Condon factors of a suitable excited state with the rovibrational ground state have allowed for efficient transfer to the rovibrational ground state by spontaneous decay [Dei08b]. A large population transfer from highly excited states to the vibronic ground state for Feshbach associated Cs₂, Rb₂, KRb molecules has been accomplished in [Dan08, Lan08, Osp08] using stimulated Raman adiabatic passage (STIRAP) [Ber98].

Methods that provide cold samples of naturally abundant molecules are classified as direct methods. Typically, cold molecules are extracted from thermal/cryogenic reservoirs or produced by supersonic beam sources. Supersonic beams/pulses are produced by free expansion of a high-pressure gas mixture (molecules in a carrier gas) through a nozzle into vacuum [Pau00]. The collisions the molecules experience in the expansion process result in an internally cold sample of molecules (rotational temperatures of $\sim 1 - 10$ K) which have acquired supersonic speed. Such molecular beams exhibit a very narrow velocity distribution in the comoving frame (a few K or even colder). Stark or Zeeman deceleration can be employed to obtain cold molecular samples at rest in the laboratory frame [Bet99, Bet02, Van07, Nar07c, Nar08b, Hog08a]. These techniques allow for deceleration of a certain fraction of molecules from a pulsed supersonic beam by means of time-varying inhomogeneous electric or magnetic fields. For example, for polar molecules that experience a Stark shift in an electric field this is realized by a series of high voltage electrodes aligned along the propagation direction of the supersonic beam, which are switched on and off in synchrony with the motion of the pulse. The electric fields are modulated in a way such that the molecules experience a net force directed opposite to their motion. The technique is based on the principles of a linear decelerator (accelerator) for charged particles. Nowadays several types of Stark decelerators are being developed ranging from optical Stark decelerators that take advantage of the high electric field gradients in focussed laser pulses [Ful04, Ful06a] to micro-fabricated Stark decelerators on a chip [Mee08, Mee09]. Experiments including cold collisions [Gil06, Kir10], trap loading [Bet00, Bet02], lifetime measurements [Gil07], etc., have been performed with Stark-decelerated and subsequently trapped molecules.

There are several other methods that can bring samples of cold molecules from a supersonic-expansion to rest in the laboratory frame. This has, for example, been realized by supersonic expansion from a counter-spinning rotor [Gup99, Gup01]. Other schemes include reflection of a supersonic beam from a moving surface [Nar07a] or kinematic cooling [Eli03, Kay09] established by collisions between a molecular beam and a beam of noble gas atoms.

For applications where only the temperature of the external degrees of freedom is of importance electric velocity filtering can be used to obtain large samples of slow polar molecules [Ran03, Jun04a]. An electric guide is used to extract slow polar molecules from a thermal reservoir. This technique has been developed in our group and it is discussed in detail in this thesis and in publications from our group [Jun04a, Jun05, Mot10]. This technique has, for example, been used to study collisions between slow molecules and ion crystals [Wil08a].

One prominent technique to obtain cold molecules in the gas phase is buffer gas cooling. Here, an inert buffer gas is enclosed in a container (buffer-gas cell), which is cooled to cryogenic temperatures by a refrigerator (helium refrigerator, pulse tube cooler etc.). Molecules entering the buffer-gas cell dissipate their kinetic and internal energy through collisions with cold buffer-gas atoms. Most experiments use helium buffer gas, for which temperatures down to ~ 200 mK can be attained. By adding a magnetic field minimum in the buffer-gas cell, buffer gas cooled magnetic molecules can be trapped. This has been accomplished for a variety of molecular and atomic species [Wei98, Cam07, Hum08, Sto08]. Long trapping times can only be obtained when the buffer gas is removed after the cooling process has ended. In such a magnetic trap Bose-Einstein condensation has been achieved for buffer-gas-cooled metastable helium atoms by evaporative cooling [Dor09].

The molecular gas can be introduced into the buffer-gas cell via a variety of different techniques, for example by means of laser ablation from a solid target [Wei98]. Other options are beam loading through a small aperture in the buffer-gas cell [Ego02, Ego04], or discharge etching in which frozen atoms/molecules on the surface of the buffer-gas cell are released by an electrical discharge plasma [Ngu05]. Capillary filling [Mes84, Pat07] is another demonstrated method which has been used for the experiments described in this thesis [vB09, Som09]. Here, the molecules are injected into the buffer-gas cell by a heated capillary. This technique is particularly suitable for the production of continuous molecular beams. It is valid for a large class of naturally abundant molecules. A cold molecular beam can be formed by employing an additional aperture in the buffer-gas cell through which the buffer gas cooled molecules can leave the buffer-gas cell. The molecules can be extracted from the buffer gas environment with a magnetic or electric guide and delivered elsewhere as shown in this work.

1.4 This thesis

The generation of cold guided beams of polar molecules by combining buffer-gas cooling with electric velocity filtering constitutes the main topic of this thesis. These two techniques are joined in a newly developed setup, which is characterized by various measurements. Also a new scheme for obtaining molecular pulses by means of electric velocity filtering is addressed in the text.

In **chapter 2** we outline the theoretical background for the Stark effect that describes the behavior of polar molecules in external electric fields. Here, the Stark effect is predominantly apparent at the molecular rotational levels due to their close energy spacing. To determine the Stark splitting between molecular rotational states the rotational-state structure in the rigid rotor approximation is explained in great detail.

In **chapter 3** the principles of electric guiding are presented, with an emphasis on measurements employing the newly developed velocity selection method. This technique allows to extract molecular pulses with narrow velocity distribution from the continuous guided beam. The selection procedure as well as the measurement results are discussed in great detail.

Chapter 4 describes the measurements of cold polar molecules produced with the cryogenic source during this thesis work. The new setup adds buffer-gas cooling to our velocity filtering technique. Here, an atomic buffer gas at cryogenic temperatures is used to cool the warm molecules before they are extracted by an electric guide. The general principles of buffer-gas cooling are discussed. Afterwards, the setup used in our experiments is described. Measurements with ammonia (ND_3) and formaldehyde (H_2CO) are performed to demonstrate the cooling efficiency for the internal degrees of freedom. For formaldehyde, quantitative results for cooling the internal degrees of freedom are obtained from depletion spectroscopy. The generality of the source is demonstrated by using molecules with different masses, dipole moments, and rotational constants (CH_3F , CF_3H and ND_3). Furthermore, we have performed a test case for cold chemistry experiments to demonstrate a possible future application for such a source. The generation of stable strongly-boosted molecular beams is addressed in text as well. These beams promise to have orders of magnitude larger fluxes.

Chapter 2

Theory of molecules and their interaction with an external electric field

In this chapter we outline the theory that is needed to describe the interaction between a polar molecule and an external electric field. We start with the complete molecular Hamiltonian to derive the energy and state relations for the rotational degrees of freedom, which are primarily relevant in this interaction.

2.1 The molecular Hamiltonian

The complete Hamiltonian of a molecule includes the kinetic and potential energies of all of its constituents, which are the nuclei and the electrons. To simplify this many-body problem, the Born-Oppenheimer approximation is used [Bor27]. It is based on the concept that, due to the large difference between the mass of the electrons and nuclei light and thereby fast electrons, respond almost instantaneously to displacements of the nuclei from their equilibrium positions. In this approximation, the nuclei are regarded as fixed to their position with respect to the motion of the electrons. Therefore, the electrons's motion can be separated from the nuclei's motion [Dem03]. In this case the eigenfunctions of the Hamiltonian can be factorized into electronic and nuclear eigenfunctions

$$\psi(\mathbf{x}_e, \mathbf{x}_n) = \psi_e(\mathbf{x}_e, \mathbf{x}_n)\psi_n(\mathbf{x}_n), \quad (2.1)$$

where \mathbf{x}_e (\mathbf{x}_n) and ψ_e (ψ_n) represent the generalized coordinates and the wave functions of the electrons (nuclei), respectively. It is important to point out that \mathbf{x}_n is not a variable of $\psi_e(\mathbf{x}_e, \mathbf{x}_n)$ but a parameter since the electron distribution follows the motion of the nuclei adiabatically.¹ Therefore, there exists a well-defined wave function $\psi_e(\mathbf{x}_e, \mathbf{x}_n)$ and electron distribution to each \mathbf{x}_n .

¹No differentiation or integration of ψ_e with respect to \mathbf{x}_n takes place.

The total Hamiltonian of a molecule without external electric or magnetic fields is given by

$$H_{mol} = T_e + T_n + V_{ee} + V_{nn} + V_{ne}, \quad (2.2)$$

where T_e and T_n are the kinetic energies of the electrons and nuclei, respectively, and V_{ee} , V_{nn} , and V_{ne} are the Coulomb interaction energies between the electrons, between the nuclei, and between the electrons and the nuclei, respectively. Potential energy terms considering spin-dependent interactions between the particles are ignored. Using Eq. 2.1, the Schrödinger equation of the full problem can be separated into the Schrödinger equation for the electrons

$$H_e|\psi_e\rangle = [T_e + V_{ee} + V_{ne} + V_{nn}]|\psi_e\rangle = W_{(e,n)}|\psi_e\rangle \quad (2.3)$$

and the Schrödinger equation for the nuclei

$$H_n|\psi_n\rangle = [T_n + W_{(e,n)}]|\psi_n\rangle = W_n|\psi_n\rangle. \quad (2.4)$$

Here, the energy $W_{(e,n)}$ of the electronic state depending on \mathbf{x}_n acts as the potential energy for the nuclear motion. By setting the zero of energy to the minimum value of $W_{(e,n)}$ we obtain the Schrödinger equation for the motion of the nuclei in the potential $V_{(e,n)} = W_{(e,n)} - W_{(e,n)|min}$:

$$[T_n + V_{(e,n)}]|\psi_n\rangle = W_n|\psi_n\rangle \quad (2.5)$$

This equation is in general different for each electronic eigenstate.

The kinetic energy of the nuclei can be expressed by

$$T_n = \frac{1}{2} \sum_{\alpha} m_{\alpha} \dot{\mathbf{x}}_{\alpha}^2, \quad (2.6)$$

where \mathbf{x}_{α} designates the generalized coordinates of the α -th nucleus. To investigate the nuclear motion, the kinetic-energy term is modified to include small displacements from the equilibrium configuration of the molecule [Bun06]. Towards this end, \mathbf{x}_{α} is expressed as

$$\mathbf{x}_{\alpha} = \mathbf{x}^c + \mathbf{S}^{-1}(\mathbf{q}_{\alpha}^0 + \mathbf{r}_{\alpha}) \quad (2.7)$$

which is applicable to each of the N nuclei constituting the molecule. In this expression, \mathbf{x}^c is the center-of-mass position in the space-fixed frame and \mathbf{S}^{-1} is the inverse of a 3×3 rotation matrix \mathbf{S} . This matrix relates the coordinates in the molecule-fixed frame $\mathbf{q}_{\alpha}^0 + \mathbf{r}_{\alpha}$ to the coordinates in the space-fixed frame \mathbf{x}_{α} by rotations at the three Euler angles (see Fig. 2.1) [Kro75]. \mathbf{q}_{α}^0 denotes the equilibrium position of the α -th nucleus in the molecule-fixed frame with its origin pinned down at the center of mass \mathbf{x}^c .² \mathbf{r}_{α} is the displacement of the α -th nucleus from its equilibrium position.

² $\sum_{\alpha} m_{\alpha} \mathbf{q}_{\alpha}^0 = 0$.

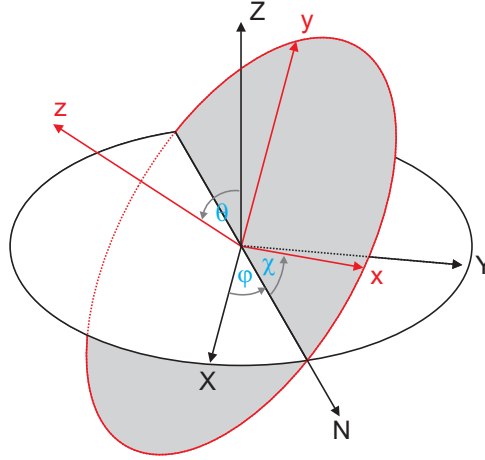


Figure 2.1: The Eulerian angles (φ, θ, χ) demonstrate the transformation from the space-fixed coordinate system (X, Y, Z) to the molecular coordinate system (x, y, z) performed by the \mathbf{S} matrix. Thereby they show the orientation of a molecule with respect to the space-fixed axes. The N -axis is given by the cut of the XY - and xy -plane. The figure is taken from [Tow75, Mul09b].

To treat small molecular vibrations, the following conditions, referred to as Eckart conditions [Eck35], are imposed:

$$\sum_{\alpha} m_{\alpha} \mathbf{r}_{\alpha} = 0, \quad (2.8)$$

$$\sum_{\alpha} m_{\alpha} \mathbf{q}_{\alpha}^0 \times \mathbf{r}_{\alpha} = 0. \quad (2.9)$$

The first condition guarantees that the center of mass does not change upon vibrations, while the second one ensures that vibrations do not lead to altering of the overall angular momentum of the molecule. The constraints require that $3N - 6$ of the $3N$ displacement coordinates $r_{\alpha i}$ are independent.³ By substitution of \mathbf{x}_{α} in the kinetic energy term using Eq. 2.7 and by ignoring the center of mass motion, one obtains

$$T_n = \frac{1}{2} \boldsymbol{\omega}^T \mathbf{I} \boldsymbol{\omega} + \frac{1}{2} \sum_{\alpha} m_{\alpha} \dot{\mathbf{r}}_{\alpha}^2 + \sum_{\alpha} m_{\alpha} \boldsymbol{\omega} \cdot (\mathbf{r}_{\alpha} \times \dot{\mathbf{r}}_{\alpha}), \quad (2.10)$$

with the angular velocities $\boldsymbol{\omega}$ derived from $(\mathbf{S}\dot{\mathbf{S}}^{-1})_{ln} = -\epsilon_{klm}\omega_k$ and the moment of inertia tensor $I_{kl} = \sum_{\alpha} m_{\alpha} (\delta_{kl}(q_{\alpha m}^0)^2 - q_{\alpha k}^0 q_{\alpha l}^0)$, where the second subindexes n, k and l each designate the three spatial coordinates. A detailed derivation is given in [Kro75]. The first term describes the rotational energy of the rigid molecule, the second term describes the kinetic energy of its vibrations, and the third term describes the vibration-rotation interaction term.

³ $3N - 5$ for linear molecules.

In the case of very small vibrations and rotations, the vibration-rotation interaction term can be ignored, and the angular momentum can be approximated by $J_k = \partial T_n / \partial \omega_k = I_{kl} \omega_l$. This yields the following expression for the rotational energy:

$$T_{rot} = \frac{1}{2} \mathbf{J}^T \mathbf{I}^{-1} \mathbf{J}. \quad (2.11)$$

Diagonalization of the symmetric matrix I_{kl} leads to the moment of inertia tensor along its principal axes a, b, c , resulting in

$$T_{rot} = \frac{1}{2} (I_a \omega_a^2 + I_b \omega_b^2 + I_c \omega_c^2) = A J_a^2 + B J_b^2 + C J_c^2, \quad (2.12)$$

where $A = 1/(2I_a)$, $B = 1/(2I_b)$, and $C = 1/(2I_c)$ are the principal rotational constants.⁴

In the Hamiltonian H_{rot} that describes the rotation of the rigid molecule no contribution from the potential $V_{(e,n)}$ is included because $V_{(e,n)}$ depends solely on the displacement coordinates $r_{\alpha i}$. Therefore, the Hamiltonian describing the molecular rotation H_{rot} is identical to T_{rot} .

2.2 The rigid rotor

In classical mechanics the rotational constants are ordered as $A \geq B \geq C$ to satisfy $I_a \leq I_b \leq I_c$ [Kuy83]. Four main groups of rotors are distinguished:

- | | | |
|------------------------------|-----------------------------|--------|
| (1) Spherical top molecules | $I_a = I_b = I_c$ | (2.13) |
| (2) Symmetric top molecules | $I_a < I_b = I_c$ (prolate) | |
| | $I_a = I_b < I_c$ (oblate) | |
| (3) Asymmetric top molecules | $I_a < I_b < I_c$ | |
| (4) Linear molecules | $I_a = I_b = 0$. | |

In this section we investigate the symmetric and the asymmetric top Hamiltonians, which describe the rotational states of the molecules used in our experiments.

2.2.1 Symmetric top molecules

Based on the principles outlined in Eq. 2.13, the rotational Hamiltonian for a prolate symmetric top is described by

$$\begin{aligned} H_{rot}^{pro.} &= [A J_a^2 + B(J_b^2 + J_c^2)] \\ &= [A J_a^2 + B(\mathbf{J}^2 - J_a^2)] \\ &= [B \mathbf{J}^2 + (A - B) J_a^2], \end{aligned} \quad (2.14)$$

⁴Energy in units of frequency.

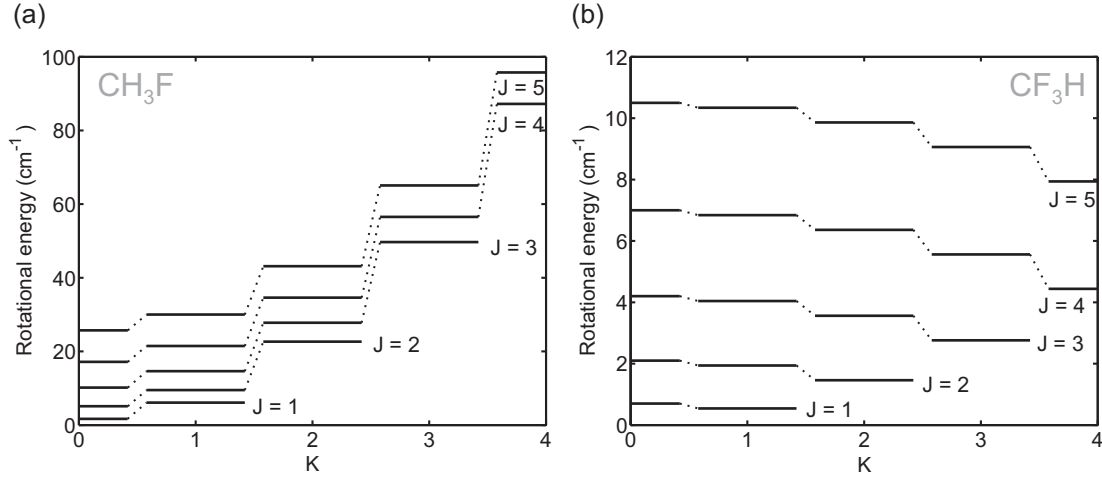


Figure 2.2: Rotational energy levels for a prolate (a) and an oblate (b) symmetric top molecule. As an example the rotational energy levels of CH₃F (CF₃H) molecules are presented for the prolate (oblate) case. Energy levels up to $J = 5$ are shown.

while the Hamiltonian for an oblate symmetric top has the form

$$\begin{aligned} H_{rot}^{obl.} &= [B(J_a^2 + J_b^2) + CJ_c^2] \\ &= [B\mathbf{J}^2 + (C - B)J_c^2]. \end{aligned} \quad (2.15)$$

Here, J_a (J_c) is the projection of the angular momentum \mathbf{J} on the molecular symmetry axis in the prolate (oblate) case. From these equations we derive the eigenvalues for the angular momentum eigenstates $|JK\rangle$ in the molecular frame (see Fig. 2.2):

$$W_{rot}^{pro.} = BJ(J + 1) + (A - B)K^2 \quad (2.16)$$

$$W_{rot}^{obl.} = BJ(J + 1) + (C - B)K^2. \quad (2.17)$$

Here, J and K are the quantum numbers associated with \mathbf{J} and J_a (J_c) [Kro75]. The angular momentum eigenstates are also eigenstates of the prolate and oblate symmetric top Hamiltonian.

J_a , J_b and J_c are the projections of the angular momentum on the molecular frame. Nevertheless, we have to consider the projections on the space fixed coordinates as well to obtain the general symmetric top eigenstates. The transformation from the molecule-fixed to the space-fixed projections is given by $J_\alpha = S_{\alpha i}J_i$ with $\alpha \in \{A, B, C\}$ and $i \in \{X, Y, Z\}$. Since the rows and the columns of the \mathbf{S} matrix⁵ are vector operators with respect to J_i and J_α [Kro75], the following relations are fulfilled:

$$\begin{aligned} [J_i, S_{\alpha j}] &= i\epsilon_{ijk}S_{\alpha k} \\ [J_\alpha, S_{\beta i}] &= -i\epsilon_{\alpha\beta\gamma}S_{\gamma i}. \end{aligned} \quad (2.18)$$

⁵The components of the \mathbf{S} matrix are referred to as direction cosine matrix elements. They are presented in [Kro75].

Table 2.1: Character table of the D_∞ symmetry group and the assignment to the K quantum number. $2C_\phi$ and ∞C_2 are the conjugacy classes of the continuous rotations around the z -axis and the two-fold rotations around any axis perpendicular to the z -axis, respectively. The table is adapted from [Bun06, Mul09b].

$ K $	D_∞	E	$2C_\phi$	∞C_2
0	Σ_1 (even J)	1	1	1
0	Σ_2 (odd J)	1	1	-1
1	Π	2	$2 \cos(\phi)$	0
2	Δ	2	$2 \cos(2\phi)$	0
3	Φ	2	$2 \cos(3\phi)$	0
\vdots	\vdots	\vdots	\vdots	\vdots

This results in

$$[J_i, J_\alpha] = 0. \quad (2.19)$$

Therefore, the eigenstates of the symmetric top Hamiltonian must be simultaneously eigenstates of \mathbf{J}^2 , J_Z and J_a (J_c) in the prolate (oblate) case. They are described by $|JKM\rangle$ and fulfill the relations

$$\mathbf{J}^2|JKM\rangle = J(J+1)|JKM\rangle \quad (2.20)$$

$$\underbrace{J_a|JKM\rangle}_{\text{prolate}} = \underbrace{J_c|JKM\rangle}_{\text{oblate}} = K|JKM\rangle \quad (2.21)$$

$$J_Z|JKM\rangle = M|JKM\rangle \quad (2.22)$$

$$J^\pm|JKM\rangle = \sqrt{(J \mp K)(J \pm K + 1)}|JK \pm 1 M\rangle \quad (2.23)$$

$$J_\pm|JKM\rangle = \sqrt{(J \mp M)(J \pm M + 1)}|JKM \pm 1\rangle, \quad (2.24)$$

where $J^\pm = (J_x \mp iJ_y)$ (prolate: $x = b$, $y = c$, oblate: $x = a$, $y = b$) and $J_\pm = (J_X \pm iJ_Y)$.

The general characteristics of a symmetric top can be understood from group theory as well. The symmetry group of the symmetric top allows to assign symmetry properties to the individual energy levels of a symmetric top molecule.

The symmetric top rotor belongs to the D_∞ symmetry group, which is the rotation group of a cylinder [Bun06, Mul09b]. It includes continuous rotations about one axis, and two-fold rotations about any axis perpendicular to the previous one. The infinitely many representations (see Tbl. 2.1) are each assigned to a definite $|K|$ value, with the exception of $|K| = 0$ where two representations are assigned depending on whether J is even or odd. The twofold degeneracy of the representations with $|K| > 0$ corresponds to the two cases $K = \pm|K|$.

In the upcoming paragraph, the asymmetric rotor eigenstates are defined by superpositions of symmetric top eigenstates. Here, the symmetry representations associated with a given symmetric top state can be used to determine which symmetric top states do and do not contribute in a superposition.

2.2.2 Asymmetric top molecules

The Hamiltonian of an asymmetric rotor is described by Eq. 2.12. For further analysis it can be cast into a more convenient form:

$$\begin{aligned}
H_{rot}^{asym.} &= AJ_a^2 + BJ_b^2 + CJ_c^2 & (2.25) \\
&= \frac{1}{2}(A+C)(J_a^2 + J_c^2) + BJ_b^2 + \frac{1}{2}(A-C)(J_a^2 - J_c^2) \\
&= \frac{1}{2}(A+C)\mathbf{J}^2 + \frac{1}{2}(A-C) \left[J_a^2 + \frac{2B-A-C}{A-C} J_b^2 - J_c^2 \right] \\
&= \frac{1}{2}(A+C)\mathbf{J}^2 + \frac{1}{2}(A-C)H(\kappa).
\end{aligned}$$

The constant $\kappa = (2B - A - C)/(A - C)$ defines the parameter of asymmetry with $\kappa \in \{-1, 1\}$ [Kin43]. For $B = C$ we obtain $\kappa = -1$ and $H_{rot}^{asym.}$ reduces to the prolate symmetric top Hamiltonian, while for $B = A$ with $\kappa = 1$ the oblate symmetric top Hamiltonian is obtained.

The matrix elements of the asymmetric top Hamiltonian can be expressed in the symmetric-top basis states $|JKM\rangle$:

$$\langle JKM | H_{rot}^{asym.} | JKM \rangle = \frac{1}{2}(A+C)J(J+1) + \frac{1}{2}(A-C)\langle JKM | H(\kappa) | JKM \rangle \quad (2.26)$$

$$\langle J, K \pm 2, M | H_{rot}^{asym.} | JKM \rangle = \langle J, K \pm 2, M | H(\kappa) | JKM \rangle. \quad (2.27)$$

Non-vanishing matrix elements exist only for $\Delta K = 0$ and $\Delta K = \pm 2$. The matrix elements of the reduced Hamiltonian $H(\kappa)$ are given by

$$\langle JKM | H(\kappa) | JKM \rangle = F[J(J+1) - K^2] + GK^2 \quad (2.28)$$

$$\langle J, K \pm 2, M | H(\kappa) | JKM \rangle = H[f(J, K \pm 1)]^{1/2}, \quad (2.29)$$

where the function $f(J, K \pm 1)$ is defined by

$$f(J, K \pm 1) = \frac{1}{4}[J(J+1) - K(K \pm 1)] \times [J(J+1) - (K \pm 1)(K \pm 2)]. \quad (2.30)$$

To obtain the matrix elements given in Eq. 2.28 and Eq. 2.29, the relations

$$\langle JK | J_x^2 | JK \rangle = \langle JK | J_y^2 | JK \rangle = \frac{1}{2}[J(J+1) - K^2] \quad (2.31)$$

$$\begin{aligned}
\langle JK | J_y^2 | J, K+2 \rangle &= \frac{1}{4}\{[J(J+1) - K(K+1)] \times [J(J+1) - (K+1)(K+2)]\}^{1/2} \\
&= -\langle JK | J_x^2 | J, K+2 \rangle
\end{aligned} \quad (2.32)$$

have been used. The coefficients F, G, H are given in Tbl. 2.2 for the different identifications of the principal axes a, b, c with a right-handed, body-fixed, coordinate

Table 2.2: Identifications of the principal axes a, b, c in a right-handed, body-fixed, coordinate system x, y, z and the corresponding coefficients F, G, H used in the matrix elements (see Eq. 2.28 and Eq. 2.29) of the Hamiltonian. The table is adapted from [Kin43].

	x	y	z	F	G	H
I^r	b	c	a	$\frac{1}{2}(\kappa - 1)$	1	$-\frac{1}{2}(\kappa + 1)$
II^r	c	a	b	0	κ	1
III^r	a	b	c	$\frac{1}{2}(\kappa + 1)$	-1	$\frac{1}{2}(\kappa - 1)$

system x, y, z . Note that the resulting energy-level structure is independent of the representation. The choice of a specific representation has, however, consequences for the ease of calculating the energy-level structure. For an asymmetry value $\kappa \rightarrow 1$ the identification III^r is most convenient, while for $\kappa \rightarrow -1$ and $\kappa \rightarrow 0$ the identifications I^r and II^r are the best choice. This is due to the fact that the coefficient H of the off-diagonal elements becomes small and vanishes in the limiting cases of ($\kappa = 1, III^r$) and ($\kappa = -1, I^r$) (Tbl. 2.2). For $\kappa = 0$ in the II^r identification H does not vanish but the coefficients for the diagonal elements F and G do.

Diagonalization of the asymmetric top Hamiltonian leads to the eigenstates and eigenenergies (see Fig. 2.3)

$$|J\tau M\rangle = |JK_A K_C M\rangle = \sum_K a_K^{J\tau M} |JKM\rangle \quad (2.33)$$

$$W_{J\tau M} = \frac{1}{2}(A + C)J(J + 1) + \frac{1}{2}(A - C)W_{J\tau M}(\kappa). \quad (2.34)$$

The eigenstates, which are labelled either by $|J\tau M\rangle$ or $|JK_A K_C M\rangle$, are defined in the symmetric top basis. $\tau = K_A - K_C$ is a pseudo-quantum number derived from the quantum numbers K_A and K_C of the limiting prolate and oblate case. The parameter τ ranges from $-J$ to J and labels the states with increasing energy. The assignment is described in the following. The quantum numbers K_A and K_C are alternately increased and decreased from 0 to J and from J to 0, respectively. This assignment guarantees that there are no crossings of the energy levels over the entire range of κ (see Fig. 2.3).

The quantum numbers K_A and K_C display the symmetry properties of the asymmetric rotor states: In contrast to the symmetric rotor, which belongs to the D_∞ symmetry group (rotations about the symmetry axis), the asymmetric rotor belongs to the D_2 symmetry group consisting of the group elements (E, C_2^a, C_2^b, C_2^c) [Kin43]. Here, E is the identity and C_2^i is a rotation by π about the i -axis. Table 2.3 shows the irreducible representations of the group and the character assignments to the conjugacy classes which in this case are given by the group elements themselves. Here, the representation A behaves symmetrically with respect to rotations by π about any axis, while the representations B_i behave symmetric only for rotations about the i -axis. All representations are one-dimensional. Therefore the action of a

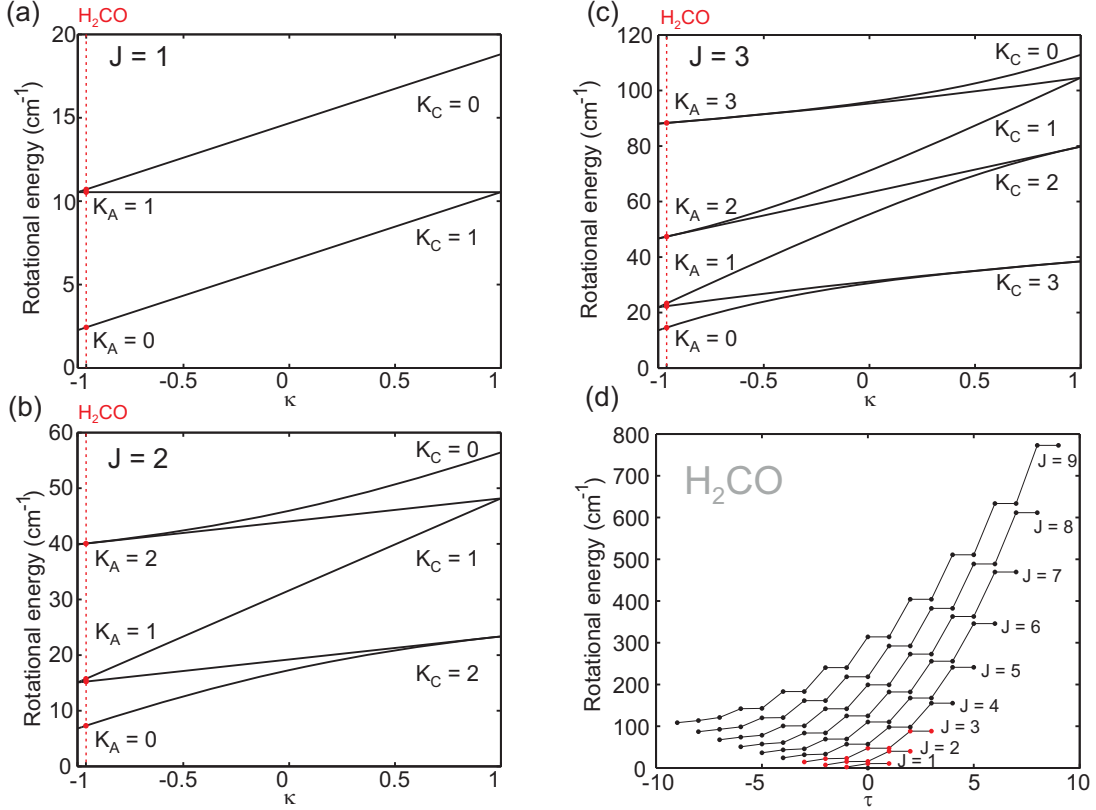


Figure 2.3: Rotational energy levels for $J = 1$ (a), $J = 2$ (b) and $J = 3$ (c) of the asymmetric rotor as a function of the asymmetry parameter κ . The rotational constants $A = 9.4 \text{ cm}^{-1}$ and $C = 1.3 \text{ cm}^{-1}$ are taken from formaldehyde (H₂CO), and B is varying linearly with κ [Mot08]. The rotational energy levels of formaldehyde are obtained for $B = 1.13 \text{ cm}^{-1}$ corresponding to $\kappa = -0.96$, which is indicated by the red dashed lines. For $\kappa = -1$ ($\kappa = 1$) the asymmetric rotor passes into a prolate (oblate) symmetric top. In (d) the energy levels of formaldehyde up to $J = 9$ are presented as functions of the pseudo-quantum number τ .

group element and its attributed character in a given representation are the same. The assignment of an asymmetric rotor eigenstate with quantum numbers K_A and K_C (or τ) to an irreducible representation presented in Tbl. 2.3 is therefore obtained from the relations

$$C_2^a |JK_A M\rangle = e^{i2\pi K_A/2} |JK_A M\rangle = (-1)^{K_A} |JK_A M\rangle \quad (2.35)$$

$$C_2^c |JK_C M\rangle = e^{i2\pi K_C/2} |JK_C M\rangle = (-1)^{K_C} |JK_C M\rangle, \quad (2.36)$$

which are valid in the limiting prolate and oblate cases.

The asymmetric rotor states $|J\tau M\rangle$ are eigenstates of the D_2 -symmetry group. As denoted by Eq. 2.33 the asymmetric rotor eigenstates can be expanded as superpositions of symmetric top eigenstates $|JKM\rangle$. These are, however, not eigenstates

Table 2.3: Character table for the symmetry group D_2 and symmetry properties of the asymmetric rotor levels as a function of K_A and K_C . e and o designate even and odd parity of the quantum numbers K_A and K_C . The table is adapted from [Kin43].

D_2	E	C_2^a	C_2^b	C_2^c	K_A	K_C
A	1	1	1	1	e	e
B_a	1	1	-1	-1	e	o
B_b	1	-1	1	-1	o	o
B_c	1	-1	-1	1	o	e

Table 2.4: Representation classification of symmetric rotor Wang linear combinations (D_∞) under the representations of the asymmetric rotor (D_2) states. The representation assignments are given for a general coordinate system (x, y, z) in the molecular frame, which can be identified with I^r , II^r and III^r . (Table adapted from [Kin43] and [Mul09b].)

K	D_∞	$J + \gamma$	D_2	I^r	II^r	III^r
0	Σ_1	e	A	A	A	A
0	Σ_2	o	B_z	B_a	B_b	B_c
o	Π, Φ , etc.	e	B_y	B_c	B_a	B_b
o		o	B_x	B_b	B_c	B_a
e	Δ, Γ , etc.	e	A	A	A	A
e		o	B_z	B_a	B_b	B_c

of the D_2 -symmetry group. On the other hand, Wang linear combinations of symmetric top eigenstates belong to the D_2 -symmetry group [Kro75]. They are defined by

$$|J|K|M\gamma\rangle = \frac{1}{\sqrt{2}}\{|J|K|M\rangle^* + (-1)^\gamma|J - |K|M\rangle^*\} \quad (2.37)$$

$$|J0M0\rangle = |J0M\rangle^*, \quad (2.38)$$

where $|JKM\rangle^* = (-1)^\beta|JKM\rangle$ with $\beta = \max\{K, M\}$ and $\gamma \in \{0, 1\}$.⁶ They can be used to assign irreducible representation of the D_2 -symmetry group to irreducible representation of the D_∞ -symmetry group, as shown in Tbl. 2.4. In an expansion of an asymmetric rotor state by Wang linear combinations the symmetry must be preserved. This can be used to find out which symmetric top eigenstates contribute in an expansion. This leads to a significant simplification in the diagonalization of the asymmetric rotor Hamiltonian.

⁶ $\gamma = 0$ for $K = 0$.

2.3 The response of a neutral molecule to an external electric field

The properties of molecules exposed to an electric field are versatile. Irrespective of the charge neutrality, an asymmetric charge distribution will lead to interactions with an external electric field. In this section the basic properties of polar molecules in a static electric field are described. To derive an expression for the behavior of a neutral molecule in an external electric field, the Hamiltonian describing the dynamics of its charged building blocks and their interaction with the external electric field is used. The Hamiltonian is given by

$$H = H_{mol} + H_{int}, \quad (2.39)$$

where H_{mol} is the field-free Hamiltonian of the charged particles including electrons and nuclei (see Eq. 2.2) and H_{int} describes the contribution of the external electric potential. These individual parts are represented by

$$H_{mol} = \sum_{\alpha=1}^n \frac{\mathbf{p}_{\alpha}^2}{2m_{\alpha}} + \frac{1}{4\pi\epsilon_0} \sum_{\alpha=1}^n \sum_{\beta<\alpha}^n \frac{q_{\alpha}q_{\beta}}{|\mathbf{x}_{\alpha} - \mathbf{x}_{\beta}|} \quad (2.40)$$

$$H_{int} = \sum_{\alpha=1}^n q_{\alpha}\phi(\mathbf{x}_{\alpha}). \quad (2.41)$$

The scalar potential of the external field is given by $\phi(\mathbf{x})$. Here, n is the number of charged particles and \mathbf{x}_{α} (\mathbf{p}_{α}) are the spatial coordinates (momenta) of the α -th particle of charge q_{α} . To derive the collective response of the particles in the external field a Taylor-expansion of the scalar potential at the center of mass fixed at $\mathbf{x} = 0$ is used:

$$\phi(\mathbf{x}) = \phi(0) + \mathbf{x} \cdot \nabla\phi(0) + \frac{1}{2} \sum_i \sum_j x_i x_j \frac{\partial^2\phi}{\partial x_i \partial x_j}(0) + \dots \quad (2.42)$$

We can neglect the second-order quadrupole term and higher-order terms of the Taylor-expansion using the assumption that $-\nabla\phi(0) = \mathbf{E}(0)$ is constant over the dimensions of the molecule. This results in the interaction term

$$H_{int} = \sum_{\alpha=1}^n -q_{\alpha}\mathbf{x}_{\alpha} \cdot \mathbf{E}(0), \quad (2.43)$$

which is referred to as the Stark-interaction Hamiltonian. The sum $\sum_{\alpha=1}^n q_{\alpha}\mathbf{x}_{\alpha}$ is defined as the dipole moment \mathbf{d} of the molecule.

In our model we assume that the influence of $\mathbf{E}(0)$ on the structure of the molecule is small. In comparison to the inner electric forces between its charged components, the influence of $\mathbf{E}(0)$ on the trajectories \mathbf{x}_{α} can be treated as a small perturbation.

Nevertheless, this does not imply that \mathbf{d} is constant. In general \mathbf{d} depends on the external electric field \mathbf{E} .

For a molecule in the state $|\psi\rangle$ the average dipole moment $\langle\mathbf{d}\rangle$ can be obtained from the average value of the interaction Hamiltonian

$$W_{int} = \langle\psi|H_{int}|\psi\rangle. \quad (2.44)$$

Making use of the Hellmann-Feynman theorem [Atk05], the average molecular dipole moment is obtained from

$$\langle\mathbf{d}\rangle = -\nabla_{\mathbf{E}}W_{int} = -\langle\psi|\nabla_{\mathbf{E}}H_{int}|\psi\rangle. \quad (2.45)$$

With the expansion of Eq. 2.44 with respect to the electric field \mathbf{E}

$$W_{int}(\mathbf{E}) = W_{int}(0) + \nabla_{\mathbf{E}}W_{int}(0) \cdot \mathbf{E} + \frac{1}{2} \sum_i \sum_j \frac{\partial^2 W_{int}}{\partial E_i \partial E_j}(0) E_i E_j + \dots, \quad (2.46)$$

and considering Eq. 2.45, the dipole moment can be approximated by

$$\langle\mathbf{d}\rangle(\mathbf{E})_i = -\nabla_{\mathbf{E}}W_{int}(0)_i - \frac{1}{2} \sum_j \frac{\partial^2 W_{int}}{\partial E_i \partial E_j}(0) E_j - \dots \quad (2.47)$$

$$= d_i^0 + \sum_j a_{ij} E_j + \dots \quad (2.48)$$

Here \mathbf{d}^0 is the permanent dipole moment and \mathbf{a} the linear polarizability tensor, which defines the components of the induced dipole moment to the first order.

2.4 Stark interaction of a rigid rotating molecule

The Born-Oppenheimer approximation outlined in section 2.1 allows for a separation of the molecular state into an electronic $|\psi_e\rangle$ and a nuclear part which describes the rotational and vibrational (rovibrational) motions of the nuclei $|\psi_{rv}\rangle$, $|\psi\rangle = |\psi_e\rangle |\psi_{rv}\rangle$. The rovibrational state can be factored further into a vibrational and rotational part $|\psi_{rv}\rangle = |\psi_v\rangle |\psi_r\rangle$. This is a valid approximation in the limit of low excitations, where the vibration-rotation interaction term in Eq. 2.10 can be neglected. Therefore, the average value of the dipole moment can be expressed by

$$\langle\psi|\mathbf{d}|\psi\rangle = \langle\psi_r|\langle\psi_v|\langle\psi_e|\mathbf{d}|\psi_e\rangle|\psi_v\rangle|\psi_r\rangle = \langle\psi_r|\mathbf{d}_{ev}|\psi_r\rangle. \quad (2.49)$$

Here, the operator \mathbf{d}_{ev} is obtained from the dipole moment operator \mathbf{d} evaluated for the electronic state $|\psi_e\rangle$ and vibrational state $|\psi_v\rangle$. The molecules used in our experiments are in their electronic and vibrational ground state, except for the molecules experiencing vibrational inversion motion as discussed in section 2.4.1.

In an external electric field the Stark effect mixes states which are coupled by the electric dipole moment. For typical laboratory electric fields strong mixing is particularly pronounced for the rotational states $|\psi_r\rangle$, due to their closely spaced energy levels.⁷ This results in the orientation of the molecule and with it the dipole moment \mathbf{d}_{ev} along the electric field direction. Therefore, we strongly focus on the rotational states in the following discussions.

In the case of a rigid rotating molecule, in the rotational state $|\psi_r\rangle$ the dipole moment operator can be expressed by

$$(\mathbf{d}_{ev})_i = S_{i\alpha}^{-1} \mu_\alpha = S_{\alpha i} \mu_\alpha, \quad (2.50)$$

where μ_α are the projections of the dipole moment on the molecule-fixed axes and \mathbf{S} the matrix which relates the molecule-fixed axes (α) to the space-fixed axes (i) [Kro75]. The \mathbf{S} -matrix determines the orientation of the molecule with respect to an external electric field \mathbf{E} , which defines the space fixed axes.

Since all types of rigid rotor states $|\psi_r\rangle$ can be described by a sum $|\psi_r\rangle = \sum_{JKM} a^{JKM} |JKM\rangle$ of the symmetric rotor states $|JKM\rangle$, the evaluation of the matrix elements

$$\langle JKM | (\mathbf{d}_{ev})_i | J'K'M' \rangle = \mu_\alpha \langle JKM | S_{\alpha i} | J'K'M' \rangle \quad (2.51)$$

is sufficient. By employing the Wigner-Eckart theorem [Sak94], we derive

$$\langle JKM | S_{\alpha i} | J'K'M' \rangle = \langle J || \mathbf{S} || J' \rangle \langle JK | s_\alpha | J'K' \rangle \langle JM | s_i | J'M' \rangle, \quad (2.52)$$

where the Clebsch-Gordan coefficients $\langle JK | s_\alpha | J'K' \rangle$ and $\langle JM | s_i | J'M' \rangle$ contain the K and M dependence and $\langle J || \mathbf{S} || J' \rangle$ describes the reduced matrix element [Sak94]. The values of these factors are taken from [Kro75] and listed in Tbl. 2.5.

2.4.1 Stark effect for symmetric top molecules

In the case of a symmetric-top molecule the states $|JKM\rangle$ are eigenstates of the unperturbed symmetric-top Hamiltonian (see subsection 2.2.1). The applied external electric field $\mathbf{E} = E_Z \mathbf{e}_Z$ defines the quantization axis Z . This results in

$$(\mathbf{d}_{ev})_Z = \mu_Z = S_{xZ} \mu_x + S_{yZ} \mu_y + S_{zZ} \mu_z \quad (2.53)$$

$$= S_{zZ} \mu_z, \quad (2.54)$$

since $\mu_x = \mu_y = 0$ for symmetric top molecules.⁸ This leads to the matrix elements

$$\begin{aligned} \langle JKM | \mu_Z | J'K'M' \rangle &= \mu_z \langle JKM | S_{zZ} | J'K'M' \rangle \\ &= \mu_z \langle J || \mathbf{S} || J' \rangle \langle JK | s_z | J'K' \rangle \langle JM | s_Z | J'M' \rangle \delta_{KK'} \delta_{MM'}, \end{aligned} \quad (2.55)$$

⁷Apart from accidental degeneracies, the energy-level spacing for electronic and vibrational states is typically orders of magnitude larger than the spacing between rotational energy levels [Dem03].

⁸Here, $z = a$ ($z = c$) for a prolate (oblate) symmetric rotor. x and y are assigned to principal axes concordantly.

Table 2.5: Direction cosine matrix elements for symmetric top states. The table is adapted from [Kro75].

	$J' = J + 1$	$J' = J$	$J' = J - 1$
$\langle J \mathbf{S} J' \rangle$	$\frac{1}{(J+1)\sqrt{(2J+1)(2J+3)}}$	$\frac{1}{J(J+1)}$	$\frac{1}{J\sqrt{(2J+1)(2J-1)}}$
$\langle JK s_z J'K \rangle$	$\sqrt{(J+K+1)(J-K+1)}$	K	$\sqrt{(J+K)(J-K)}$
$\langle JK s^\pm J'K \pm 1 \rangle$	$\mp\sqrt{(J \pm K + 1)(J \pm K + 2)}$	$\sqrt{(J \mp K)(J \pm K + 1)}$	$\pm\sqrt{(J \mp K)(J \mp K - 1)}$
$\langle JM s_z J'M \rangle$	$\sqrt{(J+M+1)(J-M+1)}$	M	$\sqrt{(J+M)(J-M)}$
$\langle JM s_\mp J'M \pm 1 \rangle$	$\mp\sqrt{(J \pm M + 1)(J \pm M + 2)}$	$\sqrt{(J \mp M)(J \pm M + 1)}$	$\pm\sqrt{(J \mp M)(J \mp M - 1)}$

^a $s^\pm = s_x \pm is_y$ and $s_\mp = s_x \mp is_y$.

which are diagonal with respect to K and M . Using the expressions for the direction cosines provided in Tbl. 2.5 we obtain

$$\langle JKM | \mu_z | JKM \rangle = \mu_z \frac{KM}{J(J+1)}, \quad (2.56)$$

$$\langle JKM | \mu_z | J+1KM \rangle = \mu_z \left[\frac{(J+K+1)(J-K+1)(J+M+1)(J-M+1)}{(J+1)^2(2J+1)(2J+3)} \right]^{1/2}, \quad (2.57)$$

$$\langle JKM | \mu_z | J-1KM \rangle = \mu_z \left[\frac{(J+K)(J-K)(J+M)(J-M)}{J^2(2J-1)(2J+1)} \right]^{1/2}. \quad (2.58)$$

To obtain the eigenenergies and eigenstates for a symmetric top molecule in an electric field, the full Hamiltonian $H_{rot}^{sym} + H_{int}$ has to be diagonalized. This is shown for CH_3F and CF_3H in Fig. 2.4a and Fig. 2.4b, respectively.

A rough estimate of the Stark splitting in an electric field can be obtained by the perturbation method. To second order the Stark-energy is given by

$$\begin{aligned} W_{int} &= \langle JKM | H_{int} (|JKM\rangle + |\Phi'\rangle + \dots) \quad (2.59) \\ &= \langle JKM | H_{int} | JKM \rangle + \sum_{J' \neq J} \langle JKM | H_{int} | J'KM \rangle \langle J'KM | \Phi' \rangle + \dots \\ &= \langle JKM | H_{int} | JKM \rangle + \sum_{J' \neq J} \frac{\langle JKM | H_{int} | J'KM \rangle \langle J'KM | H_{int} | JKM \rangle}{W_{JK} - W_{J'K}} + \dots \\ &= -\mu_z E_Z \frac{KM}{J(J+1)} \\ &\quad + \frac{\mu_z^2 E_Z^2}{2Bh} \left[\frac{(J^2 - K^2)(J^2 - M^2)}{J^3(2J-1)(2J+1)} - \frac{[(J+1)^2 - K^2][(J+1)^2 - M^2]}{(J+1)^3(2J+1)(2J+3)} \right] + \dots \end{aligned}$$

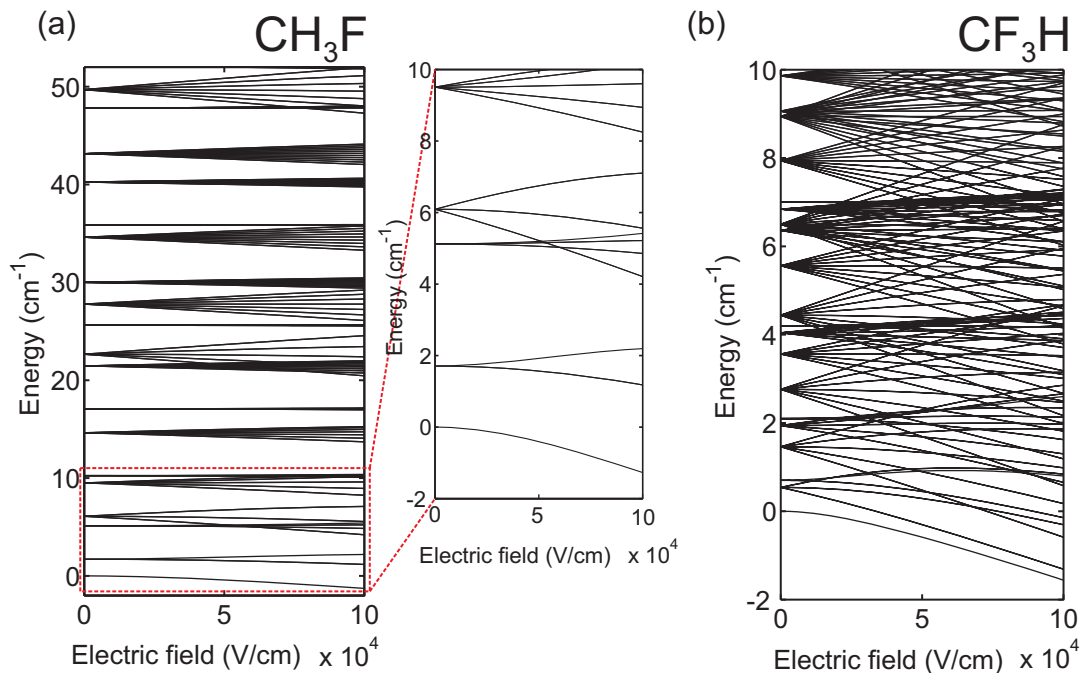


Figure 2.4: Stark splittings for CH_3F (prolate) and CF_3H (oblate) are presented in (a) and (b), respectively. The lines are obtained from a diagonalization of the respective symmetric rotor Hamiltonian's. In (a) the energy levels up to 10 cm^{-1} are magnified.

The expression

$$|\Phi'\rangle = \sum_{J' \neq J} \frac{\langle J'KM | H_{int} | JKM \rangle}{W_{JK} - W_{J'K}} |J'KM\rangle \quad (2.60)$$

is the first-order correction of the unperturbed molecular state $|JKM\rangle$ due to the interaction potential. The first term of Eq. 2.59 describes the linear Stark-shift $d_Z^0 E_Z$ due to the permanent dipole moment (see Eq. 2.48), while the second-order term in Eq. 2.59 determines the linear polarizability contribution $a_{ZZ} E_Z^2$ of the Stark-shift. The sum over the K and M values is ignored because the matrix elements shown in Eq. 2.55 are diagonal for these quantum numbers.

A particle possesses a permanent electric dipole moment and linear Stark shifts only if a degeneracy of opposite parity eigenstates exists. This leads to non-parity eigenstates of the Hamiltonian in the presence of an external electric field [Sak94]. The appearance of a permanent electric dipole moment for symmetric-top molecules results from the $\pm|K|$ degeneracy, as evident from Eq. 2.16 and Eq. 2.18. The $|J|K|M\rangle$ states are not parity eigenstates.⁹ Since the molecules have to obey parity conservation in free space, they appear in the degenerate superposition states

⁹The $|JKM\rangle$ states are not eigenstates of the parity transformation $\sigma_v |JKM\rangle = (-1)^{J+K} |J-KM\rangle$ (see [Kro75]), which describes a reflection in the ac -plane when c is the symmetry axis ($C_2^b E^* = \sigma_v$).

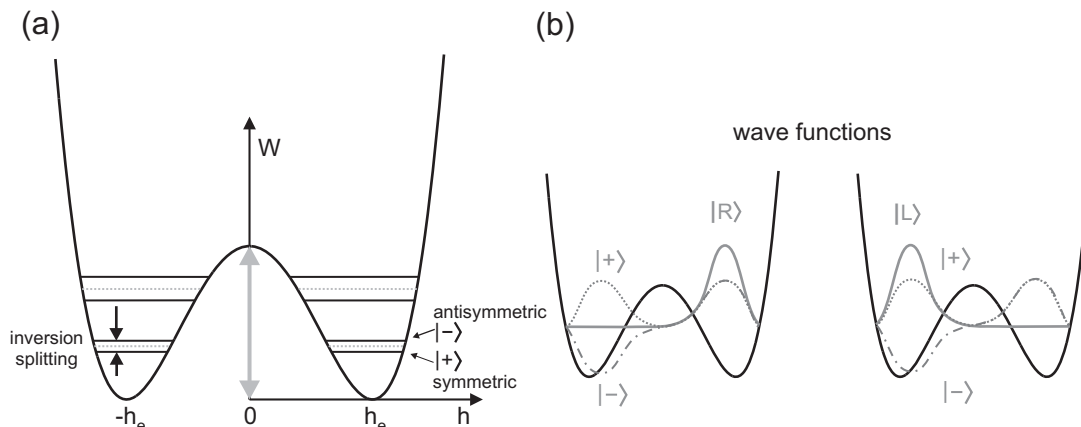


Figure 2.5: (a) Potential energy of the inversion vibration motion. The inversion motion is described by the coordinate h along the molecular symmetry axis. The positions of the potential minima are designated by $\pm h_e$. The two lowest lying states are given by the symmetric vibrational ground state $|+\rangle$ and the antisymmetric first excited state $|-\rangle$. In (b) the wave functions of the non-stationary states $|R\rangle$ ($|L\rangle$) as superpositions of $|+\rangle$ ($|-\rangle$) are illustrated.

$|\psi_{\pm}\rangle = 1/\sqrt{2}\{|J|K|M\rangle \pm |J-|K|M\rangle\}$, which are eigenstates of opposite parity. They are eigenstates of $H_{rot}^{sym.}$ but not eigenstates of $H_{rot}^{sym.} + H_{int}$ in the asymptotic limit $|\mathbf{E}| \rightarrow 0$. On the other hand, the degenerate symmetric-top eigenstates $|J \pm |K|M\rangle$ which are superpositions of the $|\psi_{\pm}\rangle$ states, are eigenstates of $H_{rot}^{sym.} + H_{int}$ in the asymptotic regime. Therefore, symmetric-top molecules possess a nonvanishing permanent electric dipole moment and show a linear Stark shift (described by Eq. 2.59) in an electric field.

Inversion splitting

For symmetric top molecules experiencing vibrational inversion such as NH_3 , the Stark interaction behavior as discussed previously has to be revisited. When the space inversion symmetry operation E^* (see appendix B) becomes a feasible symmetry operation no permanent dipole moment and thereby no linear Stark shift exists in the vibrational-ground state [Bun06]. In the case where the (symmetric) ground-state $|+\rangle$ and the (antisymmetric) first excited state $|-\rangle$ of the inversion vibrational motion (states of opposite parity) are close to degeneracy a permanent dipole moment appears when these states are strongly mixed by an external electric field.¹⁰

Here, for each rotational state $|JKM\rangle$ we obtain two by an energy of W_{inv} different Stark-interacting states $|\pm\rangle|JKM\rangle$. If the Stark energy for these two states

¹⁰This is the case, when the energy difference of these vibrational states lies in the energy range of the Stark energy.

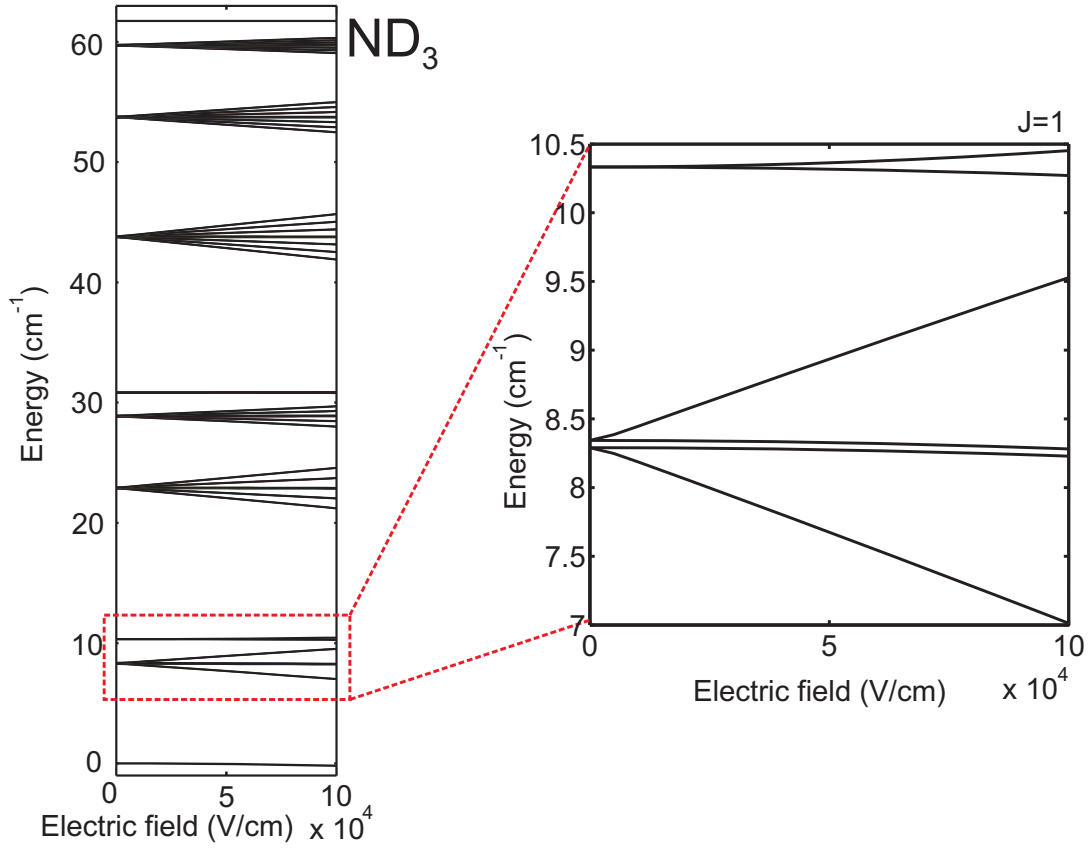


Figure 2.6: Stark splitting for ND_3 including inversion splitting ($W_{inv} = 0.053 \text{ cm}^{-1}$). The curves are obtained from a diagonalization of the ND_3 rotational Hamiltonian. The curves for $J = 1$ are magnified.

$|\pm\rangle|JKM\rangle$ with respect to a given electric field strength is comparable or greater than the inversion energy W_{inv} , the states are strongly coupled and a solution can no longer be obtained by means of perturbation theory.

By neglecting all other higher-lying rotational states that can interact with the given rotational state $|JKM\rangle$ (see Tbl. 2.5) an exact solution that incorporates the closely spaced inversion states can be found. The Schrödinger equation of this problem is formed by

$$H|\psi\rangle = (H_{rot} + H_{inv} + H_{int})|\psi\rangle = W|\psi\rangle, \quad (2.61)$$

which leads to the matrix equation

$$\begin{pmatrix} \langle +|H|+ \rangle & \langle +|H|- \rangle \\ \langle -|H|+ \rangle & \langle -|H|- \rangle \end{pmatrix}_{J,K,M} \begin{pmatrix} a_1 \\ a_2 \end{pmatrix} = W \begin{pmatrix} a_1 \\ a_2 \end{pmatrix} \quad (2.62)$$

$$\Leftrightarrow \begin{pmatrix} W_{rot} - W & -\mu_{\pm}|\mathbf{E}|\frac{MK}{J(J+1)} \\ -\mu_{\pm}|\mathbf{E}|\frac{MK}{J(J+1)} & W_{rot} + W_{inv} - W \end{pmatrix} \begin{pmatrix} a_1 \\ a_2 \end{pmatrix} = 0 \quad (2.63)$$

for a given rotational state $|JKM\rangle$. The coefficients a_1 and a_2 describe the superposition ratios of $|\pm\rangle|JKM\rangle$ for the new eigenstates, where $\mu_{\pm} = \langle +|\mu|-\rangle$ is the dipole moment evaluated for the inversion vibration states, and W_{inv} describes the inversion energy splitting. Solutions for the molecular energy in an electric field are given by

$$W_{1,2} = W_{rot} + \frac{W_{inv}}{2} \pm \sqrt{\left(\frac{W_{inv}}{2}\right)^2 + \left(\mu_{\pm}|\mathbf{E}|\frac{MK}{J(J+1)}\right)^2}. \quad (2.64)$$

The corresponding eigenstates are formed by $|\psi_1\rangle = (a_2|+\rangle + a_1|-\rangle)|JKM\rangle$ and $|\psi_2\rangle = (a_1|+\rangle - a_2|-\rangle)|JKM\rangle$. The electric-field dependence for the mixing coefficients is given by the equations [Tow75]

$$a_{1,2}(|\mathbf{E}|) = \left(\frac{\sqrt{W_{inv}^2 + 4\left(\mu_{\pm}|\mathbf{E}|\frac{MK}{J(J+1)}\right)^2} \pm W_{inv}}{2\sqrt{W_{inv}^2 + 4\left(\mu_{\pm}|\mathbf{E}|\frac{MK}{J(J+1)}\right)^2}} \right)^{1/2}. \quad (2.65)$$

In the case when $\mu_{\pm}|\mathbf{E}|MK/(J(J+1))$ is smaller than the inversion splitting W_{inv} , the Stark energy depends on $|\mathbf{E}|^2$, while a linear dependence on the electric field is observed in the case where $\mu_{\pm}|\mathbf{E}|MK/(J(J+1))$ is greater than the inversion splitting. In the limiting cases of the electric field, the coefficients $a_{1,2}$ take on the following values:

$$\lim_{|\mathbf{E}| \rightarrow 0} \Rightarrow a_1 \rightarrow 1 \quad a_2 \rightarrow 0 \quad (2.66)$$

$$\lim_{|\mathbf{E}| \rightarrow \infty} \Rightarrow a_1 \rightarrow \frac{1}{\sqrt{2}} \quad a_2 \rightarrow \frac{1}{\sqrt{2}}. \quad (2.67)$$

In high electric fields the molecular inversion is strongly hindered due to the higher splitting caused by the electric field. This results in the asymptotic states $|R\rangle = 1/\sqrt{2}(|+\rangle + |-\rangle)$ and $|L\rangle = 1/\sqrt{2}(|+\rangle - |-\rangle)$. These are not parity eigenstates. They display the fixed orientation of the molecular symmetry axis with respect to the electric-field axis. This can be visualized by the corresponding wave function (see Fig. 2.5b), which is largely concentrated on the right ($|R\rangle$) or left side ($|L\rangle$) with respect to the mirror plane of the molecule inversion. An example for the Stark effect of a molecule exhibiting inversion splitting is presented in Fig. 2.6 for ND_3 . Note that we use ND_3 and not NH_3 due to the larger inversion splitting of the latter one ($W_{inv}^{\text{ND}_3} = 0.053 \text{ cm}^{-1}$ and $W_{inv}^{\text{NH}_3} = 0.79 \text{ cm}^{-1}$). The larger energy spacing for NH_3 results in lower mixing of the Stark interacting states and therefore in a weaker Stark shift as compared to ND_3 .

Table 2.6: The dipole-moment-coupling relations for the different rotational states of an asymmetric rotor are shown in the table. The selection rules for the quantum numbers K_A and K_C are presented as well. The table is adapted from [Kro75].

μ_a	$A \leftrightarrow B_a$	$B_b \leftrightarrow B_c$	$\Delta K_A = \text{even}$
	ee	eo oo oe	$\Delta K_C = \text{odd}$
μ_b	$A \leftrightarrow B_b$	$B_a \leftrightarrow B_c$	$\Delta K_A = \text{odd}$
	ee	oo eo oe	$\Delta K_C = \text{odd}$
μ_c	$A \leftrightarrow B_c$	$B_a \leftrightarrow B_b$	$\Delta K_A = \text{odd}$
	ee	oe eo oo	$\Delta K_C = \text{even}$

2.4.2 Stark effect for asymmetric-top molecules

The interaction Hamiltonian for an asymmetric top molecule in an external electric field $\mathbf{E} = E_Z \mathbf{e}_Z$ is given by

$$H_{int} = -(\mathbf{d}_{ev})_Z E_Z = -\mu_Z E_Z = -E_Z (S_{aZ} \mu_a + S_{bZ} \mu_b + S_{cZ} \mu_c). \quad (2.68)$$

When the eigenstates $|J\tau M\rangle$ of the unperturbed asymmetric rotor Hamiltonian, are expressed in terms of their expansion in the symmetric top basis described by Eq. 2.33, the matrix elements of the dipole moment operator are found to be:

$$\begin{aligned} \langle J\tau M | \mu_Z | J'\tau' M' \rangle &= \sum_{\alpha} \mu_{\alpha} \langle JK M | S_{\alpha Z} | J'K' M' \rangle \\ &= \sum_{\alpha} \mu_{\alpha} \langle J || \mathbf{S} || J' \rangle \langle JM | s_Z | J'M' \rangle \delta_{MM'} \\ &\quad \times \sum_{KK'} a_K^{J\tau M} a_{K'}^{J'\tau' M'} \langle JK | s_{\alpha} | J'K' \rangle \end{aligned} \quad (2.69)$$

In contrast to the matrix elements of the symmetric top given in Eq. 2.55, the matrix elements are diagonal in M only. Due to the larger number of coupling terms, a rough estimate of the Stark splitting from perturbation theory as described in subsection 2.4.1 is hardly possible. Therefore, the eigenenergies and eigenstates are in general obtained from the diagonalization of the full Hamiltonian $H_{rot}^{asym.} + H_{int}$. This is shown for formaldehyde (H_2CO) in Fig. 2.7.

To understand which eigenstates of the free asymmetric rotor Hamiltonian are coupled by the dipole moment, we use the assignment of the molecule-fixed components μ_{α} of the dipole moment operator with respect to the D_2 symmetry group. Since the vector component $\mu_{\alpha} S_{\alpha Z}$ must change sign when rotations by π are applied on the axes perpendicular to the α -axis, we derive from Tbl. 2.3 that $\mu_a S_{aZ}$, $\mu_b S_{bZ}$ and $\mu_c S_{cZ}$ belong to the B_a , B_b and B_c representation of the D_2 symmetry group, respectively [Kro75]. The matrix element $\langle J\tau M | \mu_Z | J'\tau' M' \rangle$ is non-zero only if the product of the representations Γ of the rotational states $|J\tau M\rangle$, $|J'\tau' M'\rangle$ and the dipole moment μ_Z fulfills

$$\Gamma(|J\tau M\rangle) \times \Gamma(\mu_Z) \times \Gamma(|J'\tau' M'\rangle) = A, \quad (2.70)$$

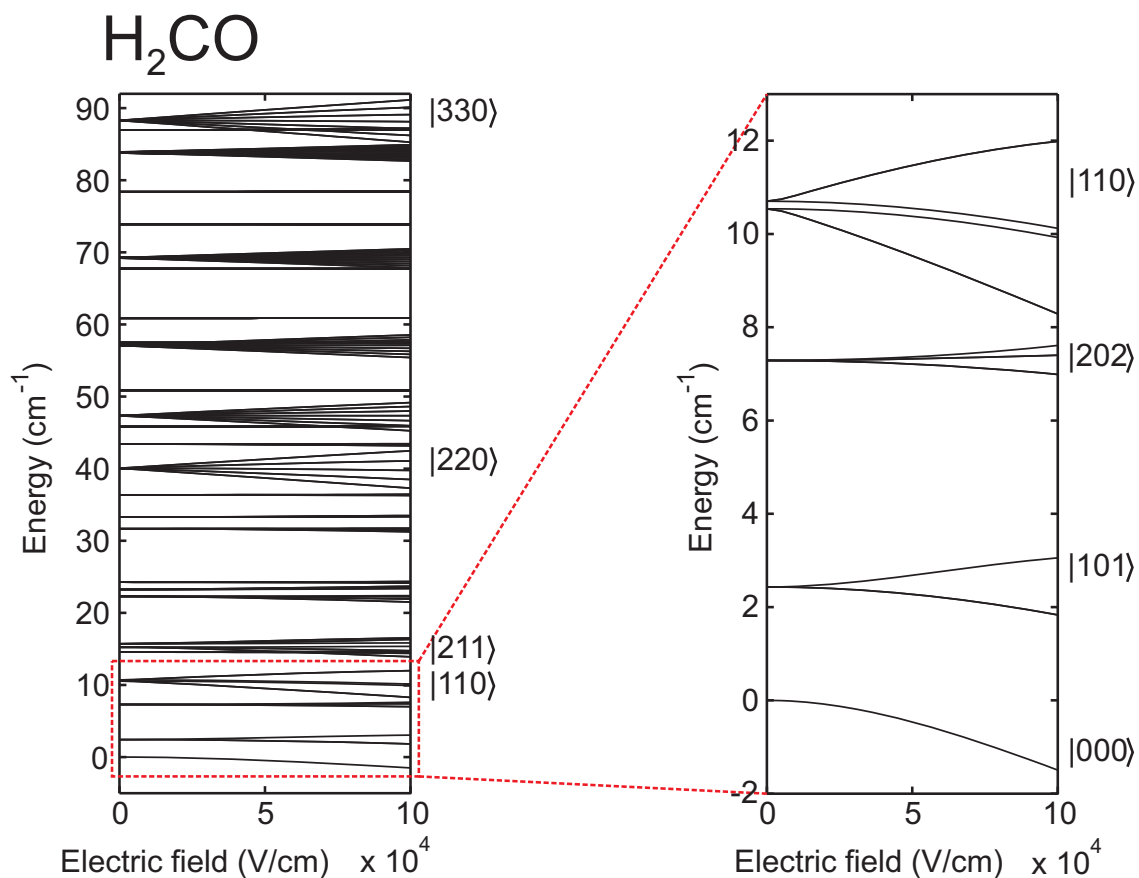


Figure 2.7: Stark splitting for H₂CO ($\mu_a = 2.34\text{D}$) for electric fields up to 100 kV/cm and rotational energies up to $\sim 90\text{ cm}^{-1}$. The curves are obtained from a diagonalization of the H₂CO asymmetric rotor Hamiltonian in the presence of an external electric field. The curves up to $J = 1, K_A = 1, K_C = 0$ are magnified.

where A is the totally symmetric representation of the symmetry group. This results from the vanishing integral rule [Bun06]. By using Eq. 2.70 we derive the coupling relations which are listed in Tbl. 2.6.

Chapter 3

Electric guiding and production of velocity-selected molecular pulses

The Stark effect, that was introduced in the preceding chapter, can be used to apply a force on (neutral but) polar molecules. This allows the confinement of slow molecules with kinetic energies in the regime below ~ 1 K in suitable electric fields. In our experiments we use a two dimensional trapping configuration to produce a guided slow molecular beam. The principles of this electric guiding technique are outlined in this chapter.

In its original form, the technique of electric guiding is a method for producing a continuous beam of slow molecules [Ran03, Jun04a]. Here, we demonstrate an extension of this technique which allows for the production of mono-energetic molecular pulses by velocity selection. The latter is reminiscent of the first velocity-selection experiment carried out by Eldrige in 1927 [Eld27] and employed in many other experiments afterwards [Sco88]. In these experiments velocity selection was achieved by mechanically chopping a continuous molecular beam effusing from a slit. In our setup the selection is done electrically by switching the voltages applied to the electrode segments of the guide on and off in a specific sequence. The switching times are adjusted to the desired molecular velocity. In this way molecular pulses with a narrow velocity distribution around a desired velocity are obtained. The main advantage of our method in comparison to a mechanical approach is the transverse confinement of the molecular pulses by the ambient electric field. This guarantees spatial addressability over large distances, which is a necessity for many further applications [Wil08a, Saw10].

3.1 Trapping polar molecules

To confine polar molecules in an inhomogeneous electric field the divergence of the Stark-force field $\nabla \cdot \mathbf{F}(\mathbf{x}) = -\nabla^2 W_{int}(|\mathbf{E}|)$ needs to be negative within the region of the trapping volume. This is known as the application of Earnshaw's theorem for polar neutral particles [Ear42]. In the case of polar molecules with a linear Stark shift $W_{int} = -\mu_{eff}|\mathbf{E}|$, where μ_{eff} is the effective dipole moment, we obtain the expression

$$\mathbf{F}(\mathbf{x}) = \mu_{eff} \nabla |\mathbf{E}(\mathbf{x})| \quad (3.1)$$

$$= \frac{\mu_{eff}}{|\mathbf{E}|} \sum_{i,j=1}^3 \left(\frac{\partial^2 \phi}{\partial x_i \partial x_j} \right) \left(\frac{\partial \phi}{\partial x_i} \right) \mathbf{e}_j \quad (3.2)$$

for the Stark force, where ϕ is the scalar potential. With ϕ obeying the Laplace equation

$$\nabla^2 \phi(\mathbf{x}) = 0, \quad \forall \mathbf{x} \in \mathbb{R}^3 \quad (3.3)$$

the divergence of the Stark force is given by

$$\nabla \cdot \mathbf{F} = \frac{\mu_{eff}}{|\mathbf{E}|^3} \sum_{i,j,k=1}^3 \left[\left(\frac{\partial \phi}{\partial x_k} \right)^2 \left(\frac{\partial^2 \phi}{\partial x_i \partial x_j} \right)^2 - \left(\frac{\partial \phi}{\partial x_i} \right) \left(\frac{\partial \phi}{\partial x_k} \right) \left(\frac{\partial^2 \phi}{\partial x_i \partial x_j} \right) \left(\frac{\partial^2 \phi}{\partial x_k \partial x_j} \right) \right], \quad (3.4)$$

where the contributions of the sum are always greater or equal to zero due to Schwarz's inequality. Therefore, the sign of the divergence depends solely on the sign of μ_{eff} . For molecules experiencing a quadratic Stark shift $W_{int} = -1/2\alpha_{eff}\mathbf{E}^2$, where α_{eff} describes the effective linear polarizability. In this case the divergence of the Stark force is given by

$$\nabla \cdot \mathbf{F} = \alpha_{eff} \sum_{i,j=1}^3 \left(\frac{\partial^2 \phi}{\partial x_i \partial x_j} \right)^2. \quad (3.5)$$

Analog to the linear Stark shift is the sign of the divergence in the case of the quadratic Stark shift solely determined by α_{eff} . In both of these cases, the sign of μ_{eff} and α_{eff} respectively, depends on the rotational state of the molecule as described in section 2.4. Therefore, we can distinguish between two classes of molecular rotational states. Molecules in 'high-field-seeking' (hfs) rotational states defined by $\mu_{eff} > 0$ (linear), $\alpha_{eff} > 0$ (quadratic) experience a negative Stark shift while molecules in 'low-field-seeking' (lfs) rotational states with $\mu_{eff} < 0$ (linear), $\alpha_{eff} < 0$ (quadratic) experience a positive Stark shift when an electric field is applied. Therefore, only molecules in low-field-seeking rotational states can be trapped in a static inhomogeneous electric field around a field minimum (except [Sek96, Jon97]).

As pointed out before the energetic limit for molecules with masses below 100 amu that can be trapped in an electric field is around kinetic energies of ~ 1 K. This

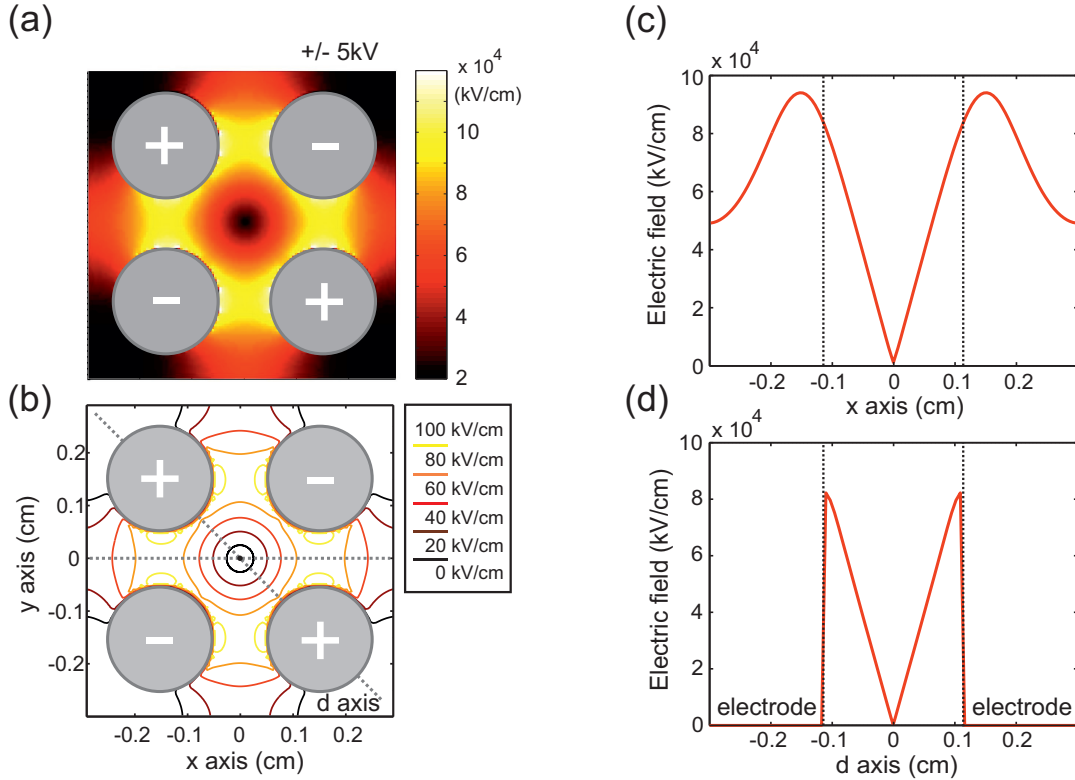


Figure 3.1: The two dimensional electric guiding potential created by four identical electrodes of alternating voltages is presented in (a). The SIMION software package is used to simulate the electric field [Man06]. In (b) a contour plot visualizing the equipotential lines is shown. The electric field along the x-axis for $y = 0$ and along the diagonal d-axis is shown in (c) and (d), respectively.

is explained by the fact that low-field-seeking molecular states transform into high-field-seeking states upon increasing electric fields beyond a certain field strength. As can be seen from Eq. 2.59 and Tbl. 2.5 higher order contributions start to dominate the Stark shift for increasing electric fields leading to this behavior.

The electric field used to confine molecules in our experiment is formed by applying high voltage to four parallel electrode rods (see Fig. 3.1). In the transverse directions the electrodes, carrying alternating voltages of the same absolute value, are positioned at the vertices of a square. In this configuration, a two dimensional trapping potential is created, in which the molecules are confined in two directions and can freely propagate in the longitudinal direction. The electric field is very well approximated by the second order polynomial solution of the two dimensional Poisson equation (see section A.1), which leads to the electric quadrupole potential

$$|\mathbf{E}|(\mathbf{x}) = a_2 \sqrt{x^2 + y^2}, \quad (3.6)$$

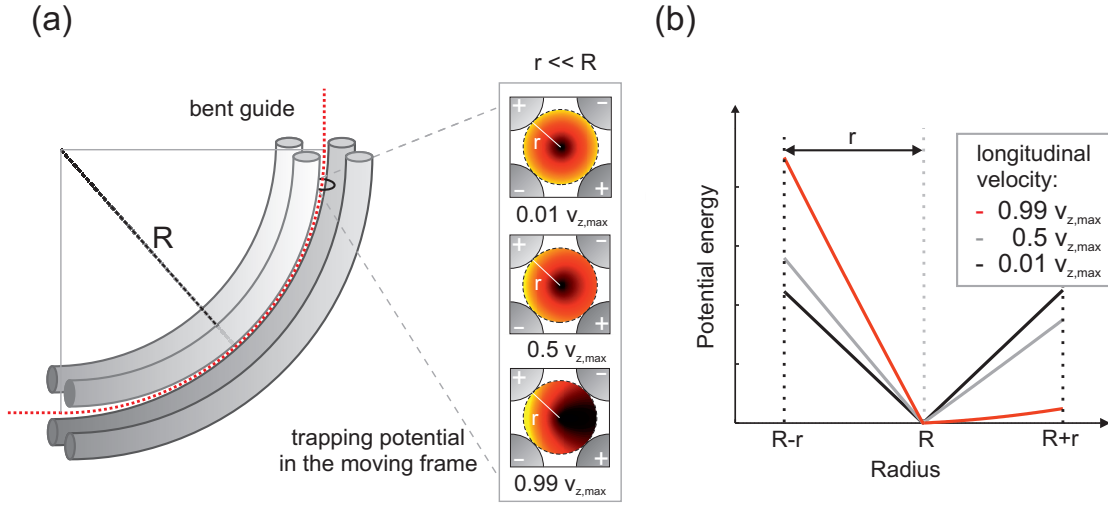


Figure 3.2: (a) bent guide electrodes and trapping potentials for different longitudinal velocities. The Stark potential is lowered by the centrifugal force in the moving frame of the molecule. The change in trap depth for a longitudinal velocity of 0.01, 0.5 and 0.99 of the longitudinal cutoff velocity is shown in (b).

where a_2 is the amplitude and x, y are the directions of confinement. Here, the voltage and the spatial separation of the electrodes give the criterium for the electric field strength.

3.2 Velocity filtering with an electric guide

The electric quadrupole transversely confines polar molecules in lfs-states, provided their kinetic energy does not exceed the potential barrier. The Stark shift $W_{int}(E_{\max})$ at the maximum of the trapping field E_{\max} determines the trap depth and thereby, the maximum transverse velocity

$$v_{t,\max} = (v_x^2 + v_y^2)^{1/2} = \sqrt{\frac{2W_{int}(E_{\max})}{m}} \quad (3.7)$$

of the molecules in the guide. Here m is the mass of the molecule. As shown in Fig. 3.2, a bend in the guide's electrodes limits the molecular velocity in the longitudinal direction. The longitudinal cutoff velocity is obtained by equating the centrifugal force mv_z^2/R to the restoring force $\sim W_{int}/r$ provided by the electric field:

$$v_{z,\max} = \sqrt{\frac{W_{int}(E_{\max})R}{rm}} = \sqrt{\frac{R}{2r}} v_{t,\max}. \quad (3.8)$$

Here, R is the radius of curvature of the bend and r is the inner radius of the guide given by the smallest distance between the guide center and the surface of the electrodes (see Fig. 3.1a). This relation is valid for the case where $R \gg r$.

3.3 Flux of guided molecules

The flux of the guided molecules can be derived from the velocity distribution of a free thermal gas in the case of an effusive source [Jun04a]. For molecules in a specific rotational state $|n\rangle$ with Stark energy $W_{int,n}$, the flux Φ_n of guided molecules is very well approximated by

$$\Phi_n \propto \int_{D_{v_x, v_y}} f^{1D}(v_x) f^{1D}(v_y) \left(\int_{v_z=0}^{v_{z,\max}} v_z f^{1D}(v_z) dv_z \right) dv_{x,y}, \quad (3.9)$$

where $D_{v_x, v_y} = \{v_x, v_y \in \mathbb{R}^2 : v_x^2 + v_y^2 \leq 2W_{int,n}/m\}$. Here, $f^{1D}(v_{x,y,z})$ describes the 1-dimensional velocity distributions $f^{1D}(v_{x,y,z}) = (\sqrt{\pi}\alpha)^{-1} \exp(-v_{x,y,z}^2/\alpha^2)$, where $\alpha = \sqrt{2k_B T/m}$, k_B the Boltzmann constant and T the temperature. For $\alpha \gg v_{t,\max}, v_{z,\max}$ we obtain from Eq. 3.9 and Eq. 3.8 that

$$\Phi_n \propto v_{t,\max}^4 \propto (W_{int,n})^2. \quad (3.10)$$

This relation is not valid anymore for a small bend radius ($R \sim r$) where Eq. 3.8 breaks down and/or a low temperature thermal gas ($\alpha \sim v_{z,\max}$ or $\alpha \sim v_{t,\max}, v_{z,\max}$).

To obtain an expression for the total flux the thermal occupation of rotational states $|n\rangle$ has to be considered. The occupation for a fixed temperature T is given by

$$p_n = \frac{1}{Z} g_n g_I e^{-W_n/k_B T}, \quad (3.11)$$

with the partition function Z , the rotation energy W_n and the degeneracy factors g_n and g_I for the rotational state and the nuclear spin states, respectively. The total guided flux is given by

$$\Phi = \sum_n p_n \Phi_n \propto \sum_n p_n W_{int,n}^2. \quad (3.12)$$

This yields that for molecules with only linear Stark shifts the flux depends quadratically on the trapping field ($\Phi \propto E_{\max}^2$). Molecules experiencing only quadratic Stark shifts yield a quartic dependence between the flux and the trapping field ($\Phi \propto E_{\max}^4$) [Mot09b].

An additional factor $\exp(-b/v_z)$ is included in the integral of Eq. 3.9 to account for collision losses in the vicinity of the molecule injection where the density is relatively high. The factor b is proportional to the density at the injection region. As described in [Mot09a], losses from the guided beam in this region are proportional to the time t_c spend in this region and thereby inversely proportional to the molecule's longitudinal

velocity v_z , since $t_c \propto 1/v_z$. In particular, the amount of guided molecules with small longitudinal velocities is strongly affected by this attenuation effect. With this included in our model, the flux is given by

$$\Phi_n \propto v_{t,\max}^2 \int_{v_z=0}^{v_{z,\max}} v_z e^{-b/v_z} f^{1D}(v_z) dv_z \propto v_{t,\max}^2 \int_{v_z=0}^{v_{z,\max}} v_z e^{-b/v_z} dv_z, \quad (3.13)$$

in the case $\alpha \gg v_{t,\max}, v_{z,\max}$. By omitting the velocity term v_z in the integral for the longitudinal velocities we obtain the guided density

$$n_n \propto v_{t,\max}^2 \int_{v_z=0}^{v_{z,\max}} e^{-b/v_z} f^{1D}(v_z) dv_z \propto v_{t,\max}^2 \int_{v_z=0}^{v_{z,\max}} e^{-b/v_z} dv_z. \quad (3.14)$$

This is derived from the relation $\Phi_n = n_n v_z A$ between the flux and density of a molecular beam with cross section A [Laf98].

3.4 Experimental setup

A schematic of the setup used to guide polar molecules is shown in Fig. 3.3. This is the same setup that has been used for previous experiments and has been described in detail elsewhere [Mot09a, Mot09b, Mot10]. It consists of three interconnected ultrahigh-vacuum chambers accommodating the electrodes of the electric quadrupole guide. Four stainless-steel rods with a diameter of 2 mm in a quadrupole configuration separated by 1 mm from each other constitute the electrodes of the guide. Ceramic insulator mounts fix the position of the metallic holders for the guide electrodes and thereby preserve the spacing between the electrodes.

The guide is split into four segments. Each guide segment is separated by a 1 mm gap from its neighboring guide segments. The guide segments A and C made of bent electrodes with a curvature radius of 5 cm are located in the first and second vacuum chamber, respectively, while the segments B and D are placed in the differential pumping sections connecting the vacuum chambers (see Fig. 3.3). The purpose of the differential pumping sections is to isolate the different vacuum chambers from each other. Each differential pumping section is made of two Macor brackets which, when clamped together enclose a long distance of the guiding electrodes. Only the hole given by the guiding volume in the section allows particles to travel from one vacuum chamber to the other, thereby allowing to maintain a pressure difference between the two adjacent vacuum chambers.

Molecules from a gas reservoir are injected into the guide through a ceramic tube with 1.5 mm diameter, that is 1 mm distant from the first guide segment to avoid discharges. The ceramic tube is thermally connected to a liquid nitrogen reservoir to reduce the temperature of the incoming molecules and thus increase the amount of slow, guidable molecules.¹ A heater is installed to make temperature adjustment

¹In addition, cooling of the nozzle/gas reduces the number of thermally populated states, as discussed in [Mot10] and serves as a basis for the idea to use buffer-gas cooling.

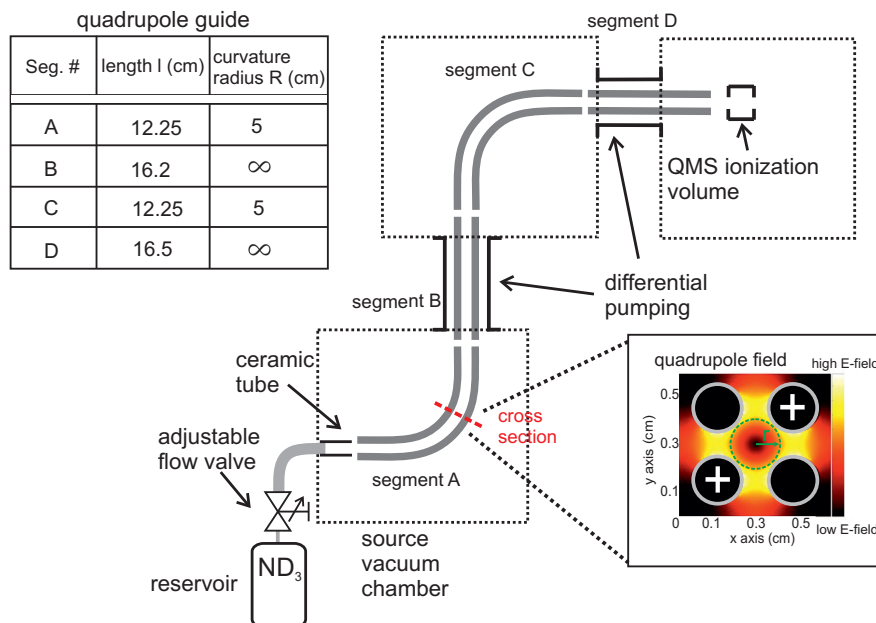


Figure 3.3: The experimental setup consists of three differentially pumped vacuum chambers. In the first vacuum chamber molecules are injected into the guide through a ceramic nozzle. A fraction of these molecules is guided via the four-segment electric guide to a quadrupole mass spectrometer (QMS) where they are detected. The inset in the lower right part of the figure depicts the transverse profile of the electric field. r is the free inner radius of the guide, at which the maximum trapping field is reached. The lengths, l , and curvatures, R , of the four segments are detailed in the table in the upper left corner of the figure.

within a range of 100–400 K. This is needed to keep a reasonably high vapor pressure and avoid resublimation of molecules on the tube. A turbo-molecular pump with a pumping speed of 500 l/s is employed, to maintain a low pressure in the first chamber. A base pressure of 10^{-9} mbar can be achieved without gas flow. Measurements are typically carried out at an ambient pressure of 10^{-7} mbar.

The guided molecules are detected in the third vacuum chamber by a quadrupole mass spectrometer (QMS, Pfeiffer QMG422) positioned 2.2 cm downstream from the guiding electrodes. The guided molecules are ionized by electron impact and mass filtered. Using a secondary-electron multiplier, single-ion counting is performed. The electronic signal of the single-ion counts is amplified and shaped to TTL pulses. With a multi-channel scalar card the TTL pulses representing single ion events are summed up in a histogram. A typical time range in an experiment is ~ 200 ms with a time resolution of $10 \mu\text{s}$.

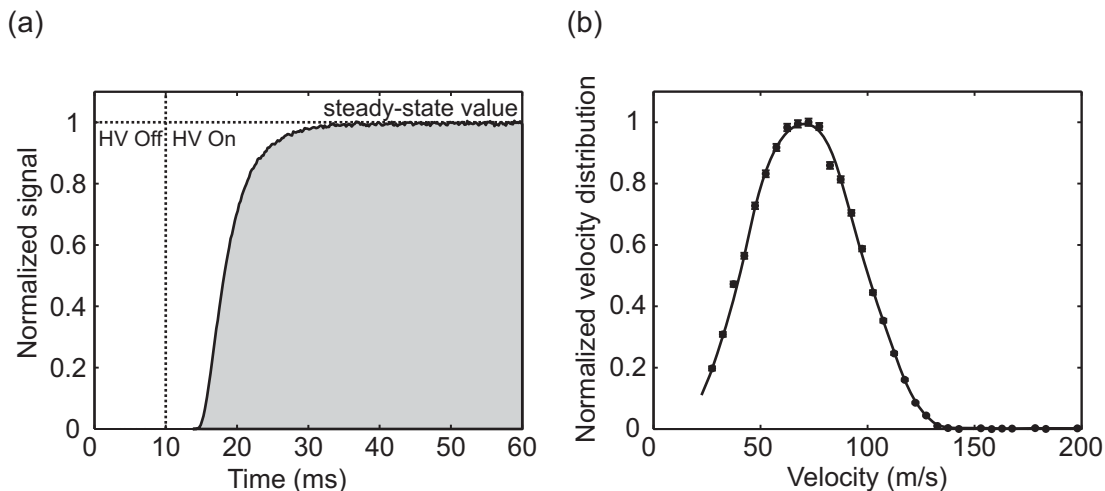


Figure 3.4: The time-of-flight signal from a continuous guided beam of ND_3 is presented in (a). At $t = 10$ ms high voltage is applied to the guiding electrodes. The fastest molecules reach the QMS after a few milliseconds. They are followed by slower molecules and molecules of the same velocity that were injected into the guide at a later time. This culminates in a steady-state-value. In (b) the velocity distribution extracted from the TOF signal in (a) is presented. The velocity distribution is derived by differentiating the TOF signal with respect to time and the conversion from time to velocity via Eq. 3.15.

3.5 Continuous guided beam

The molecules in the guide originate from a thermal (150 K) reservoir and populate therefore many rotational states. Also velocities in a wide range are accepted in the continuous beam (see section 3.3). Time-of-flight (TOF) measurements for different guiding settings are performed to determine the guided beam properties (see Fig. 3.4a). To perform these measurements, the high voltage on the guiding electrodes is switched on and off in a fixed sequence. The signal obtained by the QMS is proportional to the density of the guided molecules inside the QMS ionization volume [Mot09a]. The arrival times of the fastest molecules after having applied high voltage and the rising slope of the signal give information about the velocity distribution of the guided molecules (see Fig. 3.4b). From the steady-state QMS signal that appears after molecules of nearly every velocity of the full velocity distribution are apparent in the beam the total density and flux of molecules can be obtained. Also, the flux dependence with respect to the electrode voltage can be derived. Therefore, according to section 3.3 the guided flux is related to the signal via $S(E_{\text{max}}) \propto \Phi(E_{\text{max}})/\sqrt{E_{\text{max}}}$ due to $\Phi = n\langle v \rangle A$, where $\langle v \rangle$ is the average longitudinal velocity and A the effective area of the beam.

3.6 Velocity-selected molecular pulses

The molecules which are trapped in the electric guiding potential cover a large range of longitudinal velocities. In our experiment we start with a continuous flow of guided molecules whose flux is described by Eq. 3.13. This implies that under steady-state conditions molecules with all possible longitudinal velocities are present in the guide at every instant of time. To filter molecules with a certain longitudinal velocity out of the total flux, a velocity-dependent selection scheme is applied. All our experiments are performed at a relatively low reservoir pressure (1×10^{-2} mbar) to avoid modifications of the velocity distribution stemming from collisions of slow molecules with fast molecules near the exit of the ceramic tube [Mot09a].

3.6.1 Velocity-selection scheme

As described in section 3.4, the guide is composed of four segments, which can be switched independently to a guiding or non-guiding configuration. By applying an appropriate switching sequence to the guide segments, ideally only molecules that continuously experience a guiding field are steered to the end of the guide. Most of the other molecules are lost from the guide and do not reach the detector. This results in molecular pulses characterized by a certain velocity and velocity spread. The process is schematically presented in Fig. 3.5. At time $t = 0$ segment A is in guiding configuration while segment B and C are switched off. Segment D is on all the time to avoid switching transients in the response of the mass spectrometer. Segment A remains on for time t_A ($t_A \equiv t_A^{\text{off}}$), during which molecules with all possible longitudinal velocities below $v_{z,max}$ are guided. They cannot, however, propagate farther through segment B . At time t_B^{on} ($t_B^{\text{on}} < t_A^{\text{off}}$), shortly before the segment A is turned off, segment B is turned on. This gives rise to an overlap time interval $\Delta t_{AB} = t_A^{\text{off}} - t_B^{\text{on}}$ during which both segments are in the guiding configuration. This ensures that in this time window molecules in the gap and its immediate vicinity will experience a continuous electric quadrupole field and can enter the subsequent segment without being disturbed by the switching of the electric field. Thus the overlap interval defines a molecular pulse with duration Δt_{AB} containing molecules with all longitudinal velocities below the cutoff velocity $v_{z,max}$. This pulse traverses the gap and is launched into segment B , while segment C remains off. The time interval during which segment B is in guiding configuration depends on the desired longitudinal velocity $v_{z,set}$ according to $t_B = l_B/v_{z,set}$, where l_B is the length of segment B . Just before segment B is switched off at time t_B^{off} , segment C is turned on at time t_C^{on} , resulting in the overlap interval $\Delta t_{BC} = t_B^{\text{off}} - t_C^{\text{on}}$. This opens up a pathway for molecules to bridge the gap and enter segment C . Segment A remains in non-guiding configuration. It is important to point out that when moving along segment B , the initially short molecular pulse spreads along the propagation line as a result of longitudinal velocity dispersion. Molecules that arrive at the gap between segments B and C before segment C is switched on are

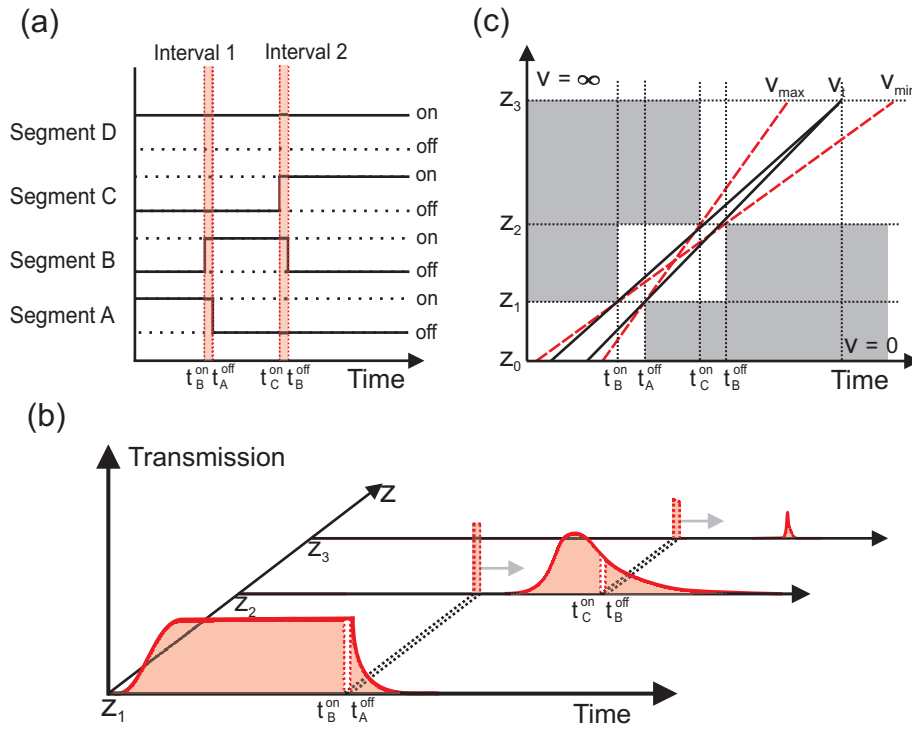


Figure 3.5: In (a) the switching sequence of the electrodes is presented. In the time intervals $[t_B^{\text{on}}, t_A^{\text{off}}]$ and $[t_C^{\text{on}}, t_B^{\text{off}}]$, respectively, two consecutive segments are in guiding configuration. The pulse-production process is sketched in (b). z_1 , z_2 , and z_3 are the distances from the exit of the ceramic tube to the entrance of segment B , to the entrance of segment C , and to the QMS, respectively. The transmission for certain velocities is schematically presented in the $z - t$ diagram in (c). The slopes of the black lines represent molecules from different starting times that can overlap each other at the QMS position. The slopes of the red dashed lines show the maximal and minimal velocities of the molecules in the pulse.

lost. The same occurs for molecules which are too slow and are still in segment B when the latter is turned off. Only the molecules whose velocity is matched to their arrival time at the gap between segments B and C experience a continuous guiding field and are accepted by segment C . Since the overlap intervals Δt_{AB} and Δt_{BC} are not infinitesimally short, the velocity distribution of the molecules has a finite width around the selected velocity. The center velocity as well as the minimum and the maximum velocity of the molecules comprising the output molecular pulse arriving at the detector can be graphically derived with the help of the $z - t$ diagram shown in Fig. 3.5. The guiding configurations are designated by the white boxes, while the grey shading designates the non-guiding configurations. The slopes of the black lines represent the lower and the upper boundaries for the velocity of the molecules

arriving at the detector at time t . The slopes of the red dashed lines mark the lowest and the highest admissible velocities in the produced pulse.

From the switching times, the maximal repetition rate of the pulses can be determined. The rate is given by the time the molecules need to move from the entrance of the first segment to the exit of the second segment. This stems from the fact that the first segment can be switched on again only when the molecular pulse has entered the third guide segment. In our setup repetition rates of the order of a few hundred Hertz can be realized for molecular pulses with velocities of a few tens of m/s. To give an example, at a velocity of 60 m/s a maximal repetition rate of ~ 210 Hz can be employed. In principle, higher repetition rates are attainable by using a configuration with shorter segments.

3.6.2 Formation of molecular pulses

To determine the properties of the molecular pulses we have performed time-of-flight measurements. The obtained information includes the shape of the pulse, its intensity, its width, and its center velocity. Figure 3.6 shows the time of flight signal $S(t)$ of a molecular pulse with a center velocity of 60 m/s. The velocities of the detected molecules are determined from their arrival times by converting the acquired signal $S(t)$ from the time domain to the velocity domain. This is done via the relation

$$S(t)\Delta t = \left[S(t) \times \left(\frac{t^2}{l} \right) \right] \Delta v_z = P(v_z)\Delta v_z, \quad (3.15)$$

where t stands for the arrival time of the molecules relative to the middle of the time interval $[t_C^{\text{on}}, t_B^{\text{off}}]$, and l is the traversed length. The bin width of the histogram, $\Delta t = 10 \mu\text{s}$, is much smaller than all relevant time scales.

To rationalize the pulse formation we analyze velocity distributions at a selected center velocity of 60 m/s (see Fig. 3.7). First, we performed time-of-flight measurements switching off all four electrodes of the respective segments of the electric guide to achieve the non-guiding regime. This non-guiding configuration of the electrodes is referred to as grounded off-configuration (Fig. 3.7 (left inset)). The resulting velocity distribution is given by the black filled-dotted curve in Fig. 3.7. The broad shape results from molecules that survive in the guide during the off-configuration. In our further discussion these molecules are referred to as residual molecules. These molecules are not guided by an electric field but manage to reach the next guiding segment simply by free rectilinear flight. The asymmetric shape of the broader velocity distribution results from the bend in segment C after the gap (see Fig. 3.3). Residual molecules whose velocities are higher than the desired velocity $v_{z,\text{set}}$ set by the switching time t_C^{on} can make it through the gap and enter segment C by free rectilinear flight. If these molecules reach the bend of segment C at times $t < t_C^{\text{on}}$ they escape from the guide. This leads to a reduction of the broadening at the high-velocity side of the velocity distribution. On the other hand, residual molecules whose velocities are smaller than the desired velocity $v_{z,\text{set}}$, can remain in segment

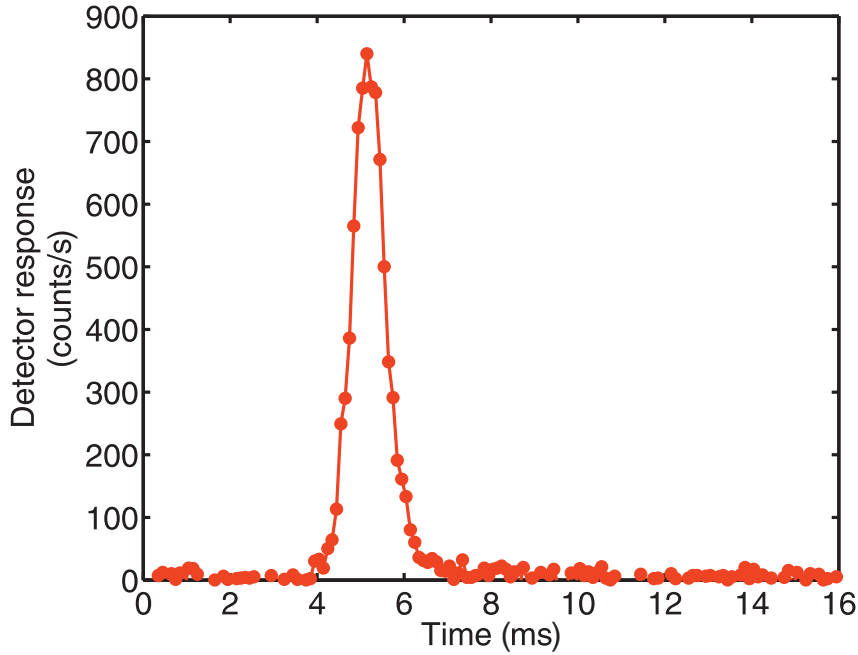


Figure 3.6: Time-of-flight signal for a pulse with a center velocity of 60 m/s. The detector response is plotted against the arrival time of the molecules. The middle of the time interval $[t_C^{\text{on}}, t_B^{\text{off}}]$ corresponds to $t = 0$ in the plot. The distance the molecules traverse during the time-of-flight measurement is the sum of the lengths of segments C and D , and the gap of 2.2 cm between the end of the guide and the QMS. The depicted pulse has been obtained with the gradient off-configuration (see text). Background contributions have been subtracted from the raw data.

B and manage to reach segment C even at times $t > t_B^{\text{off}}$ by free rectilinear flight. These molecules are guided in segment C since this segment is on for times $t > t_B^{\text{off}}$, and thus contribute to the broadening of the velocity distribution at its low-velocity side. To reduce the contribution of residual molecules to the pulse, we applied another non-guiding configuration, termed gradient off-configuration, in which three of the electrodes of the guide are switched off and one of the electrodes remains at +4 kV [Fig. 3.7 (right inset)]. This non-guiding scheme results in a deflection field of 13 kV/cm in the guide center pushing the residual molecules out of the guide. This leads to the narrowed velocity distribution given by the red open dots in Fig. 3.7. The temporal profile of the corresponding pulse is shown in Fig. 3.6.

The overlap intervals have been optimized to maximize the number of molecules per pulse without significantly increasing the width of the velocity distribution. The duration of the overlap intervals has been adjusted proportional to $1/v_{z,\text{set}}$ to ensure that for every $v_{z,\text{set}}$ the molecules travel the same distance d during the overlap times. In our experiment $d = 8.4$ mm. In this way molecules of all velocities experience the same switching transient fields. For our setup optimal overlap times around

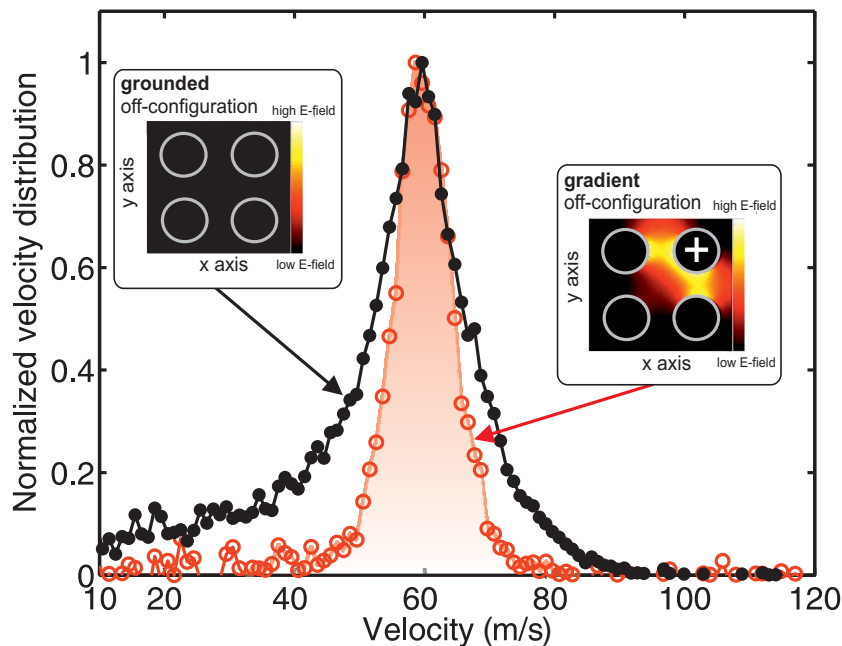


Figure 3.7: Normalized velocity distributions of pulses with an average velocity of 60 m/s measured in two modes of operation: with the grounded off-configuration (black filled dots) and with the gradient off-configuration (red open dots). For the guiding configuration, +4 kV are applied to one pair of opposite electrodes while the other pair of opposite electrodes is at 0 V, this leading to electric fields of up to ~ 40 kV/cm. In the gradient off-configuration the deflection field reduces the amount of molecules that can still enter the successive guide segment. The asymmetric shape of the grounded off-configuration peak results from the bend in segment *C* of the guide.

hundred microseconds are found. For example an overlap time of $140 \mu\text{s}$ has been used for Δt_{AB} and Δt_{BC} for the data shown in Fig. 3.7. An important parameter of the segmented-guiding technique is the number of molecules in a pulse. To determine this value we have used the background-subtracted data of the histograms representing single-molecule detections of the QMS. Using a calibration of the QMS discussed in subsection 4.3.2, we have estimated that the pulse at 60 m/s contains 10^5 molecules. This number can be increased to 10^6 molecules by increasing the pressure in the reservoir [Mot09a]. As a next step, we compare the velocity distributions at different center velocities. In Fig. 3.8 the experimentally determined velocity distributions of molecular pulses for several center velocities are displayed by red dots. Overall, good agreement between the heights of the velocity distributions of the velocity-selected pulses and the measured velocity distribution for a continuous beam of guided molecules is found. This demonstrates that electric switching does not lead to a reduction of the number of molecules at the desired center velocity of the pulse.

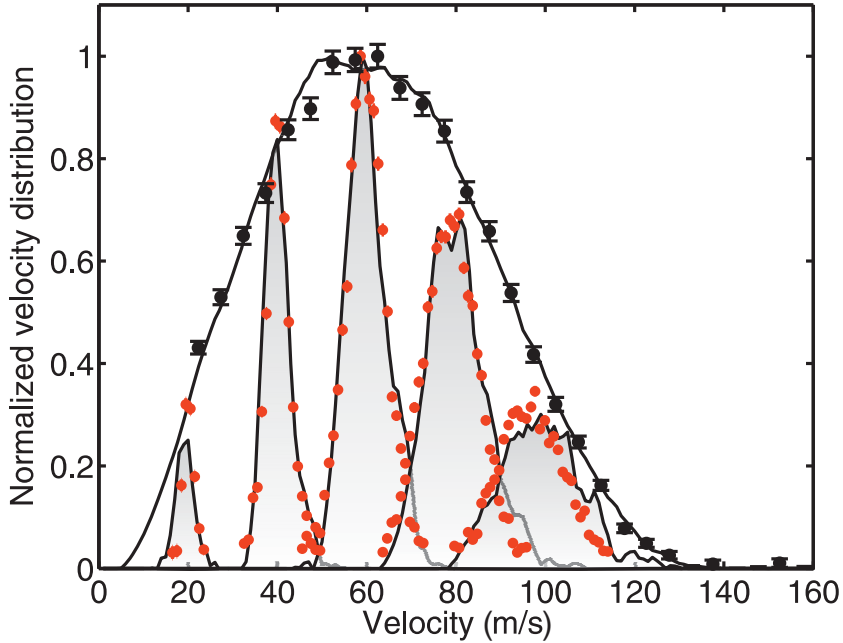


Figure 3.8: Experimental velocity distributions obtained from the continuous beam (black dots with error bars from statistical uncertainties) and from the segmented guiding (red dots). Monte-Carlo simulations of the velocity distributions are shown for continuous and pulsed operation of the molecular guide by black solid curves. Both experimental and simulated velocity distributions have been rebinned to 1 m/s.

To further substantiate the experimental results we compare them to the results from Monte-Carlo simulations for a bent electric guide. The simulations employed a model guide accounting for all physical aspects of the experiment and propagated molecules with the appropriate parameters and starting conditions. The input range of longitudinal velocities was from 10 m/s to 240 m/s. Simulations for pulsed operations as well as for continuous guiding (with all segments of the guide being on at all times) have been carried out. As in the experiment, the velocities are obtained from their arrival time in the detector with respect to the time $t_C^{\text{on}} + 1/2(\Delta t_{BC})$. Due to the relatively large statistical uncertainties the simulated peaks have been smoothed using the Savitzky-Golay smoothing filter [Pre96] employing a third-order polynomial with 6 points. The simulated continuous velocity profile has been smoothed as well using the above method with 30 points. The results of the simulations are presented in Fig. 3.8 (black solid curves). Good agreement is found between the experimental data and the simulations for the continuous beam as well as for the pulses at different longitudinal velocities $v_{z,\text{set}}$.

3.6.3 The widths of the velocity distributions

The full width at half maximum (FWHM) of the velocity distributions, Δv_z , are obtained from fits with Voigt profiles [Oli77]. In this way the ratios $\Delta v_{z,\text{set}}/v_{z,\text{set}}$ can be derived. Overall, a value of $\Delta v_{z,\text{set}}/v_{z,\text{set}} = (16 \pm 2)\%$ is obtained for the relative velocity spread. The non-zero width of the velocity distributions is attributed to two effects, the finite duration of the overlap intervals proportional to $1/v_{z,\text{set}}$, and the presence of residual molecules. In the following we describe these two effects and their contributions to the widths of the velocity distributions in more detail.

The desired longitudinal velocity is determined by $v_{z,\text{set}} = l_B/t_B$ (see subsection 3.6.1). By differentiating this expression with respect to time and by substituting $l_B/v_{z,\text{set}}$ for t_B , we obtain the following relationship between the pulse width and the width of its velocity distribution,

$$|\Delta v_{z,\text{overlap}}| = \left(\frac{v_{z,\text{set}}^2}{l_B} \right) \Delta t_B. \quad (3.16)$$

The two short but non-zero overlap intervals $\Delta t_{AB} = \Delta t_{BC} = d/v_{z,\text{set}}$ ($d \ll l_B$) determine a triangular velocity distribution resulting from a convolution of two rectangular velocity distributions. Therefore we obtain the following relation for the FWHM of the velocity distribution stemming from the finite overlap intervals,

$$\Delta v_{z,\text{overlap}} = \left(\frac{d}{l_B} \right) v_{z,\text{set}}. \quad (3.17)$$

We determine that $\Delta v_{z,\text{overlap}}/v_{z,\text{set}} = 5\%$ for our settings. From the measured widths we can conclude that residual molecules substantially contribute to the observed broadening. Therefore, decreasing the overlap intervals to smaller values does not lead to much narrower velocity distributions. Indeed, we have observed that for shorter overlap intervals of a few tens of microseconds the widths of the velocity distributions do not decrease significantly. They are an order of magnitude broader than expected from Eq. 3.17 for these short overlap times. Additionally, a substantial reduction in peak height is observed for the slowest pulse with a center velocity of 20 m/s. This additional reduction has not been seen with overlap times of a few hundred microseconds. The residual molecules manage to reach the subsequent segment shortly before or shortly after the overlap intervals. The number of these molecules depends on the mean survival time τ they can spend in the gradient off-configuration before being kicked out by the deflection field. This time τ depends on the transverse velocity of the molecules and on the strength of the deflection field. For a straight guide, both the transverse velocity and the strength of the deflection field are independent of the set velocity $v_{z,\text{set}}$. Indeed, we have verified this by fitting the transverse velocity distributions obtained from the Monte-Carlo simulations with Gaussian profiles. The fits demonstrate that for all longitudinal velocities $v_{z,\text{set}}$ the average value of the transverse velocity roughly equals 7 m/s.

To account for the broadening resulting from residual molecules in addition to the broadening stemming from the finite overlap time, we use the following model including both effects. Let $t_B = t_B^{\text{off}} - t_B^{\text{on}}$ (see Fig. 3.5). Let us also first assume that there are no residual molecules in the vicinity of the gap between segments A and B , and the overlap time $\Delta t_{AB} = 0$. This assumption implies that the broadening of the velocity distribution originates only from the finite overlap time Δt_{BC} and from residual molecules in the vicinity of the gap between segments B and C . The minimum velocity v_z^{min} at which molecules in segment B can still reach the subsequent segment C is

$$v_z^{\text{min}} = \frac{l_B}{(t_B + \tau)}. \quad (3.18)$$

The maximum velocity v_z^{max} at which some molecules remain guided in segment C is

$$v_z^{\text{max}} = \frac{l_B}{(t_B - \tau - \Delta t_{BC})}. \quad (3.19)$$

After substituting $t_B = l_B/v_{z,\text{set}}$, the above expressions are transformed into

$$v_z^{\text{min}} = \frac{l_B v_{z,\text{set}}}{(l_B + v_{z,\text{set}} \tau)} \quad (3.20)$$

$$v_z^{\text{max}} = \frac{l_B v_{z,\text{set}}}{(l_B - v_{z,\text{set}}(\tau + \Delta t_{BC}))}, \quad (3.21)$$

respectively. The difference between v_z^{max} and v_z^{min} defines a rectangular distribution of longitudinal velocities determined by the overlap time Δt_{BC} and the survival time τ of the residual molecules in the vicinity of the gap between segments B and C . By analogy, the same model is applicable to the gap between segments A and B if we assume that now there are residual molecules only in the vicinity of the gap between segments A and B , $\Delta t_{AB} > 0$, and $\Delta t_{BC} = 0$. The overall velocity distribution is thus obtained by the convolution of the two rectangular velocity distributions. The resulting velocity distribution has a triangular profile with a FWHM given by the formula

$$\Delta v_z = \frac{l_B v_{z,\text{set}}^2 (2\tau + \Delta t_{BC})}{(l_B - v_{z,\text{set}} \tau)(l_B + v_{z,\text{set}}(\tau + \Delta t_{BC}))} \quad (3.22)$$

for a guide without bends. It is obvious that for infinitesimally short survival times τ ($\tau \rightarrow 0$) and for overlap times satisfying the condition $d \ll l_B$, the above formula reduces to Eq. 3.17. In this model the survival time τ can be considered as an effective additional overlap time.

To be able to verify the analytical model and to determine τ , we have performed simulations for a segmented straight guide with experimental conditions similar to the ones in the real experiment with the bent guide. The FWHM of the velocity distributions of the molecules reaching the QMS have been fitted to Δv_z , resulting in $\tau = 244 \mu\text{s}$ as shown in Fig. 3.9. This value agrees with our estimate of $\sim 100 \mu\text{s}$ based on typical field strength of our deflection field. Note that the mean

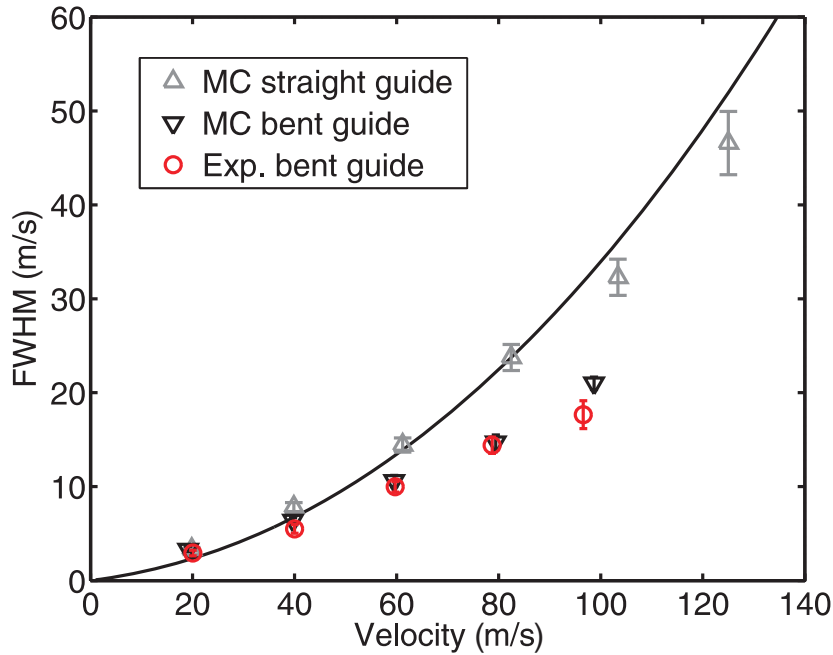


Figure 3.9: FWHM of the velocity distributions are presented as a function of the mean velocity of the distribution for both the experimental data (red circles) and the Monte-Carlo simulations for the bent guide (black inverted triangles) and the straight guide (gray triangles). The widths are obtained from fits of the velocity distributions with Voigt profiles. The solid curve represents the analytical model for $\tau = 244 \mu\text{s}$ (see text and Eq. 3.22). There are no points for the bent guide for velocities above 100 m/s since these velocities approach the longitudinal cut-off velocity of our electric guide, and hence the molecular flux is strongly reduced (see Fig. 3.8).

longitudinal velocities tend to shift to values higher than $v_{z,\text{set}}$, especially for large $v_{z,\text{set}}$ (See gray points in Fig. 3.9). This effect is caused by non-deflected molecules as well, which are more likely to reach the detector at high longitudinal velocities. For $v_{z,\text{set}} \geq 120 \text{ m/s}$ disagreement between the analytical model and the simulation appears due to the limited range of generated velocities. This shows that molecules with velocities beyond the generated range of velocities contribute to these pulses. That is why bends are required to avoid contributions from high-velocity molecules and to keep the mean velocity close to $v_{z,\text{set}}$. The FWHM of the velocity distributions for the bent guide are presented as a function of the mean velocity of the distribution for both the experimental data and the Monte-Carlo simulations in Fig. 3.9 (red circles and inverted triangles, respectively) as well. The results were obtained from fits of the velocity distributions with Voigt profiles. Good agreement is found between experimental data and simulations. This indicates that the main broadening effects, finite overlap times and contribution of residual molecules, are well understood. Compared to the straight guide, the widths increase less strongly

at high $v_{z,\text{set}}$. This is caused by the second bend, which accepts molecules only while being in guiding configuration whereas in a straight guide larger contributions arise from residual molecules (which can survive the deflection fields during time τ). This clearly shows that the second bend reduces the broadening of the peaks.

An interesting aspect is the effect of the different elements of the guide on the behavior of the molecular pulses which is important for the optimization of the experimental setup. Towards this end, we looked at the results from the Monte-Carlo simulations. We recorded the instantaneous velocities of the propagated molecules at the beginning of the guide and at the detector and compared them with velocities obtained from their time of flight. The pulses in the time domain for the velocities of 80 m/s and 100 m/s produced at the beginning of the guide are much narrower than the ones produced at the detector. This can be explained by velocity dispersion in the guide. Another reason for this effect, however, might be velocity mixing, which is most likely to occur in the bends of the molecular guide. To study this effect we compared the simulated initial (at the entrance of the guide) velocity distribution of the molecules reaching the detector with their simulated final velocity distribution at the position of the detector. The two velocity distributions are very similar, which implies that the longitudinal velocities do not alter strongly during the propagation in the guide. Therefore, we conclude that no observable velocity mixing occurs in the bends and that the only reason for the pulse broadening in the time domain under our experimental conditions is the velocity dispersion.

3.6.4 Transverse velocity distribution of velocity-selected molecular pulses

To further characterize the molecular pulses obtained by velocity selection, the QMS ionization volume is swept perpendicular to the propagation axis. This allows to map out the transverse velocity distribution of the molecules leaving the electric guide (Fig. 3.10). The QMS is placed 2.2 cm downstream from the guiding electrodes. The spatial profile of the field-free molecular beam at that distance is already determined by the transverse velocity distribution of the guided molecules and not by the spatial distribution of the molecules in the guide anymore. Note that the ionization volume is much smaller than the extent of the beam at that distance (total width of ~ 2 mm along the sweep direction [Mie10]). A rigorous treatment on electric guiding of polar molecules in a quadrupole guide is set out in the Appendix A.3.

Due to the well-known velocity of a molecular pulse in the longitudinal direction the spread of the spatial profile in the transverse directions can be directly related to transverse velocities. The error margin is dominated by the width of the longitudinal velocity distribution of the molecular pulse. From simulations we have derived that the transverse velocity distribution in the guide is independent of the longitudinal velocity. This is shown in Fig. 3.10b. The small differences in the transverse velocity distributions for the different longitudinal velocity distributions in Fig. 3.10 result from the finite size of the ionization volume.

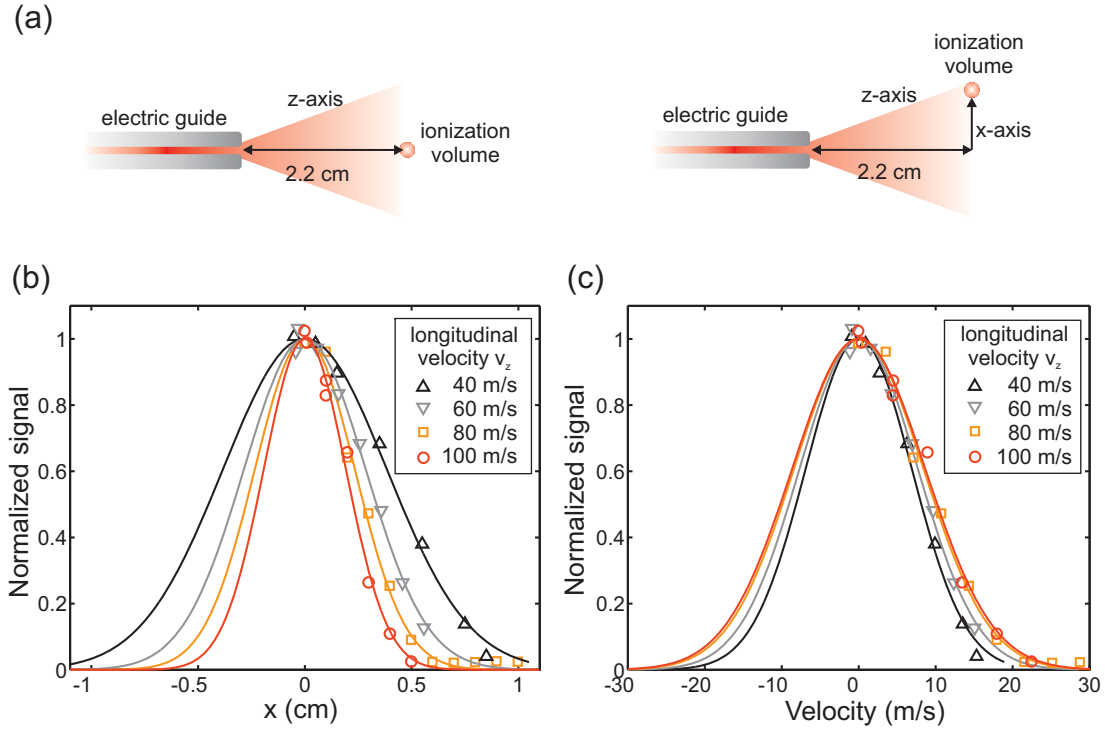


Figure 3.10: The process to obtain the transverse profiles is explained in (a). In (b) the transverse spatial distributions of pulses with different longitudinal velocities ranging from 40 to 100 m/s measured at a distance of 2.2 cm downstream from the guide exit are presented. In (c) the corresponding transverse velocity distributions are derived from the longitudinal velocity, the distance between the guide exit and the ionization volume of the QMS as shown previously, and the distance x of the ionization volume to the guide axis presented in (b). The solid lines represent Gaussian fits to the measured data.

The transverse velocity distribution of a molecular pulse can be actively manipulated. By variation of the electrode voltage of the quadrupole guide in the last segment (segment D) with respect to the voltages on the other segments, the transverse velocity distribution can be broadened by going to higher voltages or narrowed by going to lower voltages. Here, the transverse velocity distribution is not altered solely by changing of the trap depth. The voltage difference between the quadrupole fields of segments C and D creates a longitudinal component of the electric field in the gap region. Thus this field couples the transverse motion to the longitudinal motion. Thereby changes in transverse velocities (with a corresponding change in the longitudinal velocity due to energy conservation) can happen in this region. By going from a high quadrupole field in segment C to a weaker field in segment D , the field in the gap is collimating the guided beam. This causes a decrease in the transverse spread and an increase in the the longitudinal spread (see Fig. 3.11a). Therefore, an increased intensity is observed in the QMS detection signal, at the central position where the QMS is facing the exit of the guide (see Fig. 3.11d).

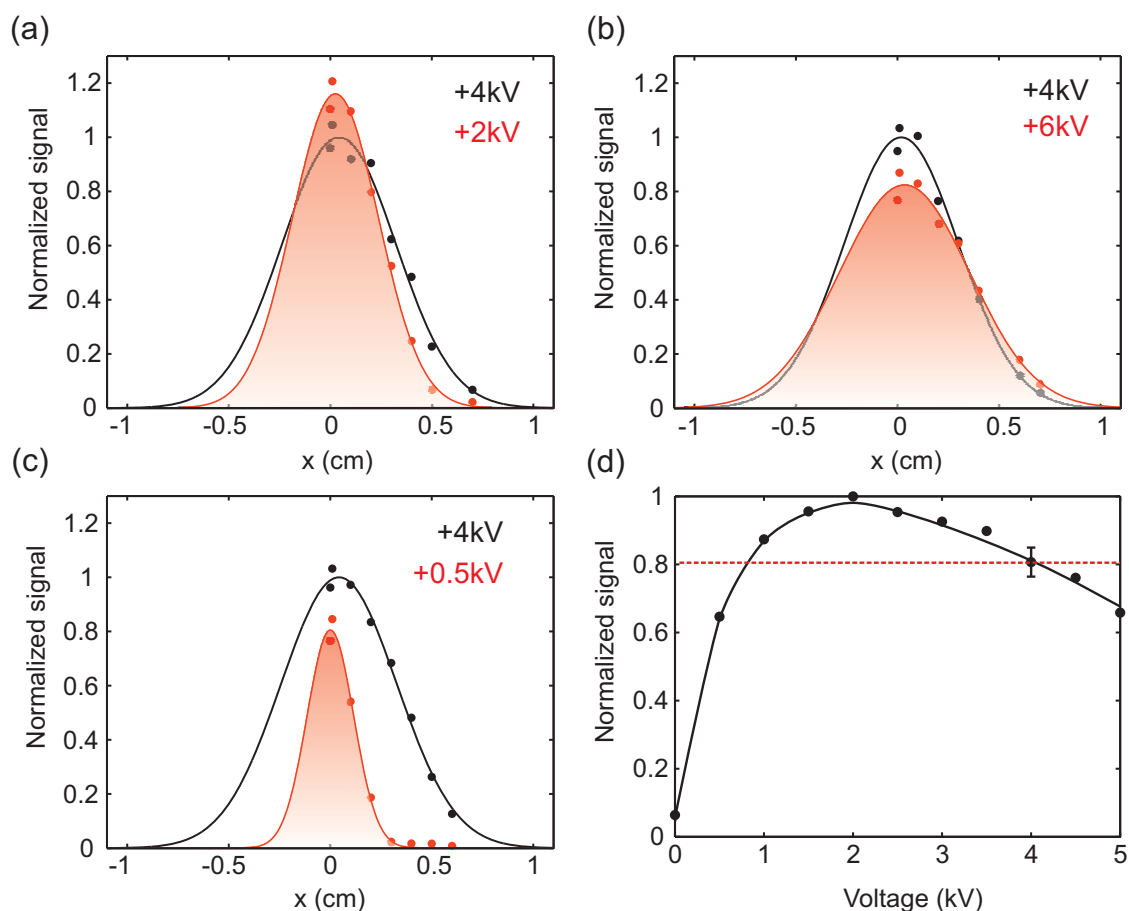


Figure 3.11: Transverse spatial distributions for pulses with longitudinal velocity $v_z = 60$ m/s. The profiles are manipulated by the voltage difference between segment C and D . The positive voltages on segment D are changed to +2 kV (a), +6 kV (b) and +0.5 kV (c) (red data points), while segment A , B and C are kept at +4 kV. This is compared to the case where all guide segments carry +4 kV (black data points). Gaussian profiles are fitted to the data. The fraction of molecules that remains guided when the voltage is changed to +2 kV (a), +6 kV (b), and +0.5 kV (c) on the last segment is 87 %, 94 %, and 32 %, respectively. In (d) the voltage dependence of the signal at position $x = 0$ is shown. A typical errorbar for the data points is shown at 4 kV. Here, the solid curve serves as a guide to the eye.

3.7 Summary

In this chapter electric guiding of polar molecules has been discussed including the production of molecular pulses. From the theoretical description on the confinement of polar molecules in electric fields, the basic properties of an electric quadrupole guide are discussed. In our experiment the electric guide is used to filter slow polar molecules out of a gas originating from a thermal reservoir. In this way continuous beams of slow polar molecules are generated. The most important features of such beams are discussed in the text. A novel technique for the production of velocity-selected molecular pulses with narrow velocity distribution extracted from a continuous beam in the guide is presented. The properties of those pulses are discussed in great detail including an analytical model of the pulse-formation process and comparison of the experimental results with those obtained from Monte Carlo simulations.

Our method for the production of velocity-selected pulses of polar molecules offers prospects for further improvements. If required, the pulse width can be reduced by applying shorter overlap times at the expense of a reduced number of molecules per pulse. This demands for a higher gradient field in the non-guiding configuration, eliminating contributions of rectilinearly flying molecules more strongly. Another approach to minimize these undesired contributions is to use a bent-guide geometry, in which the molecules are more easily expelled from the guide during the deflection period. Higher overall fluxes can be obtained by running the experiment at higher repetition rates. By segmenting the guide into more and smaller parts and employing faster switching times, multiple pulses can be stored in the guide at the same time, resulting in even higher rates. Our technique has promising applications in collision and cold-chemistry experiments. For example, collision experiments like those in [Gil06, Wil08a] can now be performed at even lower collision energies by crossing two velocity-selected pulses as proposed in [vdM09] or by guiding the slow molecules into a trapped sample. Velocity selected molecules could then collide with laser-cooled atoms stored in an electric trap [Rie07b, Sch07b]. Another realm of application of our method could be molecular interferometry. A major challenge in this field is the production of molecules with well-defined and controllable velocities [Bre03, Ger07]. The velocity-selection technique might be well-suited for such experiments with molecules having sufficiently large dipole moments.

Chapter 4

Slow molecules extracted from a cryogenic source

A warm source of polar molecules strongly limits the efficiency of electric velocity filtering due to the on average large molecular velocities exceeding the maximal (capture) velocity of the guide. Using higher fluxes at the input to circumvent this problem fails because of collisional losses that particularly effect the slowest molecules [Mot09a]. A decrease of the temperature of the molecular gas before the electric filtering process results in a higher flux of guided molecules due to a larger fraction of slow and guidable polar molecules in the thermal velocity distribution (see Fig. 4.1). This has been shown in several electric guiding experiments [Jun05, Mot07]. Lowering the temperature of the molecules also reduces the number of populated internal states [Mot07]. This results in dense samples with high state purity in which most of the molecules can be addressed by a single frequency optical or microwave radiation source [Kre09].

The nozzle temperature of an effusive source is limited by the resublimation temperature of the molecular gas, at which the vapor pressure is reduced enormously. This causes the signal of guided molecules to drop significantly. Besides the nozzle can be clogged by the resublimated molecules. With the technique of buffer-gas cooling this can be circumvented. Here, the molecules are loaded into a volume containing a buffer gas at cryogenic temperatures. The buffer gas is an inert gas used to dissipate the translational and internal energy of the molecules by collisions. The internally cold molecules and the buffer-gas atoms/molecules effuse from the gas cell through a small orifice and enter an electric quadrupole guide. Only the polar molecules are guided, since the non-polar buffer-gas atoms/molecules do not experience a strong Stark shift in the electric field of the guide.

The cooling does not strongly depend on the energy-level structure of the particles, and hence it is applicable to a large variety of species. In most applications helium is used as a buffer gas due to its appreciably high saturated vapor density down to temperatures below 1 K. For ^3He (^4He) with temperatures above ~ 180 mK (\sim

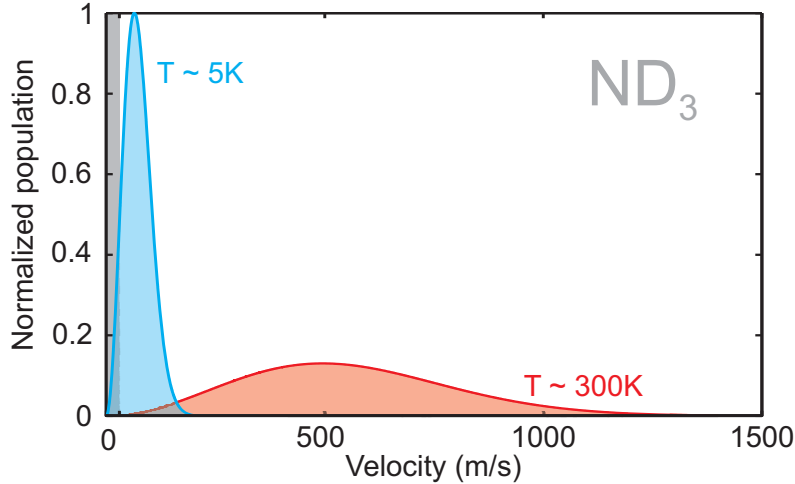


Figure 4.1: Maxwell-Boltzmann-velocity distributions for ND_3 at $T = 300\text{ K}$ (red curve) and $T = 5\text{ K}$ (blue curve). The grey shaded area indicates velocities corresponding to temperatures below 1 K that can be confined by electric fields. For $T = 300\text{ K}$ ($T = 5\text{ K}$) this corresponds to $\sim 0.01\%$ ($\sim 10\%$) of the overall velocity distribution.

500 mK) saturated vapor densities higher than 10^{14} cm^{-3} are obtained [Kre09]. At higher temperatures other buffer gases can be used as well.

4.1 Theory of buffer-gas cooling

In this section the basic principles of buffer-gas cooling of external and internal degrees of freedom are summarized. The description of the cooling process as well as the characteristics of buffer-gas-cooled molecular beams are adapted from [Laf98, Kre09, Pat10].

4.1.1 Translational thermalization

In this section we theoretically treat the cooling of the external degrees of freedom of molecules by elastic collisions with buffer-gas atoms. The number of collisions that is needed to reduce the translational temperature of the molecules to the buffer-gas temperature for the translational degrees of freedom is derived in the following. The theoretical treatment is based on the model of hard-sphere elastic collisions. The model is schematically presented in Fig. 4.2.

Let \mathbf{v}_i and \mathbf{V}_i be the velocities of the two colliding partners in the lab frame prior and after the impact, respectively. We decompose the above velocities into components which are parallel (\parallel) and perpendicular (\perp) to the line connecting the centers of the two particles at the time of impact, respectively. Thus we can write

$\mathbf{v}_i = v_{i,\parallel}\mathbf{e}_{\parallel} + v_{i,\perp}\mathbf{e}_{\perp}$ and $\mathbf{V}_i = V_{i,\parallel}\mathbf{e}_{\parallel} + V_{i,\perp}\mathbf{e}_{\perp}$, $i \in \{1, 2\}$. For hard sphere collisions, we obtain from momentum conservation

$$m_1\mathbf{v}_1 + m_2\mathbf{v}_2 = m_1\mathbf{V}_1 + m_2\mathbf{V}_2. \quad (4.1)$$

Note that $v_{i,\perp} = V_{i,\perp}$ because the collision changes only the velocity components which are parallel to the line connecting the two centers at impact. Thus the expression for momentum conservation in this case can be cast in the form:

$$m_1(v_{1,\parallel} - V_{1,\parallel}) = m_2(V_{2,\parallel} - v_{2,\parallel}). \quad (4.2)$$

On the other hand, from energy conservation

$$\frac{1}{2}m_1\mathbf{v}_1^2 + \frac{1}{2}m_2\mathbf{v}_2^2 = \frac{1}{2}m_1\mathbf{V}_1^2 + \frac{1}{2}m_2\mathbf{V}_2^2, \quad (4.3)$$

we obtain the relation:

$$m_1(v_{1,\parallel}^2 - V_{1,\parallel}^2) = m_2(V_{2,\parallel}^2 - v_{2,\parallel}^2). \quad (4.4)$$

If we divide Eq. 4.4 by Eq. 4.2, we get the following relationship between the incoming and the outgoing velocities:

$$v_{1,\parallel} + V_{1,\parallel} = V_{2,\parallel} + v_{2,\parallel}. \quad (4.5)$$

Combining this relation with relation 4.2 allows us to express the velocities of the colliding partners after impact with the ones before impact:

$$V_{1,\parallel} = \frac{(m_1 - m_2)v_{1,\parallel} + 2m_2v_{2,\parallel}}{m_1 + m_2} \quad (4.6)$$

$$V_{2,\parallel} = \frac{(m_2 - m_1)v_{2,\parallel} + 2m_1v_{1,\parallel}}{m_1 + m_2}. \quad (4.7)$$

Let us now apply the above model to the collision between a molecule and a buffer-gas atom. Let, for definiteness, $|\mathbf{v}_2|$ be the initial velocity of the buffer-gas atom, which, in general, is much smaller than the magnitude of the molecule's velocity. We make the rather crude assumption that $|\mathbf{v}_2| = 0$. This leads to $\Delta E = (1/2)m_2\mathbf{V}_2^2 = (1/2)m_1(\mathbf{v}_1^2 - \mathbf{V}_1^2)$ for the energy loss of the molecule per collision. The fractional loss per collision is given by

$$\kappa^{-1} = \frac{(\mathbf{v}_1^2 - \mathbf{V}_1^2)}{\mathbf{v}_1^2} = \frac{4m_1m_2}{(m_1 + m_2)^2} \left(\frac{v_{1,\parallel}^2}{\mathbf{v}_1^2} \right), \quad (4.8)$$

where $\kappa^{-1} = \Delta E/E_{tot}$ and $E_{tot} = (1/2)m_1\mathbf{v}_1^2$ the total collision energy. Here, $v_{1,\parallel}^2/\mathbf{v}_1^2 = \cos^2(\theta)$, where θ is the angle of incidence between \mathbf{v}_1 and the center line

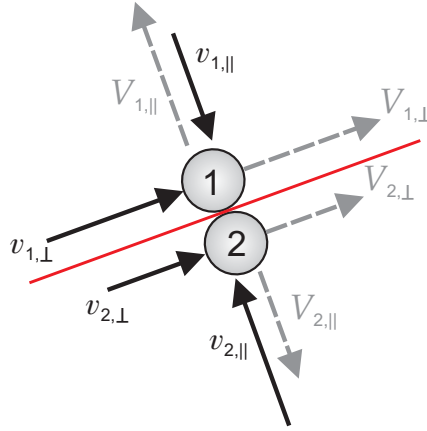


Figure 4.2: Velocity components in the hard-sphere elastic collision. The velocities before and after the impact are marked by black and grey arrows, respectively. Here, (\parallel) and (\perp) designate the parallel and perpendicular velocity components to the line going through the centers of the two particles at the time of impact, respectively. The plane perpendicular to the line of centers is shown in red. The figure is adapted from [Laf98].

at the collision in the lab-frame. Since $\langle \cos^2(\theta) \rangle = 1/2$ the inverse of the fractional loss averaged over all directions is given by

$$\kappa = \frac{(m_1 + m_2)^2}{2m_1m_2}. \quad (4.9)$$

If each molecule experiences on average one collision with a buffer-gas atom the energy $\Delta E = (3/2)k_B\Delta T = (3/2)k_B(T_1 - T_2)$ is removed from the thermal-molecular gas. Here, T_1 and T_2 are the temperatures of the molecular gas and the buffer gas before the two gases have collided. In contrast to the buffer gas, which is permanently cooled by the cell walls to the temperature T_2 , the temperature of the molecules T will change in the mixture until $T = T_2$. The continuous change of temperature as a function of the average number of collisions l can be modeled by the differential equation

$$\frac{dT}{dl} = -\frac{(T - T_2)}{\kappa}. \quad (4.10)$$

Using the initial condition $T(0) = T_1$ the solution of the differential equation is given by

$$\frac{T(l)}{T_2} = \left(\frac{T_1}{T_2} - 1 \right) e^{-l/\kappa} + 1. \quad (4.11)$$

The number of collisions needed for the temperature of the molecular gas to fall within a close vicinity of the buffer-gas temperature T_2 can be obtained from $l = -\kappa \ln[(T(l) - T_2)/(T_1 - T_2)]$. For example, for a helium buffer gas of ~ 5 K and initially hot ammonia (ND_3) molecules of ~ 295 K, $l \sim 19$ collisions are needed to

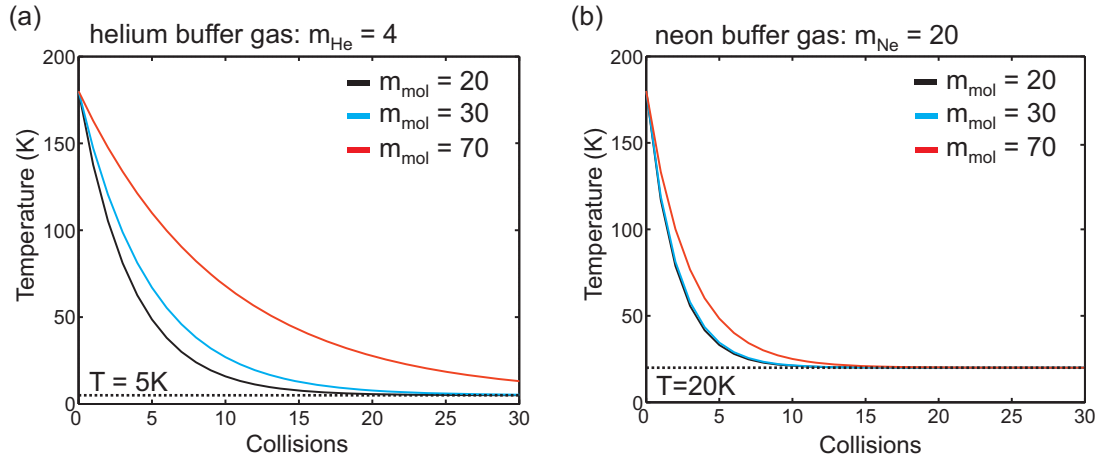


Figure 4.3: The thermalization of the translational temperature described by Eq.4.11 is shown in (a) for mass 20 (ND_3), mass 30 (H_2CO) and mass 70 (CF_3H) in helium buffer gas at $T_2 = 5\text{K}$. In (b) the same is presented for neon buffer gas at $T_2 = 20\text{K}$. The initial temperature of the molecular gas is set to be $T_1 = 180\text{K}$. Except for the higher thermalization temperature neon buffer gas is better suited for cooling heavier molecules because of faster thermalization.

cool to within 30% of the helium buffer-gas temperature. For $T_1 = 180\text{K}$, $l \sim 17$ collisions are needed to reach the same temperature. Several examples of Eq. 4.11 are presented in Fig. 4.3 for helium and neon buffer gas, which are both used in this work. As can be seen from Fig. 4.3, the heavier neon gas is better suited to cool heavier species. Note, however, that the final temperature achievable with neon is higher due to its lower saturation density.

4.1.2 Rotational relaxation and rotational state population

In contrast to elastic collisions, which govern translational relaxation, a simple expression for the number of collisions necessary for rotational thermalization cannot be found easily. The rotational relaxation rates depend strongly on the molecular structure.¹ There are not many restrictions in the sense of collisional selection rules. For example for symmetric top molecules these are outlined in the appendix chapter C.1. Keeping this in mind we see that a transition from a highly excited rotational state to a lowly excited state is possible by a single collisional process if the cross section is sufficiently high. Therefore the steps needed to obtain thermalization are strongly dependent on the ratios of the cross-sections for the different relaxation channels and the thermal occupations at the beginning of the cooling process.

¹The rotational relaxation rates depend strongly on the anisotropy of the molecules, which mostly defines the angular anisotropy of the collision potential.

The probability for a rotational deexcitation step can be higher by many orders of magnitude compared to a vibrational relaxation step. At low temperatures typical rotational relaxation occurs in the range of every 10 to 100 elastic collisions while vibrational relaxation typically takes place after more than $\sim 10^8$ elastic collisions [For99, Kre09]. This is confirmed for rotational relaxations by measurements of De Lucia and coworkers [Bal98, Bal99, Men00]. There, inelastic cross sections in the range of $1 \times 10^{-16} \text{ cm}^2$ to $1 \times 10^{-15} \text{ cm}^2$ at temperatures around a few Kelvin have been found, which are about one to two orders of magnitude smaller than typical elastic cross sections at these temperatures [Wei98, Wei02, Cam07]. This is explained by the fact that a typical vibrational motion is much faster than a collision of a molecule with a cold buffer-gas atom [Kre09]. Therefore, changes in the interaction potential are basically averaged out. On the other hand, the collision timescales are of the same order as the molecular rotation periods. This explains the larger inelastic collision cross sections for rotational deexcitations in comparison with vibrational deexcitations.

In thermal equilibrium the population of an internal rotational state of a molecule with quantum numbers (J, n, M) ² is given by the evaluation of the canonical ensemble

$$\langle JnM | Z^{-1} \exp\left(-\frac{1}{k_B T} H_{rot}\right) | JnM \rangle = Z^{-1} g_{M,I} \exp\left(-\frac{1}{k_B T} W_{J,n,M}\right), \quad (4.12)$$

where $Z = \sum_{J,n,M} g_{M,I} \exp(-W_{J,n,M}/k_B T)$ is the partition function and $W_{J,n,M}$ is the rotational energy of the state $|J, n, M\rangle$. The degeneracy of the state is given by the factor $g_{M,I} = g_M g_I$ which is the product of the M degeneracy ($g_M = 2J + 1$) and the nuclear spin degeneracy factor g_I . In contrast to g_M the spin degeneracy factor depends strongly on the symmetries of the molecule (see appendix chapter B). For example, for symmetric-top molecules with a threefold axis of symmetry like ND_3 , CF_3H , CH_3F etc., where three identical nuclei lie equidistantly in a plane perpendicular to the molecular symmetry axis, the nuclear spin statistical weights depend on the ortho and para states labeled by the K quantum number (see appendix B and C.1). The results of the spin statistical weights for a symmetric top with a threefold axis of symmetry are given in Tbl. 4.1. The weights are obtained by finding all possible eigenstates of an eigenvalue of the Hamiltonian that are also eigenstates of the symmetry operations of the molecular symmetry group, which preserve the right symmetry upon exchange of identical nuclei. This is described in the appendix B. The spin statistical weights for a planar asymmetric rotor molecule like H_2CO with a twofold axis of symmetry are listed in Tbl. 4.2. These two classes of molecules are used in our experiments.

Unlike the molecule-molecule collisions, collisions between molecules and (isotropic) buffer-gas atoms do not result in the same thermal-equilibrium state for the rotational degrees of freedom. As described in the appendix C.1, for a molecule with

² n is given by K in the case of a symmetric top and by τ in the case of an asymmetric top molecule

Table 4.1: Statistical weights for a symmetric-top molecule with a threefold axis of symmetry. Examples for such molecules are ND_3 , NH_3 , CFH_3 , CH_3F etc., all of which have been used in this work. Here, a nucleus from the indistinguishable hydrogen (deuterium) atoms of such a molecule can have a nuclear spin $I = 1/2$ ($I = 1$). The table is adapted from [Tow75] and derived in appendix B.

	statistical weights g_I	type
$K \in \{K K = \pm 3n, n \in \mathbb{N}\}$	$\frac{1}{3}(2I + 1)(4I^2 + 4I + 3)$	
$K \in \{K K \neq \pm 3n, n \in \mathbb{N}_0\}$	$\frac{1}{3}(2I + 1)(4I^2 + 4I)$	
$K = 0$ no vib. inversion	$\frac{1}{3}(2I + 1)(4I^2 + 4I + 3)$	
$K = 0$ vib. inversion	$\frac{1}{3}(2I + 1)(2I - 1)I$	fermion
J even, $ +\rangle$ or J odd, $ -\rangle$	$\frac{1}{3}(2I + 1)(2I + 3)(I + 1)$	boson
$K = 0$ vib. inversion	$\frac{1}{3}(2I + 1)(2I + 3)(I + 1)$	fermion
J odd, $ +\rangle$ or J even, $ -\rangle$	$\frac{1}{3}(2I + 1)(2I - 1)I$	boson

Table 4.2: Statistical weights for formaldehyde H_2CO , a planar asymmetric top molecule with a twofold axis of symmetry. Each of the indistinguishable hydrogen atoms possesses a nuclear spin $I = 1/2$. The table is adapted from [Tow75] and derived in appendix B.

K_A	K_C	$I = 1/2$
e	e	$(2I + 1)I$
e	o	$(2I + 1)I$
o	e	$(2I + 1)(I + 1)$
o	o	$(2I + 1)(I + 1)$

a n -fold axis of symmetry, the ortho and para levels do not mix by collisions with buffer-gas atoms. In this case the thermalization process with the cold buffer-gas atoms must be considered separately for the ortho and para configuration of the molecules. This is presented for ND_3 (H_2CO) molecules in Fig. 4.4 (Fig. 4.5).

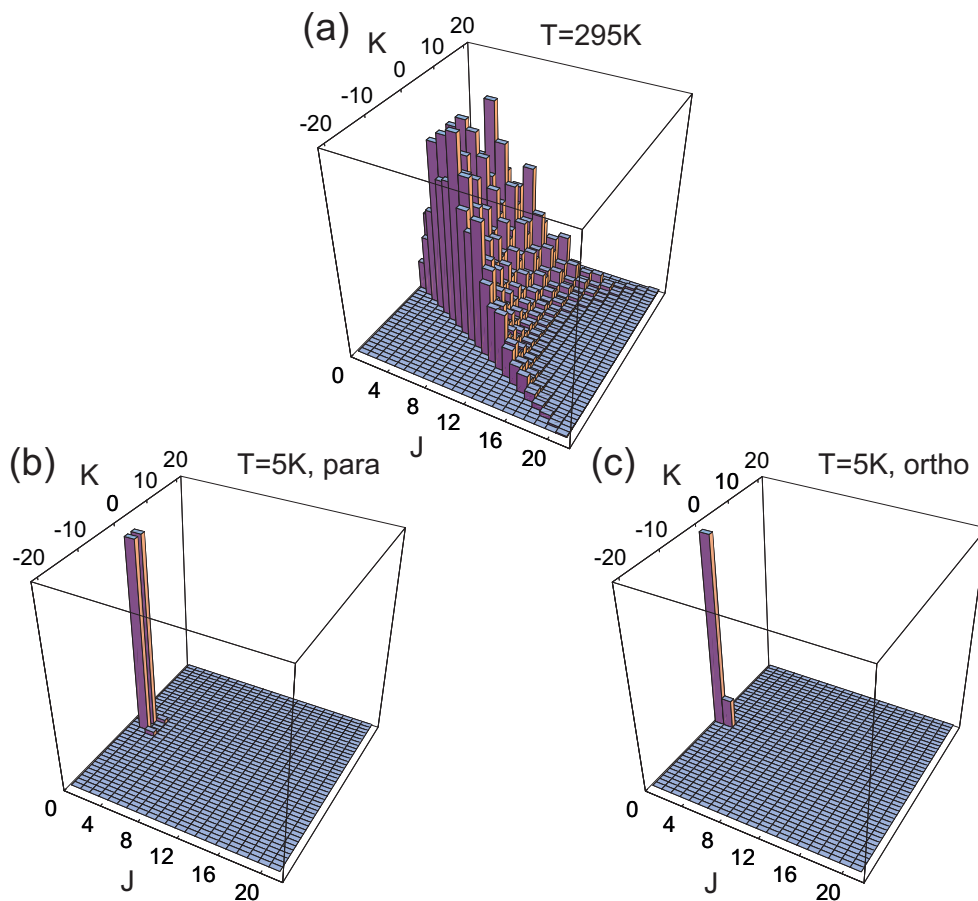


Figure 4.4: In (a) the rotational-state distribution for ND_3 at $T = 295\text{ K}$ is presented. The degeneracy in M and nuclear spin statistics are included. The state distributions in (b) and (c) are given for the para and ortho states at $T = 5\text{ K}$, respectively, which thermalize separately when cooled by an atomic buffer gas.

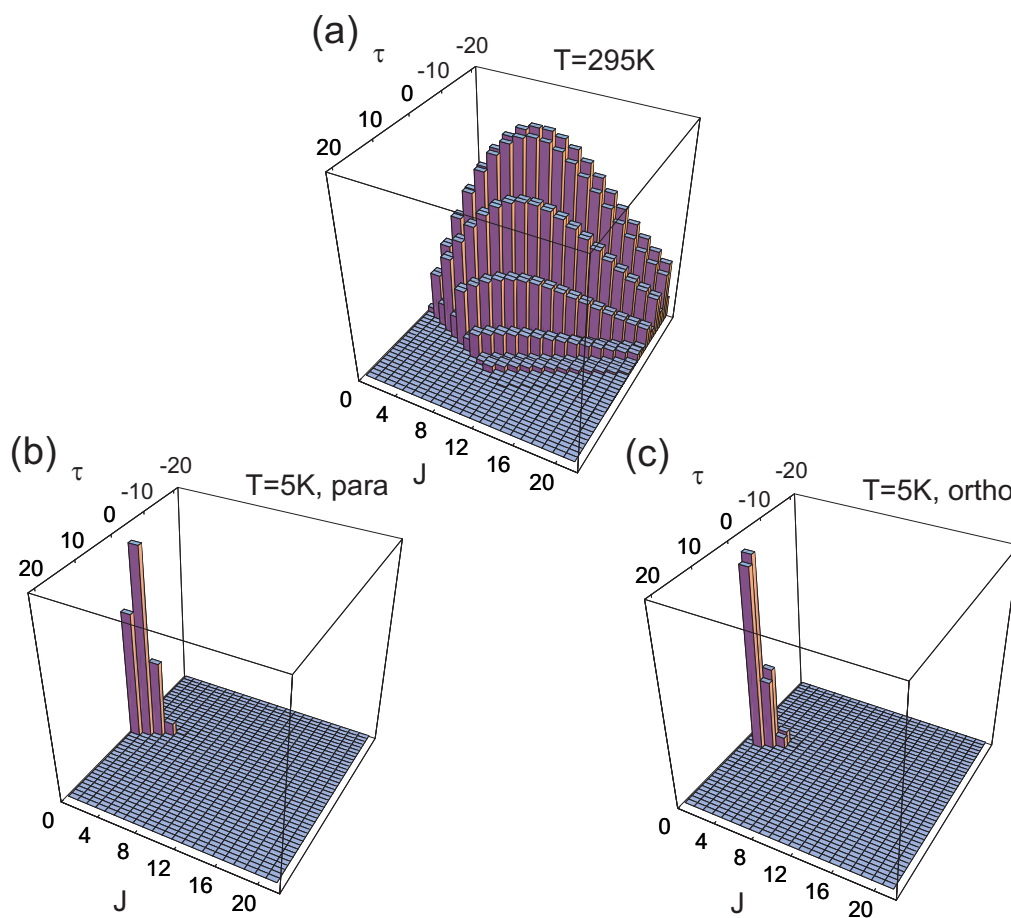


Figure 4.5: In (a) the rotational-state distribution for H_2CO at $T = 295\text{ K}$ is presented. The rotational states are labeled by $|J\tau\rangle$ quantum numbers. The state distributions in (b) and (c) are given for the ortho and para states at $T = 5\text{ K}$, respectively.

4.1.3 Molecular beams emerging from a buffer-gas source

Cold beams of molecules can be created by making an exit aperture in one of the walls of the buffer-gas container (buffer-gas cell). After being cooled by collisions, most molecules will diffuse to the cell walls and stick. A small fraction will find the exit aperture and form a beam. In our experiment, we use an electric guide to extract these beams from the cryogenic environment and transport them to a detection region at room temperature. The beam parameters are determined by the dimensions of the buffer-gas cell, where the buffer-gas cooling takes place, the exit through which molecules leave the cell, as well as by the densities and temperatures of the buffer gas and the molecular gas in the cell.

In our experiments, the ratio between the densities of the molecules n_{mol} and the buffer-gas atoms n_{BG} is small ($n_{\text{mol}}/n_{\text{BG}} \ll 1$). This guarantees that molecule-molecule collisions can be neglected. The buffer-gas density n_{BG} is kept constant by continuously flowing cold buffer gas into the buffer-gas cell. This is necessary because of the loss of atoms through the exit aperture.

In the following discussion we use a cuboid cell geometry with volume $D \times D \times L$, where $L \leq D$ (see section 4.2). The area of the cuboid holding the molecule input or exit aperture is given by D^2 . The length L determines the distance between the molecule input and the exit aperture. Here, we assume that the molecule inlet and the exit aperture are facing each other. The diameter of the exit aperture is designated by d ($d \ll D, L$).

It is desirable that the molecules have already thermalized to the buffer-gas temperature before they leave the cell through the exit aperture. Therefore, it must be guaranteed that the molecules have experienced a sufficient number of collisions l_T over the dimensions of the buffer-gas cell. Here, the number of collisions l_T is derived from Eq. 4.11. With l_T and the mean free path λ_T of the molecules undergoing thermalization in the buffer gas, the spatial expansion characterized by the thermalization length R_T of the molecular sample during the thermalization period can be estimated. The mean free path in the thermalization process is given by [Pre58]

$$\lambda_T = \frac{1}{n_{\text{BG}} \sigma_T \sqrt{1 + m_{\text{mol}}/m_{\text{BG}}}}. \quad (4.13)$$

Here, σ_T is the thermal average of the elastic collision cross-section for molecule-atom collisions [Pat10]. This results in the thermalization length

$$R_T = \alpha \lambda_T, \quad (4.14)$$

where α depends only on l_T . In the regime where the molecular motion in the buffer-gas cell is characterized by diffusion the relation $\alpha = \sqrt{l_T}$ is obtained. This is derived from the diffusion length $r = 2\sqrt{\delta\tau_T}$ during the thermalization period τ_T , where δ is the diffusion constant [Pre58]. The diffusion length can be identified with the thermalization length R_T in the diffusive regime.³ Since $\tau_T \propto l_T$ we obtain $R_T \propto \sqrt{l}$

³The diffusion length r describes how far the molecules have propagated in one direction in a buffer gas during a time τ .

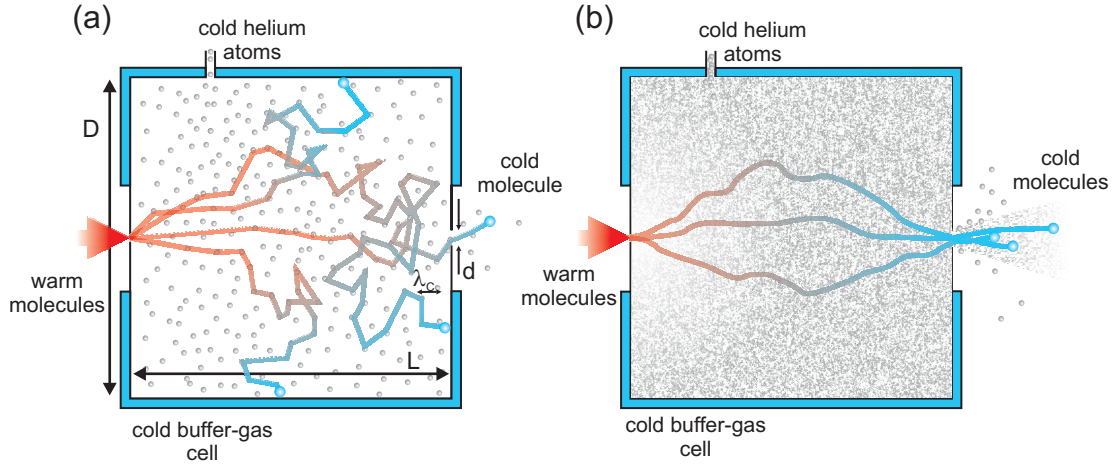


Figure 4.6: Schematic of (a) the diffusive and (b) the hydrodynamic regime in a buffer-gas cell. The figure is adapted from [Kre09].

in the diffusion regime. In the purely ballistic flow regime which is characterized by few or zero collisions with buffer-gas atoms, we obtain $\alpha = l_T$. To obtain molecules in the beam that are fully thermalized the condition $L \geq R_T$ must be fulfilled.

Hot molecules originating from a common starting point diffuse to the cell walls. Only those molecules that propagate to the location of the exit aperture can leave the cell. As a result of $d \ll D, L$, most molecules hit the cell walls and form an ice layer that grows over time. At low buffer-gas densities the ratio between molecules leaving the cell through the exit and the ones sticking to the cell walls is approximated by the ratio $A_{\text{exit}}/(4\pi(L/2)^2)$, which gives the geometric probability for a molecule to exit the cell, when it starts diffusing from the center of the cell.⁴ Here, A_{exit} is the area of the exit aperture.

By increasing the buffer-gas density a different regime can be reached, where the limit on the output efficiency set by the geometric probability can be overcome. In this regime the molecules are entrained in a macroscopic (hydrodynamic) buffer-gas flow which is directed to the exit of the cell.

For a given set of parameters (densities and cell geometry) a distinction which regime is dominant (diffusive or hydrodynamic) can be made. A relation that determines which case is present is obtained from the ratio between the diffusion time τ_{diff} and the pump-out time τ_{pump} . The diffusion time τ_{diff} describes the average time a molecule needs to reach the cell wall and it is expressed by:

$$\tau_{\text{diff}} \sim \frac{L^2}{4\delta}. \quad (4.15)$$

⁴If no buffer gas is applied (purely ballistic flow) and the input and exit of the molecules are facing each other the ratio is much better approximated by A_{exit}/L^2 . This is derived from the fact that for a straight beam the molecular flux density changes with $1/r^2$ over a distance r .

Here $\delta = 3/(16\sigma_c n_{\text{BG}}) \times \sqrt{2\pi k_B T/\mu}$ describes the diffusion constant [Pre58], where σ_c is the elastic collision cross-section for molecule-atom collisions at buffer-gas temperature and $\mu = (m_{\text{BG}} m_{\text{mol}})/(m_{\text{BG}} + m_{\text{mol}})$ is the reduced mass. Again the diffusion time is derived from $r = 2\sqrt{\delta\tau_{\text{diff}}}$. The diffusion length r is set to L , which defines the shortest cell dimension and therefore defines the shortest time period during which molecules can reach the cell wall.

The pump-out time τ_{pump} describes the time that is needed for molecules to traverse the cell by being entrained along with the macroscopic buffer-gas flow. It is expressed by:

$$\tau_{\text{pump}} = \frac{N_{\text{tot}}}{\Phi_{\text{BG}}} \sim \frac{4D^2L}{d^2v_{\text{BG},c}}. \quad (4.16)$$

Here, $v_{\text{BG},c} = \sqrt{2k_B T_{\text{BG}}/m_{\text{BG}}}$ is the buffer-gas velocity and $N_{\text{tot}} = D^2 L n_{\text{BG}}$ is the number of buffer-gas atoms in the cell. Eq. 4.16 uses the definition of the buffer-gas flux through an aperture in the molecular flow regime [Ram90]:

$$\Phi_{\text{BG}} = (v_{\text{BG},c} n_{\text{BG}} A_{\text{exit}})/4 \sim (v_{\text{BG},c} n_{\text{BG}} d^2)/4. \quad (4.17)$$

The velocity of the macroscopic buffer-gas flow through the cell is approximated by $v_{\text{flow}} \sim (d/D)^2 v_{\text{BG},c}$, which results from $\tau_{\text{pump}} = L/v_{\text{flow}}$. The regime governing the molecular outflow of the cell can be determined from the ratio

$$\xi = \frac{\tau_{\text{diff}}}{\tau_{\text{pump}}} = \frac{\hat{\kappa} L d^2 \sigma_c n_{\text{BG}}}{3D^2}. \quad (4.18)$$

Here, $\hat{\kappa}$ is a dimensionless constant of order unity [Pat10]. For $\xi \ll 1$ the molecular motion in the cell is diffusive. In this case most of the molecules stick to the wall and the fraction of thermalized molecules that leave the cell through the exit is determined by the solid angle subtended on the exit aperture (see Fig. 4.6a). For $\xi \gg 1$ the molecular motion is governed by the macroscopic flow in the cell (see Fig. 4.6b). This macroscopic flow drags the molecules to the exit aperture, resulting in a much higher cell transport efficiency and therefore to a much higher outgoing flux. Unfortunately, these molecules have a much higher velocity $v_{\text{mol},c} < v_{\text{mol}} \leq v_{\text{BG}}$ and there are hardly any slow molecules left that can be trapped in electric or magnetic fields. This is explained in the following.

The effect described here is similar to the collision-loss effect described previously in section 3.3 for a thermal source. The velocities of the molecules are influenced by collisions in the proximity of the exit aperture. Due to a large density gradient in this region, molecules leaving the cell undergo collisions primarily with forward (towards the exit aperture) moving buffer-gas atoms. Therefore, the forward velocities of the molecules exiting the cell are shifted (boosted) to higher values [Max05]. This effect, called ‘boosting’, is described by the following model. The time molecules need to traverse the proximity of the exit aperture is roughly approximated by $t_e \sim d/v_{\text{mol},c}$,

where $v_{\text{mol},c}$ describes the molecular velocity at buffer-gas temperature. The number of collisions with buffer-gas atoms in this region can be estimated by

$$N_e \sim n_{\text{BG}} \sigma_c v_{\text{BG},c} t_e \sim \left(\frac{d}{\lambda_c} \right) \sqrt{\frac{m_{\text{mol}}}{m_{\text{BG}}}}. \quad (4.19)$$

For each collision a molecule with a velocity v_{mol} experiences a momentum transfer of $\Delta p_{\text{mol},c} = m_{\text{mol}} \Delta v \sim 2\mu(v_{\text{BG},c} - v_{\text{mol}})$. For collisions between a helium buffer-gas atoms at $T \sim 5$ K ($v_{\text{He}} = 144$ m/s) and ammonia (ND_3) molecules with $v_{\text{ND}_3} \sim 0$ m/s, a change of $\Delta v \sim 48$ m/s is expected for approximately one collision. The change of velocity Δv is already close to the thermal velocity $v_{\text{ND}_3,c} = \sqrt{2k_B T / m_{\text{ND}_3}} = 64$ m/s. From Eq. 4.19 it is apparent that when the exit aperture dimensions are comparable to the mean-free path dimensions ($\lambda_c \simeq d$), the boosting effect can alter the thermal velocity distribution significantly although the molecular motion in the cell is still diffusive.

4.2 Experimental setup

In our setup we have combined the buffer-gas technique with electric filtering and guiding to produce a slow beam of cold polar molecules. The guide can deliver the buffer-gas cooled molecules to a separate ultrahigh vacuum environment where the molecules can be used for further experiments [Rie05, Wil08a]. The technical implementation of buffer-gas cooling in our setup is presented in detail in this section.

The basic structure of the cryogenic source is described in the following (see Fig. 4.7). The source consists of a cryogenic cooler to which a copper buffer-gas cell is mounted. The copper cell can be filled with the buffer-gas via a gas supply line which can be thermally connected to the cooling stages of the cryogenic cooler. Via a second gas supply line which is thermally isolated from the buffer-gas cell, molecular gas is introduced. At a distance of 1 mm from the exit aperture of the cell the electric-quadrupole guide is mounted to extract the buffer-gas cooled molecules. These parts of the system are located in a stainless steel vacuum vessel (height ~ 60 cm and $\varnothing \sim 40$ cm). The electric guide extends to a separate ultrahigh vacuum chamber located on top of the main vacuum vessel. Except for the turbo-molecular pump (~ 550 ls^{-1}), all components are mounted on the top flange to allow for easy servicing of the system. In the following subsections the individual parts of the system are discussed in more detail.

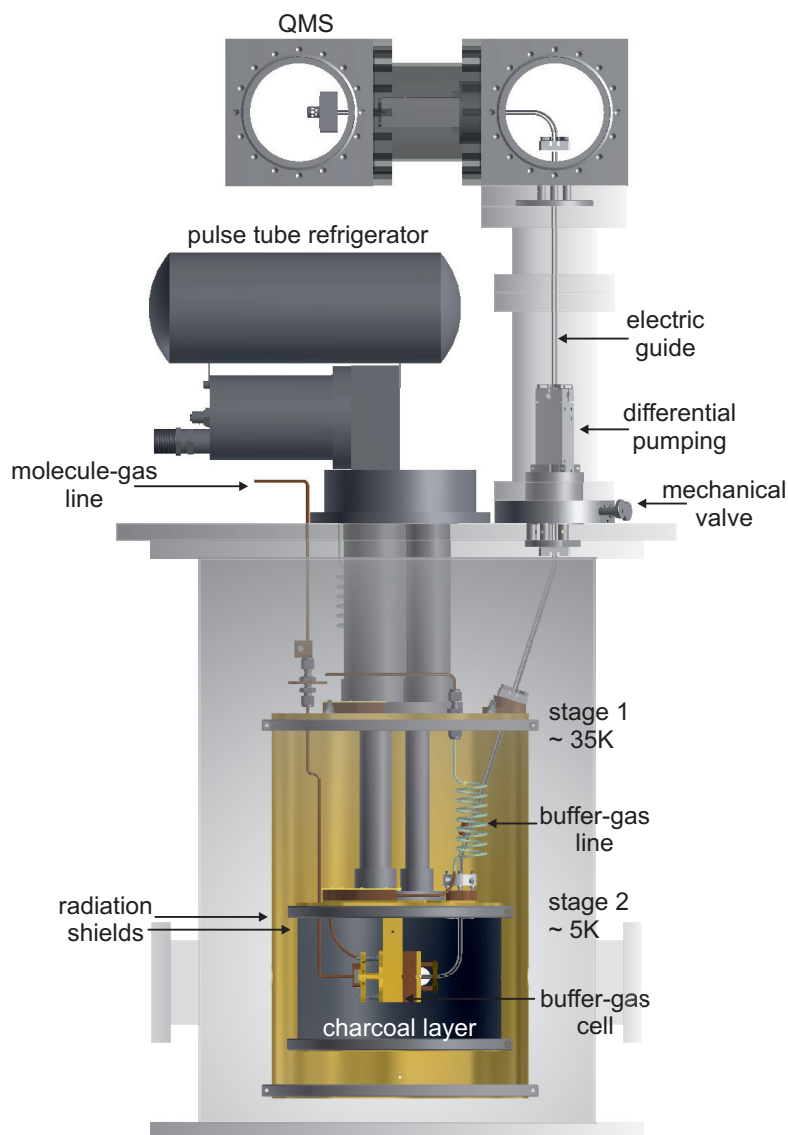


Figure 4.7: Experimental setup. The inner assembly is mounted directly to the refrigerator. With two capillaries, buffer gas and molecular gases are injected into the buffer-gas cell. With an electric quadrupole guide molecules are extracted from the buffer gas and transported to a ultrahigh vacuum environment, positioned above the vessel. During warm up, a mechanical valve can isolate these two regions.

4.2.1 Cryogenic system

The buffer-gas cell where the cooling of the molecules takes place is mounted on the second cooling stage of a cryogenic cooler. We use a commercially available pulse-tube cryocooler (CRYOMECH PT410). A pulse-tube cooler is a device where the refrigeration is provided by a closed-loop system. This avoids, as required in systems with liquid helium, the continually refilling of the refrigerant. The principle of operation is illustrated in [Rad00, Eki06] and outlined below.

A simplified description of the cooling process in a pulse tube cooler is presented in the following. The refrigeration cycle starts by connecting the pulse tube cooler to the high pressure helium reservoir provided by a compressor. The compressed helium gas flows into the regenerator (heat exchanger). The regenerator is made of materials with a high volumetric heat capacity and low thermal conductivity (porous metal). Therefore during the compression cycle heat from the compressed helium gas is taken up and stored in the regenerator matrix material thus making the process isothermal. The regenerator acts as a precooler for the helium gas. Due to the increased pressure helium gas on the other end of the regenerator enters the pulse tube by passing the cold stage. The pulse tube is basically an open tube that thermally isolates the incoming helium gas. The pulse tube insulates the processes at its two ends which are the cold stage at the bottom and the room temperature heat exchanger at the top. It guarantees that the gas in the pulse tube traverses only part way from each end. Thereby, the helium flow from the cold end never reaches the warm end and vice versa. The gas in the middle portion of the pulse tube never leaves the pulse tube and forms a temperature gradient that insulates the two ends. The gas in the middle acts like a displacer (gas plug) for the gas of the cold and the warm end. Due to the increased pressure, helium gas in the pulse tube close to the warm end of the pulse tube is adiabatically compressed. This gas possesses a higher pressure and temperature than the gas in the buffer (room-temperature reservoir) (see Fig. 4.8). This results in a flow of helium gas into the reservoir. In the buffer the gas can thermalize to room temperature. Via an inertance tube (or orifice) used for flow restriction the helium gas enters the buffer. The gas flow out of the pulse tube stops when the average pressure in the reservoir equals the pressure in the pulse tube. This leads to the second half of the cooling cycle where the system on the entrance at the regenerator is connected to the low pressure reservoir of the compressor. The gas in the pulse tube is adiabatically expanded and thus cools down. Cold helium gas flows now in the reverse direction past the cold stage at the lower end of the pulse tube where it absorbs heat and enters the regenerator. Note that the helium gas also traverses only part way through the generator in both half cycles. The helium gas at the cold end oscillates between the regenerator and the pulse tube and stays closely around the cold stage. The helium gas at the warm end oscillates between the pulse tube and the buffer. Therefore, the pulse tube transmits hydrodynamic power (acoustic power) in an oscillating gas from the cold end to the warm end across a temperature gradient.

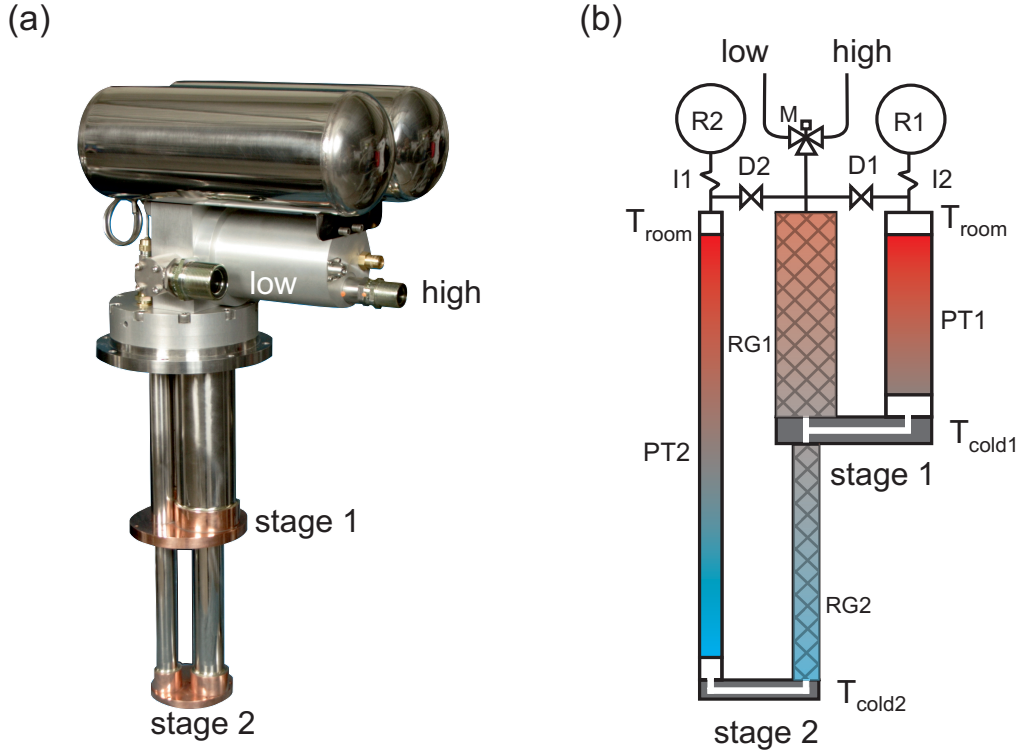


Figure 4.8: Pulse-tube cryostat. In (a) the CRYOMECH PT410 is presented. A schematic drawing of the apparatus is given in (b). Here, R1, R2 are helium gas reservoirs; PT1, PT2 are pulse tubes; RG1, RG2 are regenerators and I1, I2 are the inertia lines. D1 and D2 are secondary orifices that allow direct flow, between the compressor line and the warm end of the pulse tube for a small fraction of the gas [Eki06]. The schematic is adapted from [Yan04].

For our experiment a two stage pulse tube cooler is used (see Fig. 4.8). Here, the first stage can be used to insulate the second stage from thermal radiation of the vacuum vessel. This is achieved by a round gold-plated copper radiation shield that is installed on the cold plate of the first stage. A second radiation shield is installed on the cold plate of the second stage to reduce the heat load from the first stage.

We use silicon diode temperature sensors (LAKESHORE DT470) and (PT-100) resistance thermometers to monitor the temperature on the radiation shields, the buffer-gas cell and the gas-supply lines. The diode temperature sensors allow temperature measurements in the range of 1.4 K to 475 K with an accuracy of ± 0.5 K at low temperatures. A typical cool down of the experiment is shown in Fig. 4.9.

The inside of the radiation shield mounted to the second stage is covered with a layer of activated charcoal (see Fig. 4.10). At cryogenic temperatures activated charcoal acts as an adsorbent pump for helium. Large pumping speeds can be obtained due to its large effective area. Because of its simplicity it represents the optimal solution for our experiment. It is applied in our setup to keep the pressure within

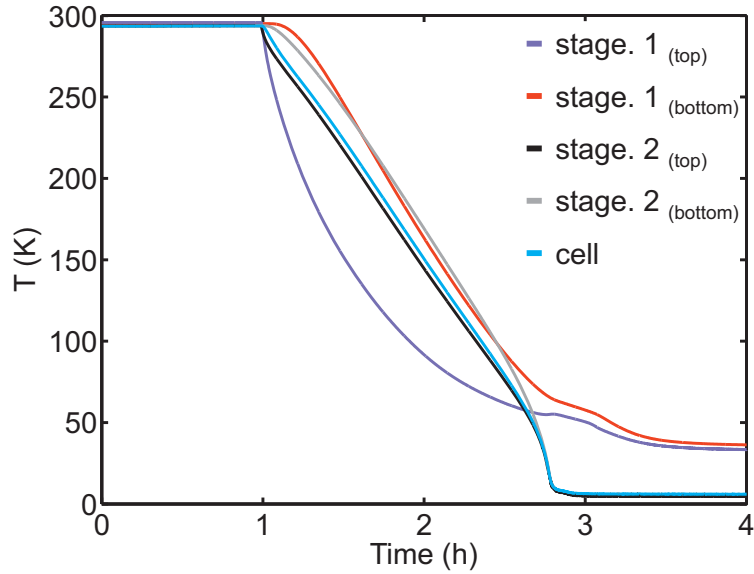


Figure 4.9: Measurement of temperature at various positions during a typical cool-down of the cryogenic source source [Poh07]. Radiation shields are mounted on stage 1 and 2. Temperature sensors (LAKESHORE DT470) are attached to the first (second) stage (stage.1(2)_(top)) and to the bottom of the corresponding first (second) radiation shield (stage.1(2)_(bottom)).

the radiation shields as low as possible. From test experiments we concluded that for pressures lower than $\sim 10^{-6}$ mbar collisions of guided molecules with background gas are negligible. A reasonable vacuum is also required to prevent discharges between oppositely charged guiding electrodes. We use coconut-based granular activated carbon (Chemviron Carbon 207C). A surface of roughly 1000 cm^2 is covered with a layer of this material, resulting in a pumping speed of $\sim 5000 \text{ ls}^{-1}$ at cryogenic temperatures. The gas (mainly helium buffer gas) adsorbed by the charcoal is released during warm up of the cryogenic system after which it is pumped out of the vacuum vessel by the turbo-molecular pump at the bottom of the vessel.

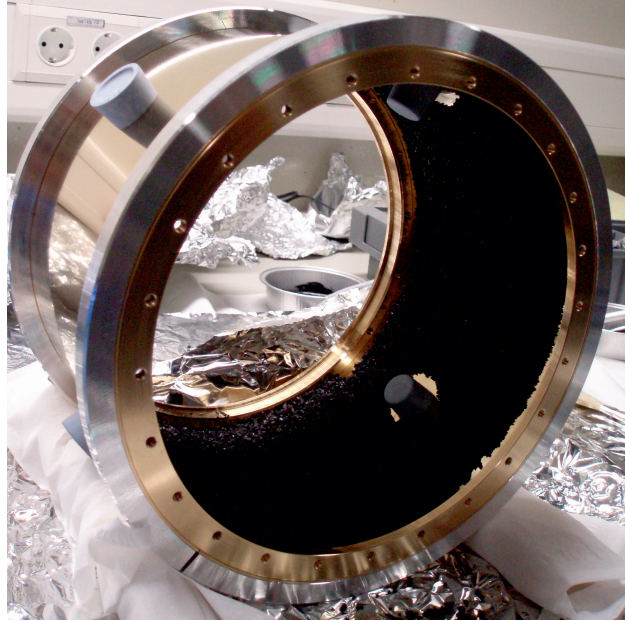


Figure 4.10: Charcoal layer on the inner surface of the second-stage-radiation shield. We use Stycast glue to attach the charcoal to the copper surface [Poh07].

4.2.2 Buffer-gas cell and gas supply system

The buffer-gas cell consists of a gold-plated hollow copper block that is clamped to the lower (low temperature) stage of the cryostat (see Fig. 4.7 and Fig. 4.11).⁵ The inner volume of the main body of the buffer-gas cell is $4.2 \times 4.2 \times 1 \text{ cm}^3$. The side walls are 0.6 cm thick. Additional extensions can be inserted in between the exit plate and the main body of the cell (see Fig. 4.11a). Here we use 1 cm long extensions given by 0.6 cm thick copper frames that have a 5.4 cm outer and 4.2 cm inner dimension. On the side walls of the extension frames several screw holes are drilled that allow for access to the closed buffer-gas cell (for example wiring for sensors). The wall on the back has a large hole with a diameter of $\sim 3.6 \text{ cm}$, which is covered by a patch of a $25 \mu\text{m}$ thick polyamide (Kapton) foil clamped to the outer side of the wall (see Fig. 4.11b). An aperture in the Kapton foil is punched against the molecule gas-supply line, which serves as an inlet for the warm molecules into the buffer-gas cell. The foil is used to reduce the heat conductance between the cell and the warm molecular gas line. The opposite side of the cell is a $\sim 0.5 \text{ cm}$ thick copper plate (exit plate) with a 1 cm opening in the middle. This opening is covered by a Kapton foil sheet, which is clamped onto the plate by stainless-holders. An 1 mm aperture in the middle of the Kapton foil sheet serves as the exit for the molecules from the cell. The thin foil is used to limit clogging and allows for local heating (see section 4.4.2). The exit aperture is placed against the input aperture.

⁵The position of the cell is adjustable along the electric guide direction

A vacuum feed through for several 6 mm wide gas lines (inner diameter) is installed on the top plate (top vacuum flange) of the vessel to bring both the molecular gas and the helium gas into the buffer-gas cell. The molecular gas line as well as the buffer-gas line are attached to one of the feed through lines. Inside the vacuum the buffer-gas line has a 3 mm outer and 1 mm inner diameter. The total buffer-gas line consists of four connected segments. The first segment is given by a stainless steel pipe which is connected to the feed through by a SWAGELOK adaptor (6 mm to 3 mm outer diameter), and on the other side to the second segment. The stainless-steel line contains several windings to increase the length and thereby reducing the heat conductance of the gas line. Since the buffer-gas needs to be cooled down on its way to the cell, the second segment is given by a copper line with the same dimensions as the former one. This copper part of the line is tightly connected to the first stage of the cryocooler for pre-cooling of the buffer gas to the first stage temperature (~ 35 K). It then enters into the volume enclosed by the outer radiation shield, where it is connected to another stainless steel pipe of equal dimensions forming the third segment of the buffer-gas line. Also for this line segment the heat conductance is reduced by several windings. The stainless steel gas line is again passed over into another copper line segment, which is tightly mounted to the second stage of the cryocooler. This line is the fourth and last segment of the buffer-gas supply line. Its terminal part is clamped with an indium-sealed copper block to an opening of the cell wall.

The molecular-gas line is made of a stainless steel pipe of 6 mm outer and 5 mm inner diameter, The gas line goes directly from the feed through to the cell inlet and is thermally isolated from the cold parts of the experiment. Several electric heaters are installed on various locations to maintain a sufficiently high vapor pressure and to avoid resublimation of the gas. To regulate the temperature of the heaters PT100 and DT470 temperature sensors are placed nearby. For the molecules employed in this work, we used temperatures of the input capillary above 140 K (for ND_3 above 180 K and H_2CO at room temperature). The end of the line is inserted into a gold plated copper inlet ($\varnothing 3$ mm) that has a reduced inner diameter of 1 mm close to the end (see Fig. 4.12).

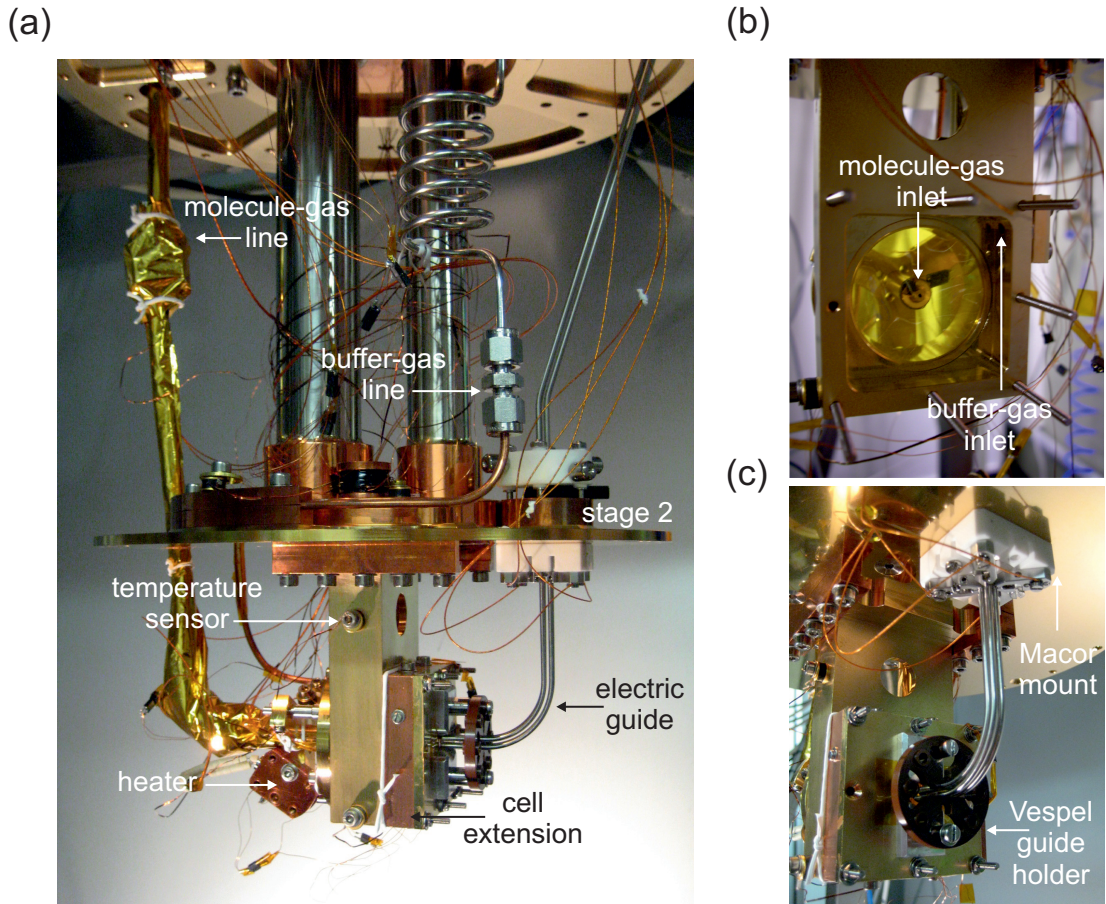


Figure 4.11: (a) General view of the buffer-gas cell in the cryogenic environment. The helium line enters the copper cell from the back side. The heated molecular line is connected to a special inlet assembly, which has a bad thermal connection to the buffer-gas cell. This allows for heating of the inlet without considerably affecting the temperature of the buffer-gas cell much. The length of the cell can be varied by placing 1 cm long copper extensions in between the main frame of the cell and the exit plate. (b) Buffer-gas cell interior. (c) Assembly view: buffer-gas cell and quadrupole guide.

A small Viton O-ring is used to seal the transition between the gas line and the inlet. To avoid heat transport from the molecular gas line to the cell, the inlet frame is clamped to stainless steel rods of the cell via small glass balls. The used materials and point contacts of the balls heavily reduce the thermal coupling of the gas line to the cell. The conical tip of the inlet is glued onto the Kapton foil. Due to the low thermal conductivity of Kapton the heat conductance from the heated inlet tip to the cell metal frame is minimized. Therefore cryogenic temperatures are maintained even for a gas line temperature of ~ 300 K.

The flow of the molecular and buffer gas is controlled via a gas handling system (see Fig. D.1). To sensitively regulate the gas flows, electrically controlled needle valves adjust and maintain the inlet pressure with the assistance of a pressure gauge (capacitance gauges) mounted on the room-temperature part of each line.

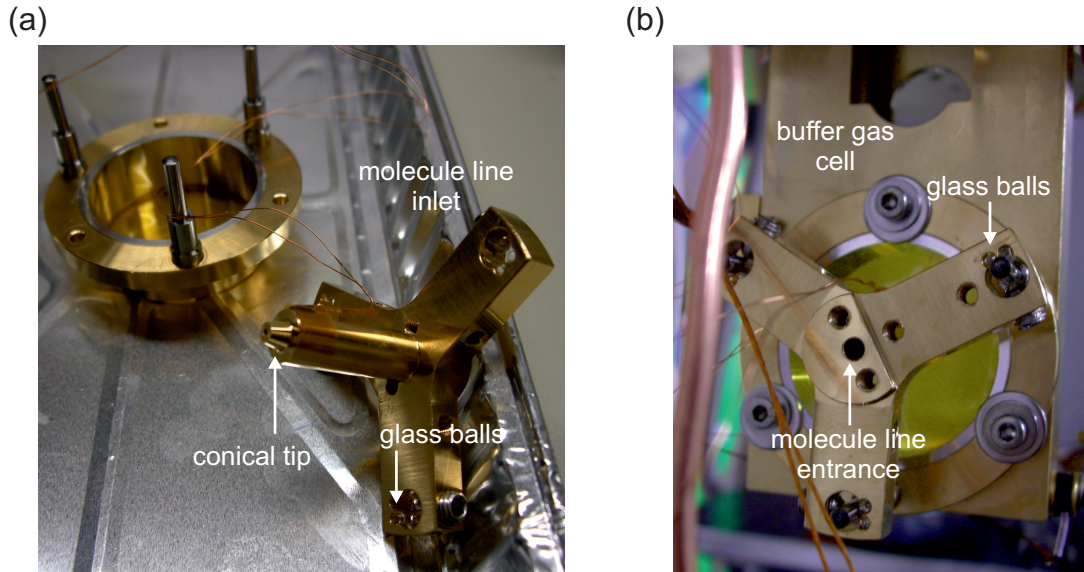


Figure 4.12: The molecule-line-inlet is presented in (a). The molecular gas line is connected to this inlet. It ends in a conical shape which is glued to a thin Kapton foil to reduce heat loads. This foil is clamped to the cell and forms the back wall of the cell. Stainless steel rods and glass balls are used to position the inlet without high additional heat load. A picture of the inlet attached to the buffer-gas cell is shown in (b).

4.2.3 Electric guide

The electric quadrupole guide in the cold source is constructed in a similar way as in the room-temperature setup discussed in chapter 3, except for smaller bends with a 2.5 cm radius of curvature. The total guide consists of four quadrupole segments separated by 1 mm gaps. Two segments are located in the vacuum vessel that contains the buffer-gas cell. The first segment with a length of 12 cm includes a bend of 90° while the second segment measures 31.4 cm and contains two bends of 18° each. The other two segments with lengths of 36.6 cm and 26.8 cm, respectively, are in the high-vacuum region, placed above the vacuum vessel enclosing the cryogenic source. The fourth segment also contains a bend of 90° at the beginning before it passes into a straight run. These segments are used to deliver the guided molecules to the detector where the last straight part of the fourth segment allows for depletion spectroscopy by overlapping the central axis of the guide with a laser beam (see section 4.5.2).

We use a similar quadrupole mass spectrometer with a crossbeam ion source (PFEIFFER QMA 410), as for the experiments described in chapter 3. The mass spectrometer is mounted on a translation stage to be able to vary the position of the ionization volume relative to the guide exit.



Figure 4.13: Mechanical valve and differential pumping sections. In (a) the mechanical valve is presented. Here, a small stainless sheet is pushed into the space between two guide segments and onto an isolating O-ring. In (b) the differential pumping section above the valve is shown. It consists of two Macor brackets that enclose the electric guide. Its purpose is to reduce the conductance to the next vacuum section.

4.2.4 Ultrahigh-vacuum chamber and differential pumping

The ultrahigh-vacuum region is separated from the vessel by a thin valve (see Fig. 4.13a). The valve consists of a stainless-steel mechanical shutter, which can be pushed through the 1 mm gap between the second and third guide segment. From below it is sealed by a Viton O-ring. In this way a vacuum better than $\sim 10^{-8}$ mbar can be maintained in the next ultrahigh vacuum region, even when atmospheric pressure is applied inside the vessel. This enables us to warm up the source without polluting the ultrahigh-vacuum region. Also modifications can be made to the source without breaking the vacuum near the detection. Therefore, the detection chamber is constantly pumped and permanently under ultrahigh-vacuum condition. This ensures low background contributions in our detection. To preserve a low pressure ($< 10^{-9}$ mbar) in the detection chamber during measurements with large amounts of buffer gas, we use differential pumping stages. The first stage is placed above the mechanical valve and the other one between the two cubes inside the high-vacuum region (see Fig. 4.13b). The differential pumping sections consist of two Macor brackets of ~ 10 cm length, which are clamped directly to the guide rods via metallic holders. In doing so the Macor brackets do not touch the guide electrodes. It allows molecules to travel between the different vacuum regions only through the small opening in the middle of the quadrupole guide.

To maintain a low pressure in the high-vacuum region, we use three turbo molecular pumps (two with pumping speeds of ~ 60 ls^{-1} and one in the detection chamber with a pumping speed of ~ 210 ls^{-1}) backed by another turbo pump and membrane pump. Pressures of 10^{-9} mbar in the region behind the valve and 10^{-10} mbar in

the detection chamber are obtained. Pressure values in this range are measured by Bayard-Alpert pressure gauges.

4.2.5 Data acquisition

To determine the number of guided molecules with the QMS and to distinguish the signal they produce from the background signal, we switch the high voltage on the guide on and off repeatedly. The difference in count rate reflects the contribution of guided molecules. Velocity distributions can be obtained from the time-of flight (TOF) signal after switching on the high-voltage, as described in section 3.5 and shown in Fig. 3.4. The first and the second guide segments are connected to high-voltage transistor push-pull switches (BEHLKE HTS 151 – 03–GSM), each housed in a copper box to prevent the generated radio frequency from being radiated. TTL pulses from a pulse generator are applied to the switches to set the on ($T_{\text{ON}} = 110$ ms) and off ($T_{\text{OFF}} = 100$ ms) configurations. This timing scheme allows for detection of molecular velocities down to about 10 m/s, well within the regime where noise and systematic errors become dominant. This is comparable to the effects found in our previous guiding experiments [Jun04a, Mot09a]. The third and fourth segment are permanently at high voltage to avoid pick-up currents on the QMS electrodes.

The QMS ion counter signal is sent to a TTL pulse shaper that generates ~ 100 ns TTL pulses if the amplitude of the incoming count signal exceeds a fixed threshold voltage. The threshold is used to eliminate noise. The TTL pulses are recorded by a MCS (Multi Channel Scalar) card, which creates histograms of the counts as a function of time. The trigger for the scalar card is generated by the pulse generator and starts 10 ms before the high voltage is switched on. Data from the temperature and pressure sensors are recorded every 8 s with a LabVIEW interface.

4.3 Flux and density calibration

To determine the number of molecules guided to the mass spectrometer and thereby extract the respective flux as well as densities inside the guide, calibrations have to be performed. The densities of molecules and buffer-gas atoms inside the cell can be estimated from calibrations of the gas flows through the gas line. The methods that have been applied to obtain these numbers are discussed in this section.

4.3.1 Gas line calibration

The calibrations of the gas-supply lines of the buffer-gas cell are used to convert the pressures at room temperature into densities in the buffer-gas cell at a few Kelvin. To determine the conductance of the gas lines we have removed the radiation shields. Gas is fed through one of the gas lines into the vacuum vessel and pumped by the turbo molecular pump. The pressures in the gas handling system (p_{gas}), and in the vessel (p_{vessel}) are recorded together with the signal of a quadrupole mass

spectrometer (PFEIFFER Prisma QMS 200) mounted on the side of the vessel. The mass spectrometer is used to confirm whether the flown gas is responsible for the change in pressure. For various values of p_{gas} the flux into the chamber is determined via

$$\Phi = \frac{p_{\text{vessel}} S_{\text{pump}}}{k_B T_{\text{room}}}, \quad (4.20)$$

with $T_{\text{room}} = 295 \text{ K}$.⁶ The conductance C_{line} of the gas line can be obtained by taking the pressure in the gas handling system p_{gas} into account. We derive

$$C_{\text{line}} = \frac{\Phi k_B T_{\text{room}}}{p_{\text{gas}}}. \quad (4.21)$$

The conductances of the molecular line are obtained for N_2 and ND_3 at room temperature. We observe a strong deviation from direct scaling valid for the molecular regime ($C_{\text{line}}^{\text{mol}} = C_{\text{line}} \sqrt{m_{\text{N}_2}/m_{\text{mol}}}$).

In a similar way, we have obtained the fluxes through the buffer-gas line. Here, the measurements are done at low temperature ($T_{\text{cell}} = 18 \text{ K}$). Lower temperatures could not be reached without radiation shields. We assume that the buffer gas thermalizes with the warm vessel before being pumped. Therefore, T_{room} can be employed in Eq. 4.20.

Using the conductance of a 1 mm aperture in the exit plate,[Laf98]

$$C_{\text{exit}} = A \sqrt{\frac{R_0 T_{\text{cell}}}{2\pi M_m}}, \quad (4.22)$$

where M_m is the molar mass of the species used for calibration, R_0 the universal gas constant and A the aperture area at T_{cell} , we determine the buffer-gas density in the cell from

$$n_{\text{cell}} = \frac{\Phi}{C_{\text{exit}}}. \quad (4.23)$$

No corrections are being made for changes in T_{cell} . Note that these corrections will be relatively small.

4.3.2 Guided flux calibration

To determine the flux of guided molecules, the sensitivity of the QMS for the guided species has to be determined. To calibrate the QMS, a constant flow of molecular gas (of the same species as the molecules that have been guided) is applied to the detection chamber through a needle valve, mounted on a side flange of the detection chamber. The density inside the chamber is determined from the pressure measured by an Bayard-Alpert gauge. After the pressure has stabilized, a mass

⁶The pumping efficiency of the turbo pump (located at the bottom of the vessel) is specified by the manufacturer for nitrogen gas ($S_{\text{pump}} = 550 \text{ ls}^{-1}$ for N_2), ammonia or neon gas ($S_{\text{pump}} = 551.4 \text{ ls}^{-1}$ for ND_3) and helium gas ($S_{\text{pump}} = 600 \text{ ls}^{-1}$ for He).

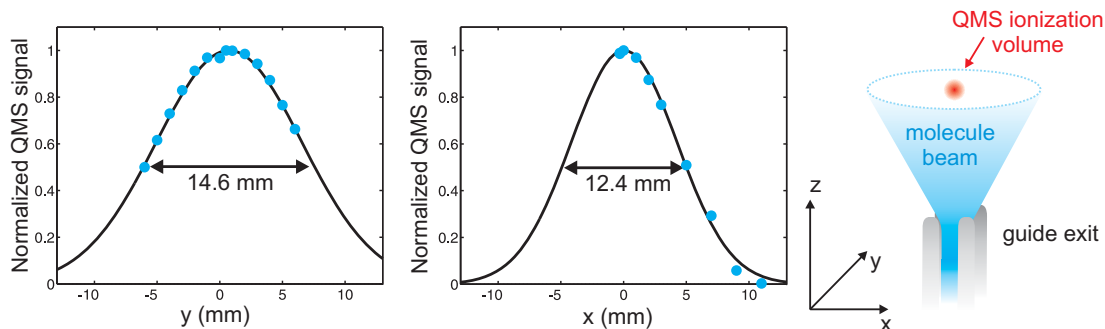


Figure 4.14: Measurement of the beam shape in the y - and x -directions fitted by a Gaussian distribution. The distance between the guide exit and the ionization volume of the mass spectrometer is ~ 25 mm along the z -direction. The profile in the y -direction is wider compared to the x -direction due to the larger width of the ionization volume along this direction [Mie10]. The larger integration area widens the profile. For the beam in the guide a profile with a radial standard deviation of $\sigma = 400 \mu\text{m}$ is assumed.

spectrum ($1 - 100$ amu) is taken to determine the masses that contribute to the increase in pressure. The next step is to measure the count rate at the mass of the guided molecules. This is repeated for various densities in the detection chamber. To determine the density in the detection chamber, the ionization probability of the used species needs to be taken into account. Since the mass spectrometer is operated in a regime far from saturation for our guided molecules, the QMS signal is proportional to the density of the molecules in its ionization volume [Mot09a]. By variation of the ionization current no signs of saturation have been apparent, not even for slow molecules.

Since the mass spectrometer detects only molecules that enter the ionization volume, the fraction of the guided beam reaching the QMS ionization volume has to be determined. By varying the position of the QMS in the plane perpendicular to the guide exit, the beam spread is obtained (see Fig. 4.14). Since the width of the ionization volume is smaller than the expanded beam [Mie10], the beam shape can be resolved.⁷ The beam profile in the plane is well described by a Gaussian distribution. With this distribution the ratio of undetected to detected molecules is determined by a simple integration of the normalized Gaussian over its peak, with the integration boundaries given by the ionization region. Using this factor together with, the average velocity of the guided molecules obtained from the measured velocity distribution and the measured density inside the ionization volume, a total guided flux of $(7 \pm 7) \times 10^{10} \text{ s}^{-1}$ for ND_3 is obtained. Also, we obtain a peak density in the guide of $(1.0 \pm_{0.6}^{1.0}) \times 10^9 \text{ cm}^{-3}$.

⁷The total width is ~ 2 mm along the x -direction and ~ 1 cm along the y -direction according to [Mie10]. The asymmetry is due to the assembly of the ionization stage of the QMS.

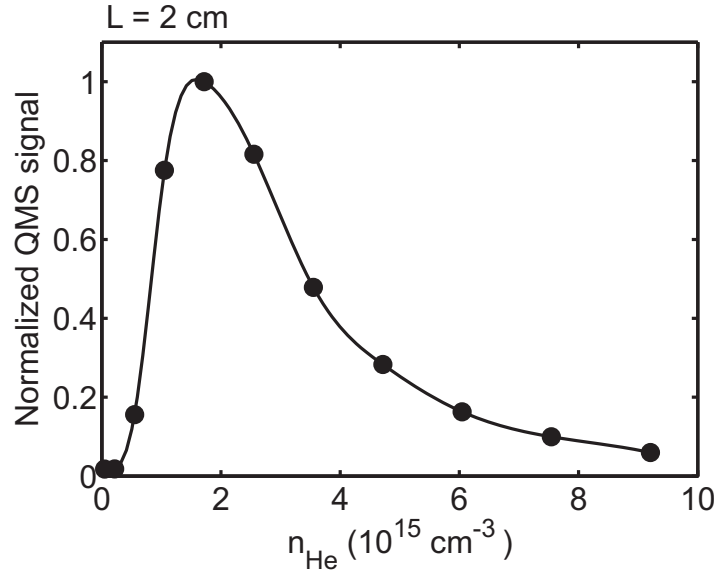


Figure 4.15: Normalized QMS signal for ND_3 as a function of the helium density in a 2-cm-long cell. The density of ND_3 is fixed to $\sim 1.4 \times 10^{16} \text{ cm}^{-3}$ at the input of the cell. The buffer-gas density is varied over about one order of magnitude. The rising edge indicates the region of insufficient cooling. The falling edge displays the effect of boosting as discussed in the text. At the peak position of n_{He} a flux of order of $10^{10} - 10^{11} \text{ s}^{-1}$ is obtained. The curve connecting the data points is a guide for the eye.

4.4 Optimization of the source

Several parameters of the source are optimized to maximize the flux of slow molecules and to optimize the cooling process. Different cell lengths, gas densities and exit apertures are tested in our setup. Ultimately a compromise is found since optimal parameters for the flux, internal cooling and runtime of the source are not concurrent.

4.4.1 Flux optimization

In this section, the optimization of the flux with respect to the buffer-gas and molecular-gas densities is presented. Most of the discussed measurements are performed with a 2 cm long cell, although we also investigated other cell lengths. Helium is used as a buffer-gas.

The normalized QMS signal of guided molecules is shown for different buffer-gas densities in Fig. 4.15. The characteristics of this curve are explained in the following. For low helium densities, where only few or no collisions take place most of the molecules are too fast and escape from the bent quadrupole guide (as pointed out in section 3.2). With higher buffer-gas densities the cooling increases, and the signal rises to the maximum. If the density is raised to higher values the signal

begins to drop. This is explained by the boosting that is described in section 4.1.3. At the maximum signal, the exit aperture dimension (\varnothing 1 mm) becomes comparable and for higher densities larger than the mean free path between the helium atoms in the cell. This leads to a high probability for molecules, which are leaving the cell, to be accelerated (boosted) in the forward direction.

From the ammonia density scans at fixed helium densities we can see that the molecular flux saturates. Here, various amounts of ND_3 are injected into the cell at fixed helium densities (see Fig. 4.16). We attribute the saturation to the limited heat capacity of the helium gas. For low He densities only a limited amount of ammonia can be cooled down to cryogenic temperatures. This explanation is supported by the fact that a larger helium density can support a larger ND_3 flux at a larger saturation density.

Similar examinations performed with a 1 cm and 3 cm cell length indicate that the maximal flux is obtained in a 2 cm long cell. This can be understood as follows. In a shorter cell less collisions take place to cool down the molecules for equal buffer-gas densities. Therefore, higher buffer-gas densities have to be applied to a 1 cm long cell to obtain efficient cooling, in comparison to a 2 cm long cell. However with a higher helium density the boosting is increased, which reduces the flux. For 1 cm cell length the guided flux is by a factor of two lower than in the 2 cm configuration. If the cell is extended to 3 cm, we get a reduction of the flux due to the smaller ratio of exit aperture to inner surface of the cell as described in section 4.1.3. This means that less molecules find their way to the exit and a large fraction of them adhere to the walls of the cell. Lowering the temperature on the inlet of the molecular input capillary helps to increase the guided flux. By reducing the temperature of the molecular-gas line from ~ 295 K to ~ 180 K a gain in flux by a factor of two to three can be achieved. This can be explained by the reduced heat load on the buffer gas close to the vicinity of the injection and the decreased number of collision needed for thermalization (Eq. 4.11).

We conclude that the highest flux is obtained for a buffer-gas density of $n_{\text{He}} \sim 2 \times 10^{15} \text{ cm}^{-3}$ and an ammonia density of $n_{\text{ND}_3} \sim 5 \times 10^{16} \text{ cm}^{-3}$ in the inlet of a 2 cm long cell at a temperature just above the point where molecules condense. We define these parameter settings as the optimal flux settings for ND_3 for helium buffer-gas cooling at 5 K, which can be different for other molecules, buffer-gases and cell temperatures. It is worth pointing out that the ammonia density varies over the cell extension from the inlet to the exit (see section 4.1.3, illustrated by Fig. 4.16a). The highest value is obtained at the inlet, which is reduced approximately by more than two orders of magnitude to the exit.

4.4.2 Runtime optimization

The measurement time in our setup is limited by the sticking of molecular gas to the walls of the buffer-gas cell, which happens long before the saturation of the charcoal by adsorbed helium gas. The charcoal can pump helium gas for several days in the density regimes we use in our system. However, we observe a steady decrease of the flux of guided molecules with a half life of ~ 5 hours, which we attribute to molecules clogging the entrance and the exit aperture of the cell. The ice formation has been observed directly after the installation of viewing ports in the vacuum vessel and radiation shields [Poh07]. In particular, in the exit aperture, large blocks of molecular ice appear after several hours of operation; for a small opening of ~ 0.5 mm instead of 1 mm this time reduces to barely 30 min. The ice reduces the diameter of the exit aperture and with it the amount of molecules that can enter the guide. Since the warm up of the complete setup takes ~ 8 hours, a different solution had to be found. We use a Nichrome heater wire ($10 \Omega/\text{m}$), attached with cyanoacrylate based fast-acting glue to a 4 mm diameter copper foil that has a 1 mm opening in the middle. This heater plate is glued to a Kapton foil with the wires pointing into the cell.⁸ The coil is additionally covered with Stycast 2850 epoxy for better adherence and thermal connection. To carefully monitor the temperature a Pt100 temperature sensor is glued to the copper plate as well. Since the heater is glued to the Kapton foil and has a very low thermal contact with the buffer-gas cell we can easily rise the temperature of the exit aperture. From Fig. 4.17 we see that the signal indeed recovers each time a heater pulse is applied to the exit aperture. However, we see that the measurement periods after recovery get smaller. We attribute this to the growing ammonia layer within the cell. Effectively the cell dimensions are reduced due to the growing layer. Therefore, molecules have a higher probability to hit a wall.

After 9 hours of measurement with optimal flux settings of the helium density and an ammonia density of $\sim 1.4 \times 10^{16} \text{ cm}^{-3}$ at the inlet of the cell, we approach the time limit for continuous operation. At this ammonia density we achieve $\sim 50\%$ of the maximum flux (see subsection 4.3.2). Of course, we could run at higher ammonia densities, but at the expense of shorter running times due to faster solid ammonia formation. The initial flux can be fully recovered by warming up the cell to release the frozen molecular gas. Then the system is ready for operation again.

⁸to avoid problems with the charged electrodes of the guide.

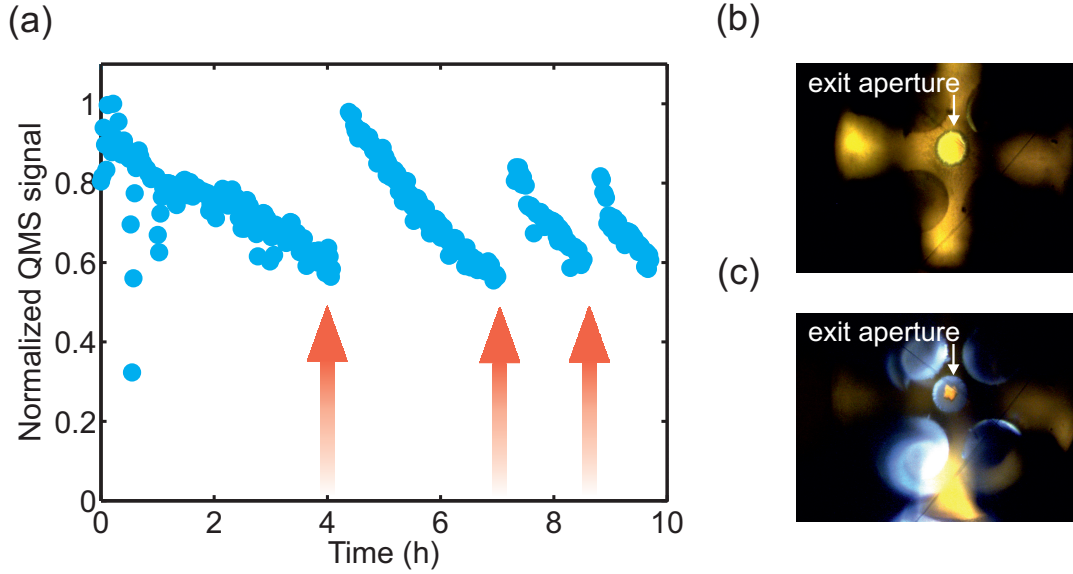


Figure 4.17: (a) ND_3 guiding signal as a function of time showing the decrease in signal due to ice formation for a period of ~ 9 hours and three de-icing heater pulses, indicated by red arrows. Heater pulses of ~ 0.3 W are applied for ~ 1 min. The formation of solid ammonia at the exit aperture is shown in (b) and (c) [Poh07].

4.5 Internal cooling

In this section the cooling of the rotational degrees of freedom is discussed. A signature of cooling is obtained from velocity distributions of buffer gas cooled ammonia (ND_3). With an additional laser setup, allowing for the implementation of depletion spectroscopy for the guided beam, quantitative characterization of the rotational-state population is obtained for formaldehyde (H_2CO), which gives clear evidence of rotational cooling.

4.5.1 Qualitative measurement

Information about the internal cooling of the molecules can be extracted from the velocity distributions for different buffer-gas densities. This is possible because the cut-off velocity in the longitudinal direction (highest velocity that is present in the velocity distribution) depends on the state-dependent Stark shift of the molecules. In a test case measurement we use ND_3 . The Stark shift of ammonia is given in the first order approximation by the formula

$$\Delta W = \left(\left(\frac{W_{\text{inv}}}{2} \right)^2 + \left(\mu |\mathbf{E}|_{\text{max}} \frac{MK}{J(J+1)} \right)^2 \right)^{1/2} - \frac{W_{\text{inv}}}{2} \quad (4.24)$$

Table 4.3: Rotational energies, Stark energies, and longitudinal cut-off velocities for the lowest-lying low-field-seeking rotational states of ND₃ up to $J = 2$. The Stark shifts and the corresponding maximal longitudinal velocities of the rotational states are calculated for an electric field strength of ~ 90 kV/cm. The rotational constants of deuterated ammonia are taken from [Her45].

J	$ K $	$ M $	$E_{\text{rot}}/\text{cm}^{-1}$	Stark energy/ cm^{-1}	$v_{z,\text{max}}^{J,KM}/(\text{m/s})$
1	1	1	8.29	1.13	123
2	1	1	28.85	0.38	71
2	1	2	28.85	0.76	100
2	2	1	22.88	0.76	100
2	2	2	22.88	1.51	142

derived from Eq. 2.64, which is valid for electric fields $|\mathbf{E}|$ in the range 0–100 kV/cm. The dipole moment of deuterated ammonia is $\mu = 1.5$ D, and $W_{\text{inv}} = 0.053 \text{ cm}^{-1}$ is the inversion splitting of ND₃. The Stark shift of the different rotational states is shown in Fig. 2.6. From Eq. 3.8 the state dependent cut-off velocities for the first five guidable states are determined and listed in Tbl. 4.3 for $|\mathbf{E}|_{\text{max}} \sim 90$ kV/cm corresponding to voltages of ± 5 kV applied to the guide electrodes. The cut-off velocity is a marker for the state with the largest Stark shift contributing to the signal of the guided molecules. To obtain information on the cooling process for the internal degrees of freedom, we compare the calculated cut-off velocities from Tbl. 4.3 with measured velocity distributions. Large populations in low-lying rotational states are expected at low temperatures. In particular for ND₃ at ~ 5 K approximately 29% of the molecules leaving the buffer-gas cell are predicted to be in the ($J = 1, MK = -1$) state (see Fig. 4.4). Note that the extracted beam is expected to be pure with 99% of the guided molecules in the lowest guidable state ($J = 1, MK = -1$).

The velocity distributions presented in Fig. 4.18a for a 1 cm long buffer-gas cell show no signature of internal cooling, even for relatively high buffer-gas densities ($n_{\text{He}} = 4.2 \times 10^{15} \text{ cm}^{-3}$) where significant boosting is apparent. No (trace of) a shift of the cut-off velocity of the velocity distribution towards the cut-off velocity of the lowest guidable state ($J = 1, MK = -1$) is visible.

On the other hand, the velocity distributions obtained with a 2 cm long buffer-gas cell show a different behavior. As can be seen from Fig. 4.19, the fraction of the normalized distribution above the cut-off velocity of the lowest-lying guidable rotational state ($J = 1, MK = -1$) is reduced for helium densities above $0.2 \times 10^{15} \text{ cm}^{-3}$. If the helium density is increased above $0.4 \times 10^{15} \text{ cm}^{-3}$ the cut-off velocity does not change any more.

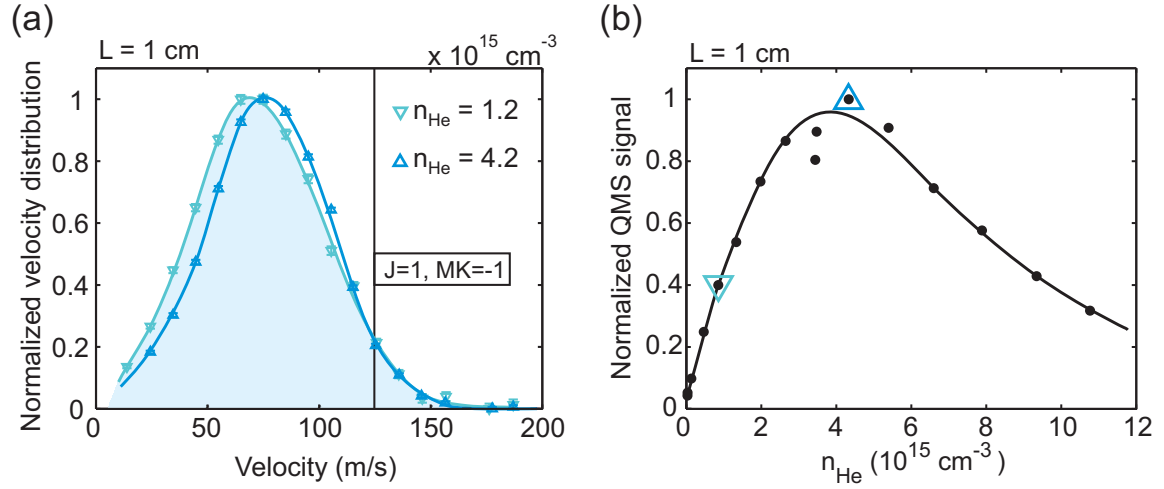


Figure 4.18: In (a) velocity distributions at $n_{\text{He}} = 1.2 \times 10^{15} \text{ cm}^{-3}$ and $n_{\text{He}} = 4.2 \times 10^{15} \text{ cm}^{-3}$ are presented for a 1 cm long cell. The cut off velocity for the lowest guidable rotational state is marked by a straight line. The corresponding helium buffer-gas density scan is shown in (b). Even for a high buffer-gas density of $n_{\text{He}} = 4.2 \times 10^{15} \text{ cm}^{-3}$, at which the maximal flux is obtained, no signature of cooling of the rotational degrees of freedom is observed.

Therefore the conclusion can be drawn that the population of higher rotational states and especially of those with a higher Stark shift than ($J = 1, MK = -1$) is negligibly small in these cases. The velocity distributions presented in Fig. 4.19 indicate that the molecules are rotationally cooled in the buffer-gas environment of a 2 cm long buffer-gas cell.

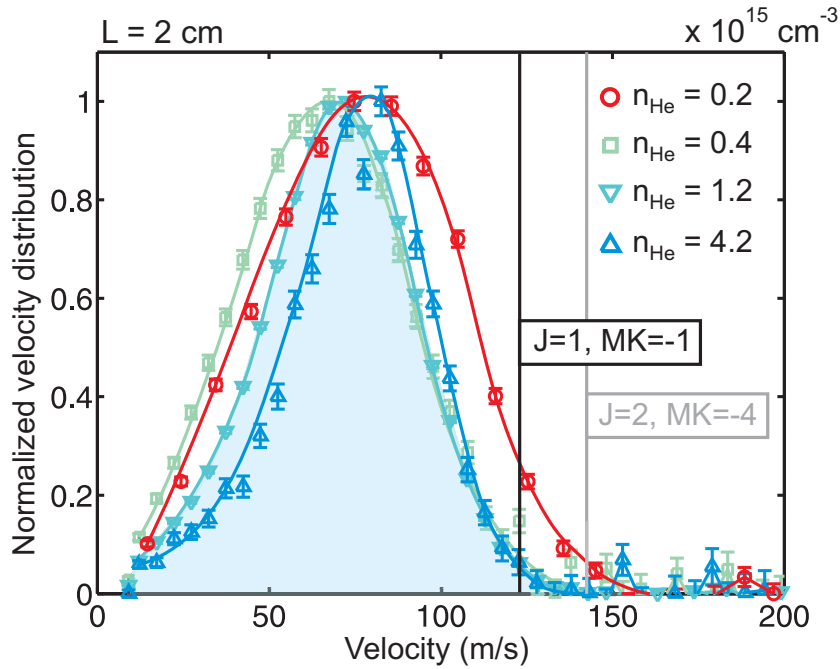


Figure 4.19: Normalized velocity distribution for a 2 cm long buffer-gas cell for different helium densities. The molecular density of ND_3 at the cell entrance is fixed to $\sim 1.4 \times 10^{16} \text{ cm}^{-3}$. The cut-off velocities of the lowest-lying low-field-seeking rotational state ($J = 1, MK = -1$) and of the first higher-lying low-field-seeking state ($J = 2, MK = -4$) are marked by straight lines. The data taken at the lowest buffer-gas density ($0.2 \times 10^{15} \text{ cm}^{-3}$) show contributions of velocities higher than the cut-off velocity of the ($J = 1, MK = -1$) state. This indicates the presence of higher-lying rotational states and, therefore, insufficient rotational cooling. Compared to this, the curve at $0.4 \times 10^{15} \text{ cm}^{-3}$ is shifted to lower velocities, indicating better cooling. The identical high-velocity sides of the largest two densities indicate that the internal state distribution has stabilized. However, the high helium densities above $0.4 \times 10^{15} \text{ cm}^{-3}$ do lead to boosting, the shift of the rising edge to higher velocities. For these high densities, the signals at $v_z < 20 \text{ m/s}$ are not trustworthy due to noise and systematic effects that become dominant in the TOF signals close to the steady-state value. The curves connecting the data points are guides to the eye.

4.5.2 Quantitative measurement by depletion spectroscopy

To quantitatively determine the rotational-state population and thereby the purity of the cold guided beam, individual rotational states have to be resolved. The detection by a quadrupole mass spectrometer is not state selective, since the measured signal is proportional to the sum of the populations of all guided rotational states. To distinguish between individual rotational states, we combine the QMS detection with laser spectroscopy (depletion spectroscopy). Since ND_3 has no easily accessible optical transitions, we performed these measurements with formaldehyde (H_2CO)⁹. Here a UV laser beam (waist 150 – 200 μm) is overlapped with the guided molecular beam (waist $\sim 0.4\text{ mm}$ from simulation) to excite molecules occupying a certain rotational state. The laser beam and the guided molecular beam are overlapped in the straight section before the ionization volume of the QMS. Molecules in a specific rotational state are addressed via the $\tilde{X}^1A_1 \rightarrow \tilde{A}^1A_2$ transition (around 330 nm, see Tbl. 4.5) and excited in the $2_0^14_0^3$ rovibrational band [Mot08].¹⁰ Upon excitation to the \tilde{A}^1A_2 electronic state, the molecules dissociate and are lost from the guide (dissociation efficiency $> 90\%$ [Moo83]). The loss is visible by a drop in the QMS signal, which is proportional to the occupation of the addressed rotational state in the guided beam for sufficient laser power [Mot07].

The laser setup is presented in Fig. 4.20. Tunable UV laser light is produced by second-harmonic generation of the light from a continuous-wave (cw) ring dye laser in an external enhancement cavity (Coherent MBD-200, BBO crystal). This light is narrow band to ensure that only an individual rotational state is addressed. The ring dye laser (Coherent 899, pumped by a Coherent VERDI) is frequency stabilized to a temperature-stabilized reference cavity resulting in a linewidth of $\sim 0.5\text{ MHz}$. The resonance frequency of the enhancement cavity is locked to the frequency of the ring dye laser light by the Hänsch-Couillaud method [Hän80]. To observe and correct shifts in the beam-pointing when the frequency of the UV light is varied, two CCD cameras are used to monitor the beam position. With a telescope of two cylindrical lenses for astigmatism compensation¹¹ and a pinhole for mode cleaning a high-quality Gaussian beam profile is obtained. The UV laser beam is brought to the cryogenic setup via free space. Using two additional CCD cameras for the beam-pointing correction, the laser beam is overlapped with the beam of the guided molecules.

For the measurement the guide is switched to a voltage of $\pm 3\text{ kV}$, which comprises between high flux and small line broadening due to the inhomogeneous electric field in the guide [Mot10, Sch07]. The data shown here are taken at high laser power ($P_{\text{laser}} \sim 100\text{ mW}$) for which the depletion values reach $\sim 99\%$ of the high-power limit, determined by extrapolating the measured power dependence (see Fig. 4.21).

⁹Switching these gases required only minor changes to the gas handling system (see Fig. D.1).

¹⁰The $\tilde{X}^1A_1 \rightarrow \tilde{A}^1A_2$ transition is a symmetry forbidden transition. Due to the transition into the out-of-plane bending mode ν_4 designated by 4_0^3 the symmetry is lifted.

¹¹The UV beam shows a different divergence in the horizontal and vertical direction resulting from the Type II phase matching used in the second harmonic generation.

Table 4.4: $\tilde{X}^1A_1 \rightarrow \tilde{A}^1A_2$ transitions in formaldehyde (H_2CO) that have been used in this work. The table is adapted from [Mot10].

$\tilde{X}^1A_1 \rightarrow \tilde{A}^1A_2$		Frequency (cm^{-1})
$ J'', K''_A, K''_C\rangle \rightarrow J', K'_A, K'_C\rangle$		
$ 1, 1, 0\rangle \rightarrow 2, 2, 1\rangle$		30364.38
$ 2, 1, 1\rangle \rightarrow 3, 2, 2\rangle$		30365.74
$ 2, 2, 0\rangle \rightarrow 3, 3, 1\rangle$		30377.26
$ 3, 3, 0\rangle \rightarrow 4, 4, 1\rangle$		30387.98

The states of H_2CO are labeled by $|J, K_A, K_C\rangle$ according to subsection 2.2.2. Because of varying electric field strength and orientation along the laser beam, all guidable sub-states with different M values contribute to the measured depletion signal. We have simulated the experiments assuming that the molecules are injected into the buffer-gas cell from a thermal ensemble at temperature $T = 295$ K. Nuclear spin statistics and Stark shifts of the rotational states in the guiding fields are included. The Stark shifts are calculated by numerical diagonalization of the asymmetric rotor Hamiltonian in the presence of an electric field (see Fig. 2.7). During the cooling in the inert buffer gas the ortho and para states of H_2CO do not mix as described in C.1.

From simulations at $T = 5$ K, we expect contributions higher than 1% from the $|1, 0, 1\rangle$, $|1, 1, 0\rangle$ and $|2, 1, 1\rangle$ low-field seeking states. These are measured together with the $|2, 2, 0\rangle$ and $|3, 3, 0\rangle$ states, which possess relatively large Stark shifts and which contribute at higher temperatures. For all measured states the depletion signal changes as function of T_{cell} as shown in Fig. 4.22. Highest populations are found for the $|1, 1, 0\rangle$ state. At $T_{\text{cell}} \sim 5$ K no contribution of the $|1, 0, 1\rangle$ state is found. Since this state is expected to have its highest contribution at our minimal T_{cell} due to its low rotational energy of 2.4 cm^{-1} we did not probe it in the other measurements. For the data shown in Fig. 4.22, the pressure in the buffer-gas line measured at room temperature was kept constant at the optimal settings described in subsection 4.4.1, causing variations in n_{He} depending on T_{cell} . Still, the increase of the $|2, 2, 0\rangle$ and $|3, 3, 0\rangle$ data (rotational energies of 40 and 88 cm^{-1} , respectively) and the decrease of the $|1, 1, 0\rangle$ and $|2, 1, 1\rangle$ data (rotational energies of 11 and 16 cm^{-1} , respectively) indicate clearly a dependence of the rotational temperature on the temperature of the buffer gas. From the data we can not conclude whether the molecules completely thermalize inside the buffer-gas cell. Therefore, a further increase of the $|1, 1, 0\rangle$ population might be feasible by increasing n_{He} at minimal T_{cell} , as discussed below.

In Fig. 4.23 depletion measurements as function of n_{He} at $T_{\text{cell}} \sim 5$ K are presented. Again, highest populations are found for the $|1, 1, 0\rangle$. At low densities, the population increases strongly with n_{He} , caused by the onset of rotational cooling of the molecules by collisions with cold helium gas.

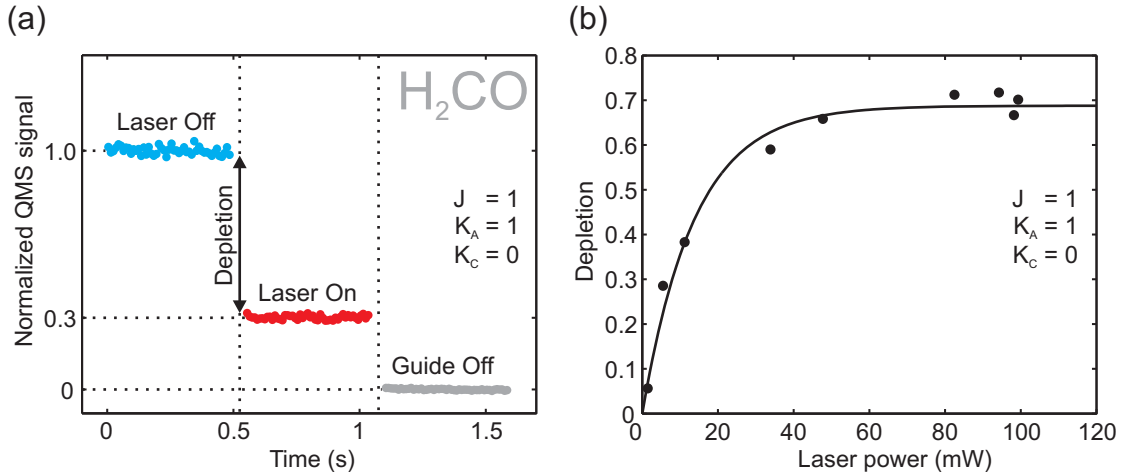


Figure 4.21: In (a) the normalized QMS signal with and without UV-laser light is shown for the $|1, 1, 0\rangle$ state at $T_{\text{cell}} = 5 \text{ K}$, $n_{\text{He}} \sim 2 \times 10^{15} \text{ cm}^{-3}$ and $\pm 3 \text{ kV}$ on the guiding electrodes. The laser frequency is set to the maximum of the transition $|1, 1, 0\rangle \rightarrow |2, 2, 1\rangle$ [Mot07]. A laser power of $P_{\text{laser}} \sim 100 \text{ mW}$ is used to obtain the data. According to the power dependence measurement presented in (b) depletion is close to the high-power limit.

Also a decrease in the relatively high-energetic $|3, 3, 0\rangle$ state is visible. For $n_{\text{He}} \geq 3 \times 10^{15} \text{ cm}^{-3}$ the populations converge to constant values. In this range, the total depletion signal of the addressed states sums up to 80%-90%, illustrating the low number of states in the guided beam. The remaining 10%-20% is attributed to molecular orbits which do not interact with the laser beam and to molecules which do not dissociate, but decay back into guidable states. A similar fraction was found in our previous experiments performed at room temperature [Mot07]. Taking this into account the population in the $|1, 1, 0\rangle$ state of H_2CO is $(82 \pm 10)\%$ for the optimal setting of n_{He} .

A possible explanation for the absence of the $|1, 0, 1\rangle$ state in the beam is given by its relatively low Stark shift. We know from the velocity distributions (see Fig. 4.19) at high n_{He} , that molecules can be accelerated when leaving the cell (see subsection 4.1.3). Therefore, this Stark shift might be too low to keep the molecules guided in the quadrupole bend. At low n_{He} the velocity boost is small, but in this case the data ($n_{\text{He}} \leq 2 \times 10^{15} \text{ cm}^{-3}$ in Fig. 4.23) indicate higher rotational temperatures for which the population in $|1, 0, 1\rangle$ is expected to decrease rapidly.

To understand this behavior we model the guided state distribution for different temperatures. The model includes the boosted guided densities from Eq. 3.14 for the different rotational states, weighted with the state population according to Eq. 3.11, which are summed to the total guided density. The model assumes that the molecules are fully thermalized in the buffer-gas. The rotational-state distribution of formaldehyde at 295 K (see Fig. 4.4) is used to normalize the ortho and para rotational-state distributions at low temperatures. In Fig. 4.24 the results of the an-

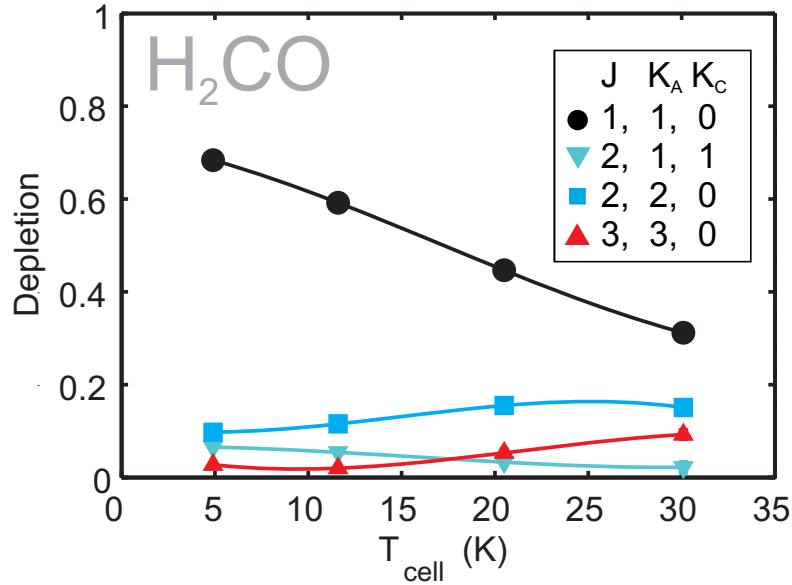


Figure 4.22: Depletion as a function of T_{cell} for different rotational states. The helium density is fixed to $n_{\text{He}} \sim 2 \times 10^{15} \text{ cm}^{-3}$ and $\pm 3 \text{ kV}$ are applied to the guide electrodes. The solid curves are guides to the eye.

alytic model are presented for different buffer-gas temperatures. A boosting factor of $b = 220 \text{ m/s}$ is used in the analytical model. The data shown in Fig. 4.22 are compared with the analytical model. Note that the data points are shifted by $\Delta T = 13 \text{ K}$ and corrected by 10 % upwards to compensate for molecules moving on non addressable molecular orbits. Quite good agreement is found between the model and the temperature-shifted data points. Except for the slight deviation of the data points for the $|3, 3, 0\rangle$, all data points coincide with the calculated lines. Also the absence of the $|1, 0, 1\rangle$ state in the depletion data is reproduced from the temperature shift and the strong boosting. Notwithstanding the good agreement it is not clear whether the buffer gas temperature is slightly higher than the cell temperature or whether the molecules are fully thermalized at a buffer-gas density of $n_{\text{He}} \sim 2 \times 10^{15} \text{ cm}^{-3}$. An explanation for the higher buffer-gas temperature can be given by the temperature gradient that extends from the molecule inlet ($T_{\text{inlet}} = 295 \text{ K}$) to the exit foil of the buffer gas cell. This could result in a higher average temperature, which the molecules experience in the buffer-gas cell. The large heat load from the inlet and the long distance to the cell walls (see section 4.2.2) in the transverse directions could result in a local increase of the buffer gas temperature. This argument is supported also by the fact that the signal of guided molecule increases when the inlet temperature is reduced (see section 4.4.1).

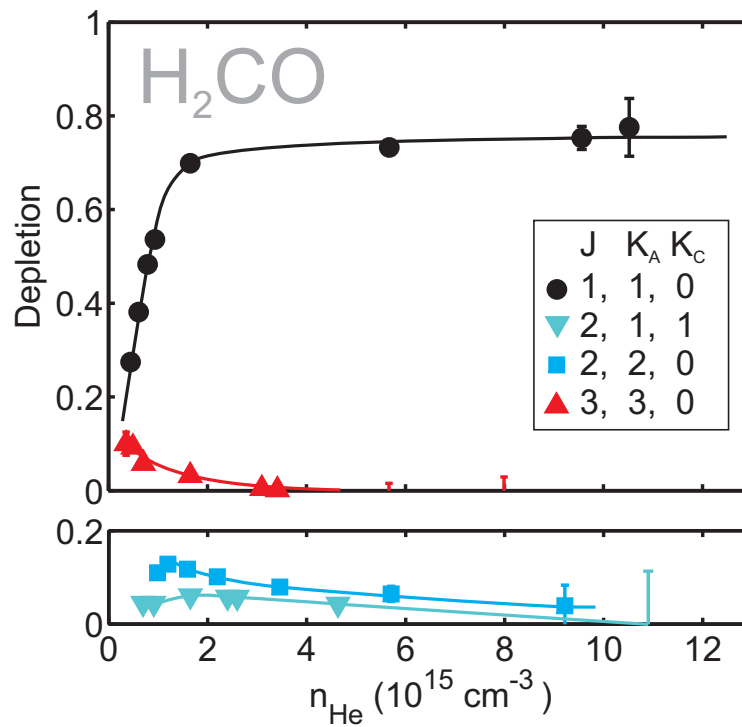


Figure 4.23: Depletion as a function of n_{He} for different rotational states. The large statistical error bars at high n_{He} are caused by the relatively low count rates at these settings. Here the cell temperature is fixed to ~ 5 K and ± 3 kV are applied to the guide electrodes. The solid curves are guides to the eye.

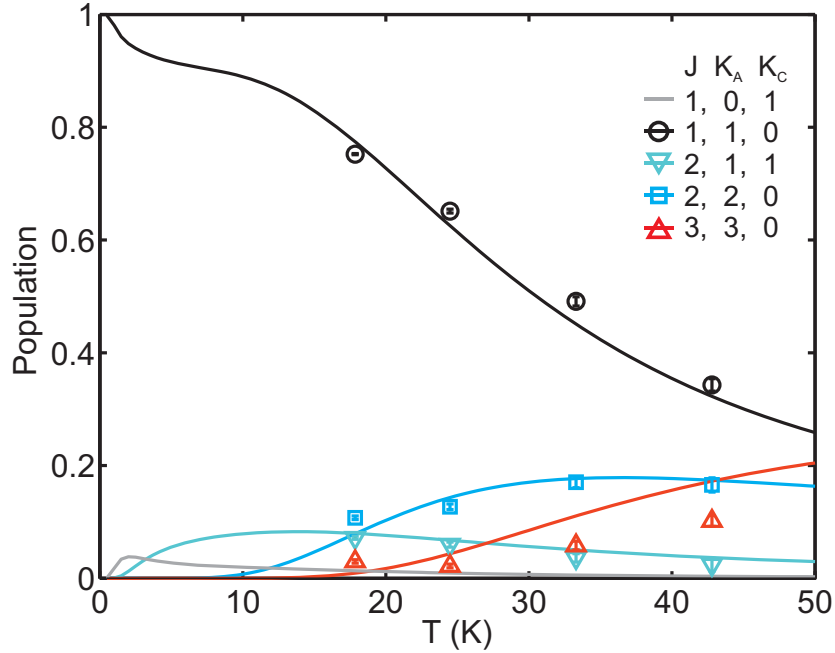


Figure 4.24: The depletion data as a function of T_{cell} , shown in Fig. 4.22, are compared to the values derived from an analytical model of the guided state population (solid lines). Good agreement is found with the analytical model for a uniform temperature shift of the measured data points by 13 K resulting in $T = T_{\text{cell}} + 13$ K. The analytical model uses the boosted velocity distribution ($b = 220$ m/s) of molecules injected into the guide presented in Eq. 3.14 and includes the population of the individual rotational states at a temperature T (see Fig. 4.5) weighted with their respective Stark shifts (see Fig. 2.7). The data points are shifted upwards by 10% to account for non-addressable molecular orbits in the guide. A low contribution of the $|1,0,1\rangle$ state in the guided beam (grey colored line) is predicted by the model. The large guided population of the $|1,1,0\rangle$ state even at very low temperatures results from the fact that the $|1,1,0\rangle$ state is the ortho ground state of formaldehyde.

4.6 Cold beams of different molecular species

Most of our measurements are performed with deuterated ammonia (ND_3) and formaldehyde (H_2CO) because these molecules have been used in our previous room-temperature experiments [Jun04a, Mot07] and because ND_3 has also been employed in buffer-gas cooling experiments [Wil04]. To demonstrate that our cryogenic source is a versatile tool for generating cold molecules, we also investigated the production of cold guided beams consisting of other symmetric top molecules such as trifluoromethane (CF_3H) and fluoromethane (CH_3F). The masses, dipole moments and cut-off velocities of the lowest guidable state ($J = 1, MK = -1$) of these molecules are listed in Tbl. 4.5. Note that we determined the cut-off velocity for CH_3F and CF_3H from

$$v_{z,\text{max}}^{J,KM} = \left[\left(\mu |\mathbf{E}|_{\text{max}} \frac{MK}{J(J+1)} \right) \frac{R}{m_{\text{mol}} r} \right]^{1/2}, \quad (4.25)$$

since they lack inversion splitting. The measurements with CF_3H and CH_3F are performed without any change to the cryogenic source except for the gas handling system. Due to the higher vapor pressure of these molecules, the molecular gas line was heated to only $T \sim 140\text{ K}$ instead of $T \geq 180\text{ K}$ as is necessary for ND_3 . In Fig. 4.25a, buffer-gas scans are presented for the different species. To cool down heavy molecules, more collisions with helium are needed than for light molecules. Therefore the position of the peak of the buffer-gas scan for the heavier CF_3H is shifted to higher n_{He} as compared to the lighter molecules. This is in agreement with the prediction made by Fig. 4.3. The QMS signals obtained for CF_3H and CH_3F are only a factor of two lower than the ND_3 signal. Since we have calibrated the QMS only for ND_3 , we cannot determine absolute numbers for the guided fluxes of the other species. However, we conclude from these high signals that fluxes and densities comparable to those for ND_3 are feasible with this setup, showing the universality of our source. In these measurements we have not compensated for the change in the conductance of the molecular gas line resulting from the different molecular masses and different gas-line temperatures. This change causes the molecular densities in the inlet to vary for the different data sets but we expect no large effects on the results. Note the shift in the peak position of the buffer-gas scan of ND_3 in Fig. 4.25a in comparison to Fig. 4.15. This probably results from a rebuild of the buffer-gas

Table 4.5: Masses, dipole moments and maximal longitudinal velocities evaluated for the ($J = 1, MK = -1$) state of of deuterated ammonia ND_3 , fluoromethane CH_3F , and trifluoromethane CF_3H .

	mass/ amu	dipole moment/ D	$v_{z,\text{max}}^{J,KM} / (\text{m/s})$
ND_3	20	1.5	123
CH_3F	34	1.86	105
CF_3H	70	1.65	69

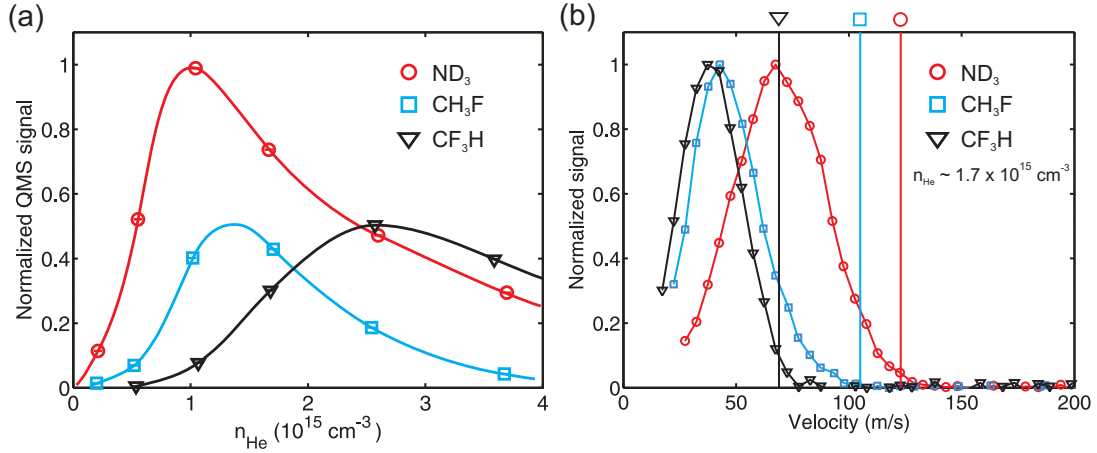


Figure 4.25: (a) Buffer-gas scans for ND_3 , CH_3F and CF_3H , normalized to the peak value of the ND_3 curve. For higher masses the optimal value of the buffer-gas scan is shifted to higher densities since more collisions are needed to slow down the heavier molecules. The curves in (a) are guides to the eye. In (b) the velocity distributions for the three different species at a similar buffer-gas density ($n_{\text{He}} \sim 1.7 \times 10^{15} \text{ cm}^{-3}$) are compared. The cut-off velocities of the distributions are shifted to lower velocities for higher masses. The vertical lines indicate the calculated positions of the cut-off velocities for the $|J = 1, MK = -1\rangle$ low-field-seeking state.

cell between these two measurements. As observed from several rebuilds, the peak position can shift by $\sim (\pm 1) \times 10^{15} \text{ cm}^{-3}$ after such an intervention. Therefore buffer-gas scans are performed after each rebuild of the system to relocate the optimal setting for n_{He} .

The velocity distributions of the three different species are shown in Fig. 4.25b for a fixed helium density of $n_{\text{He}} \sim 1.7 \times 10^{15} \text{ cm}^{-3}$. The vertical lines indicate the cut-off velocities of the lowest guidable state for each molecule. The velocity distributions of both ND_3 and CH_3F converge to zero at the cut-off velocities of the lowest guidable state. This is not the case for CF_3H as discussed below. Since ΔW for states with $J^2 = |MK|$ increases for higher J values for symmetric top molecules in first order according to Eq. 2.59, the CH_3F and ND_3 data indicate that the beams consist mainly of states with $J = 1$.¹² Large populations in higher J states would show higher cut-off velocities due to contributions of states with $J^2 = |MK| > 1$. In other words, Fig. 4.25b shows that the ND_3 and CH_3F molecules are rotationally cooled by collisions with the buffer-gas. We also performed measurements at different buffer-gas densities for CF_3H and CH_3F . Fig. 4.26 shows two velocity distributions for both CH_3F and CF_3H . One distribution is taken at the optimal flux setting of n_{He} and the other for a lower value of n_{He} . The data taken at low n_{He} display a marginally smaller boosting than the data taken at the optimal flux settings for both gases.

¹²For ND_3 Eq. 2.64 is valid.

Although the low n_{He} data of CH_3F exhibit smaller boosting, the data show larger contributions at high velocities. This is explained by population in higher rotational states for which the cut-off velocities are larger than for the ($J = 1, MK = -1$) state.

We have shown in Fig. 4.23 that the internal cooling for H_2CO is already near its maximal value at the optimal flux setting of n_{He} and also the velocity distributions of ND_3 and CH_3F indicate qualitatively that most of the molecules are in the lowest guidable state at this setting. Therefore, we could expect that the CF_3H molecules are rotationally cold at their optimal flux setting of n_{He} as well. However, comparing data taken at different buffer-gas densities does not reveal any effect of internal cooling as shown in Fig. 4.26b. This can be explained by the small rotational constants of CF_3H ($C = 0.19 \text{ cm}^{-1}$ and $B = 0.35 \text{ cm}^{-1}$ [Wen79]), causing population in higher states even at temperatures around 5 K. Since W_{int} (in the first order approximation of Eq. 2.59) converges to $\mu|\mathbf{E}|_{\text{max}}$ for high J states with $J^2 = |MK|$, a distinct shift towards smaller cut-off velocities is only visible between molecules populating mainly $J = 1$ states and molecules populating states with higher J . Therefore, we conclude that although the guided beam of CF_3H is not pure, it is likely to consist of a few states only with low rotational quantum numbers and low rotational energy. To increase the purity even more, one could deplete higher rotational states if light for the transitions is available. This would, however, cause an overall reduction of the flux. A better option would be to reduce the temperatures of the buffer gas even further. For CF_3H , temperatures around 1 K would suffice to increase the purity strongly. The cooling of CaH and CaF molecules in buffer gases with temperatures below 1 K has already been demonstrated [Mau05, Wei98]. In summary, we were able to produce cold guided beams of several different molecular species. Our data suggest that these beams consist of molecules in low rotational states, where the number of populated states depends on the density of rotational states at low temperature.

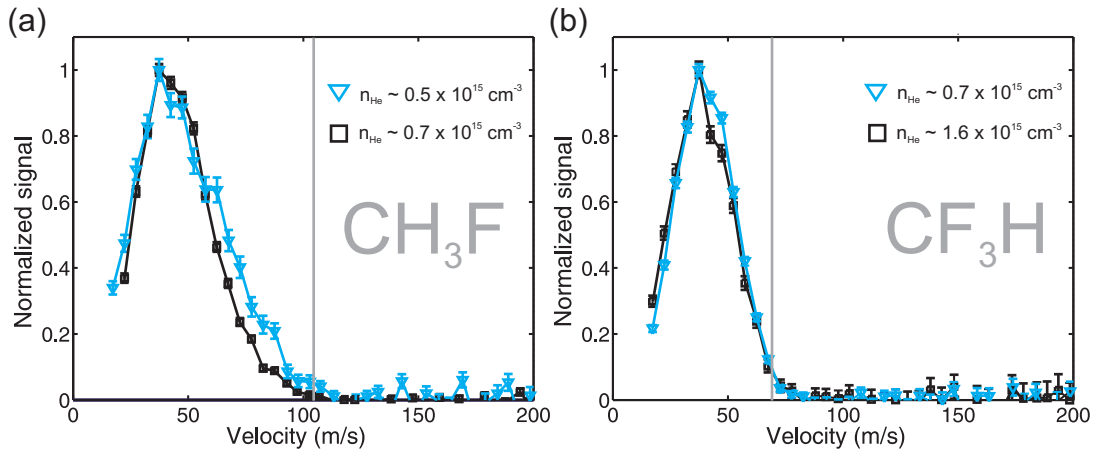


Figure 4.26: Velocity distributions of CH₃F (a) and CF₃H (b), normalized to the maximum value. Helium densities resulting in maximum flux and below the optimal value are used to illustrate the effect of cooling. In the case of CH₃F the data at low $n_{\text{He}} \sim 0.5 \times 10^{15} \text{ cm}^{-3}$ show a negligibly smaller boosting than the data taken at the optimal flux settings of $n_{\text{He}} \sim 0.7 \times 10^{15} \text{ cm}^{-3}$. Even with this smaller boosting, the low n_{He} data show higher contributions at high velocities. This indicates population in higher rotational states for which the cut-off velocities can be higher than for the $J = 1, MK = -1$ state. The vertical lines indicate the calculated positions of the cut-off velocities for the ($J = 1, MK = -1$) low-field-seeking state. A similar behavior is shown for ND₃ in Fig. 4.19. For CF₃H we do not observe any change in the cut-off velocity in the data at different n_{He} , however we observe a very small difference in boosting. This can be explained by the small rotational constants of CF₃H, causing populations in higher states even at temperatures around 5 K.

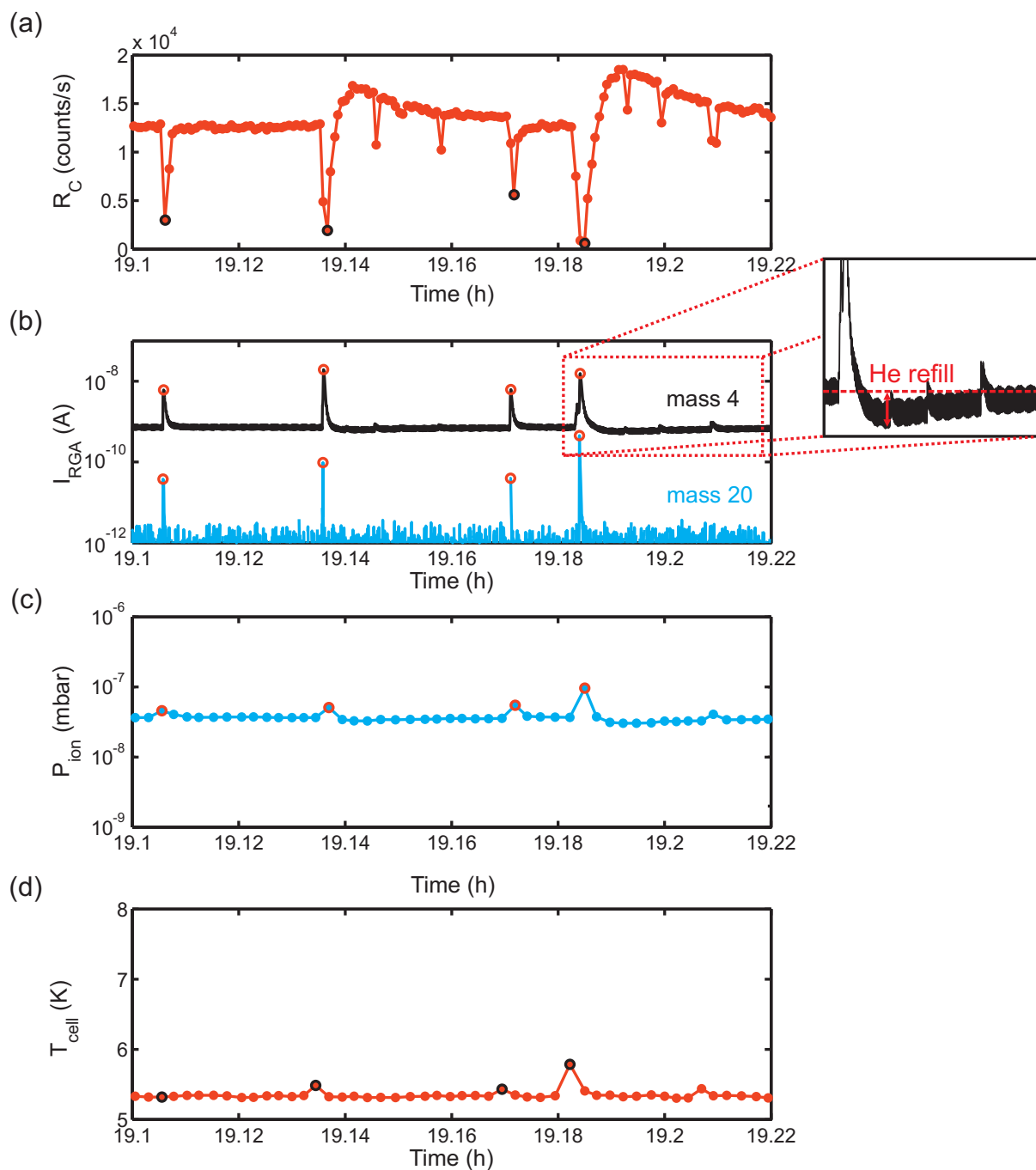


Figure 4.27: Instabilities of the guided signal. The QMS (a), RGA (b), Bayard-Alpert gauge (c) and cell-temperature signal (d) at optimal settings for ND_3 are plotted over a time of 7.2 min. The spikes in the signals from the RGA and the Bayard-Alpert gauge, respectively, and the cell temperature coincide in time with the dips in the QMS signal for the largest instabilities.

4.7 Stability of the cold beam

The measurement presented in Fig. 4.17 shows the signal of the guided molecules over a time period of ~ 9 hours with a time resolution of $\sim 1/2$ minute at optimal settings. The cell temperature is ~ 5 K. If one zooms in and takes a closer look many signal drops become apparent (see Fig. 4.27a). These instabilities of the guided signal are not periodic but appear with large probability after a certain time period (~ 1 min).

To investigate the cause for this behavior the setup has been modified. The mass spectrometer (rest gas analyzer “RGA”) monitoring the presence of residual gases in the vessel is relocated to the flange straight against the exit aperture of the buffer-gas cell. The windows on the two gold coated copper shields, which allowed for direct visual access to the exit aperture, are removed.¹³ Thereby the RGA is facing the exit aperture. Straight flying molecules from the cold source, which are not extracted by the guide can be detected by the RGA. The RGA detects also buffer gas from the cell moving in forward direction as well as residual gases residing in the vessel. Changes in the ion-currents for individual masses give information about both slow and abrupt changes in the vessel. This combined with data from the QMS and the pressure gauges of the vessel allows to fully monitor the output of the buffer-gas cell (see Fig. 4.27).

Different settings have been probed. For these tests we increased the rate at which the data is read out to have better temporal resolution. For example, if helium is applied to the cell without ND_3 , no abrupt changes in the ion current of the RGA or changes in the pressure gauge values as well as in the monitored temperatures are visible. When ND_3 is added to the buffer-gas cell strong fluctuations are detected after a couple of minutes by the various sensors. The RGA and the Bayard-Alpert gauge detect an increase in the ion current (spikes) while the guided signal is reduced at the same time (dips). The temperatures measured on the cell, the exit foil and the charcoal-coated shield increase at such events. On average every minute a small spike is detected. Other gases such as CF_3H , CF_3CCH etc. also show similar behavior.

By resolving the shape of a single spike (or dip) by a higher time resolution in the detection, as it is shown in Fig. 4.27b, it is apparent that a sharp rising edge is followed by a slow decay. This could indicate that a given volume needs to be refilled or pumped down after a sudden change in pressure. In Fig. 4.28a the QMS signal of the guided molecules during such a dip is shown with respect to the ion current of the RGA at the helium mass.¹⁴ The data show exactly the same outline as the buffer-gas scan presented in Fig. 4.15. This behavior can be explained as follows. At the beginning of a dip in the QMS signal (see Fig. 4.27a) the helium gas in the cell is suddenly emptied (burst) leading to a fast increase in the ion current of the helium

¹³The windows were placed in $\varnothing 2.5$ cm and $\varnothing 1$ cm apertures in the inner and outer shield and used to look around and in the cell with a microscope to observe ice formation [Poh07].

¹⁴Fig. 4.28b demonstrates the linear relation between the measured current in the RGA and the observed pressure in the vessel.

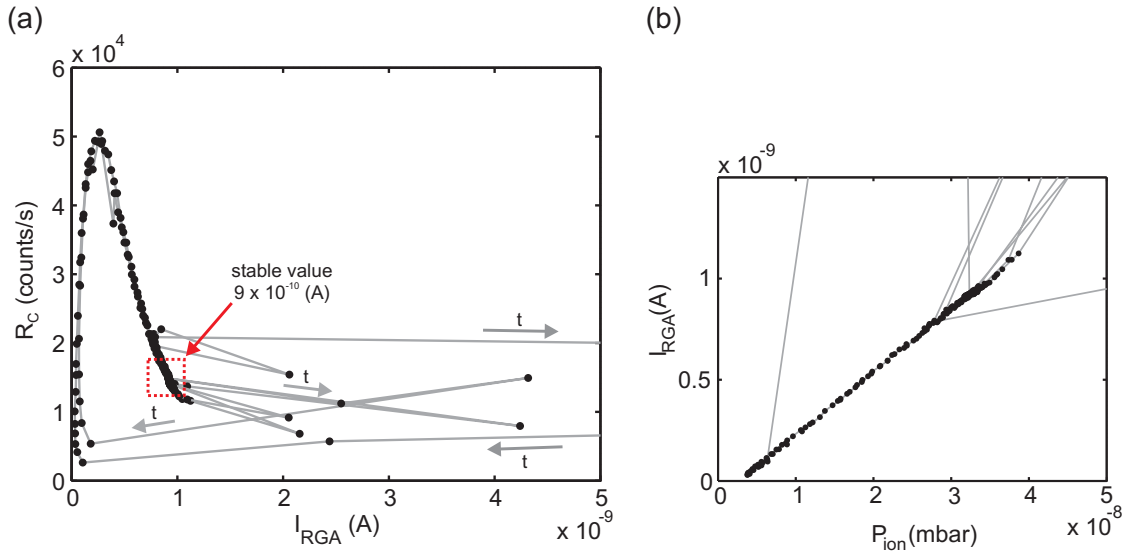


Figure 4.28: In (a) the signal of the guided molecules from the QMS is shown as a function of the RGA signal for mass 4. The same shape as in the buffer-gas scan of Fig. 4.15 is observed. The grey arrows indicate the direction of time in the measurement. In (b) the linear behavior of the RGA signal with respect to the pressure in the vessel detected by an Bayard-Alpert gauge is visualized. This gives the correlation to the helium density in the cell.

mass and a similar increase in the ion current of mass 20 at the RGA (see Fig. 4.27b). The increase in detected mass 20 at the RGA results from ammonia transported by the helium burst and from ammonia which due to the missing helium-buffer gas is not cooled and therefore not guided anymore. After the burst the ion current of helium at the RGA drops quickly to a lower value compared to the stable flow condition. Thereafter the helium density in the cell is slowly restored to its original value. This is isochronous with the reduction of the detected ammonia at the RGA and an increase in the guided signal at the QMS due to increased cooling.

If the cell temperature is increased to a higher temperature the occurrence of instabilities in the guided flux is reduced. At a cell temperature above ~ 12 K a nearly complete removal of the fluctuations is present indicating that a stable signal demands higher cell temperatures (see Fig. 4.29). Unfortunately, this sacrifices internal state purity and flux of guided molecules.

These instabilities have also been observed in other experiments with buffer-gas cooled beams [Pat10]. The current hypothesis to explain for this phenomenon is the following. When icicles of resublimated molecular gas reach the heated inlet they evaporate and create a massive heat load on the system. Due to the sudden increase in pressure the buffer-gas is rapidly released from the cell. This leads to

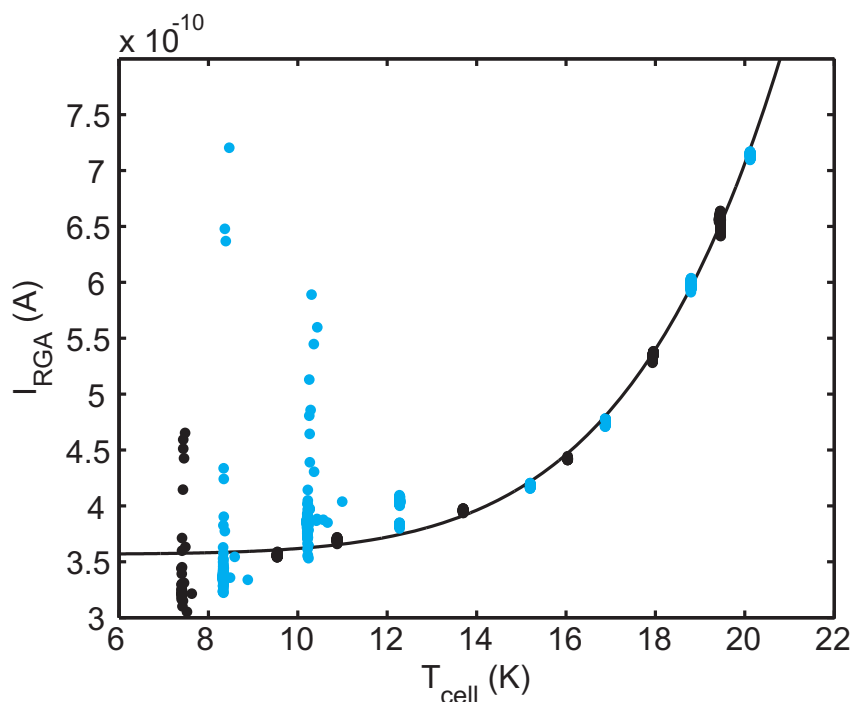


Figure 4.29: Recovery of stable signal by raising the buffer-gas cell temperature. The dots show the variation of the RGA current due to spikes measured for different cell temperatures. The black and blue colors are used to distinguish between different sets of measurements, because the spikes can slightly change the cell temperature.

the behavior that has been described above. This is a plausible explanation but it has not been experimentally confirmed since.

4.8 Applications

Several additional experiments are discussed in this section. For example, the implementation of the velocity-selection scheme presented in chapter 3 is demonstrated for the cold source. The application of the cold source for cold chemistry experiments is exemplified by hydrogen-deuterium exchange reactions for a $\text{NH}_3\text{-ND}_3$ mixture in a helium buffer-gas environment. These measurements emphasize the usability of our source for cold chemistry experiments. Thus the buffer-gas technique can be a feasible alternative to cold chemistry experiments performed with other techniques e.g. CRESU (Cinetique de Reaction en Ecoulement Supersonic Uniforme) technique [Smi06].

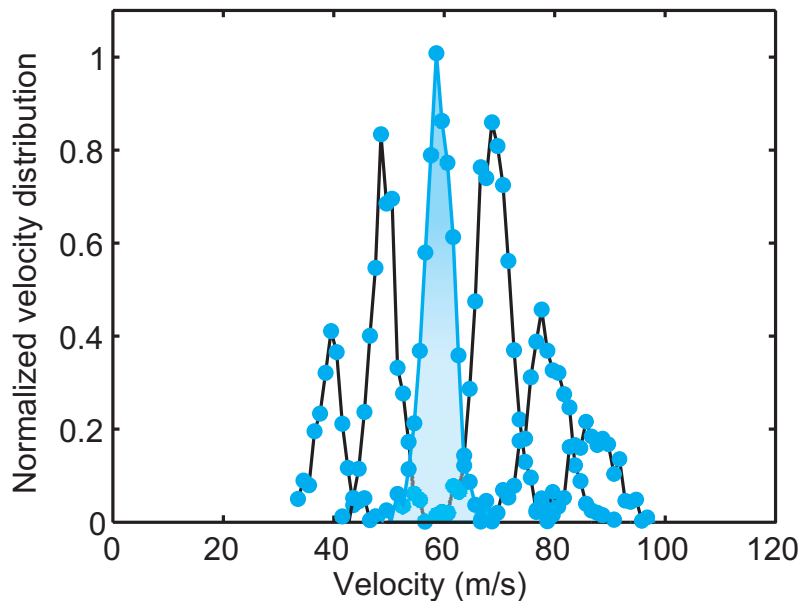


Figure 4.30: Velocity distributions of state- and velocity-selected molecular pulses. The filtering scheme discussed in chapter 3 has been used. In light blue the velocity distribution of the 60 m/s pulse is shown, which concerning the magnitude serves as a reference for the other pulses.

4.8.1 Buffer-gas cooling with Neon

For cell temperatures above 16 K, where a stable flux of guided molecules can be obtained, neon (Ne) can be used as a buffer gas as well. Neon has a larger mass ($m_{\text{Ne}} = 20$ amu) compared to helium and therefore a lower thermal velocity $v_{\text{Ne},16\text{K}} = 115$ m/s. This is even lower than helium at 5 K, $v_{\text{He},5\text{K}} = 144$ m/s. Experiments are undertaken for a cell temperature of $\sim 20 - 25$ K with ND_3 gas. In comparison with data from helium buffer-gas cooling at similar conditions no significant differences are visible in the guided flux and velocity distribution.

4.8.2 Velocity-selected molecular pulses from the cold beam

As it has been shown in the previous sections, molecular beams of high state purity can be obtained by means of buffer-gas cooling. To obtain molecular samples that apart from a high internal state purity show also well defined kinetic properties, we apply the velocity selection method presented in section 3.6.1 to the continuous guided beam of the buffer-gas cooled molecules. The switching times are matched to the guide segments. Always two subsequent measurements are performed. A measurement of a pulse with the selected velocity is followed by a measurement of a reference pulse. The velocity of the reference pulse is given by the average velocity of the continuous guided beam (~ 60 m/s) due to its high contrast. The

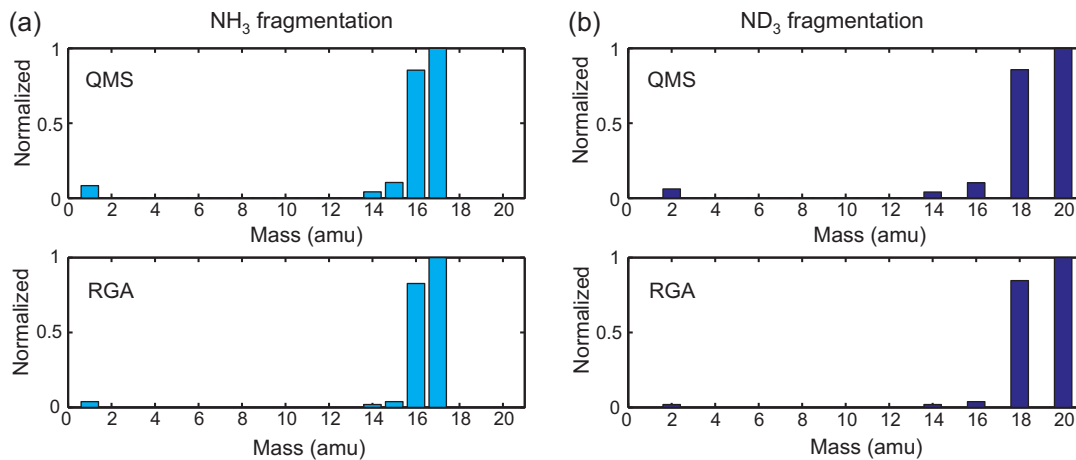


Figure 4.31: Normalized mass spectrum resulting from fragmentation of NH_3 (mass 17)(a) and ND_3 (mass 20) measured with QMS and RGA, respectively.

magnitudes of the reference pulses are compared for the different measurements. This procedure guarantees that the signal is not influenced by changes in the guided flux which can result from resublimation of molecular gas in the cell and the exit aperture as discussed in subsection 4.4.2, or signal instabilities as discussed in section 4.7. The reference is used to rescale the magnitudes of different velocity selection measurements. A joint velocity distribution composed of individual velocity-selected molecular pulses at different velocities is obtained (see Fig. 4.30).

4.8.3 Reactions at low temperatures

In this section we investigate the applicability of our cryogenic system for cold chemistry experiments. In a test case experiment with NH_3 and ND_3 we attempt to witness hydrogen-deuterium exchange reactions in a helium buffer-gas environment around ~ 18 K in our setup. Measurements at room temperature with and without buffer gas are used as a reference to determine changes in the distributions of the reactants. To perform these measurements the setup has been modified. An additional entrance capillary for hot molecules is installed. It is displaced from the first input capillary to make sure that the different species only interact with each other within the buffer-gas cell. One of the threaded holes on the side of the extension frame is used for the input (see Fig. 4.11). The second molecular input capillary is made similar to the buffer-gas capillary. It has an inner diameter of $\varnothing 1$ mm and can be attached to the cold plates of the cryo cooler by small copper blocks.¹⁵ However this is not done in these experiments to prevent resublimation of the molecular gases inside the line. A small stainless needle of $\varnothing 0.2$ mm is attached to the end part of the capillary. The needle is loosely covered with Kapton foil and inserted in the side

¹⁵Therefore, it can be used as a secondary buffer-gas line.

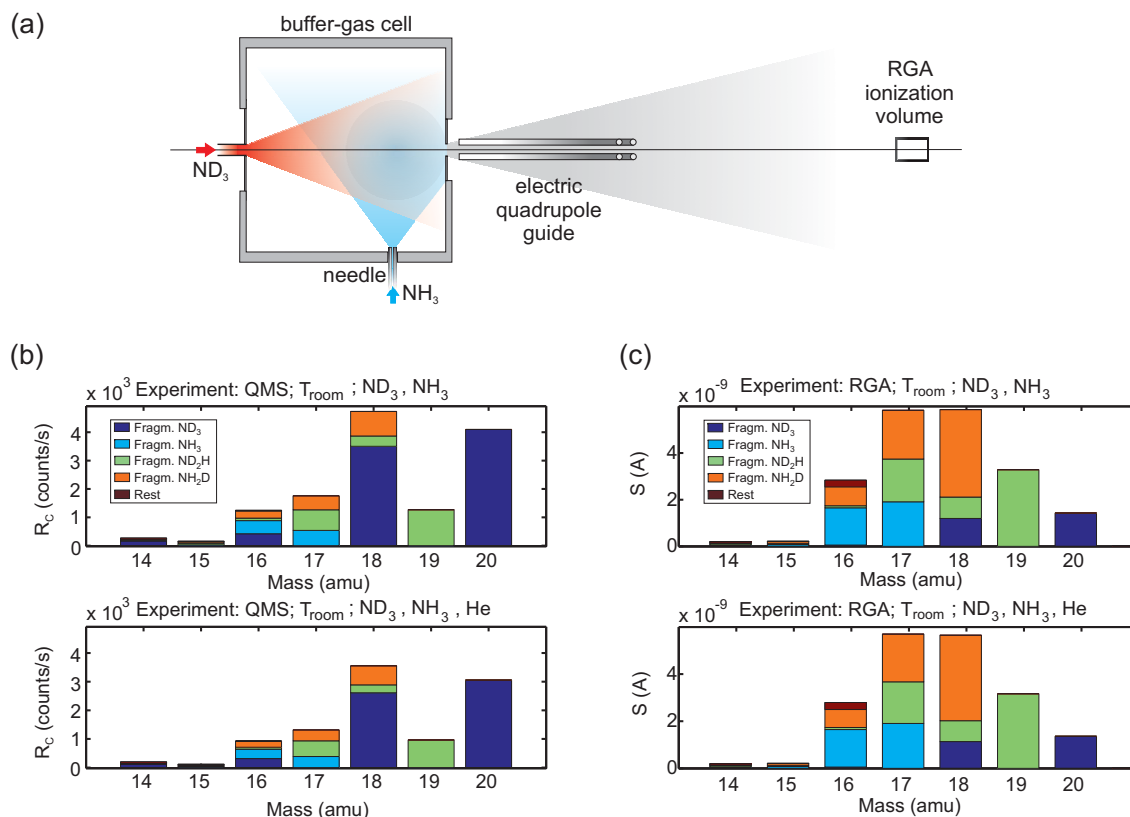


Figure 4.32: Hydrogen-deuterium exchange reaction for ND_3 and NH_3 , with and without helium gas. In (a) a sketch of the modified setup is shown. In both measurements an entrance density of $n_{\text{NH}_3, \text{ND}_3} \sim 2 \times 10^{14} \text{ cm}^{-3}$ for NH_3 and ND_3 is used. In (b) the QMS fragmentation data of the mixture measurements at room temperature are presented. The lower plot shows an experiment where warm helium buffer gas was added ($n_{\text{He}} \sim 1 \times 10^{14} \text{ cm}^{-3}$). In (c) the detection results by the RGA for the unguided molecules is presented. The RGA signal is recorded simultaneously with the QMS signal.

aperture of the extension frame of the buffer-gas cell. The Kapton guarantees that the thermal connection between the needle and the copper frame of the buffer-gas cell is marginal. To avoid cold spots heater wires are wrapped around the capillary at several positions. The heater wires are covered with Stycast to improve the thermal contact with the supply line. The heater close to the needle is used to set the temperature of the molecules before they are injected into the buffer gas. The temperature of the line is monitored with PT-100 resistance thermometers. The two mass spectrometers are used to detect the contribution of the different species. The detection with the QMS can resolve smaller abundances than the RGA due to the lower background in the QMS detection chamber and the higher detection efficiency. On the other hand, this signal is convoluted with the guiding efficiency of the contributing species.

Table 4.6: Fragmentation distribution of the different species. The factors f_i ($i \in \{1, 2, 3\}$) are obtained from the signal of the ND_3 and NH_3 fragments in Fig. 4.31, normalized to the non-fragmented contribution, where i hydrogen or deuterium atoms are removed. Since ND_3 and NH_3 have similar fragmentation rates the factors f_i are used for both species.

mass	NH_3	ND_3	NH_2D	ND_2H
20	0	1	0	0
19	0	0	0	1
18	0	f_1	1	$f_1/3$
17	1	0	$2f_1/3$	$2f_1/3$
16	f_1	f_2	$f_1/3 + f_2/3$	$2f_2/3$
15	f_2	0	$2f_2/3$	$f_2/3$
14	f_3	f_3	f_3	f_3

At first, measurements are performed at room temperature without buffer gas to observe the background contribution at different masses. Note that background subtraction is included in the QMS signal for guided species due to the detection sequence with high voltage on and off (see section 4.2.5). These are followed by separate measurements of the individual species without helium buffer gas. The two mass spectrometers monitor the masses of the respective species. Also different masses than the actual mass of ND_3 or NH_3 have to be observed. The detection of the mass spectrometer by electron impact ionization can lead to fragmentation of the detected molecule. Hence all fragmentation mass channels must be monitored (see Fig. 4.31). This is necessary to distinguish in upcoming experiments between species originating from exchange reactions appearing at a certain mass channel and species appearing at the same mass channel but descending simply from fragmentation of the input molecules. Therefore, the fragmentation distributions from the QMS and RGA for NH_3 (see Fig. 4.31a) and ND_3 (see Fig. 4.31b) respectively are later used to extract the contributions from the reactants and their fragments. From these measurements we confirmed that the loss of one hydrogen or deuterium atom is equal in a fragmentation process. This is also valid for the loss of two or three atoms. We use the observed fragmentation rates to extract the fragmentation fractions of ND_2H and NH_2D , respectively (see Tbl. 4.6).

The mixture experiments presented in Fig. 4.32 where both ND_3 and NH_3 are introduced into the buffer-gas cell via the two molecule injection lines are performed at room temperature for similar densities of ND_3 and NH_3 ($n_{\text{NH}_3, \text{ND}_3} \sim 2 \times 10^{14} \text{ cm}^{-3}$) without helium buffer gas and with helium buffer-gas ($n_{\text{He}} \sim 1 \times 10^{14} \text{ cm}^{-3}$). For these different experiments the contributions of the reactants ND_2H and NH_2D are extracted. Especially the contribution of the mass of ND_2H (mass 19) is easily obtained because its mass does not coincide with the masses from the fragments of ND_3 . To obtain the contributions of other reactions, we need to subtract contribu-

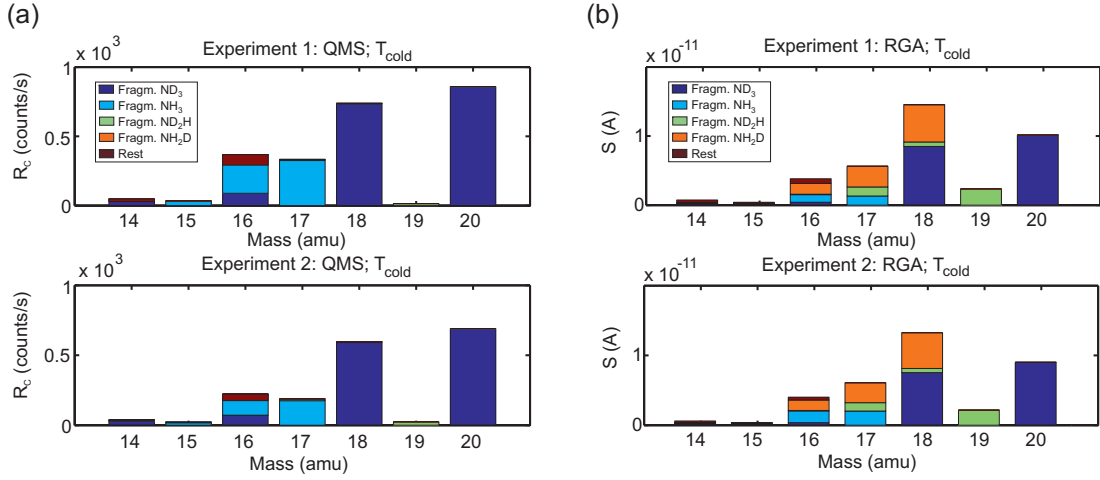


Figure 4.33: Hydrogen-deuterium exchange reaction for ND_3 and NH_3 at $T_{\text{cell}} \sim 18 \text{ K}$. The QMS data, shown in (a), consists mainly of the fragments of the injected species. Therefore, there is no evidence for reactions at low temperatures. The RGA signal shown in (b), does however provide information that reactions have occurred. For example see mass 19. The upper plots show measurements with a helium buffer-gas density $n_{\text{He}} \sim 4 \times 10^{14} \text{ cm}^{-3}$. The lower plots show measurements where the same conditions are applied except that more helium buffer gas is added ($n_{\text{He}} \sim 1 \times 10^{15} \text{ cm}^{-3}$). The RGA signal is recorded simultaneously with the QMS signal.

tions of fragments from the observed signal. For example the contribution $S_{\text{NH}_2\text{D}}$ of NH_2D at mass 18 is estimated by

$$S_{\text{NH}_2\text{D}} = S_{18} - S_{\text{ND}_3}f_1 - S_{\text{ND}_2\text{H}}\frac{f_1}{3}, \quad (4.26)$$

where S_{18} is the observed signal at mass 18, S_{ND_3} is the signal of ND_3 at mass 20 and $S_{\text{ND}_2\text{H}}$ is the signal of ND_2H at mass 19 (see Tbl. 4.6).

In Fig. 4.32 the measurements with and without helium buffer gas are compared. The only significant difference is seen in the height of the contributions from the guided beam measured by the QMS. When helium buffer gas is applied the contributions are reduced equally for all the different masses. This is due to the increased boosting. The relative amount of reactants remains the same.

The same measurements are repeated at low temperature ($T_{\text{cell}} \sim 18 \text{ K}$) including helium buffer gas. The results are shown in Fig. 4.33. Much higher NH_3 and ND_3 entrance densities ($n_{\text{NH}_3, \text{ND}_3} \sim 1 \times 10^{15} \text{ cm}^{-3}$) are applied to the system due to the fact that most of the molecules are pumped by the walls (and just a few find their way to the exit). Also the buffer-gas density is increased to guarantee sufficient cooling. Here, basically no guided reactants are detected by the QMS (see Fig. 4.33a). In the RGA signal however relatively large contributions from reactants are observed (see Fig. 4.33b). This indicates that it is much more difficult to guide the reaction

products. The measurements are performed for low ($n_{\text{He}} \sim 4 \times 10^{14} \text{ cm}^{-3}$) and high ($n_{\text{He}} \sim 1 \times 10^{15} \text{ cm}^{-3}$) buffer-gas densities. This is done to verify that the reactions happened at low temperatures. As expected (with respect to the results shown in Fig. 4.19), the data in Fig. 4.33b show no significant difference for these two density settings.

A direct comparison between the data obtained at room temperature (see Fig. 4.32) and the data acquired at 18 K (see Fig. 4.33) is hampered by various reasons. Those descend primarily from differences in the experimental conditions, which are difficult to quantify and control. For instance, one has to take into consideration the differences in the ratios of ND^3 and NH^3 as well as the large difference in the number of reactive collisions in case of the room temperature and the cold regime, respectively. Those differences stem from the different pumping of the cell walls at the two temperature regimes.

The measurements demonstrate that it is possible in principle to perform cold chemistry experiments in a cryogenic buffer-gas cell. Still, our measurements require improvements for detection and control. Especially, low temperatures are expected, but it is not absolutely clear at what temperatures the reactions happened. In a more sophisticated setup which enables precise temperature measurements and state-selective detection in the buffer-gas cell [Wei98, Sko10], more quantitative results could be obtained.

4.9 Operation of the cryogenic source in the hydrodynamic regime

The measurements presented so far are all carried out with low buffer-gas densities. The buffer-gas density is optimized for minimal boosting and sufficient cooling to obtain large samples of slow and internally cold polar molecules. This is motivated by the applicability of our setup as a cold molecule source in further experiments. For example experiments investigating cold collision [Saw10] or experiments employing sympathetic and optical cooling schemes [Bar09, Zep09], where long interaction times and spatial addressability of the molecules are required. These needs can be met by a trap which confines molecules in three dimensions. Since electric traps are limited to trap depth of $\sim 1 \text{ K}$ (see section 3.1 or [Rie05]) only molecules from a source with corresponding low velocities can be trapped.

On the other hand, the fluxes and densities in the guided beam obtained from buffer-gas cooling in the diffusion regime are limited. The limitations are conditioned by the geometric probability for a molecule to find the exit aperture of the buffer-gas cell and the probability for a subsequent acceptance by the quadrupole guide. These limitations are overridden when working in the hydrodynamic regime. In the latter the probability for a molecule to leave the buffer-gas cell can be brought to nearly unity. Also, more molecules exit the cell in the forward direction because of the boosted velocity distribution [Max05, Pat07].

In this section results of measurements that show the performance of our source in the strongly boosted hydrodynamic regime are presented. For detection we use the RGA mounted to the vessel (see section 4.7) and the pressure gauges. The QMS only detects guided molecules at low buffer-gas densities since the guide has a bend radius of 2.5 cm and cannot extract molecules from a strongly boosted beam.

The measurements are done with ND_3 and CF_3H in helium and neon buffer gas, respectively.¹⁶ Except for the higher temperature of the neon buffer gas which results in a lower guided flux and a broader rotational state distribution, it provides several advantages over helium in our setup. The major improvement is given by the reduced background-gas density at high buffer-gas flows, which results from the improved pumping efficiency of the cold surfaces including the charcoal. In contrast to helium, neon gas resublimates on the ~ 5 K shields due to its higher resublimation temperature. It allows for higher heat loads on the shields and thereby guarantees that larger buffer-gas densities can be applied to the system before the absorbed gas gets released. Also, the thermal velocity of neon at 20 K ($v_{\text{Ne}} = 129$ m/s) is slightly lower than the thermal velocity of helium at 5 K ($v_{\text{He}} = 144$ m/s) as stated in subsection 4.8.1.

In Fig. 4.34 a buffer-gas scan of ND_3 with helium densities reaching up to 10^{17} cm^{-3} is presented. Here both the QMS and the RGA are used as detectors. The QMS data are represented by the black data points in Fig. 4.34 and show the buffer-gas scan region where electric guiding is still efficient. The signal of the RGA drops after helium buffer-gas is applied but strongly increases for densities above 10^{16} cm^{-3} . The drop of the signal at the beginning is explained by the increased cooling due to helium-buffer-gas in the cell. Without helium buffer-gas the molecules are not cooled and most of them can escape the guiding fields. Also, due to the higher velocity of the warm molecular beam ($v_{\text{ND}_3} \rightarrow v_{\text{He}}$) more molecules reach the RGA by free rectilinear flight. Applying buffer gas diffuses the molecular beam inside the cell and reduces the average velocity of the molecules. The strong signal increase for densities above 10^{16} cm^{-3} cannot be explained by boosting alone, which contributes to the gain only by a more forward directed beam. Because of the higher transfer efficiency of molecules from the inlet to the exit in the hydrodynamic regime (see section 4.1.3) a larger signal is achieved.

¹⁶We choose CF_3H instead of ND_3 for Ne-buffer gas since deuterated ammonia and neon possess the same mass and cannot be differentiated in a mass spectrometer.

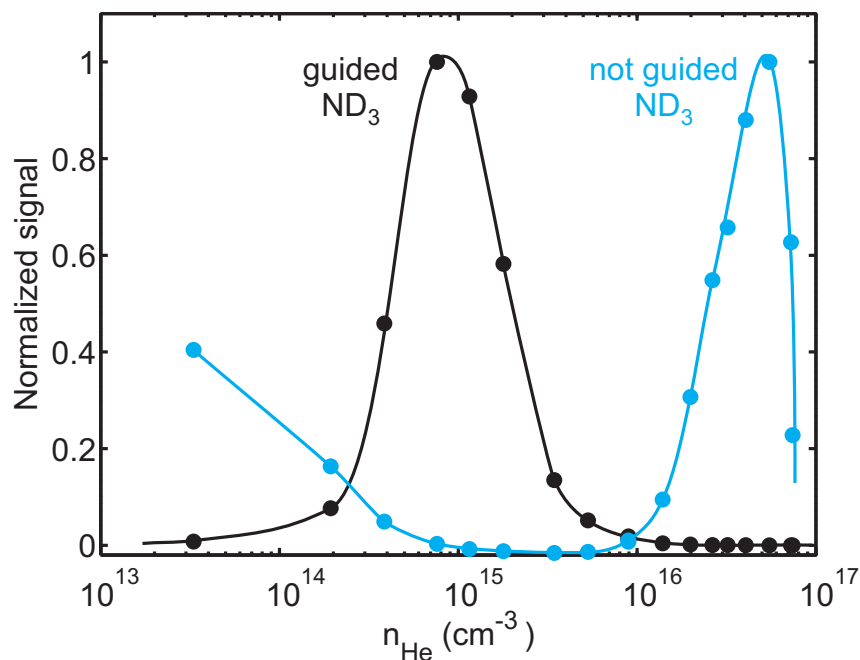


Figure 4.34: Hydrodynamic enhancement. The blue (black) points show the average magnitude of the signal obtained with the RGA (QMS). The black data points describe a typical buffer-gas scan (see Fig. 4.15), where no signal is observed for high buffer-gas densities because of boosting. The blue data points show a signal drop in the diffusive regime ($n_{\text{He}} < 10^{16} \text{ cm}^{-3}$) where molecules are extracted by the guide. This is followed by a strong increase in signal in the hydrodynamic regime. We attribute the second drop to ice formation on the guide electrodes, blocking the path to the RGA. The data show an increase by a factor of two in the hydrodynamic regime, compared to the case without buffer gas (see first blue dot on the left). Much higher values (up to two orders of magnitude) can be obtained. The gain is only limited by scattering with background gas at high densities and the heat load on the cryogenic system. The temperature of the cell is $\sim 7 \text{ K}$. The solid lines are guides to the eye. Note that both curves have been individually normalized.

4.10 Summary

In this chapter a newly developed source for cold polar molecules has been presented. In the source a continuous beam of polar molecules is cooled in of a cryogenic buffer gas, after which it is delivered into a separate ultrahigh vacuum chamber by means of an electric quadrupole guide. The source can operate for many hours with fluxes up to $(7 \pm 4) \times 10^{10} \text{ s}^{-1}$ and peak densities of $(1.0 \pm_{0.6}^{1.0}) \times 10^9 \text{ cm}^{-3}$ for ammonia (ND_3) inside the quadrupole guide. The internal temperature of the molecules is reduced by collisions with the helium buffer gas. This results in a strong increase of the state purity in the guided beam, which is shown for formaldehyde (H_2CO) by depletion spectroscopy measurements of the guided molecules. at optimal settings a state purity of $\sim 80\%$ is obtained. Signatures of internal cooling are obtained as well from the velocity distributions of ND_3 taken at different buffer-gas densities. The characteristics of the source are examined with respect to variations in the molecular density, helium buffer-gas density and cell length. From these studies, optimized settings for the system are found to produce maximal fluxes. By comparing the cooling and guiding characteristics for four different species, we have shown that our source is applicable to a wide variety of molecular gases.

Also, we have demonstrated that sophisticated experiments can be performed with our setup. For example, we have observed hydrogen-deuterium exchange reactions in buffer gas cooled NH_3 , ND_3 mixtures. Also hydrodynamic enhancement is witnessed by applying high buffer-gas densities to the cell [Max05, Pat07].

With the current setup further experiments can be carried out. For example, molecules in the ro-vibrational ground state (high-field-seeking states) could be guided by applying alternating electric fields to the guide [Jun04b]. The laser depletion technique itself could be used as a tool for further purification of the guided beam. The extracted beam can be employed to load electric traps [Rie05] in which collisions and chemistry at low temperatures can be observed. Slow molecules from the same or different species could be brought into collision under controlled conditions [Wil08a]. Because of the high purity of our beam, these processes can be investigated in a state-selective manner. Our source can also be employed to improve the resolution in high-precision experiments [Hud02, Kaw04].

Chapter 5

Outlook

In this thesis we have demonstrated that the method of electric guiding and velocity filtering of polar molecules can be combined with buffer-gas cooling. In this way not only the slowest molecules are filtered out of a molecular source (see chapter 3) but also the number of populated internal states is strongly reduced (see chapter 4). We have also shown that the method of electric guiding can be extended towards the production of mono-energetic molecular pulses (see chapter 3). This allows for a wider variety of applications, as outlined in the respective chapters.

Despite these new developments some issues still remain. The main shortcomings of the technique and the existing experimental setup, are addressed in the following. Possible solutions to these limitations as well as new concepts are also highlighted.

To obtain molecular samples with well-defined velocity by means of velocity selection our source must operate in a pulse mode. As a result a large number of molecules from the continuous beam, having the desired properties, are inevitably sacrificed, and thus the out-coming flux is largely reduced. Additionally, the dispersion of the molecules in the electric guide results in pulses which are spatially and temporally broadened along the guiding direction. The broadening increases proportionally to the length of the guide segment remaining after the pulse generation process. This leads to a reduction in density. The reduction can be minimized by producing the molecular pulse as close as possible to the end of the guide. In this way a high density for subsequent applications is retained. Nevertheless, no active way for preserving the size of the molecular package along the guiding direction and thereby maintaining the phase space density of the sample is present in the current setup. Since the longitudinal velocity distribution is narrow one could in principle use a buncher as in a Stark decelerator [Cro02], to obtain longitudinal focussing.

An adverse effect accompanying the formation of cold molecular beams from a buffer-gas source is the large boosting caused by the buffer gas emerging through the aperture of the cell. Therefore cold molecules with kinetic energies below a typical trap depth are hardly available. The problem could be solved by a new deceleration scheme for continuous guided beams, which is currently under development in our group. The deceleration scheme is designed to slow down the velocity boosted

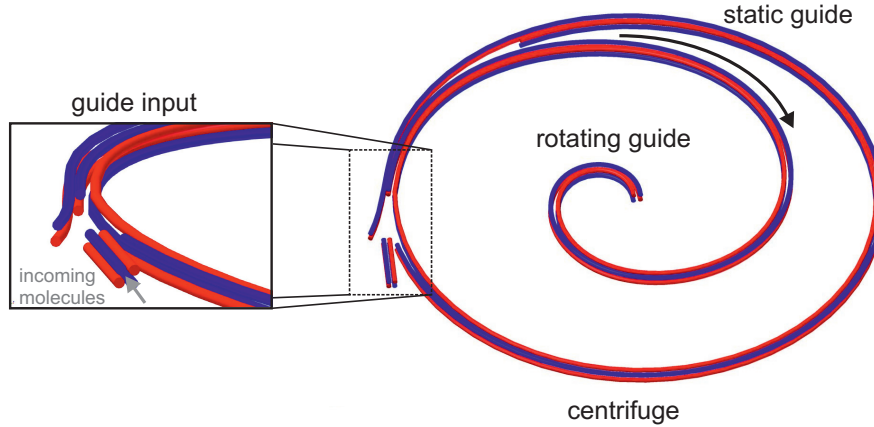


Figure 5.1: Centrifuge decelerator for continuous guided beams of cold polar molecules. The molecules are guided from the periphery to the center of the rotating spiral shaped electric guide, where their kinetic energy is transformed into centrifugal potential energy.

molecular beam from the cryogenic source by employing the centrifugal potential in a rotating frame (see Fig. 5.1). The concept is to electrically guide the molecules from the periphery to the center of the rotation along a spiral trajectory, thus transforming their initial kinetic energy into centrifugal potential energy. Only molecules within a certain velocity range are decelerated towards the end of the guide. The rotational speed of the centrifuge decelerator is tunable, which enables it to operate in a wide range of input velocities. By varying the rotational speed of the centrifuge one can transfer different ranges of input velocities into a certain range of output velocities determined by the particular purposes.

This setup can be employed after the buffer-gas source to obtain a source that delivers a (quasi)-continuous beam of slow and internally cold polar molecules, where the molecules possess velocities that can be confined in an electric three dimensional trap. The highest yield is expected to be obtained with our cryogenic source operated in the hydrodynamic regime (see chapter 4). In this mode reasonably high buffer-gas flows are used to efficiently transfer the molecules through the buffer-gas cell. The molecules undergo large boosting in this regime, but by tuning the rotation frequency of the centrifuge to the maximum of the velocity distribution of the output beam from the cryogenic source in the hydrodynamic regime, high fluxes of slow and internally cold molecules could be obtained. These molecules can be loaded into electric traps, where further experiments ranging from controlled collision experiments [Kre08] to novel cooling schemes [Zep09] can be realized.

Appendix A

Theoretical aspects of polar molecules in a quadrupole guide

In this appendix we investigate models and analytical solutions for the motion of polar molecules in an electric quadrupole guide.

A.1 Electric guiding potential

The electric fields that are used to confine the moving molecules by altering their trajectories result from a scalar potential [Jac99]. Here the Laplace equation is valid, which constrains the possible solutions,

$$\Delta\phi(\mathbf{x}) = 0 \quad \forall \mathbf{x} \in \mathbb{R}^3. \quad (\text{A.1})$$

Due to symmetry, the coordinate parallel to the guide axis can be omitted. This results in the Laplace equation in two dimensions. Solutions of the Laplace equation in two dimensions can be found by mapping \mathbb{R}^2 to the complex numbers \mathbb{C} by $(x, y) \mapsto z = x + iy = \rho \exp(i\varphi)$. Due to the connection of harmonic and holomorphic functions by the Cauchy-Riemann equations for complex differentiability [Jae04], general solutions are formed by expansions

$$\phi = \sum_{n=0}^{\infty} \phi_n = \sum_{n=0}^{\infty} a_n z^n. \quad (\text{A.2})$$

Polynomial solutions are derived from the elements of the expansion and presented in Tbl. A.1:

$$\phi_n = \begin{cases} a_n \operatorname{Re}(z^n) & : \quad \rho^n \cos(n\varphi) \\ a_n \operatorname{Im}(z^n) & : \quad \rho^n \sin(n\varphi) \end{cases} \quad (\text{A.3})$$

From the equipotential lines of these solutions the geometric form and the spatial arrangement of the electrodes to create a suitable trapping potential can be determined.

Table A.1: Polynomial solutions of the Laplace equation.

	cartesian	cylindrical
0 order	1	1
1 st order	x, y	$\rho \cos(\varphi + \varphi_1)$
2 nd order	$xy, x^2 - y^2$	$\rho^2 \cos(2\varphi + \varphi_2)$
3 rd order	$xy^2 - \frac{1}{3}x^3, x^2y - \frac{1}{3}y^3$	$\rho^3 \cos(3\varphi + \varphi_3)$
4 th order	$x^3y - xy^3, x^2y^2 - \frac{1}{6}(x^4 + y^4)$	$\rho^4 \cos(4\varphi + \varphi_4)$
⋮		

The potential resulting from the Stark shift depends on the absolute value of the electric field. Therefore superpositions of the polynomial solutions of the Laplace equation of the form

$$|\mathbf{E}|(\mathbf{x}) = \left(\sum_{n,m} a_n a_m \nabla \phi_n(\mathbf{x}) \cdot \nabla \phi_m(\mathbf{x}) \right)^{1/2} \quad (\text{A.4})$$

are used to generate the guiding potential. Here, n, m are polynomial orders. In our case we restrict ourselves to the case of the second order potential, which leads to a quadrupole potential as shown in Eq. 3.6. It gives a good approximation of the electric field in the guide presented in Fig. 3.1.

A.2 Molecular trajectories in a quadrupole guide

The potential of our electric guide is well approximated by a quadrupole potential (see Fig. 3.1). By using Eq. A.4 up to the second order scalar potential in Tbl. A.1, the electric potential is obtained. The equations of motion for the guided molecules can be derived from the Hamiltonian

$$H_T = \frac{\mathbf{p}^2}{2m} + V(\mathbf{x}) = \frac{\mathbf{p}^2}{2m} - \mathbf{d} \cdot \mathbf{E}(\mathbf{x}). \quad (\text{A.5})$$

For molecules in low-field-seeking states the Hamiltonian takes the form

$$H_{T,n} = \frac{\mathbf{p}^2}{2m} + \mu_n^{eff} (|\mathbf{E}|(\mathbf{x}))^n \quad n \in \{1, 2\}. \quad (\text{A.6})$$

Here $|\mathbf{E}|(\mathbf{x}) = A\sqrt{x^2 + y^2}$ is the electric field for the quadrupole configuration. μ_n^{eff} represents the effective dipole moment for a dominantly linear Stark shift ($n = 1$) and the effective linear polarizability for a dominantly quadratic Stark shift ($n = 2$). Due to the rotational symmetry along the z -axis it is convenient to use cylindrical

coordinates $\{x = \rho \cos(\phi), y = \rho \sin(\phi), z = z\}$. Therefore the Hamiltonian takes the form

$$H_{T,n}^c = \frac{p_\rho^2 + p_z^2}{2m} + \frac{p_\phi^2}{2m\rho^2} + \mu_n^{eff} A^n \rho^n \quad n \in \{1, 2\}. \quad (\text{A.7})$$

This leads to the equations of motion

$$\dot{p}_\rho = -\mu_n^{eff} A^n \rho^{n-1} + \frac{p_\phi^2}{m\rho^3}, \quad \dot{\phi} = \frac{p_\phi}{m\rho^2}, \quad \dot{z} = \frac{p_z}{m}, \quad (\text{A.8})$$

where $p_\phi = L = \text{const}$ denotes the conserved angular momentum of a molecular trajectory in the guide. $p_z = \text{const}$ implies free motion in the direction perpendicular to the confinement, which leads to energy conservation for the motion perpendicular to the z-axis

$$W_\perp = \frac{m\dot{\rho}^2}{2} + \frac{L^2}{2m\rho^2} + \mu_n^{eff} A^n \rho^n. \quad (\text{A.9})$$

general solutions are given by

$$t = m \int \frac{\rho d\rho}{\sqrt{2m(W_\perp \rho^2 - \mu_n^{eff} A^n \rho^{n+2}) - L^2}} + t_0 \quad (\text{A.10})$$

$$\phi = L \int \frac{d\rho}{\rho \sqrt{2m(W_\perp \rho^2 - \mu_n^{eff} A^n \rho^{n+2}) - L^2}} + \phi_0. \quad (\text{A.11})$$

For quadratic Stark shifts ($n = 2$), general analytic solutions in Cartesian coordinates are given by

$$x(t) = C_x \cos(\omega t + \varphi_x) \quad , \quad y(t) = C_y \cos(\omega t + \varphi_y). \quad (\text{A.12})$$

The solutions can be parameterized by the transverse energy W_\perp and the angular momentum L . The amplitudes can be defined by $C_x = m\omega\rho_{\min}/L$ and $C_y = m\omega\rho_{\max}/L$, where

$$\rho_{max,min} = \frac{\sqrt{2mW_\perp \pm \sqrt{(2mW_\perp)^2 - 8m\mu_2^{eff} A^2 L^2}}}{2\sqrt{m\mu_2^{eff} A^2}}. \quad (\text{A.13})$$

The phases are fixed by the relation

$$\varphi_x - \varphi_y = \arcsin\left(\frac{L}{m\omega C_x C_y}\right). \quad (\text{A.14})$$

For molecules in a certain low-field-seeking state the oscillation frequency $\omega = \sqrt{2\mu_2^{eff} A^2/m}$ is the same for all the different forms of trajectories in the transverse directions, which range from radial oscillations via ellipses to circular trajectories.

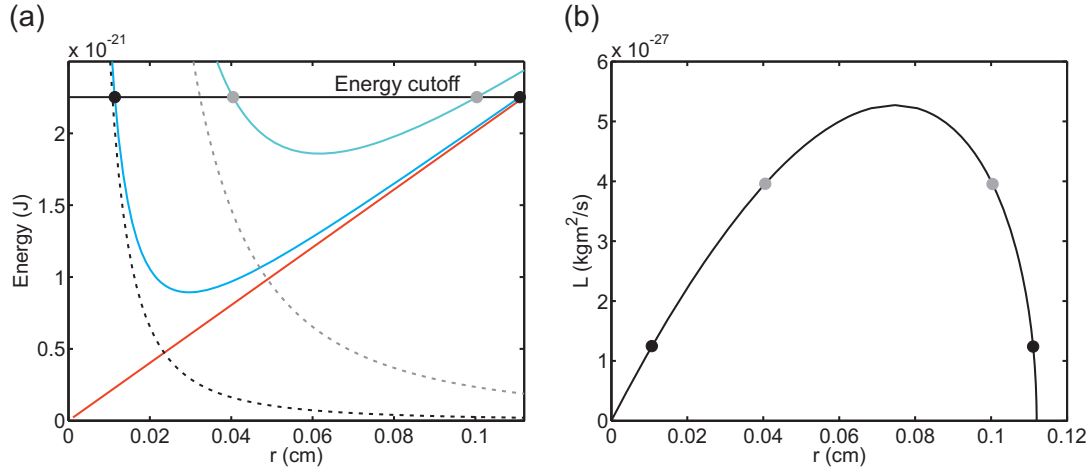


Figure A.1: In (a) guiding potentials described by Eq. A.7 in cylindrical coordinates in case of a linear Stark shift (Stark shift of ND_3) are presented for two different values of the orbital angular momentum of the guided molecule trajectories. The dashed curves show the centrifugal potential, respectively. The minimal and maximal radii (see Eq. A.18 and Eq. A.19) that the trajectories can reach for a fixed energy are shown in (a) by the black and grey dots and are plotted in (b) for all orbital angular momenta.

For linear Stark shifts analytic solutions cannot be found except for radial oscillations or circular trajectories, which have a closed orbit. Radial oscillations for a definite transversal energy W_\perp are given by parabolas

$$\rho(t) = -\frac{\mu_1^{eff} A}{2m} t^2 + \sqrt{\frac{2W_\perp}{m}} t. \quad (\text{A.15})$$

The oscillation frequency is given by $f_\rho(W_\perp) = 1/T = \mu_1^{eff} A / \sqrt{32W_\perp m}$ where T is defined as the oscillation period which depends on the transverse energy. The axial motion for circular orbits is described by

$$\varphi(t) = \left(\frac{(\mu_1^{eff} A)^2}{mL} \right)^{1/3} t + \varphi_0. \quad (\text{A.16})$$

Here, the oscillation frequencies differ for the different forms of trajectories. For example the radial solution of Eq. A.15 has different oscillation frequencies for different energies W_\perp , while the solutions for the circular motion presented in Eq. A.16 show different oscillation frequencies for different angular momenta. In contrast to molecular states experiencing a quadratic Stark effect, the coherence of the molecule trajectories for states experiencing a linear Stark effect is easily lost in an electric quadrupole potential.

Analytic solutions for more general trajectories cannot be found. However, the radial range of a trajectory in the guiding potential can be obtained. From the

condition $\dot{\rho} = 0$, the minimal (ρ_{\min}) and maximal (ρ_{\max}) radius of a trajectory can be acquired, which included in Eq. A.9 results in the third order equation

$$\rho^3 - \frac{W_{\perp}}{\mu_1^{\text{eff}} A} \rho^2 + \frac{L^2}{2m\mu_1^{\text{eff}} A} = 0. \quad (\text{A.17})$$

With $a = W_{\perp}/\mu_1^{\text{eff}} A$ and $b = L^2/2m\mu_1^{\text{eff}} A$ the solutions with $\rho > 0$ are formed by

$$\rho_1 = -\frac{(1 + i\sqrt{3})(3\sqrt{3}\sqrt{27b^2 - 4a^3b} + 2a^3 - 27b)^{1/3}}{6(2)^{1/3}} - \frac{(1 - i\sqrt{3})a^2}{3(2)^{2/3}(3\sqrt{3}\sqrt{27b^2 - 4a^3b} + 2a^3 - 27b)^{1/3}} + \frac{a}{3} \quad (\text{A.18})$$

$$\rho_2 = \frac{(3\sqrt{3}\sqrt{27b^2 - 4a^3b} + 2a^3 - 27b)^{1/3}}{3(2)^{1/3}} + \frac{(2)^{1/3}a^2}{3(3\sqrt{3}\sqrt{27b^2 - 4a^3b} + 2a^3 - 27b)^{1/3}} + \frac{a}{3}, \quad (\text{A.19})$$

which are both real for $b \leq 4a^3/27$.

With $b = 4a^3/27$ the radii for the axial trajectories Eq. A.16 in the guide can be derived for a given angular momentum and are expressed by

$$\rho_{\text{axial}} = \frac{2}{3(2)^{1/3}} \left(\frac{27L^2}{4m\mu_1^{\text{eff}} A} \right)^{1/3}. \quad (\text{A.20})$$

A.3 Distributions of guided molecules for quadrupole boundary conditions

The guided molecules in our experiment originate from a thermal or quasi-thermal reservoir. Molecules can move into the guiding potential through a nozzle or a small aperture close to the guiding electrodes. Since we work at low pressures close to the effusive regime, the thermal distribution of the molecules before entering the guide can be described by the Maxwell-Boltzmann velocity distribution

$$f_{\mathbf{v}} dv_{x,y,z} = \frac{1}{\pi^{3/2}\alpha^3} \exp\left(-\frac{(v_x^2 + v_y^2 + v_z^2)}{\alpha^2}\right) dv_{x,y,z}. \quad (\text{A.21})$$

The distribution is given in Cartesian coordinates and $\alpha = \sqrt{2k_B T/m}$ is the most probable velocity. The selectivity of the guiding field is based on the Stark shifts of the individual rotational states. This leads to a change of the internal state population from a free thermal gas to a guided beam. For the external degrees of freedom of a molecules, the thermal statistics are not influenced. Therefore the spatial and

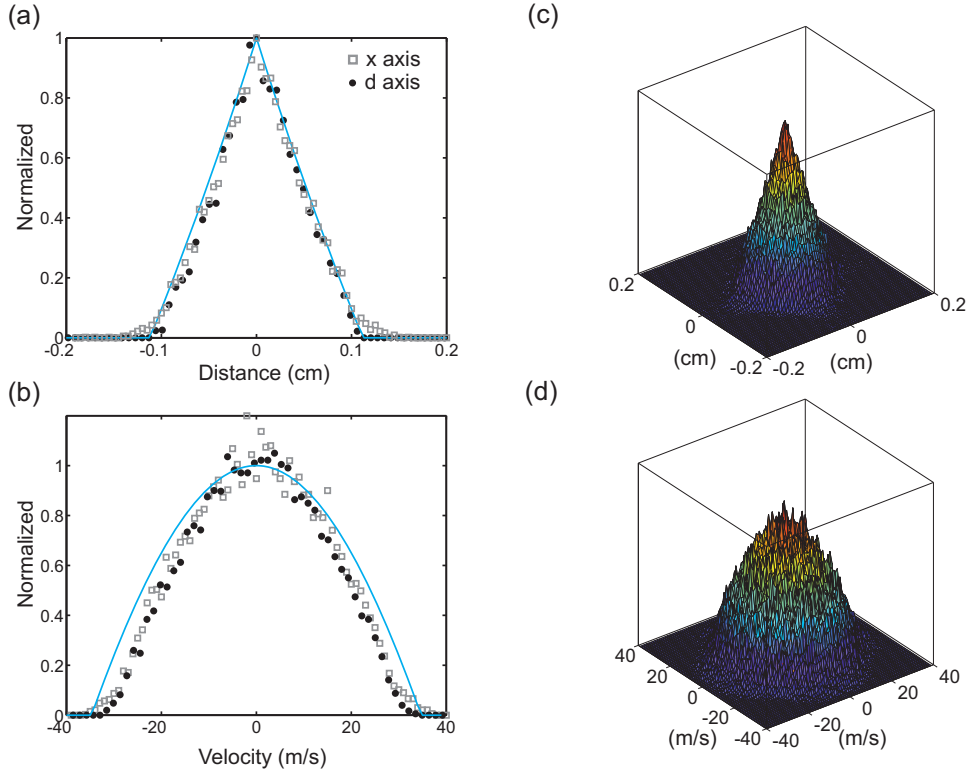


Figure A.2: In (a) the spatial distribution in the guide for $n = 1, (J = 1, KM = -1)$ at $T = 5$ K is shown. The data are obtained from computer Monte Carlo simulations and plotted for the diagonal d-and x axis. The same is done for the guided transverse velocity distribution in (b). The data are compared to the model described in the text. In (c) and (d) the full 3-dimensional plots of the guided distributions for the spatial and velocity degrees of freedom are presented. The small deviations result from the non perfect quadrupole field that is generated by the four electrode rods (see Fig. 3.1).

momentum distributions of the guided molecules in a quadrupole guiding potential can be described by a thermal gas experiencing quadrupole-potential boundary conditions.

In the presence of these boundary conditions the spatial distribution as well as the momentum distribution for guided molecules in the transverse directions to the guide axis are approximated by

$$f^{2D} = \frac{1}{Z^{2D}} \int_{D_\sigma} d\sigma \exp(-\beta H) \quad (\text{A.22})$$

$$H(x, y, p_x, p_y) = \left(\frac{p_x^2 + p_y^2}{2m} + \mu_n^{eff} A^n (\sqrt{x^2 + y^2})^n \right). \quad (\text{A.23})$$

Here n gives the order of the Stark shift and D_σ describes the integration areas for these two cases. They are defined as

$$D_{p_x, p_y} = \left\{ p_x, p_y \in \mathbb{R}^2 : p_x^2 + p_y^2 \leq 2m(W_{max} - \mu_n^{eff} A^n (\sqrt{x^2 + y^2})^n) \right\} \quad (\text{A.24})$$

$$D_{x, y} = \left\{ x, y \in \mathbb{R}^2 : (\sqrt{x^2 + y^2})^n \leq \frac{(2mW_{max} - p_x^2 - p_y^2)}{2m\mu_n^{eff} A^n} \right\}. \quad (\text{A.25})$$

For the spatial distribution of the molecules in the guide we derive from Eq. A.22 and Eq. A.24

$$f_{x, y}^{2D} = C_n (\exp(-\beta\mu_n^{eff} A^n (\sqrt{x^2 + y^2})^n) - \exp(-\beta W_{max})), \quad (\text{A.26})$$

where C_n is a normalization constant. The momentum distribution for molecules experiencing a linear Stark shift is given by

$$f_{p_x, p_y}^{2D} = B_1 \left(e^{-\beta((p_x^2 + p_y^2)/2m)} - \left[1 - \beta \left(W_{max} - \frac{(p_x^2 + p_y^2)}{2m} \right) \right] e^{-\beta W_{max}} \right). \quad (\text{A.27})$$

For a quadratic Stark shift the momentum distribution is given by

$$f_{p_x, p_y}^{2D} = B_2 \left(e^{-\beta((p_x^2 + p_y^2)/2m)} - e^{-\beta W_{max}} \right). \quad (\text{A.28})$$

In the case of $n = 1$, i.e, linear Stark shift, the trajectories of the particles are distributed chaotically in the range of movement. The only parameters of a trajectory that are conserved in the guide are the total energy and the total angular momentum with respect to the guide axis. In the case of a thermal gas of molecules in a single low-field-seeking rotational state confined by quadrupole-potential boundary conditions, the angular momentum distribution in the guide can be derived from Eq. A.22 in cylindrical coordinates.¹ With the boundary condition

$$D_{p_\rho} = \left\{ p_\rho \in \mathbb{R} : p_\rho^2 \leq 2m(W_{max} - \frac{L^2}{2m\rho^2} - \mu_1^{eff} A\rho) \right\} \quad (\text{A.29})$$

we obtain from Eq. A.22 the joined angular momentum-radial distribution

$$f_{\rho, L}^{2D} = B_3 \left(\text{erf} \left(\sqrt{\beta \left(W_{max} - \frac{L^2}{2m\rho^2} - \mu_1^{eff} A\rho \right)} \right) e^{-\beta(L^2/2m\rho^2 + \mu_1^{eff} A\rho)} \right). \quad (\text{A.30})$$

Here the equipotential lines of this distribution are given by the solutions (Eq. A.18) of Eq. A.17 with L varied for a fixed W_{max} .

¹the phase-space volume element obeys the relation $dx dy dp_x dp_y = d\rho d\phi dp_\rho dL$

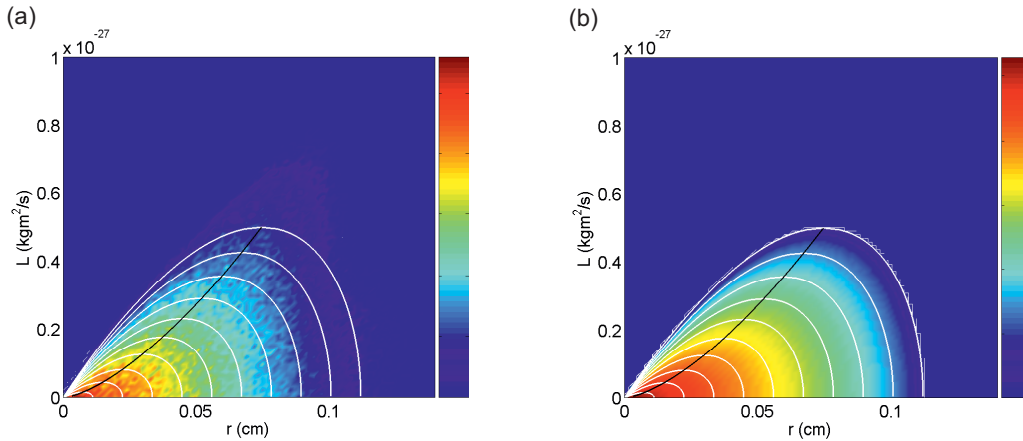


Figure A.3: The distribution in (a) obtained from a Monte Carlo simulation and (b) derived from Eq. A.30 show the population in the guide as a function of the orbital angular momentum and the radial position in the guide in the case of linear Stark shift. The simulation and calculation parameters have been fixed to ND_3 in the lowest guidable state at a temperature of $T = 5$ K. The white lines show the minimal and maximal radii according to Eq. A.18, which are defined by the orbital angular momentum L and the trap depth W_{max} . To obtain the curves the trap depth is varied from 0 to W_{max} in $W_{max}/10$ steps, where W_{max} is the trap depth that has been used in the Monte Carlo simulation (corresponding to ± 5 kV on the electrodes). The curves form the equipotential lines of the distributions. The black line represents Eq. A.20 and shows the orbital angular momenta and radial positions of the axial trajectories. The simulation deviates from the analytic model at large radii and large orbital angular momenta, due to deviations in the guiding potential (see Fig. 3.1) from a quadrupole potential (see Eq. 3.6) at large radii.

Appendix B

Nuclear spin statistics

In this appendix the effects of molecular symmetry on molecular states are discussed. The spin states of the nuclei have to be considered to obtain the eigenstates of the Hamiltonian, which are also eigenstates of the symmetry operations. As an example, the construction of the eigenstates of a symmetric top molecule with a threefold axis of symmetry (C_{3v} or D_{3h} symmetry group) and of an asymmetric top molecule with a two-fold axis of symmetry (C_{2v} symmetry group) are described. Examples for these classes of molecules are ND_3 (NH_3) and H_2CO , respectively.

B.1 Symmetric top with a threefold axis of symmetry

To describe the action of symmetry operations it is necessary to define a coordinate system. Here (X, Y, Z) is used for the space-fixed coordinates while (x, y, z) defines the molecule-fixed coordinates. We consider three identical nuclei A_1 , A_2 and A_3 in the plane perpendicular to the axis of symmetry. The nuclei are ordered in a way that the right-hand rule defines the positive direction of the z -axis, which is along the axis of symmetry. The first nucleus A_1 is positioned on the x -axis [Gre80, Tow75]. In the case where the molecule experiences vibrational-inversion motion, we use the h coordinate along the z -axis to describe the motion. The rotational motion is described by the Euler angles (θ, ϕ, χ) which rotate the space-fixed coordinates (X, Y, Z) with respect to the molecule-fixed coordinates (x, y, z) . The Euler angles are visualized in Fig. 2.1.

Rotations of $2\pi/3$ about the symmetry axis, the interchange of two nuclei of the set $\{A_1, A_2, A_3\}$ and the space inversion operation E^* transforming (x, y, z) to $(-x, -y, -z)$ leave the molecular Hamiltonian unchanged. Therefore, the eigenstates should respond in the same way or change sign.

The effect of the space inversion on the symmetric top eigenstates $|JKM\rangle$ is given by

$$E^*|JKM\rangle = e^{iK\pi}|JKM\rangle = (-1)^K|JKM\rangle. \quad (\text{B.1})$$

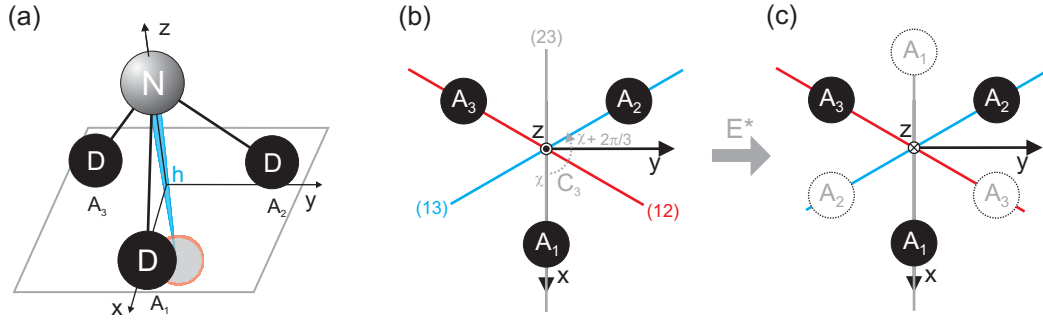


Figure B.1: The vibrational inversion motion is sketched in (a) in the case of ammonia (ND_3). In (b) the operations C_3 , (23), (12), and (13) are illustrated. The action of the space inversion operation E^* can be derived from (b) and (c). The transformations of the Euler angles for these symmetry operations can be obtained from Fig. 2.1, respectively.

This relation can be justified in the following way. Due to the space inversion the Euler angles θ and ϕ remain unchanged while $\chi \rightarrow \chi + \pi$. The result in Eq. B.1 can be derived from the rotation eigenfunctions $\psi_{JKM} = e^{iM\phi} e^{iK\chi} \Theta_{JKM}(\theta)$ of the symmetric top eigenstates $|JKM\rangle$ [Kro75].

The effect of the interchange of nuclei described by the permutation operators (12), (13), and (23) can be described in the following way [Gre80, Bun06]. For the operation (23), for example, the Euler angles are changed by $\theta \rightarrow \pi - \theta$, $\phi \rightarrow \pi + \phi$ and $\chi \rightarrow \pi - \chi$. With $\Theta_{JKM}(\pi - \theta) = (-1)^{J+M} \Theta_{J-KM}(\theta)$ one derives

$$(23)|JKM\rangle = (-1)^{J+K} |J-KM\rangle. \quad (\text{B.2})$$

For the remaining transpositions the relations (12) = $C_3(23)$ and (13) = $C_3(12)$ are used, where the operator $C_3 = (123)$ represents the rotation by an angle $2\pi/3$ about the molecular symmetry axis. This rotation operation is described by $\chi \rightarrow \chi + 2\pi/3$ for the Eulerian angles. With these expressions, we obtain

$$(12)|JKM\rangle = (-1)^J e^{-i2\pi K/3} |J-KM\rangle \quad (\text{B.3})$$

$$(13)|JKM\rangle = (-1)^J e^{-i4\pi K/3} |J-KM\rangle. \quad (\text{B.4})$$

Unless K is a multiple of 3, direct superpositions of the states $|JKM\rangle$ and $|J-KM\rangle$ do not lead to eigenstates of these symmetry operations. Taking into account the nuclear spin states $\gamma_{\sigma_i} = |I_i, \sigma_i\rangle$ of the nuclei with $I_i = I_j$ for all $i, j \in \{1, 2, 3\}$, and $\sigma_i \in \{-I, -I+1, \dots, I-1, I\}$, new eigenstates with the proper symmetry properties can be generated. If K is not a multiple of 3, the superpositions

$$\begin{aligned} |J|K|M\epsilon\rangle &= \frac{1}{\sqrt{6}} \{ |JKM\rangle (\gamma_{\sigma_1} \gamma_{\sigma_2} \gamma_{\sigma_3} + \gamma_{\sigma_3} \gamma_{\sigma_1} \gamma_{\sigma_2} e^{i2\pi K/3} + \gamma_{\sigma_2} \gamma_{\sigma_3} \gamma_{\sigma_1} e^{i4\pi K/3}) \\ &+ \epsilon |J-KM\rangle (\gamma_{\sigma_1} \gamma_{\sigma_2} \gamma_{\sigma_3} + \gamma_{\sigma_3} \gamma_{\sigma_1} \gamma_{\sigma_2} e^{-i2\pi K/3} + \gamma_{\sigma_2} \gamma_{\sigma_3} \gamma_{\sigma_1} e^{-i4\pi K/3}) \} \end{aligned} \quad (\text{B.5})$$

give the right eigenstates, where $(\gamma_{\sigma_1}, \gamma_{\sigma_2}, \gamma_{\sigma_3}) \notin \{(\gamma_{\sigma_1}, \gamma_{\sigma_2}, \gamma_{\sigma_3}) | \gamma_{\sigma_1} = \gamma_{\sigma_2} = \gamma_{\sigma_3}\}$. $\epsilon = \pm 1$. If K is a multiple of 3, the eigenstates are given by

$$|J|K|M\epsilon\rangle = \frac{1}{\sqrt{6}}\{|JKM\rangle + \epsilon|J - KM\rangle\}(\gamma_{\sigma_1}\gamma_{\sigma_2}\gamma_{\sigma_3} + \gamma_{\sigma_3}\gamma_{\sigma_1}\gamma_{\sigma_2} + \gamma_{\sigma_2}\gamma_{\sigma_3}\gamma_{\sigma_1}) \quad (\text{B.6})$$

for $(\gamma_{\sigma_1}, \gamma_{\sigma_2}, \gamma_{\sigma_3}) \notin \{(\gamma_{\sigma_1}, \gamma_{\sigma_2}, \gamma_{\sigma_3}) | \gamma_{\sigma_1} = \gamma_{\sigma_2} = \gamma_{\sigma_3}\}$. Additionally, we get the eigenstates

$$|J|K|M\epsilon\rangle = \frac{1}{\sqrt{2}}\{|JKM\rangle + \epsilon|J - KM\rangle\}\gamma_{\sigma_1}\gamma_{\sigma_2}\gamma_{\sigma_3} \quad (\text{B.7})$$

for $(\gamma_{\sigma_1}, \gamma_{\sigma_2}, \gamma_{\sigma_3}) \in \{(\gamma_{\sigma_1}, \gamma_{\sigma_2}, \gamma_{\sigma_3}) | \gamma_{\sigma_1} = \gamma_{\sigma_2} = \gamma_{\sigma_3}\}$.

The effects of symmetry operations in case of inversion vibrational motion is considered for the vibrational eigenstates $|\pm\rangle$, where $|+\rangle$ is the vibrational ground state and $|-\rangle$ the first excited state. The corresponding eigenfunctions of the eigenstates $|\pm\rangle$ are described by $\psi_{\pm} \sim f(h_e - h) \pm f(h_e + h)$, respectively, where $f(h')$ describes a function that is strongly peaked near $h' = 0$. Here, $h = \pm h_e$ are the two equilibrium positions in the double-well potential (see Fig. 2.5). From the eigenfunctions the action's of the symmetry operations can be obtained. With E^* and any interchange of two nuclei resulting in $h \rightarrow -h$ we obtain:

$$E^*|\pm\rangle = \pm|\pm\rangle \quad (\text{B.8})$$

$$(23)|\pm\rangle = \pm|\pm\rangle \quad (\text{B.9})$$

$$C_3|\pm\rangle = |\pm\rangle. \quad (\text{B.10})$$

Upon exchange of identical nuclei the total state of the molecule must change (keep) its sign in the case of fermionic (bosonic) nuclei. For molecules in the electronic ground state this is described by

$$(23)|\pm\rangle|J|K|M\epsilon\rangle = \pm\epsilon(-1)^J|\pm\rangle|J|K|M\epsilon\rangle \quad (\text{B.11})$$

and is valid for any interchange of two nuclei. This leads to the relations

$$\pm\epsilon(-1)^J = -1 \text{ \{for fermions\}}, \quad \pm\epsilon(-1)^J = 1 \text{ \{for bosons\}}. \quad (\text{B.12})$$

These conditions fix the possible state configuration that can be obtained. In particular for $K = 0$, where $\epsilon = +$, we derive from Eq. B.12 that only one of the two inversion states is allowed by symmetry restrictions. By finding all the allowed states from Eq. B.5, Eq. B.6, Eq. B.7 and Eq. B.12 with respect to the quantum numbers J and K , the spin statistical weights presented in Tbl. 4.1 are obtained.

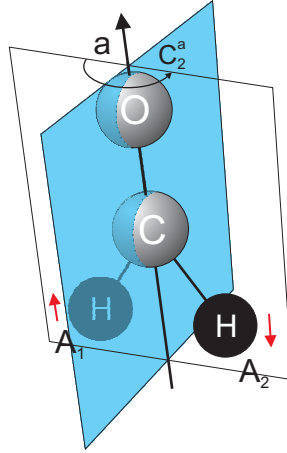


Figure B.2: Formaldehyde as an example of an asymmetric top with a twofold axis of symmetry. The a -axis forms the symmetry axis. The symmetry operation C_2^a describes a rotation by π about the symmetry axis, which results in an interchange of the two hydrogen nuclei. The spin of an hydrogen atom is marked by a red arrow.

B.2 Asymmetric top with a twofold axis of symmetry

Here, we investigate the case of a planar molecule with two equivalent nuclei and a symmetry axis which is the intersection between the plane in which the molecule is embedded and the perpendicular bisector of the line joining the two equivalent nuclei. This symmetry axis is a principal axis of the molecule. A rotation of π about this axis interchanges the position of the two equivalent nuclei. Therefore an interchange of both the position and spin coordinates must leave the states

$$|\psi\rangle = |J\tau M\rangle |\psi\rangle_{spin} \quad (\text{B.13})$$

unchanged up to the sign¹. From the spin state $\gamma_\sigma(i) = |I_i, \sigma_i\rangle$ of an individual nucleus with $i \in \{1, 2\}$, where σ has $2I + 1$, values we obtain the states of the two nuclei

$$\gamma_\sigma(1)\gamma_{\sigma'}(2) \quad \text{for } \sigma = \sigma' \quad (\text{B.14})$$

$$\gamma_\sigma(1)\gamma_{\sigma'}(2) \pm \gamma_\sigma(2)\gamma_{\sigma'}(1) \quad \text{for } \sigma \neq \sigma' \quad \begin{cases} + & = \text{symmetric} \\ - & = \text{antisymmetric} \end{cases} \quad (\text{B.15})$$

which are not altered by the interchange of the two nuclei up to a change of sign. The $(2I + 1)^2$ possible combinations include $2I + 1$ combinations from the states in

¹We assume that for the electronic and vibrational motion the molecule is in the ground state

Eq. B.14 and $((2I+1)^2 - (2I+1))/2$ for the states presented in Eq. B.15. Therefore we obtain

$$N_+ = (2I+1)(I+1) \quad \text{symmetric} \quad (\text{B.16})$$

$$N_- = (2I+1)I \quad \text{antisymmetric} \quad (\text{B.17})$$

for the number of states N_{\pm} with respect to symmetry. The symmetry of the rotational states $|J\tau M\rangle$ must match the symmetry of the spin state $|\psi\rangle_{spin}$ upon exchange of identical bosonic (fermionic) nuclei, to guarantee that the total state (see Eq. B.13) maintains (changes) its sign. The exchange of identical nuclei is described by a rotation by π about the symmetry axis. Here the symmetry of a rotational state defined by the K_A, K_C quantum numbers of the asymmetric rotor limiting cases, as stated in section 2.2.2 is found from Tbl. 2.3. For example, for H_2CO with two identical hydrogen atoms and the symmetry axis formed by the a -principal axis, states belonging to the representations A and B_a maintain their sign upon the action of the symmetry operation C_2^a . On the other hand states belonging to the representations B_b and B_c experience a change in sign. Therefore, molecules with $K_A = \text{even}$ are assigned to the antisymmetric spin state while states with $K_A = \text{odd}$ are assigned to the symmetric spin states. This leads to the spin statistical weight assignment shown in Tbl. 4.2.

Appendix C

Collision theory

The basic principles for a collision between a symmetric top molecule and an isotropic buffer-gas atom are outlined in the text below. These are the collisions taken place in the buffer-gas cell to cool-down the molecules. The theory is adapted from [Art06, Gre76].

C.1 Collision properties of atoms and symmetric-top molecules

To simplify the description of collisions between a symmetric-top molecule and an atom, first the right choice of coordinates has to be made. The total Hamiltonian of the system is given by

$$H = H_{mol}^{rot}(\mathbf{\Omega}) + T(\mathbf{r}) + V(\mathbf{\Omega}, \mathbf{r}) \quad (\text{C.1})$$

in space-fixed coordinates with the origin at the center of mass of both particles [Gre76]. The kinetic energy of the collision is described by $T(\mathbf{r}) = -(\hbar^2/2\mu)\nabla_{\mathbf{r}}^2$, where μ is the reduced mass of the colliding particles. The collision coordinate is given by $\mathbf{r} = (r, \hat{\theta}, \hat{\varphi})$ which ranges from the center of mass of the molecule to the atom. The orientation of the molecule is described by the Euler angles $\mathbf{\Omega} = (\theta, \varphi, \chi)$. The interaction potential $V(\mathbf{\Omega}, \mathbf{r})$ depends on the orientation of the symmetric top and the location of the buffer-gas atom [Art06, Gre76].

The Schrödinger equation of this problem is defined by

$$H\Psi_{jkl}^{JM} = E_{tot}\Psi_{jkl}^{JM} = (E_{jk} + E)\Psi_{jkl}^{JM}. \quad (\text{C.2})$$

The states Ψ_{jkl}^{JM} describe the eigenstates of the full Hamiltonian of the collision complex which are also eigenstates of the total angular momentum operator of the system with quantum numbers J and M . Therefore, the total angular momentum is conserved in the collision process. The quantum numbers jkl define the state of the collision complex at the entrance channel of the collision.¹ Here, j and k are the

¹Before the collision happened.

rotational quantum numbers of the symmetric top and l is the angular momentum of the collision complex. Therefore, E_{jk} is the rotational energy of the symmetric top at the collision entrance channel and $E = E_{tot} - E_{jk}$ the kinetic energy. To describe the eigenstates of the collision complex in the collision process we use the expansion

$$\Psi_{jkl}^{JM} = \sum_{j'k'l'} \frac{1}{r} u_{j'k'l'}^{JMjkl}(r) |JMj'k'l'\rangle, \quad (\text{C.3})$$

where

$$|JMjkl\rangle = \sum_m \langle jmlm_l | JM \rangle |jkm\rangle |lm_l\rangle. \quad (\text{C.4})$$

Here $|jkm\rangle$ are the eigenstates of the rigid rotor, $|lm_l\rangle$ are the eigenstates of the orbital angular momentum and $\langle jmlm_l | JM \rangle$ defines the Clebsch-Gordon coefficient. We substitute this expression into the Schrödinger equation C.2 and by multiplication with $\langle JMj'k'l' |$ from the left we derive

$$\left[\frac{d^2}{dr^2} - \frac{l'(l'+1)}{r^2} + \kappa_{j'k'jk}^2 \right] u_{j'k'l'}^{JMjkl}(r) = \frac{2\mu}{\hbar^2} \sum_{j''k''l''} \langle JMj'k'l' | V | JMj''k''l'' \rangle u_{j''k''l''}^{JMjkl}(r) \quad (\text{C.5})$$

where $\kappa_{j'k'jk}^2 = (2\mu/\hbar^2)(E + E_{jk} - E_{j'k'})$. The energy E contains the contribution from the kinetic term $T(\mathbf{r})$ at infinity where $\lim_{r \rightarrow \infty} V(\mathbf{\Omega}, \mathbf{r}) = 0$.

The solutions to this problem are further restricted by the boundary condition $u_{j'k'l'}^{JMjkl}(0) = 0$ at the origin and the asymptotic behavior at infinity. The latter can be found by investigating the solutions for the case $V = 0$. Here the Schrödinger equation

$$\left[\frac{d^2}{dr^2} - \frac{l(l+1)}{r^2} + \kappa^2 \right] u_l(r) = 0 \quad (\text{C.6})$$

can be solved by $u_l^r(r) = \kappa r j_l(\kappa r)$ and $u_l^{ir}(r) = \kappa r n_l(\kappa r)$ where $j_l(\kappa r)$ is a spherical Bessel function and $n_l(\kappa r)$ a spherical Neumann function. The asymptotic behavior for $r \rightarrow \infty$ is defined by $u_l^r(r) \sim \sin(\kappa r - l\pi/2)$ and $u_l^{ir}(r) \sim \cos(\kappa r - l\pi/2)$ [Chi74, Fri06]. $u_l^r(r)$ is the regular solution because $u_l^r(0) = 0$, while the irregular solution $u_l^{ir}(r)$ does not vanish at the origin. Therefore the regular solution $u_l^r(r)$ solves Eq. C.6 including the boundary condition at the origin. In the case where a short-ranged potential is present each coupled solution $u_{j'k'l'}^{JMjkl}(r)$ from Eq. C.5 should be described as a superposition of the two uncoupled free equations $u_l^r(r)$ and $u_l^{ir}(r)$ in the asymptotic regime.

To obtain incoming and outgoing solutions we use the basis transformation

$$u_l^+(r) = u_l^{ir}(r) + i u_l^r(r) \sim e^{i(\kappa r - l\pi/2)} \quad (\text{C.7})$$

$$u_l^-(r) = u_l^{ir}(r) - i u_l^r(r) \sim e^{-i(\kappa r - l\pi/2)}. \quad (\text{C.8})$$

The coupled solutions for the entrance channel $jdkl$ in the asymptotic limit are given by

$$u_{j'k'l'}^{JMjkl}(r) \sim \delta_{jj'}\delta_{kk'}\delta_{ll'}e^{-i(\kappa_{jkjk}r-l\pi/2)} - \left(\frac{\kappa_{jkjk}}{\kappa_{j'k'jk}}\right)^{1/2} S^J(jkl; j'k'l')e^{i(\kappa_{j'k'jk}r-l'\pi/2)}. \quad (\text{C.9})$$

$S^J(jkl; j'k'l')$ describes the scattering S matrix and $\sqrt{\kappa_{jkjk}/\kappa_{j'k'jk}}$ accounts for the change in relative motion due to inelastic scattering incidents leading to a change in momentum from the incoming to the outgoing solution.

An expression for $S^J(jkl; j'k'l')$ can be given within the framework of the distorted wave approximation which assumes that $|u_{j'k'l'}^{JMjkl}(r)|^2 \ll |u_{jkl}^{JMjkl}(r)|^2$ [Art06]. Here the solution of the uncoupled equation

$$\left[\frac{d^2}{dr^2} - \frac{l'(l'+1)}{r^2} + \kappa_{j'k'jk}^2 - \frac{2\mu}{\hbar^2} \langle JMj'k'l' | V | JMj'k'l' \rangle \right] u_{j'k'l'}^{JMjkl}(r) = 0, \quad (\text{C.10})$$

which represents elastic scattering, is defined by

$$u_{j'k'l'}^{JMjkl}(r) = \delta_{jj'}\delta_{kk'}\delta_{ll'}w_{jkl}^{JMjkl}(r), \quad (\text{C.11})$$

where

$$w_{j'k'l'}^{JMjkl}(r) \sim \sin(\kappa_{j'k'jk}r - l\pi/2 + \eta_{j'k'l'}^{JMjkl}). \quad (\text{C.12})$$

This is valid in the asymptotic regime. $\eta_{j'k'l'}^{JMjkl} \in \mathbb{R}$ is the phase shift due to elastic scattering. The solution given by Eq. C.11 forms the zeroth-order approximation in an iteration procedure [Art06].

The solution of the equation

$$\left[\frac{d^2}{dr^2} - \frac{l'(l'+1)}{r^2} + \kappa_{j'k'jk}^2 - \frac{2\mu}{\hbar^2} \langle JMj'k'l' | V | JMj'k'l' \rangle \right] u_{j'k'l'}^{JMjkl}(r) - \frac{2\mu}{\hbar^2} \langle JMjkl | V | JMj'k'l' \rangle (1 - \delta_{jj'}\delta_{kk'}\delta_{ll'}) w_{jkl}^{JMjkl}(r) = 0, \quad (\text{C.13})$$

which uses the zero-order approximation given by Eq. C.11 defines the first-order approximation. It is given by

$$\begin{aligned} u_{j'k'l'}^{JMjkl}(r) &= \delta_{jj'}\delta_{kk'}\delta_{ll'}w_{jkl}^{JMjkl}(r) + (1 - \delta_{jj'}\delta_{kk'}\delta_{ll'}) \\ &\times [v_{j'k'l'}^{JMjkl}(r) \int_0^r w_{j'k'l'}^{JMjkl}(r') \langle JMjkl | V | JMj'k'l' \rangle w_{jkl}^{JMjkl}(r') dr' \\ &+ w_{j'k'l'}^{JMjkl}(r) \int_r^\infty v_{j'k'l'}^{JMjkl}(r') \langle JMjkl | V | JMj'k'l' \rangle w_{jkl}^{JMjkl}(r') dr'] \end{aligned} \quad (\text{C.14})$$

where $v_{j'k'l'}^{JMjkl}(r)$ describes the solution of Eq. C.10 with asymptotic behavior $v_{j'k'l'}^{JMjkl}(r) \sim \exp(i(\kappa_{j'k'jk}r - l\pi/2 + \eta_{j'k'l'}^{JMjkl}))$ derived by a transformation as given by Eq. C.7. By comparison of Eq. C.9 and Eq. C.14

$$S^J(jkl; j'k'l') = e^{i(\eta_{j'k'l'}^{JMjkl} + \eta_{jkl}^{JMjkl})} \left(\frac{\kappa_{j'k'jk}}{\kappa_{jkl}} \right)^{1/2} [\delta_{jj'}\delta_{kk'}\delta_{ll'}(1 - 2i\beta_{j'k'l'}^{JMjkl}) + 2i\beta_{j'k'l'}^{JMjkl}] \quad (\text{C.15})$$

is obtained [Art06]. Here $\beta_{j'k'l'}^{JMjkl} = \int_0^\infty w_{j'k'l'}^{JMjkl}(r) \langle JMjkl|V|JMj'k'l' \rangle w_{jkl}^{JMjkl}(r) dr$.

The derivation shows that solutions as shown in Eq. C.9 depend strongly on the coupling matrix elements $\langle JMjkl|V|JMj'k'l' \rangle$. Simplified expressions for the coupling matrix elements can be found by using an expansion of the interaction potential by spherical harmonics [Gre76]. The interaction potential in the body-fixed frame with axes along the principal moments of inertia of the rotor can be expanded to

$$V(r, \tilde{\theta}, \tilde{\varphi}) = \sum_{\lambda\mu} v_{\lambda\mu}(r) Y_{\lambda\mu}(\tilde{\theta}, \tilde{\varphi}) \quad (\text{C.16})$$

Therefore the coupling matrix elements can be expressed by

$$\begin{aligned} \langle JMjkl|V|JMj'k'l' \rangle &= \langle JMjkl| \sum_{\lambda\mu} v_{\lambda\mu}(r) Y_{\lambda\mu}(\hat{\mathbf{r}}) |JMj'k'l' \rangle \\ &= \sum_{\lambda\mu} \left[\frac{(2j+1)(2j'+1)(2l+1)(2l'+1)(2\lambda+1)}{4\pi} \right]^{1/2} \\ &\quad \times \begin{pmatrix} l & l' & \lambda \\ 0 & 0 & 0 \end{pmatrix} \begin{pmatrix} j & j' & \lambda \\ k & -k' & \mu \end{pmatrix} \left\{ \begin{matrix} j' & l' & J \\ l & j & \lambda \end{matrix} \right\} \\ &\quad \times (-1)^{j+j'+k-J} v_{\lambda\mu}(r) \end{aligned} \quad (\text{C.17})$$

where the round brackets describe $3-j$ symbols while the object enclosed by the curly brackets is a $6-j$ symbol [Sak94]. The connection between $3-j$ symbols and Clebsch-Gordan coefficients results in the collision selection rule

$$\mu = k' - k. \quad (\text{C.18})$$

For example, symmetric top molecules with C_{3v} (D_{3h}) symmetry, apparent in a 3-fold axis of symmetry only possess spherical harmonics with $\mu \in \{3n | n \in \mathbb{N}\}$. Therefore the two independent series of levels with $k = 3n$ (ortho) and $k = 3n \pm 1$ (para) do not interconnect in the scattering process and can be considered separately in the collision process.

Appendix D

Additional plots and pictures

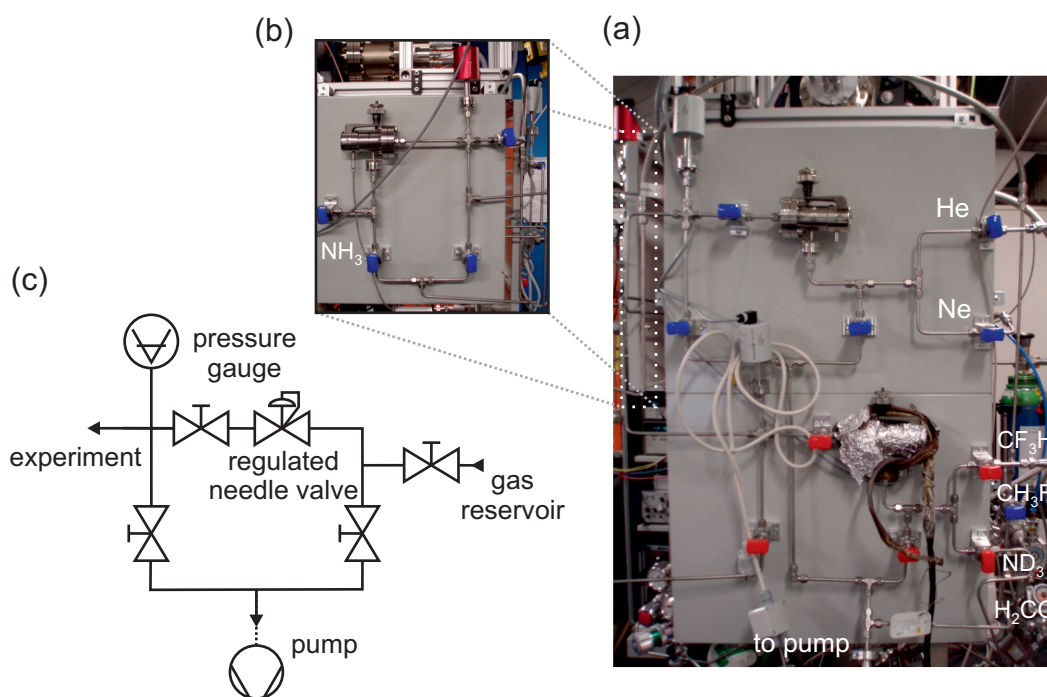


Figure D.1: In (a) the main gas handling system is presented. On this board the gas handling system for the buffer gases as well as for the molecule gases that are injected into the first molecular line are shown. In (b) the gas handling system for the second molecular line is presented. The basic principles of the gas handling system are outlined in (c).

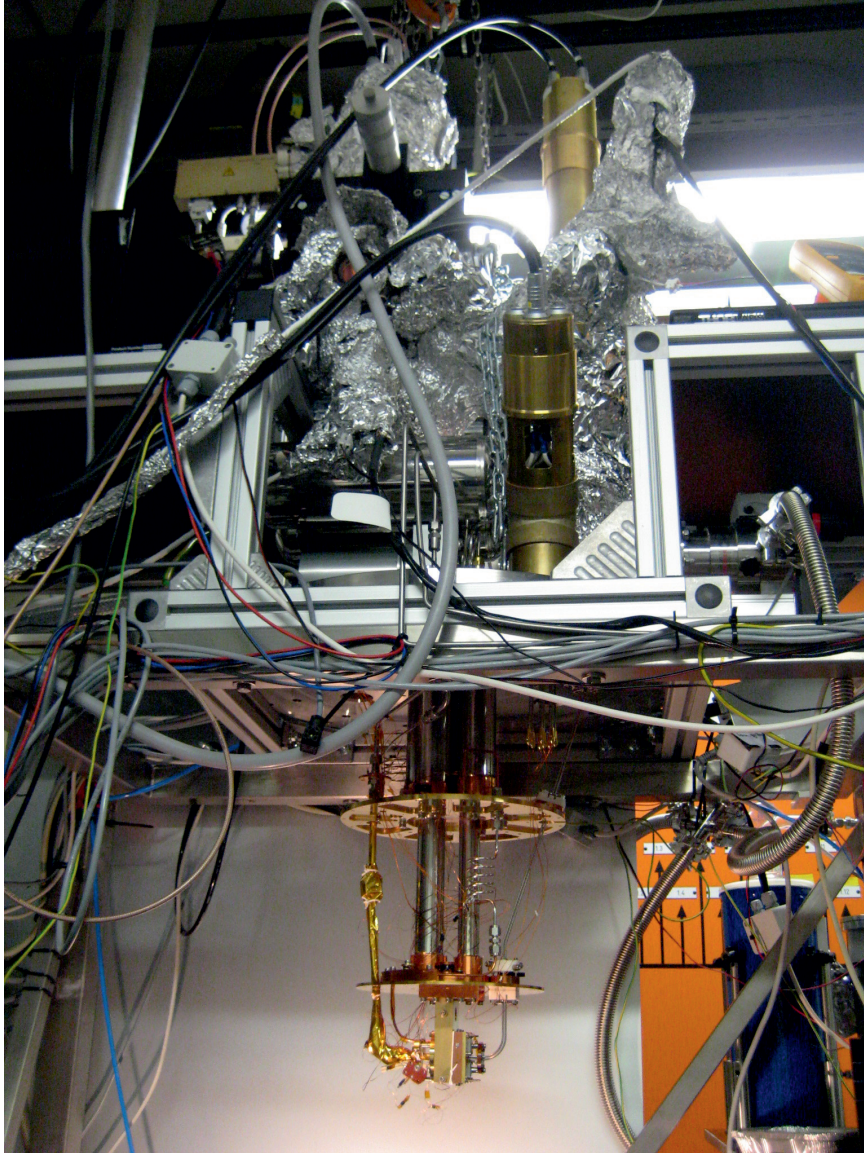


Figure D.2: The complete cryogenic setup. The vacuum vessel and the radiation shields are removed.

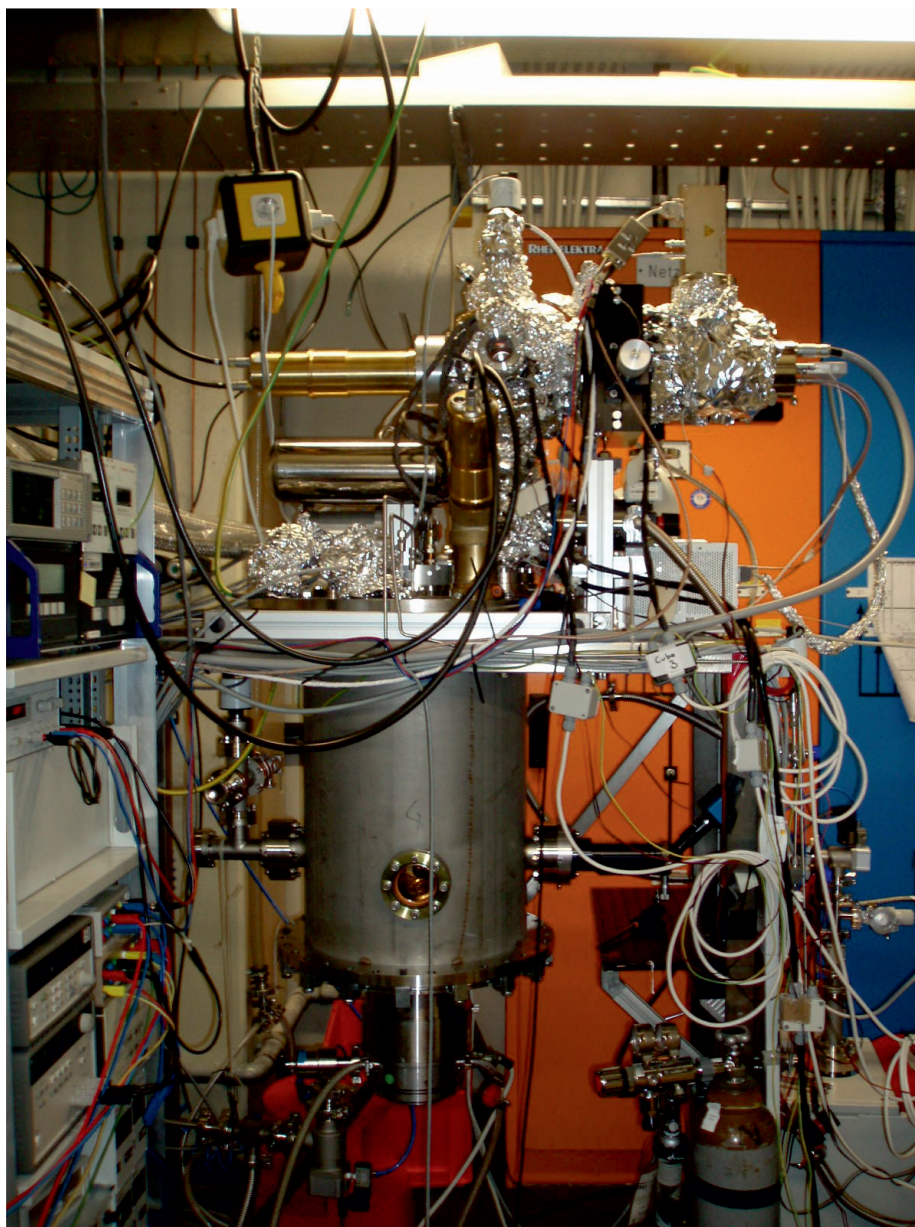


Figure D.3: The complete cryogenic setup including the vacuum vessel. The photograph has been taken before the assembly of the depletion-spectroscopy-vacuum chamber.

Bibliography

- [Abr95] E. R. I. Abraham, N. W. M. Ritchie, W. I. McAlexander, and R. G. Hulet. Photoassociative spectroscopy of long-range states of ultracold ${}^6\text{Li}_2$ and ${}^7\text{Li}_2$. *J. Chem. Phys.* **103**, 7773 (1995).
- [And95] M. H. Anderson, J. R. Ensher, M. R. Matthews, C. E. Wieman, and E. A. Cornell. Observation of Bose-Einstein Condensation in a Dilute Atomic Vapor. *Science* **269**, 198 (1995).
- [And06] A. André, D. DeMille, J. M. Doyle, M. Lukin, S. Maxwell, P. Rabl, R. Schoelkopf, and P. Zoller. A coherent all-electrical interface between polar molecules and mesoscopic superconducting resonators. *Nature Phys.* **2**, 636 (2006).
- [Art06] A. M. Arthurs and A. Dalgarno. The Theory of Scattering by a Rigid Rotator. *Proc. R. Soc. Lond. A* **256**, 540 (1960).
- [Atk05] P. Atkins and R. Friedman. *Molecular Quantum Mechanics*. Oxford University Press, New York (2005).
- [Avd02] A. V. Avdeenkov and J. L. Bohn. Collisional dynamics of ultracold OH molecules in an electrostatic field. *Phys. Rev. A* **66**, 052718 (2002).
- [Bal01] N. Balakrishnan and A. Dalgarno. Chemistry at ultracold temperatures. *Chem. Phys. Lett.* **341**, 652 (2001).
- [Bal02] N. Balakrishnan and A. Dalgarno. Erratum to: "Chemistry at ultracold temperatures" [Chem. Phys. Lett. 341 (2001) 652]. *Chem. Phys. Lett.* **351**, 159 (2002).
- [Bal98] C. D. Ball, and F. C. De Lucia. Direct Measurement of Rotationally Inelastic Cross Sections at Astrophysical and Quantum Collisional Temperatures. *Phys. Rev. Lett.* **81**, 305 (1998).
- [Bal99] C. D. Ball, and F. C. De Lucia. Direct observation of Λ -doublet and hyperfine branching ratios for rotationally inelastic collisions of NO-He at 4.2 K. *Chem. Phys. Lett.* **300**, 227 (1999).

- [Bar01a] M. Baranov, L. Dobrek, K. Goral, L. Santos and M. Lewenstein. Ultracold dipolar gases - a challenge for experiments and theory. Nobel symposium 'Coherence and Condensation in Quantum Systems', Göteborg (2001).
- [Bar01b] P. F. Barker and M. N. Shneider. Optical microlinear accelerator for molecules and atoms. *Phys. Rev. A* **64**, 033408 (2001).
- [Bar02] P. F. Barker and M. N. Shneider. Slowing molecules by optical microlinear deceleration. *Phys. Rev. A* **66**, 065402 (2002).
- [Bar09] P. F. Barker, S. M. Purcell, P. Douglas, P. Barletta, N. Coppedale, C. Maher-McWilliams, and J. Tennyson. Sympathetic cooling by collisions with ultracold rare gas atoms, and recent progress in optical Stark deceleration. *Faraday Discuss.* **142**, 175 (2009).
- [Ber98] K. Bergmann, H. Theuer, and B. W. Shore. Coherent population transfer among quantum states of atoms and molecules. *Rev. Mod. Phys.* **70**, 1003 (1998).
- [Bet99] H. L. Bethlem, G. Berden, and G. Meijer. Decelerating Neutral Dipolar Molecules. *Phys. Rev. Lett.* **83**, 1558 (1999).
- [Bet00] H. L. Bethlem, G. Berden, F. M. H. Crompvoets, R. T. Jongma, A. J. A. van Roij, and G. Meijer. Electrostatic trapping of ammonia molecules. *Nature* **406**, 491 (2000).
- [Bet02] H. L. Bethlem, F. M. H. Crompvoets, R. T. Jongma, S. Y. T. van de Meerakker, and G. Meijer. Deceleration and trapping of ammonia using time-varying electric fields. *Phys. Rev. A* **65**, 053416 (2002).
- [Bet06] H. L. Bethlem, J. van Veldhoven, M. Schnell, and G. Meijer. Trapping polar molecules in an ac trap. *Phys. Rev. A* **74**, 063403 (2006).
- [Blo08] I. Bloch, J. Dalibard, and W. Zwerger. Many-body physics with ultracold gases. *Rev. Mod. Phys.* **80**, 885 (2008).
- [Boh09] J. L. Bohn, M. Cavagnero and C. Ticknor. Quasi-universal dipolar scattering in cold and ultracold gases. *New J. Phys.* **11**, 055039 (2009).
- [Bol08] P. A. Bolokhov, M. Pospelov and M. Romalis. Electric dipole moments as probes of CPT invariance. *Phys. Rev. D* **78**, 057702 (2008).
- [Bor27] M. Born and R. Oppenheimer. Zur Quantentheorie der Molekeln. *Annalen der Physik* **84** 457 (1927).
- [Bra95] C. C. Bradley, C. A. Sackett, J. J. Tollett, and R. G. Hulet. Evidence of Bose-Einstein Condensation in an Atomic Gas with Attractive Interactions. *Phys. Rev. Lett.* **75**, 1687 (1995).

- [Bre03] B. Brezger, M. Arndt, and A. Zeilinger. Concepts for near-field interferometers with large molecules. *J. Opt. B* **5**, 82 (2003).
- [Bun06] P. R. Bunker and P. Jensen. *Molecular Symmetry and Spectroscopy*. NRC Research Press, Ottawa, Ontario, Canada, 2nd edition (2006).
- [Cam07] W. C. Campbell, E. Tsikata, H. I. Lu, L. D. van Buuren and J. M. Doyle. Magnetic Trapping and Zeeman Relaxation of NH ($X^3\Sigma^-$). *Phys. Rev. Lett.* **98**, 213001 (2007).
- [Car09] L. D. Carr, D. DeMille, R. V. Krems, and J. Ye. Cold and ultracold molecules: science, technology and applications. *New J. Phys.* **11**, 055049 (2009).
- [Cav09] M. Cavagnero and C. Newell. Inelastic semiclassical collisions in cold dipolar gases. *New J. Phys.* **11**, 055040 (2009).
- [Chi74] M. S. Child. *Molecular Collision Theory*. Dover Publications, London (1974).
- [Com99] E. D. Commins. Electric Dipole Moments of Leptons. *Adv. At. Mol. Opt. Phys* **40**, 1 (1999).
- [Com07] E. D. Commins, J. D. Jackson, and D. P. DeMille. The electric dipole moment of the electron: An intuitive explanation for the evasion of Schiff's theorem. *Am. J. Phys.* **75**, 532 (2007).
- [Cro02] F. M. H. Crompvoets, R. T. Jongma, H. L. Bethlem, A. J. A. van Roij, and G. Meijer. Longitudinal Focusing and Cooling of a Molecular Beam. *Phys. Rev. Lett.* **89**, 093004 (2002).
- [Cro44] P. C. Cross, R. M. Hainer, and G. W. King. The Asymmetric Rotor, II. Calculation of Dipole Intensities and Line Classification. *J. Chem. Phys.* **12**, 210 (1944).
- [Dan08] J. G. Danzl, E. Haller, M. Gustavsson, M. J. Mark, R. Hart, N. Bouloufa, O. Dulieu, H. Ritsch, and H.-C. Nägerl. Quantum Gas of Deeply Bound Ground State Molecules. *Science* **321**, 1062 (2008).
- [Dav95] K. B. Davis, M. O. Mewes, M. R. Andrews, N. J. van Druten, D. S. Durfee, D. M. Kurn, and W. Ketterle Bose-Einstein Condensation in a Gas of Sodium Atoms. *Phys. Rev. Lett.* **75**, 3969 (1995).
- [Dei08b] J. Deiglmayr, A. Grochola, M. Repp, K. Mörtlbauer, C. Glück, J. Lange, O. Dulieu, R. Wester, and M. Weidemüller. Formation of Ultracold Polar Molecules in the Rovibrational Ground State. *Phys. Rev. Lett.* **101**, 133004 (2008).

- [Dem03] W. Demtröder. *Molekülphysik: Theoretische Grundlagen und experimentelle Methoden*. Oldenbourg publishing, München (2003).
- [Dem03a] W. Demtröder. *Laser Spectroscopy: Basic Concepts and Instrumentation*. Springer, Berlin, 3rd edition (2003).
- [Dor09] S. C. Doret, C. B. Connolly, W. Ketterle, and J. M. Doyle. Buffer-Gas Cooled Bose-Einstein Condensate. *Phys. Rev. Lett.* **103**, 103005 (2009).
- [Doy04] J. M. Doyle, B. Friedrich, R. V. Krems, and F. Masnou-Seeuws. Editorial: Quo vadis, cold molecules? *Eur. Phys. J. D* **31**, 149 (2004).
- [DR04] M. D. Di Rosa. Laser-cooling molecules. *Eur. Phys. J. D* **31**, 395 (2004).
- [Dul06] O. Dulieu, M. Raoult, and E. Tiemann. Cold molecules: a chemistry kitchen for physicists? *J. Phys. B* **39** (2006).
- [Ear42] S. Earnshaw. On the nature of the molecular forces which regulate the constitution of the luminiferous ether. *Trans. Camb. Phil. Soc.* **7**, 97 (1842).
- [Eck35] C. Eckart. Some Studies Concerning Rotating Axes and Polyatomic Molecules. *Phys. Rev.* **47**, 552 (1935).
- [Ego02] D. Egorov, T. Lahaye, W. Schöllkopf, B. Friedrich, and J. M. Doyle. Buffer-gas cooling of atomic and molecular beams. *Phys. Rev. A* **66**, 043401 (2002).
- [Ego04] D. Egorov, W. C. Campbell, B. Friedrich, S. Maxwell, E. Tsikata, L. D. van Buuren, and J. M. Doyle. Buffer-gas cooling of NH via the beam loaded buffer-gas method. *Eur. Phys. J. D* **31**, 307 (2004).
- [Eki06] J. W. Ekin. *Experimental Techniques for Low-Temperature Measurements*. Oxford University Press, Oxford (2006).
- [Eld27] J. A. Eldridge. Experimental Test of Maxwell's Distribution Law. *Phys. Rev.* **30**, 931 (1927).
- [Eli03] M. S. Elioff, J. J. Valentini, and D. W. Chandler. Subkelvin Cooling NO Molecules via "Billiard-like" Collisions with Argon. *Science* **302**, 1940 (2003).
- [Fri06] H. Friedrich. *Theoretical Atomic Physics*. Springer, Berlin (2006).
- [For99] R. C. Forrey, V. Kharchenko, N. Balakrishnan, and A. Dalgarno. Vibrational relaxation of trapped molecules. *Phys. Rev. A* **59**, 2146 (1999).

- [Ful04] R. Fulton, A. I. Bishop, and P. F. Barker. Optical Stark Decelerator for Molecules. *Phys. Rev. Lett.* **93**, 243004 (2004).
- [Ful06a] R. Fulton, A. I. Bishop, M. N. Shneider, and P. F. Barker. Controlling the motion of cold molecules with deep periodic optical potentials. *Nature Phys.* **2**, 465 (2006).
- [Ger07] S. Gerlich, L. Hackermueller, K. Hornberger, A. Stibor, H. Ulbricht, M. Gring, F. Goldfarb, T. Savas, M. Mueri, M. Mayor, and M. Arndt. A Kapitza-Dirac-Talbot-Lau interferometer for highly polarizable molecules. *Nature Phys.* **3**, 711 (2007).
- [Gil06] J. J. Gilijamse, S. Hoekstra, S. Y. van de Meerakker, G. C. Groenenboom, and G. Meijer. Near-Threshold Inelastic Collisions Using Molecular Beams with a Tunable Velocity. *Science* **313**, 1617 (2006).
- [Gil07] J. J. Gilijamse, S. Hoekstra, S. A. Meek, M. Metsälä, S. Y. T. van de Meerakker, G. Meijer, and G. C. Groenenboom. The radiative lifetime of metastable CO ($a^3\Pi, v = 0$). *J. Chem. Phys.* **127**, 221102 (2007).
- [Gre76] S. Green. Rotational excitation of symmetric top molecules by collisions with atoms: Close coupling, coupled states, and effective potential calculations for NH₃-He. *J. Chem. Phys.* **64**, 3463 (1976).
- [Gre79] S. Green. Rotational excitation of symmetric top molecules by collisions with atoms. II. Infinite order sudden approximation. *J. Chem. Phys.* **70**, 816 (1979).
- [Gre80] S. Green. Energy transfer in NH₃-He collisions. *J. Chem. Phys.* **73**, 2740 (1980).
- [Gri09] W. C. Griffith, M. D. Swallows, T. H. Loftus, M. V. Romalis, B. R. Heckel, and E. N. Fortson. Improved Limit on the Permanent Electric Dipole Moment of ¹⁹⁹Hg. *Phys. Rev. Lett.* **102**, 101601 (2009).
- [Gup99] M. Gupta and D. Herschbach. A Mechanical Means to Produce Intense Beams of Slow Molecules. *J. Phys. Chem. A* **103**, 10670 (1999).
- [Gup01] M. Gupta and D. Herschbach. Slowing and Speeding Molecular Beams by Means of a Rapidly Rotating Source. *J. Phys. Chem. A* **105**, 1626 (2001).
- [Hän80] T. W. Hänsch and B. Couillaud. Laser frequency stabilization by polarization spectroscopy of a reflecting reference cavity. *Opt. Comm.* **35**, 441 (1980).

- [Her45] G. Herzberg. Infrared and Raman Spectra of Polyatomic Molecules. Van Nostrand Reinhold, Inc., New York (1945).
- [Hin97] E. A. Hinds. Testing Time Reversal Symmetry Using Molecules. *Phys. Scr.* **T70**, 34 (1997).
- [Hog08a] S. D. Hogan, A. W. Wiederkehr, M. Andrist, H. Schmutz, and F. Merkt. Slow beams of atomic hydrogen by multistage Zeeman deceleration. *J. Phys. B* **41**, 081005 (2008).
- [Hud02] J. J. Hudson, B. E. Sauer, M. R. Tarbutt, and E. A. Hinds. Measurement of the Electron Electric Dipole Moment Using YbF Molecules. *Phys. Rev. Lett.* **89**, 023003 (2002).
- [Hum08] M. T. Hummon, W. C. Campbell, H.-I. Lu, E. Tsikata, Y. Wang, and J. M. Doyle. Magnetic trapping of atomic nitrogen (^{14}N) and cotrapping of NH ($X^3\Sigma^-$). *Phys. Rev. A* **78**, 050702(R) (2008).
- [Hun91] L. R. Hunter. Tests of Time-Reversal Invariance in Atoms, Molecules, and the Neutron. *Science* **252**, 73 (1991).
- [Ino04] S. Inouye, J. Goldwin, M. L. Olsen, C. Ticknor, J. L. Bohn, and D. S. Jin. Observation of Heteronuclear Feshbach Resonances in a Mixture of Bosons and Fermions. *Phys. Rev. Lett.* **93**(18), 183201 (2004).
- [Jac99] J. D. Jackson. Classical Electrodynamics. John Wiley and Sons Ltd., New York, 3rd edition (1999).
- [Jae04] K. Jänich. Funktionentheorie. Springer, Heidelberg, (2004).
- [Joc03] S. Jochim, M. Bartenstein, A. Altmeyer, G. Hendl, S. Riedl, C. Chin, J. Hecker Denschlag, and R. Grimm. Bose-Einstein Condensation of Molecules. *Science* **302**, 2101 (2003).
- [Jon06] K. M. Jones, E. Tiesinga, P. D. Lett, and P. S. Julienne. Ultracold photoassociation spectroscopy: Long-range molecules and atomic scattering. *Rev. Mod. Phys.* **78**, 483 (2006).
- [Jon97] R. T. Jongma, G. von Helden, G. Berden, and G. Meijer. Confining CO molecules in stable orbits. *Chem. Phys. Lett.* **270**, 304 (1997).
- [Jun04a] T. Junglen, T. Rieger, S. A. Rangwala, P. W. H. Pinkse, and G. Rempe. Slow ammonia molecules in an electrostatic quadrupole guide. *Eur. Phys. J. D* **31**, 365 (2004).
- [Jun04b] T. Junglen, T. Rieger, S. A. Rangwala, P. W. H. Pinkse, and G. Rempe. Two-Dimensional Trapping of Dipolar Molecules in Time-Varying Electric Fields. *Phys. Rev. Lett.* **92**, 223001 (2004).

- [Jun05] T. Junglen. Guiding and Trapping of Cold Dipolar Molecules, Ph.D. thesis, Technische Universität München (2005).
- [Kaw04] D. Kawall, F. Bay, S. Bickman, Y. Jiang, and D. DeMille. Precision Zeeman-Stark Spectroscopy of the Metastable $a(1)[^3\Sigma^+]$ State of PbO. *Phys. Rev. Lett.* **92**, 133007 (2004).
- [Kay09] J. J. Kay, S. Y. T. van de Meerakker, K. E. Strecker, and D. W. Chandler. Production of cold ND₃ by kinematic cooling. *Faraday Discuss.* **142**, 143 (2009).
- [Kin43] G. W. King, R. M. Hainer, and P. C. Cross. The Asymmetric Rotor, I. Calculation and Symmetry Classification of Energy Levels. *J. Chem. Phys.* **11**, 27 (1943).
- [Kir10] M. Kirste, L. Scharfenberg, J. Klos, F. Lique, M. H. Alexander, G. Meijer, and S. Y. T. van de Meerakker. Low-energy inelastic collisions of OH radicals with He atoms and D₂ molecules. *Phys. Rev. A.* **82**, 042717 (2010).
- [Koh06] T. Kohler, K. Goral, and P. S. Julienne. Production of cold molecules via magnetically tunable Feshbach resonances. *Rev. Mod. Phys.* **78**(4), 1311 (2006).
- [Kre03] R. V. Krems, A. Dalgarno, N. Balakrishnan and G. C. Groenenboom. Spin-flipping transitions in doublet-sigma molecules induced by collisions with structureless atoms. *Phys. Rev. A* **67**, 060703 (2003).
- [Kre05] R. V. Krems. Molecules near absolute zero and external field control of atomic and molecular dynamics. *Int. Rev. Phys. Chem.* **24**, 99 (2005).
- [Kre08] R. V. Krems. Cold controlled chemistry. *Phys. Chem. Chem. Phys.* **10**, 4079 (2008).
- [Kre09] R. V. Krems, W. C. Stwalley, and B. Friedrich. Cold Molecules: Theory, Experiment, Applications. CRC Press, Boca Raton (2009).
- [Kro75] H. W. Kroto. Molecular Rotation Spectra. John Wiley and Sons Ltd., New York (1975).
- [Kuy83] F. Kuypers. Klassische Mechanik. Physik-Verlag GmbH., Weinheim (1983).
- [Laf98] J. M. Lafferty. Foundations of Vacuum Science and Technology. John Wiley and Sons Ltd., New York (1998).
- [Lan57] L. Landau. On the conservation laws for weak interactions. *Sov. Phys. JETP* **5**, 336 (1957).

- [Lan08] F. Lang, K. Winkler, C. Strauss, R. Grimm, and J. Hecker Denschlag. Ultracold Triplet Molecules in the Rovibrational Ground State. *Phys. Rev. Lett.* **101**, 133005 (2008).
- [Man06] D. Manura. Simion 3D. Scientific Instruments Services, Inc., Ringoes, NJ (2006).
- [Mau05] K. Maxwell, D. Egorov, J. S. Helton, S. V. Nguyen, and J. M. Doyle. Zeeman Relaxation of CaF in Low-Temperature Collisions with Helium. *Phys. Rev. Lett.* **94**, 123002 (2005).
- [Max05] S. E. Maxwell, N. Brahms, R. deCarvalho, D. R. Glenn, J. S. Helton, S. V. Nguyen, D. Patterson, J. Petricka, D. DeMille, and J. M. Doyle. High-Flux Beam Source for Cold, Slow Atoms or Molecules. *Phys. Rev. Lett.* **95**, 173201 (2005).
- [Mee08] S. A. Meek, H. L. Bethlem, H. Conrad, and G. Meijer. Trapping Molecules on a Chip in Traveling Potential Wells. *Phys. Rev. Lett.* **100**, 153003 (2008).
- [Mee09] S. A. Meek, H. Conrad, and G. Meijer. Trapping Molecules on a Chip. *Science* **324**, 5935 (2009).
- [Men00] M. Mengel and F. C. De Lucia. Helium and Hydrogen Induced Rotational Relaxation of H₂CO Observed at Temperatures of the Interstellar Medium. *Astrophys. J.* **543**, 271 (2000).
- [Mes84] J. K. Messer and F. C. De Lucia. Measurement of Pressure-Broadening Parameters for the CO-He System at 4 K. *Phys. Rev. Lett.* **53**, 2555 (1984).
- [Met99] H. J. Metcalf and P. van der Straten. Laser Cooling and Trapping. Springer, Berlin (1999).
- [Mie10] M. Mielenz. Speichern von polaren Molekülen in einer mikrostrukturierten elektrischen Falle, Master thesis, Julius-Maximilians-Universität Würzburg (2010).
- [Mir10] M. H. G. de Miranda, A. Chotia, B. Neyenhuis, D. Wang, G. Quemener, S. Ospelkaus, J. L. Bohn, J. Ye, and D. S. Jin. Controlling the quantum stereodynamics of ultracold bimolecular reactions. arXiv:1010.3731v1 (2010).
- [Moo83] C. B. Moore and J. C. Weisshaar. Formaldehyde Photochemistry. *Ann. Rev. Phys. Chem.* **34**, 525 (1983).

- [Mot07] M. Motsch, M. Schenk, L. D. van Buuren, M. Zeppenfeld, P. W. H. Pinkse, and G. Rempe. Internal-state thermometry by depletion spectroscopy in a cold guided beam of formaldehyde. *Phys. Rev. A* **76**, 061402(R) (2007).
- [Mot08] M. Motsch, M. Schenk, M. Zeppenfeld, M. Schmitt, W. L. Meerts, P. W. H. Pinkse, and G. Rempe. Spectroscopy of the $\tilde{A}^1A_2 \leftarrow \tilde{X}^1A_1$ transition of formaldehyde in the 30140–30790 cm^{-1} range: the $2_0^14_0^3$ and $2_0^24_0^1$ rovibrational bands. *J. Mol. Spec.* **252**, 25 (2008).
- [Mot09a] M. Motsch, C. Sommer, M. Zeppenfeld, L. D. van Buuren, G. Rempe, and P. W. H. Pinkse. Collisional effects in the formation of cold guided beams of polar molecules. *New J. Phys.* **11**, 055030 (2009).
- [Mot09b] M. Motsch, L. D. van Buuren, C. Sommer, M. Zeppenfeld, G. Rempe, and P. W. H. Pinkse. Cold guided beams of water isotopologs. *Phys. Rev. A* **79**, 013405 (2009).
- [Mot10] M. Motsch. Cold Guided Beams of Polar Molecules, Ph.D. thesis, Technische Universität München (2010).
- [Mul09b] R. S. Mulliken. Species Classification and Rotational Energy Level Patterns of Non-Linear Triatomic Molecules. *Phys. Rev.* **59**, 873 (1941).
- [Nar07a] E. Narevicius, A. Libson, M. F. Riedel, C. G. Parthey, I. Chavez, U. Even, and M. G. Raizen. Coherent Slowing of a Supersonic Beam with an Atomic Paddle. *Phys. Rev. Lett.* **98**, 103201 (2007).
- [Nar07c] E. Narevicius, C. G. Parthey, A. Libson, M. Riedel, U. Even, and M. G. Raizen. Towards magnetic slowing of atoms and molecules. *New J. Phys.* **9**, 96 (2007).
- [Nar08a] E. Narevicius, A. Libson, C. G. Parthey, I. Chavez, J. Narevicius, U. Even, and M. G. Raizen. Stopping Supersonic Beams with a Series of Pulsed Electromagnetic Coils: An Atomic Coilgun. *Phys. Rev. Lett.* **100**, 093003 (2008).
- [Nar08b] E. Narevicius, A. Libson, C. G. Parthey, I. Chavez, J. Narevicius, U. Even, and M. G. Raizen. Stopping supersonic oxygen with a series of pulsed electromagnetic coils: A molecular coilgun. *Phys. Rev. A* **77**, 051401 (2008).
- [Ngu05] S. V. Nguyen, S. C. Doret, C. B. Connolly, R. A. Michniak, W. Ketterle, and J. M. Doyle. Evaporative cooling of metastable helium in the multi-partial-wave regime. *Phys. Rev. A* **72**, 060703(R) (2005).

- [Ni10] K.-K. Ni, S. Ospelkaus, D. Wang, G. Que'me'ner, B. Neyenhuis, M. H. G. de Miranda, J. L. Bohn, J. Ye, and D. S. Jin. Dipolar collisions of polar molecules in the quantum regime. *Nature* **464**, 1324 (2010).
- [Oli77] J. J. Olivero and R. L. Longbothum. Empirical fits to the Voigt line width: A brief review. *J. Quant. Spectrosc. Radiat. Transfer* **17**, 233 (1977).
- [Osp08] S. Ospelkaus, A. Pe'er, K.-K. Ni, J. J. Zirbel, B. Neyenhuis, S. Kotochigova, P. S. Julienne, J. Ye, and D. S. Jin. Efficient state transfer in an ultracold dense gas of heteronuclear molecules. *Nature Phys.* **4**, 622 (2008).
- [Osp10] S. Ospelkaus, K.-K. Ni, D. Wang, M. H. G. de Miranda, B. Neyenhuis, G. Que'me'ner, P. S. Julienne, J. L. Bohn, D. S. Jin, and J. Ye. Quantum-State Controlled Chemical Reactions of Ultracold Potassium-Rubidium Molecules. *Science* **327**, 853 (2010).
- [Pau00] H. Pauly. Atom, Molecule, and Cluster Beams I: Basic Theory, Production and Detection of Thermal Energy Beams. Springer, Berlin (2000).
- [Pat07] D. Patterson and J. M. Doyle. Bright, guided molecular beam with hydrodynamic enhancement. *J. Chem. Phys.* **126**, 154307 (2007).
- [Pat09] D. Patterson, J. Rasmussen, and J. M. Doyle. Intense atomic and molecular beams via neon buffer-gas cooling. *New J. Phys.* **11**, 055018 (2009).
- [Pat10] D. Patterson. Buffer Gas Cooled Beams and Cold Molecular Collisions, Ph.D. thesis, Harvard University Cambridge (2010).
- [Poh07] S. Pohle. A Cryogenic Source for Cold Polar Molecules, Master thesis, Technische Universität München (2007).
- [Pre58] R. D Present. Kinetic theory of gases. McGraw-Hill Inc., New York (1958).
- [Pre96] W. H. Press, S. A. Teukolsky, W. T. Vetterling, and B. P. Flannery. Numerical Recipes in C: The Art of Scientific Computing. Cambridge University Press, Cambridge (1996).
- [Pur50] E. M. Purcell and N. F. Ramsey. On the Possibility of Electric Dipole Moments for Elementary Particles and Nuclei. *Phys. Rev.* **78**, 807 (1950).
- [Rad00] R. Radebaugh. Development of the Pulse Tube Refrigerator as an Efficient and Reliable Cryocooler. *Proc. Institute of Refrigeration* **96**, 11 (2000).
- [Ram90] N. F. Ramsay. Molecular Beams. Oxford University Press, Oxford (1990).

- [Ran03] S. A. Rangwala, T. Junglen, T. Rieger, P. W. H. Pinkse, and G. Rempe. Continuous source of translationally cold dipolar molecules. *Phys. Rev. A* **67**, 043406 (2003).
- [Reg02] B. C. Regan, E. D. Commins, C. J. Schmidt, and D. DeMille. New Limit on the Electron Electric Dipole Moment. *Phys. Rev. Lett.* **88**, 071805 (2002).
- [Reg03] C. A. Regal, C. Ticknor, J. L. Bohn, and D. S. Jin. Creation of ultracold molecules from a Fermi gas of atoms. *Nature* **424**, 47 (2003).
- [Rie05] T. Rieger, T. Junglen, S. A. Rangwala, P. W. H. Pinkse, and G. Rempe. Continuous Loading of an Electrostatic Trap for Polar Molecules. *Phys. Rev. Lett.* **95**, 173002 (2005).
- [Rie07b] T. Rieger, P. Windpassinger, S. A. Rangwala, G. Rempe, and P. W. H. Pinkse. Trapping of Neutral Rubidium with a Macroscopic Three-Phase Electric Trap. *Phys. Rev. Lett.* **99**, 063001 (2007).
- [Rip05] J. J. Garcia-Ripoll, P. Zoller, and J. I. Cirac. Quantum information processing with cold atoms and trapped ions. *J. Phys. B: At. Mol. Opt. Phys.* **38**, S567 (2005).
- [Sak94] J. J. Sakurai. *Modern Quantum Mechanics*. Addison-Wesley Publishing Company, Inc., Reading, Massachusetts (1994).
- [San65] P. G. H. Sandars. The Electric Dipole Moment of an Atom. *Phys. Lett.* **14**, 194 (1965).
- [Saw08] B. C. Sawyer, B. K. Stuhl, D. Wang, M. Yeo, and J. Ye. Molecular Beam Collisions with a Magnetically Trapped Target. *Phys. Rev. Lett.* **101**, 203203 (2008).
- [Saw10] B. C. Sawyer, B. K. Stuhl, M. Yeo, V. Tscherbul, M. T. Hummon, Y. Xia, J. Klos, D. Patterson, J. M. Doyle and J. Ye. Cold heteromolecular dipolar collisions. arXiv:1008.5127v1 (2010).
- [Sek96] S. Sekatskii and J. Schmiedmayer. Trapping polar molecules with a charged wire. *Europhys. Lett.* **36**, 407 (1996).
- [Sch07] M. Schenk. State-selective detection of electrostatically guided cold formaldehyde, Master thesis, Technische Universität München (2007).
- [Sch07b] S. Schlunk, A. Marian, P. Geng, A. P. Mosk, G. Meijer, and W. Schöllkopf. Trapping of Rb Atoms by ac Electric Fields. *Phys. Rev. Lett.* **98**, 223002 (2007).

- [Sco88] G. Scoles. Atomic and Molecular Beam Methods, Vol. 1. Oxford University Press, New York (1988).
- [Shu10] E. S. Shuman, J. F. Barry, and D. DeMille. Laser cooling of a diatomic molecule. *Nature* **467**, 820 (2010).
- [Sko10] S. M. Skoff, R. J. Hendricks, C. D. J. Sinclair, J. J. Hudson, D. M. Segal, B. E. Sauer, E. A. Hinds, and M. R. Tarbutt. Diffusion, thermalization and optical pumping of YbF molecules in a cold buffer gas cell. arXiv:1009.5124v1 (2010).
- [Smi06] I. W. M. Smith. Reactions at Very Low Temperatures: Gas Kinetics at a New Frontier. *Angew. Chem. Int. Ed.* **45**, 2842 (2006).
- [Smi00] I. W. M. Smith and B. R. Rowe. Reaction Kinetics at Very Low Temperatures: Laboratory Studies and Interstellar Chemistry. *Acc. Chem. Res.* **33(5)**, 261 (2000).
- [Som09] C. Sommer, L. D. van Buuren, M. Motsch, S. Pohle, J. Bayerl, P. W. H. Pinkse, and G. Rempe. Continuous guided beams of slow and internally cold polar molecules. *Faraday Discuss.* **142**, 203 (2009).
- [Som10] C. Sommer, M. Motsch, S. Chervenkov, L. D. van Buuren, M. Zeppenfeld, P. W. H. Pinkse, and G. Rempe. Velocity-selected molecular pulses produced by an electric guide. *Phys. Rev. A* **82**, 013410 (2010).
- [Sti01] F. Stienkemeier and A. F. Vilesov. Electronic spectroscopy in He droplets. *J. Phys. Chem.* **115**, 10119 (2001).
- [Sto08] M. Stoll. Buffer-gas cooling and magnetic trapping of CrH and MnH molecules, Ph.D. thesis, Humboldt-Universität zu Berlin (2008).
- [Stu05] J. Stuhler, A. Griesmaier, T. Koch, M. Fattori, T. Pfau, S. Giovanazzi, P. Pedri, and L. Santos. Observation of Dipole-Dipole Interaction in a Degenerate Quantum Gas. *Phys. Rev. Lett.* **95**, 150406 (2005).
- [Stu08] B. K. Stuhl, B. C. Sawyer, D. Wang, and J. Ye. Magneto-optical Trap for Polar Molecules. *Phys. Rev. Lett.* **101**, 243002 (2008).
- [Tho87] H. R. Thorsheim, and J. Weiner. Laser-induced photoassociation of ultracold sodium atoms. *Phys. Rev. Lett.* **58**, 2420 (1987).
- [Tow75] C. H. Townes and A. L. Schawlow. Microwave Spectroscopy. Dover Publications, New York (1975).
- [Van07] N. Vanhaecke, U. Meier, M. Andrist, B. H. Meier, and F. Merkt. Multi-stage Zeeman deceleration of hydrogen atoms. *Phys. Rev. A* **75**, 031402R (2007).

- [vB09] L. D. van Buuren, C. Sommer, M. Motsch, S. Pohle, M. Schenk, J. Bayerl, P. W. H. Pinkse, and G. Rempe. Electrostatic Extraction of Cold Molecules from a Cryogenic Reservoir. *Phys. Rev. Lett.* **102**, 033001 (2009).
- [vdM08] S. Y. T. van de Meerakker, H. L. Bethlem, and G. Meijer. Taming molecular beams. *Nature Phys.* **4**, 595 (2008).
- [vdM09] S. Y. T. van de Meerakker and G. Meijer. Collision experiments with Stark-decelerated beams. *Faraday Discuss.* **142**, 113 (2009).
- [Wan98] H. Wang, and W. C. Stwalley. Ultracold photoassociative spectroscopy of heteronuclear alkali-metal diatomic molecules. *J. Chem. Phys.* **108**, 5767 (1998).
- [Wei98] J. D. Weinstein, R. deCarvalho, T. Guillet, B. Friedrich, and J. M. Doyle. Magnetic trapping of calcium monohydride molecules at millikelvin temperatures. *Nature* **395**, 148 (1998).
- [Wei02] J. D. Weinstein, R. deCarvalho, C. I. Hancox, and J. M. Doyle. Evaporative cooling of atomic chromium. *Phys. Rev. A.* **65**, 021604 (2002).
- [Wen79] W. A. Wensink, C. Noorman, and H. A. Dijkerman. Self-broadening and self-shifting of some rotational transitions of CF_3H and N_2O . *J. Phys. B: At. Mol. Phys.* **12**, 1687 (1979).
- [Wil04] D. R. Willey, R. E. Timlin Jr., C. D. Ruggiero, and I. A. Sulai. Low temperature pressure broadening of NH_3 by D_2 . *J. Chem. Phys.* **120**, 129 (2004).
- [Wil08a] S. Willitsch, M. Bell, A. D. Gingell, S. Procter, and T. P. Softley. Cold Reactive Collisions between Laser-Cooled Ions and Velocity-Selected Neutral Molecules. *Phys. Rev. Lett.* **100**, 043203 (2008).
- [Yan04] L. W. Yang, and G. Thummes. High frequency two-stage pulse tube cryocooler with base temperature below 20 K. *Cryogenics* **45**, 155 (2005).
- [Zep09] M. Zeppenfeld, M. Motsch, P. W. H. Pinkse and G. Rempe. Optoelectrical cooling of polar molecules. *Phys. Rev. A* **80**, 041401(R) (2009).
- [Zwi03] M. W. Zwierlein, C. A. Stan, C. H. Schunck, S. M. F. Raupach, S. Gupta, Z. Hadzibabic, and W. Ketterle. Observation of Bose-Einstein Condensation of Molecules. *Phys. Rev. Lett.* **91**, 250401 (2003).

List of Publications

- **Velocity-selected molecular pulses produced by an electric guide**
C. Sommer, M. Motsch, S. Chervenkov, L.D. van Buuren, M. Zeppenfeld, P.W.H. Pinkse, and G. Rempe.
Phys. Rev. A **82**, 013410 (2010).
- **Continuous guided beams of slow and internally cold polar molecules**
C. Sommer, L.D. van Buuren, M. Motsch, S. Pohle, J. Bayerl, P.W.H. Pinkse, and G. Rempe.
Faraday Discuss. **142** (2009).
- **Electrostatic Extraction of Cold Molecules from a Cryogenic Reservoir**
L.D. van Buuren, C. Sommer, M. Motsch, S. Pohle, M. Schenk, J. Bayerl, P.W.H. Pinkse, and G. Rempe.
Phys. Rev. Lett. **102**, 033001 (2009).
- **Collisional effects in the formation of cold guided beams of polar molecules**
M. Motsch, C. Sommer, M. Zeppenfeld, L.D. van Buuren, P.W.H. Pinkse, and G. Rempe.
New J. Phys. **11**, 055030 (2009).
- **Cold guided beams of water isotopologs**
M. Motsch, L.D. van Buuren, C. Sommer, M. Zeppenfeld, G. Rempe, and P.W.H. Pinkse.
Phys. Rev. A **79**, 013405 (2009).

Danksagung

Zum Abschluß möchte denjenigen danken, die zum Gelingen dieser Arbeit beigetragen haben, sowie andersweitig im Verlauf dieser Zeit Unterstützung geleistet haben.

An erster Stelle möchte ich **Prof. Gerhard Rempe** für die Möglichkeit danken, diese Arbeit in seiner Gruppe am MPQ durchzuführen. Seine sachkundigen Kommentare und Ideen waren eine große Hilfe beim Lösen von diversen Problemen am Experiment. Die rückhaltlose Unterstützung über so manche Durststrecke am Experiment haben erst die Weiterverfolgung zahlreicher Ansätze ermöglicht.

Auch **Dr. Pepijn Pinkse**, der mich in der kalten Molekülgruppe aufgenommen hat möchte ich an dieser Stelle danken. Wenn sich Probleme ergaben hat er stets zu deren Lösung einen großen Beitrag geleistet.

Dr. Laurens van Buuren möchte ich an dieser Stelle meinen besonderen Dank aussprechen. Als Zwei-Mann-Team am Experiment (mit gelegentlichen Ausnahmen) waren es manchmal schwierige Zeiten, die sich durch lange Durststrecken ausgezeichnet haben. Dank seines guten Spürsinns und genialer Auswertungsarbeit ließen sich dennoch vielfältige Ergebnisse gewinnen. Die allseits gute Arbeitsatmosphäre im Labor, die durch ihn verbreitet wurde (gute Musik trug ihr übriges dazu bei), hat so manche mühsame Messung und Umbauarbeit (Vakuunkammer auf- und zumachen) ertragbar gemacht. Ohne seine Unterstützung hätte es die Velocity-Selection-Veröffentlichung gar nicht gegeben. Wenn es Probleme gab oder ich eine Idee aussprechen wollte hat er stets zugehört (auch bei besonders kreativen Ideen) und sich bemüht den Sachverhalt klar darzustellen.

Bei **Dr. Michael Motsch** möchte ich mich an dieser Stelle für die sehr gute Zusammenarbeit und die stets guten und ehrlichen Ratschläge bedanken. Wenn man Hilfe im Labor oder beim Aufbau eines Manuskriptes brauchte, hat er einem ohne Rückhalte seine volle Aufmerksamkeit gewidmet. Seine großzügige und zuvorkommende Art ("kannst mein Labor übernehmen") hat einen wesentlichen Beitrag zum Gelingen dieser Forschungsarbeit geleistet. Auch nach Beendigung seiner Tätigkeit in der Rempe Forschungsgruppe konnte ich mich auf seine Hilfe stets verlassen.

Auch **Dr. Sotir Chervenkov** möchte ich an dieser Stelle meinen Dank aussprechen. Seine Unterstützung am Velocity-Selection Experiment hat maßgeblich zum Erfolg dieser Arbeit geführt. Die unzähligen Simulationen und die akribischen Ermittlungen hinsichtlich der theoretischen Modellierung der erworbenen Messdaten

wurden durch seine Hilfe entscheidend beeinflusst. Seine Bereitschaft für philosophische Diskussionen hat so manchen Arbeitstag verbessert.

Bei den Moleküles und Ex-Moleküles, **Martin Zeppenfeld**, **Babara Englert**, **Rosa Glöckner**, **Xing Wu**, **Markus Schenk**, **Manuel Mielenz**, **Sebastian Pohle** und **Dr. Thomas Rieger** möchte ich mich an dieser Stelle besonders bedanken. Vor allem Martin Zeppenfeld der es mir nochmals ermöglicht hat meinen Horizont bzgl. weiteren physikalischen Techniken zu erweitern und Babara Englert, die den Büroalltag aufgelockert hat und beim Testen von so mancher verrückten Idee stets bereit gewesen war, möchte ich auf diesem Wege nochmals meinen Dank aussprechen. Markus Schenk möchte ich auf diesem Wege für die lustige Zeit und den geliehenen Helium-Neon Laser danken (endlich durfte ich mal mit einem Laser spielen). Manuel Mielenz danke ich für die zahlreichen interessanten Diskussionen über die Welt und andere Dinge.

Josef Bayerl, **Helmuth Stehbeck**, **Franz Denk** und **Thomas Wiesmeier** haben einen unschätzbaren Beitrag für das Gelingen des Experiments geliefert. Die meisten technischen Ideen wurden stabiler und zuverlässiger umgesetzt, als man es zu träumen gewagt hätte.

Allen **Kavitäten**, **BEClern**, **Pistoleros**, **Q-Gates** und **Ionenfängern** sei für die reibungslose Zusammenarbeit, bereitwillige Hilfe bei der Lösung von alltäglichen Problemen, sowie für so manche interessanten Diskussionen gedankt.

Ein herzliches Dankeschön möchte ich hier meinen **Freunden** entgegenbringen. Mein Hilfeschreie wurden so manches mal erhört.

Meinen Eltern **Hans Christian Sommer** und **Josephine Nana Sommer** möchte ich auf diesem Wege meinen Dank aussprechen. Vorallem meinem Vater der mich von Kind auf an für die Wissenschaft begeistert hat. Meinem Bruder **Asher Sommer** möchte ich hier für die zahlreichen guten Ratschläge danken.